POLITECNICO DI MILANO
DEPARTMENT OF MATHEMATICS
DOCTORAL PROGRAMME IN MATHEMATICAL MODELS AND METHODS IN
ENGINEERING

# MATHEMATICAL AND NUMERICAL MODELING OF CARDIAC ELECTROMECHANICS IN VENTRICLES WITH ISCHEMIC CARDIOMYOPATHY

Doctoral Dissertation of:
**Matteo Salvador**

Supervisor:
**Prof. Alfio Maria Quarteroni**

Coadvisor:
**Prof. Luca Dede'**

The Chair of the Doctoral Program:
**Prof. Irene Maria Sabadini**

2022 – XXXIV PhD cycle

*Progress has not followed a straight ascending line,
but a spiral with rhythms of progress and retrogression,
of evolution and dissolution.*

**Johann Wolfgang von Goethe**

# ABSTRACT

The cardiac function is the result of the concerted action of several physical phenomena, ranging from the cellular scale to the organ level. Among these, an important role is played by the coupling between the electrical activity of the heart and its mechanical contraction. For this reason, numerical simulations of ventricular electromechanics play nowadays a crucial role in computational cardiology and precision medicine. Indeed, it is of outmost importance to analyze and better address pathological conditions by means of anatomically accurate and biophysically detailed individualized computational models that embrace electrophysiology, mechanics and hemodynamics.

In this thesis, we develop a novel electromechanical model for the human ventricles of patients affected by ischemic cardiomyopathy. This is made possible thanks to the introduction of a spatially heterogeneous coefficient that accounts for the presence of scars, grey zones and non-remodeled regions of the myocardium. We couple this 3D electromechanical model with either a 2-element windkessel afterload model or a ØD closed-loop circulation model by an approach that is energy preserving. Our mathematical framework keeps into account the effects of mechano-electric feedbacks, which model how mechanical stimuli are transduced into electrical signals. Moreover, it permits to classify the hemodynamic nature of tachycardias. These aspects are very important for the clinical exploitation of our electromechanical model.

We propose two segregated-intergrid-staggered (SIS) numerical schemes to solve this 3D-ØD coupled problem. Specifically, we consider two partitioned strategies for which different space-time resolutions are employed according to the specific core model. In particular, numerical models for cardiac electrophysiology require a finer representation of the computational domain and a smaller time step than those used for cardiac mechanics. For the first numerical scheme (SIS1), we introduce intergrid transfer operators based on Rescaled Localized Radial Basis Functions to accurately and efficiently exchange information among the several Partial Differential Equations (PDEs) of the electromechanical model. Different (potentially non-nested) meshes and first-order Finite Elements can be used for the space discretization of the PDEs. The second numerical scheme (SIS2) that we propose employs another flexible and scalable intergrid transfer operator, which allows to interpolate Finite Element functions between nested meshes and, possibly, among arbitrary Finite Element spaces for the different core models. We perform numerical simulations both in sinus rhythm and ventricular tachycardia for different scenarios of clinical interest.

We also design a Machine Learning method to perform real-time numerical simulations of cardiac electromechanics. Our method allows to derive a reduced-order model (ROM), written as a system of Ordinary Differential Equations, in which the right-hand side is represented by an Artificial Neural Network (ANN), that possibly depends on a set of parameters associated with the model

to be surrogated. This method is non-intrusive, as it only requires a collection of pressure and volume transients obtained from the full-order model (FOM). Once trained, the ANN-based ROM can be coupled with hemodynamic models for the blood circulation external to the heart, in the same manner as the original electromechanical model, but at a dramatically reduced computational cost. We demonstrate the effectiveness of the proposed strategy on two relevant contexts in cardiac modeling. We employ the ANN-based ROM to perform a global sensitivity analysis on both the electromechanical and the hemodynamic models. Then, we perform a Bayesian estimation of a couple of parameters starting from noisy measurements of two scalar outputs.

By replacing the FOM of cardiac electromechanics with the ANN-based ROM, we perform in a few hours of computational time all the numerical simulations, which would be unaffordable, because of their overwhelming computational cost, if carried out with the FOM. As a matter of fact, our ANN-based ROM is able to speedup the numerical simulations by more than three orders of magnitude.

**Keywords:** cardiac electromechanics, ischemic cardiomyopathy, ventricular tachycardia, numerical methods, intergrid transfer operators, numerical simulations, machine learning, reduced-order modeling, global sensitivity analysis, bayesian parameter estimation, uncertainty quantification.

# SOMMARIO

La funzione cardiaca è il risultato dell'azione concertata di diversi fenomeni fisici, che vanno dalla scala cellulare al livello dell'organo. Tra questi, un ruolo importante è svolto dall'accoppiamento tra l'attività elettrica del cuore e la sua contrazione meccanica. Per questo motivo, le simulazioni numeriche di elettromeccanica ventricolare giocano oggi un ruolo cruciale nella cardiologia computazionale e nella medicina di precisione. Infatti, risulta di massima importanza analizzare e affrontare meglio le condizioni patologiche per mezzo di modelli computazionali personalizzati, accurati anatomicamente, e dettagliati dal punto di vista biofisico, che coinvolgano elettrofisiologia, meccanica ed emodinamica.

In questa tesi, sviluppiamo un nuovo modello elettromeccanico per i ventricoli umani di pazienti affetti da cardiopatia ischemica. Ciò è reso possibile grazie all'introduzione di un coefficiente spazialmente eterogeneo che tiene conto della presenza di cicatrici, zone grigie e regioni non rimodellate del miocardio. Accoppiamo questo modello elettromeccanico 3D con un modello windkessel a 2 elementi o un modello di circolazione ØD mediante un approccio che preserva l'energia. Teniamo conto degli effetti dei feedback meccano-elettrici, i quali modellano il modo in cui gli stimoli meccanici vengono trasdotti in segnali elettrici. Inoltre, il nostro approccio permette di classificare la natura emodinamica delle tachicardie. Questi aspetti sono molto importanti per l'uso in ambito clinico del nostro modello elettromeccanico.

Proponiamo due schemi numerici per risolvere questo problema accoppiato 3D-ØD. Nello specifico, consideriamo due strategie partizionate per le quali vengono impiegate diverse risoluzioni spazio-temporali a seconda dello specifico modello. In particolare, i modelli numerici per l'elettrofisiologia cardiaca richiedono una rappresentazione più fine del dominio computazionale e un passo temporale minore rispetto a quelli utilizzati per la meccanica cardiaca. Per il primo schema numerico, introduciamo operatori di trasferimento basati su funzioni a base radiale, localizzate e riscalate, al fine di scambiare informazioni in modo accurato ed efficiente tra le diverse equazioni differenziali alle derivate parziali del modello elettromeccanico. Griglie differenti (potenzialmente non annidate) ed elementi finiti del primo ordine, possono essere usati per la discretizzazione spaziale delle equazioni differenziali. Il secondo schema numerico che proponiamo utilizza un altro operatore di trasferimento flessibile e scalabile, che consente di interpolare funzioni agli elementi finiti tra griglie annidate e, possibilmente, tra spazi agli elementi finiti arbitrari per i diversi modelli. Effettuiamo simulazioni numeriche sia in ritmo sinusale sia in tachicardia ventricolare per diversi scenari di interesse clinico.

Elaboriamo anche un metodo basato sull'apprendimento automatico per effettuare simulazioni numeriche di elettromeccanica cardiaca in tempo reale. Il nostro metodo permette di derivare un modello ridotto, scritto come un sistema

di equazioni differenziali ordinarie, in cui il membro di destra è rappresentato da una rete neurale, che dipende da un insieme di parametri associati con il modello da surrogare. Questo metodo non è intrusivo, in quanto richiede solo una raccolta di transitori per pressione e volume, ottenuti dal modello completo. Una volta trainato, il modello ridotto basato su rete neurale può essere accoppiato con modelli emodinamici per la circolazione sanguigna esterna al cuore, allo stesso modo del modello elettromeccanico originale, ma ad un costo computazionale notevolmente ridotto. Dimostriamo l'efficacia della strategia proposta in due contesti rilevanti nella modellistica cardiaca. Utilizziamo il modello ridotto basato su rete neurale per effettuare un'analisi di sensitività globale, sia sul modello elettromeccanico sia su quello emodinamico. Successivamente, eseguiamo una stima bayesiana di due parametri partendo da misurazioni rumorose di due valori scalari.

Sostituendo il modello completo di elettromeccanica cardiaca con il modello ridotto basato su rete neurale, effettuiamo in poche ore di tempo di calcolo tutte le simulazioni numeriche, le quali sarebbero insostenibili, a causa del loro enorme costo computazionale, se eseguite con il modello completo. Infatti, il nostro modello ridotto basato su rete neurale è in grado di accelerare le simulazioni numeriche di oltre tre ordini di grandezza.

**Parole chiave:** elettromeccanica cardiaca, cardiopatia ischemica, tachicardia ventricolare, metodi numerici, operatori di trasferimento, simulazioni numeriche, apprendimento automatico, riduzione di modello, analisi di sensitività globale, stima bayesiana di parametri, quantificazione dell'incertezza.

# ACKNOWLEDGEMENTS

# CONTENTS

X

## LIST OF TABLES

## LIST OF ABBREVIATIONS

ANN  Artificial neural network

AP  Action potential

APD  Action potential duration

AV  Aortic valve

AVN  Atrioventricular node

BCL  Basis cycle length

BDF  Backward differentiation formulas

CV  Conduction velocity

DADS  Delayed afterdepolarizations

DBP  Diastolic blood pressure

EADS  Early afterdepolarizations

EDP  End-diastolic pressure

EDV  End-diastolic volume

EF  Ejection fraction

ERP  Effective refractory period

ESP  End-systolic pressure

ESV  End-systolic volume

FEM  Finite element method

FOM  Full-order model

HR  Heart rate

ICI  Ionic current interpolation

ICM  Ischemic cardiomyopathy

IMEX  Implicit-explicit

LA  Left atrium

LV  Left ventricle

LGE  Late gadolinium enhancement

MAP  Mean arterial pressure

MCMC  Markov Chain Monte Carlo

MEF  Mechano-electric feedback

MRI  Magnetic Resonance Imaging

MV  Mitral valve

GMEF  Geometry-mediated MEF

ODE  Ordinary differential equation

PDE  Partial differential equation

PV  Pressure-volume

QOI  Quantity of interest

RA  Right atrium

ROM  Reduced-order model

RL-RBF  Rescaled localized radial basis function

RV  Right ventricle

SACS  Stretch-activated channels

SAN  Sinoatrial node

SIS  Segregated-intergrid-staggered

SBP  Systolic blood pressure

SCD  Sudden cardiac death

SR  Sinus rhythm

SV  Stroke volume

TTP  ten Tusscher-Panfilov

VF  Ventricular fibrillation

VT  Ventricular tachycardia

# INTRODUCTION

The heart pumps blood into the circulatory system, delivering oxygen and nutrients to all the cells of the human body while assisting in the removal of metabolic wastes [72, 83, 87]. The mechanical contraction of the heart is triggered by the electrical excitation of the cardiac cells [159, 175]. This excitation-contraction coupling, which occurs at the microscopic level and upscales to the tissue level (the macroscopic scale), is essential to determine the electromechanical activity of the heart [35, 137]. In this framework, an anatomically detailed and biophysically accurate representation of the human heart requires multiphysics and multiscale mathematical models of several physical processes, ranging from the cellular to the organ scale [8, 138, 173].

Since cardiovascular diseases are a very common cause of death worldwide [108], numerical simulations of cardiac electromechanics represent a promising tool to address both physiological and pathological conditions, such as cardiac arrhythmias, which arise from an irregular electrical activity of the human heart, as highlighted e.g. in [55, 138, 171, 183, 192, 196]. Among them, ventricular tachycardia (VT), which manifests as a fast heart rate (HR), is a life threatening rhythm disorder that predisposes patients to sudden cardiac death (SCD). Clinically, patients with ventricular dysfunction are more likely to develop severe VT, which may be classified as hemodynamically stable or unstable. If stable, antiarrhythmic drugs are generally employed, else if unstable, cardioversion is normally needed [52]. According to the specific pathogenesis, the stability of the VT remains the same or may change over time. Moreover, it may also degenerate towards ventricular fibrillation (VF), a potentially lethal condition in which the ventricular activity is fully disorganized and chaotic [164].

Personalized computational heart models are well-suited to identify fundamental mechanisms of arrhythmogenesis. Biophysically detailed models of cardiac electrophysiology are well-established and have been widely utilized for VT identification and treatment [6, 133]. Indeed, numerical simulations circumvent experimental and clinical limitations by giving the possibility to test different hypotheses and gain insights in the cardiac function [71]. However, very few studies have been able to create models that synthesize both electrical and mechanical activities into a coherent form [8, 128]. Furthermore, a missing component in the electromechanical studies is often the representation of tachycardias and the effect of heart contraction in the re-entrant circuits that underlie arrhythmias. Prior work suggests that a greater arrhythmia risk could be due to abnormal mechano-electric feedbacks (MEFs), which define greater electrical instability [85, 89, 177]. The cardiac mechano-electric coupling presents proarrhythmic effects in pathological scenarios and might induce extra stimuli, early afterdepolarizations (EADs) or delayed afterdepolarizations (DADs) [89, 179]. However, it is unknown from a clinical perspective which is the role of MEFs during VT, and it is difficult to dissect their mechanisms in a clinical study [162].

In this thesis, we propose a novel electromechanical model [8, 9, 21, 55, 92, 103, 113, 147, 173] that can be employed for human ventricles with ischemic cardiomyopathy (ICM) to study how MEFs affect the sinus rhythm (SR) behavior and VT arrhythmia dynamics. These aspects are indeed relevant in the context of computational cardiology and still not fully elucidated [36, 85, 89, 177, 179, 184, 188]. This mathematical model allows us to provide non-invasive, personalized assessments of VT circuits and the corresponding hemodynamic consequences, which have significant clinical implications [162]. Our electromechanical model results from the concerted action of several physical processes – electrophysiology, biochemistry, mechanics – interacting at different spatial and temporal scales [31, 43, 161, 171], ranging from nanometers to centimeters and from nanoseconds to seconds, respectively [19, 83]. We describe all of these phenomena by means of systems of Partial Differential Equations (PDEs) and Ordinary Differential Equations (ODEs), which realize the coupling of electrophysiology, ionic model, generation of active force or active deformation at the cellular and tissue levels, passive mechanics of the myocardium, blood fluid dynamics. For the electric part we consider the monodomain equation coupled with the ten Tusscher-Panfilov (TTP06) ionic model [132, 158, 186]. For the mechanical part we use the Guccione model [69, 70] together with either Artificial Neural Network (ANN) based active stress models [143] or a phenomenological active strain model with transmural heterogeneous thickening of the myocardium [2, 3, 13]. This 3D electromechanical model is coupled with either a 2-element windkessel afterload model or a ØD hemodynamic model of the whole cardiovascular system. In the latter case, we refer to a closed-loop 3D-ØD mathematical model, where we will always consider a 3D electromechanical description of the left ventricle only.

The 3D-ØD coupled problem is discretized by means of novel segregated schemes, where the different electromechanical core models are sequentially solved [45, 131, 148, 161]. These partitioned strategies often suffer from instability issues [54, 124, 134, 146], despite being computationally more attractive than monolithic schemes [61, 198]. Nonetheless, our numerical approaches enable to couple the core models describing the different physics in a numerically stable manner, yet allowing to adopt different space and time resolutions to match their characteristic scales [21, 55, 113, 138, 148, 161, 189]. With this aim, we develop flexible intergrid transfer operators [1, 62, 161] to accurately and efficiently interpolate relevant scalar and vector fields among the core models that are defined on different computational meshes. Moreover, we implement a staggered approach by considering different time steps according to the characteristic time scale of the different core models [45]. The computational framework presented in this thesis achieves a very favorable trade-off between the biophysical detail of the underlying mathematical models and computational efficiency of the corresponding solver. Mathematical rigor, model accuracy and computational efficiency are the landmarks of the proposed electromechanics solver.

Nevertheless, electromechanical simulations with sophisticated mathematical models and accurate anatomical descriptions are known to be computationally

demanding and time consuming [55, 138, 171, 173, 183, 192, 196]. This poses numerous challenges to their effective and reliable clinical exploitation. In recent times, Machine Learning algorithms including Gaussian Processes, ANNs, decision tree algorithms such as eXtreme Gradient Boosting and K-Nearest Neighbor have been applied in the context of cardiac modeling [27, 42, 44, 47, 98] to build suitable emulators in order to perform sensitivity analysis and parameter estimation with simplified models, settings or geometries [40, 79, 95, 100, 103, 123, 168, 181, 205]. In this thesis, we propose a Machine Learning method to build a reduced-order model (ROM) of cardiac electromechanical models [149]. Our approach relies on an ANN-based method that can learn a time-dependent differential equation from a collection of input-output pairs [141]. Conversely to existing approaches, we only surrogate the time-dependent pressure-volume relationship of the studied cardiac chamber, namely the left ventricle, while we do not reduce the model describing external circulation, whether it is a windkessel-type preload-afterload model or a closed-loop circulation model. In other terms, we derive a ROM for the computationally demanding components, while we consider the full-order model (FOM) for the lightweight ones. Unlike for emulators, for which the online phase consists in an evaluation of the map linking model parameters to Quantities of Interest (QoIs), with our approach the online phase consists instead in a numerical simulation, in which the ROM of the electromechanical model is coupled with the circulation model, at a very low computational cost. As a matter of fact, these numerical simulations can be performed in real-time on a standard laptop for arbitrarily long time ranges. This fast and reliable ROM can be exploited in numerous applications in which instead the use of the FOM would be virtually unaffordable [149]. Indeed, our ROM can be effectively employed for a quantitative evaluation on how much each parameter affects the outputs of the model, that is global sensitivity analysis and forward uncertainty quantification. Moreover, it can be used to develop fully personalized computational models, where model parameters are calibrated on a patient-specific basis. Additionally, it can be employed to quantify how uncertainty on measured data reverberates on parameter uncertainty, that is backward uncertainty quantification.

GOALS AND OBJECTIVES

The main goal of this thesis is building a multiphysics and multiscale mathematical model of cardiac electromechanics for human ventricles, with a focus on ICM, along with proper segregated-intergrid-staggered (SIS) schemes for its numerical discretization. We present a mathematical parametrization in which we model scars, i.e. infarcted areas, grey zones, i.e. peri-infarcted areas, and healthy regions. Furthermore, we develop suitable interpolants to transfer information among the core models defined on different meshes of the same computational domain, which is always represented by an idealized or realistic left ventricle.

Our mathematical approach allows to perform personalized electromechanical simulations in both physiological conditions and complex pathological sce-

narios involving arrhythmias. With respect to electrophysiological simulations, the presence of MEFs enhances our comprehension of VT dynamics, origin and nature, while providing further insights for treatment planning in patient-specific cases.

Besides the development, calibration and validation of our electromechanical model in SR and under VT, in this thesis we also aim at dramatically reducing the computational cost associated to its numerical approximation, without compromising accuracy, by means of suitable ROMs. In particular, we develop a Machine Learning method to construct a ROM of cardiac electromechanics in a non-intrusive manner, which enables real-time numerical simulations of the cardiac function. This ROM can be coupled with preload-afterload models or closed-loop circulation models to perform global sensitivity analysis, parameter estimation and uncertainty quantification in a fast and reliable way.

## DESIGN REQUIREMENTS

We aim at designing a comprehensive mathematical and numerical model of cardiac electromechanics suitable for LVs with ICM. The underlying numerical methods need to be flexible, accurate and scalable. In this manner, once imaging with contrast enhancement techniques and (possibly) pressure-volume measurements are available, personalized large scale electromechanical simulations in patient-specific cases can be performed, both in SR and under VT. Our numerical approach must allow for a high level of detail in both space and time discretizations, where millions of unknowns will be determined for each time step over several heartbeats. Our mathematical model has to encompass electrophysiology and mechanics for the heart and hemodynamics for the whole cardiovascular system. In this way, it would give novel perspectives and relevant information to address pathological conditions involving arrhythmias. Due to their intrinsic complexity, HPC facilities must be employed for this type of numerical simulations. The computational costs should vary from hours to a few days at maximum, according to the required resolution and the number of CPUs that are employed. Indeed, our parallel framework must guarantee good scalability properties up to tens of thousands of cores.

Once this detailed electromechanical model has been developed, there is certainly space for model order reduction, so that we can derive computational models that run in real-time on a standard computer without compromising accuracy. In this manner we can match the clinical time frames while providing important indications. Indeed, ROMs are intrinsically tailored to many-query applications. Among them, solution of inverse problems, sensitivity analysis and uncertainty quantification are surely landmarks that must be addressed efficiently by means of fast and reliable numerical simulations.

## ORIGINAL CONTRIBUTIONS

The original contributions of this thesis are listed as follows.

- We develop a novel 3D electromechanical model suitable for ICM that is coupled with either a 2-element windkessel afterload model or a ØD closed-loop circulation model of the whole cardiovascular system. Specifically,

  - we introduce a spatially heterogeneous coefficient in the 3D mathematical model to account for the presence of scars, grey zones and non-remodeled regions of the myocardium in the left ventricle [162].

  - we model MEFs [41, 73]. Among them, geometry-mediated contributions incorporate the effects of the mechanical displacement on the cardiac tissue, while other physiological processes, such as nonselective stretch-activated channels (SACs), act at the level of single cardiac cells [184].

  - our electromechanical framework permits to classify the hemodynamic nature of VT, which can be either stable or unstable, and to capture mechanically relevant indications of VT, such as the incomplete relaxation of sarcomeres.

  - we prove that our closed-loop 3D-ØD mathematical model satisfies a balance of mechanical energy. We provide a quantitative insight in the cardiac energy distribution by computing the different terms of this balance during a heartbeat. We highlight the features of different compartments during the different stages of the heartbeat, i.e. when energy is injected, dissipated or transformed. Thanks to our mathematical model we can also assess the validity of simplified relationships commonly used in the clinical practice to estimate the main indicators of heart energy distribution [81]. We prove that the coupling between the 3D electromechanical model and the ØD circulation model is consistent with the principles of energy conservation. Indeed, we impose a boundary condition at the base of the LV that we denote as energy-consistent boundary condition [143, 148]. Moreover, we apply a boundary condition at the epicardium that keeps into account the effect of the pericardial sac [147, 161].

- We propose two different partitioned schemes for the numerical discretization of this 3D-ØD coupled problem. Specifically,

  - space discretization is performed by means of the Finite Element Method (FEM). A first SIS (SIS1) scheme proposed is based on Rescaled Localized Radial Basis Functions (RL-RBF) [46, 56, 57], which allow to interpolate in a fast and accurate manner both scalar and vector fields approximated with first-order Finite Elements among completely independent, i.e. non-nested, tetrahedral meshes [161]. On the other hand, the second SIS (SIS2) scheme exploits the octree structure of hexahedral meshes to transfer information among nested meshes and arbitrary Finite Element spaces.

  - we design proper implicit-explicit (IMEX) schemes [137] to minimize the number of nonlinear systems to solve, limiting the use of implicit

solvers only for those core models that would otherwise lead to a severe restriction on the time step. In particular, our numerical scheme allows to update the variables of the ionic and active stress models without the need of solving any algebraic system (neither nonlinear nor linear), and it allows to update the electrical potential and active strain variable by solving a single linear system at each time iteration. The nonlinear system of our mathematical model is associated with cardiac mechanics, for which explicit or semi-implicit schemes are unstable, unless a very fine time step is employed, because of the strong nonlinearities contained in the constitutive law [138].

– we couple the 3D and the ∅D models [20, 76] in the segregated scheme by means of a novel numerical approach. We reinterpret the cavity pressure of the LV as a Lagrange multiplier to enforce a volumetric constraint to couple the ∅D circulation model and the 3D electromechanical model. We end up with a saddle-point structure for the mechanical problem, which is numerically solved by using the Schur complement reduction [18]. Our scheme is numerically stable and can be applied to all the phases of the cardiac cycle (filling phase, ejection phase and isovolumetric contraction and relaxation phases) without the need of switching among different ∅D models and without considering any change in the parameters of the equations [148, 162]. This approach enables the numerical simulation of VT.

– looking towards the patient-specific customization of our electromechanical model, we note that cardiac geometries are mostly acquired in vivo with imaging techniques. In this setting, atria and ventricles are loaded, mainly by the pressures acting on the endocardium, and present residual internal stresses. Therefore, the stress-free configuration, to which the equations for cardiac electromechanics must refer, is not known a priori. As this is necessary to set the reference configuration for the mechanical model, we formulate an inverse problem aimed at recovering such stress-free reference configuration starting from the geometry acquired from medical imaging. We also propose a novel and robust algorithm to solve this inverse problem. Our reference configuration recovery algorithm keeps into account the distribution of infarct zones, peri-infarct areas and non-remodeled regions. Nevertheless, its numerical resolution can be computationally demanding for highly refined meshes. For this reason, our algorithm for the recovery of the reference configuration is supplied by a projection technique that accurately retrieves the stress-free configuration from a coarser and independent representation of the computational domain [147, 148].

• We develop an ANN-based ROM that enables real-time electromechanical simulations. In the so-called offline phase, the ANN-based ROM is built from a database of numerical simulations that are previously obtained with

the FOM itself. Then, in the online phase, the ANN-based ROM is used as a surrogate of the FOM, e.g. to perform global sensitivity analysis or parameter estimation. Specifically,

- the ANN-based ROM of cardiac electromechanics is independent of the circulation model to which is coupled.

- our ANN-based ROM allows for reliable predictions even over longer time spans than those used during training.

- the output of the numerical simulations obtained with our ANN-based ROM is not limited to a list of scalar values, called QoIs. Indeed, it contains the transient of pressures and volumes of the heart chamber that is surrogated and of the compartments of the circulation model.

- only the variability with respect to the 3D electromechanical model needs to be learned by our ANN-based ROM, since the ∅D circulation model remains explicitly represented.

ORGANIZATION OF THE THESIS

This thesis is organized as follows.

- In Chap. 1 we provide an overview of basic cardiac anatomy, with a focus on the electromechanical function of the heart. Moreover, we explain the mechanisms of arrhythmias and the pathophysiology of ICM.

- In Chap. 2 we introduce the mathematical model of cardiac electromechanics for human ventricles with ICM. We derive the balance of mechanical energy for the 3D-∅D closed-loop model and we show the reference configuration recovery algorithm. Then, we propose two possible SIS numerical schemes to perform the space and time discretizations of this 3D-∅D coupled problem.

- In Chap. 3 we present some electromechanical simulations in SR on idealized and realistic LVs without ICM to show the features of our mathematical and numerical frameworks in physiological conditions.

- In Chap. 4 we present some electromechanical simulations on LVs with ICM, both in SR and VT. We discuss the effects of MEFs and we make comparisons with respect to electrophysiological simulations. We also manually calibrate the parameters of our electromechanical model to fit the available clinical data for a patient-specific LV with ICM.

- Chap. 5 is devoted to Machine Learning and to ROMs. We explain the mathematical approach behind the ANN-based ROM of cardiac electromechanics that we build. Then, we address variance-based global sensitivity analysis and Bayesian parameter estimation by means of the Markov Chain

Monte Carlo (MCMC) method, to show the capabilities and the performances of our ANN-based ROM.

In Conclusions, we make some final remarks and draw some perspectives for future research.

# CARDIAC ANATOMY AND PATHOPHYSIOLOGY

In this chapter we provide an overview of cardiac physiology. We consider the different physics that interact in cardiac electromechanics, namely electrophysiology, mechanical activation, passive mechanics and blood circulation. We start by giving some information on the cardiac function in healthy conditions. Then, we focus on pathological scenarios involving arrhythmias and ICM.

## 1.1 THE CARDIAC FUNCTION

The heart is a hollow muscular organ composed of cardiomyocytes, the cells that constitute the cardiac muscles. Its role is to pump blood through all the blood vessels of the circulatory system. Blood provides the body with oxygen and all kinds of necessary nutrients. It also assists in the removal of metabolic wastes produced by cellular reactions [87]. In humans, the heart is located in the middle compartment of the chest, between the lungs [35, 72, 83].

The human heart is a double pump made by four chambers. In the lower part, there are the left ventricle (LV) and the right ventricle (RV), which are also called discharging chambers. The two ventricles are divided by the interventricular septum. In the upper part, there are the left atrium (LA) and the right atrium (RA), which are separated by the interatrial septum. We refer to the atria as receiving chambers [35]. Atria and ventricles are separated by the atrioventricular septum, which contains the mitral valve (MV) in the left heart and the tricuspid valve in the right heart. The LV is connected to the aorta through the aortic valve (AV), whereas the RV has a connection with the pulmonary artery via the pulmonary valve [72]. In Fig. 1.1, we depict a schematic diagram of the human heart.

The RA receives blood mainly from the body's two major veins, the superior and inferior venae cavae. A small amount of blood comes inside the RA from the coronary circulation, through the coronary sinus, which is immediately above and to the middle of the opening of the inferior vena cava. The RA drives the blood towards the RV, which synchronously contracts, to push it through the pulmonary circulation, to the lungs and then back to the heart. The LA receives oxygenated blood back from the lungs via one of the four pulmonary veins. Then, this blood moves towards the LV. This last cardiac chamber exerts a huge force to pump oxygenated blood towards the aorta, and then to the entire systemic circulation around the body, until even the smallest vessels are all reached by nutrients and oxygen. All the presented cardiac functions, involving mechanics and hemodynamics, are triggered and coordinated by the electrical activity of the heart [83], which will be detailed in Sec. 1.3.
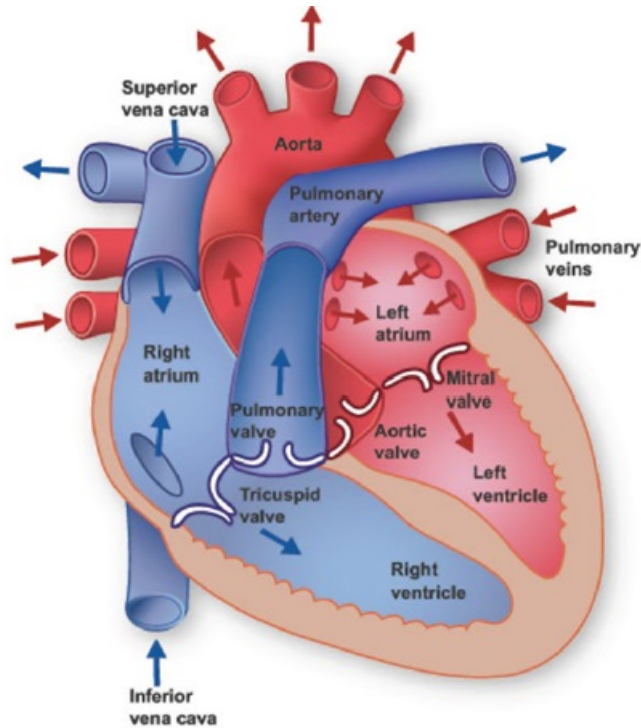
Figure 1.1: Schematic diagram of the anatomy of the heart (image taken from [35]).

The cardiac muscle is generally called myocardium. While the atria are usually quite thin, the thickness of the ventricles is never negligible [35]. In particular, atria thickness ranges from 1 to 4 mm. LV wall dimension goes from 7 to 11 mm, while the mean RV thickness ranges from 4 to 7 mm [83]. Indeed, the LV wall is known to be about two/three times thicker than the right one [83]. Atria and ventricles are differentiated into endocardium, which represents the internal wall, and epicardium, for the external one. There is also a fibro-serous, fluid-filled sac that surrounds the heart: this is the so called pericardium. In Fig. 1.2, we show the heart wall structure, going from the endocardium to the pericardial sac.

## 1.2 CLASSIFICATION OF CARDIAC CELLS

Cardiac cells can be categorized as [35]:

- Working cardiomyocytes: they define the atrial and ventricular tissues and are responsible for force development. They present a tubular structure, with a diameter of about 10-20 μm and a length of about 50-150 μm. Myocytes volume and shape can be complex and variable, according to the tissue region, developmental stage and disease processes. They are covered by a lipid membrane, the sarcolemma, and contain one or more nuclei, mitochondria, myofibrils, the sarcoplasmic reticulum, sarcomeres, the cytoskeleton anchoring the different organelles and an aqueous solution, the sarcoplasm, filling the intracellular space. The sarcolemma is a semi-
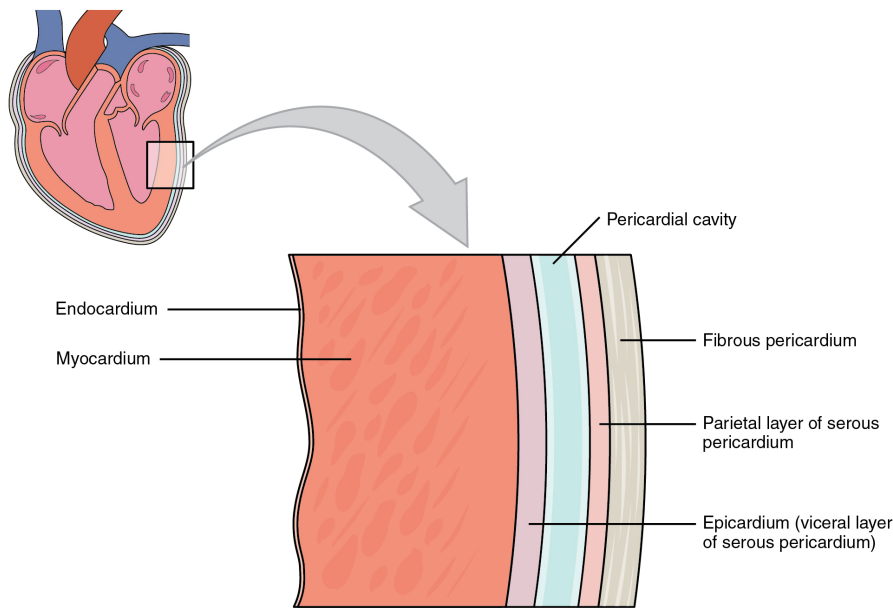
Figure 1.2: Structure of the heart wall (image taken from [200]).

permeable barrier and contains ionic channels, pumps and exchangers that allow the inward and outward currents involved in the generation of the action potential (see Sects. 1.3 and 1.4), as well as other proteins that contribute to cell adhesion and signalling. Cardiomyocytes exhibit a periodic structure with crossed striations formed by alternating segments of thick and thin protein filaments. The sarcolemma envelops the so called T-tubules, which allow quick penetration of the depolarization process to the interior of the cell and play an important role in the excitation-contraction coupling (see Sec. 1.5).

- Nodal cells: they are able to autonomously activate themselves thanks to the presence of particular ionic channels. The sinoatrial node and the atrioventricular node are made by this kind of cells (see Sec. 1.3). Compared with working myocytes, they are smaller, have limited contractile activity and lack T-tubules. They are also susceptible to autonomic influences thanks to the presence of specific innervation.

- Conduction cells: they are also known as Purkinje cells and have a lot of aspects in common with working myocytes, but with larger diameter, reduced contractile proteins and a few T-tubules. They are distributed over the ventricles of the human heart.

- Fibroblasts: they are mechano-electrical transducers (but also electrically non-excitable cells) located in areas between and surrounding cardiac myocytes. They constitute the major non-myocyte cell population in the ventricles and are responsible for the synthesis of extracellular matrix proteins such as different types of collagen. Fibroblasts can become myofibroblasts
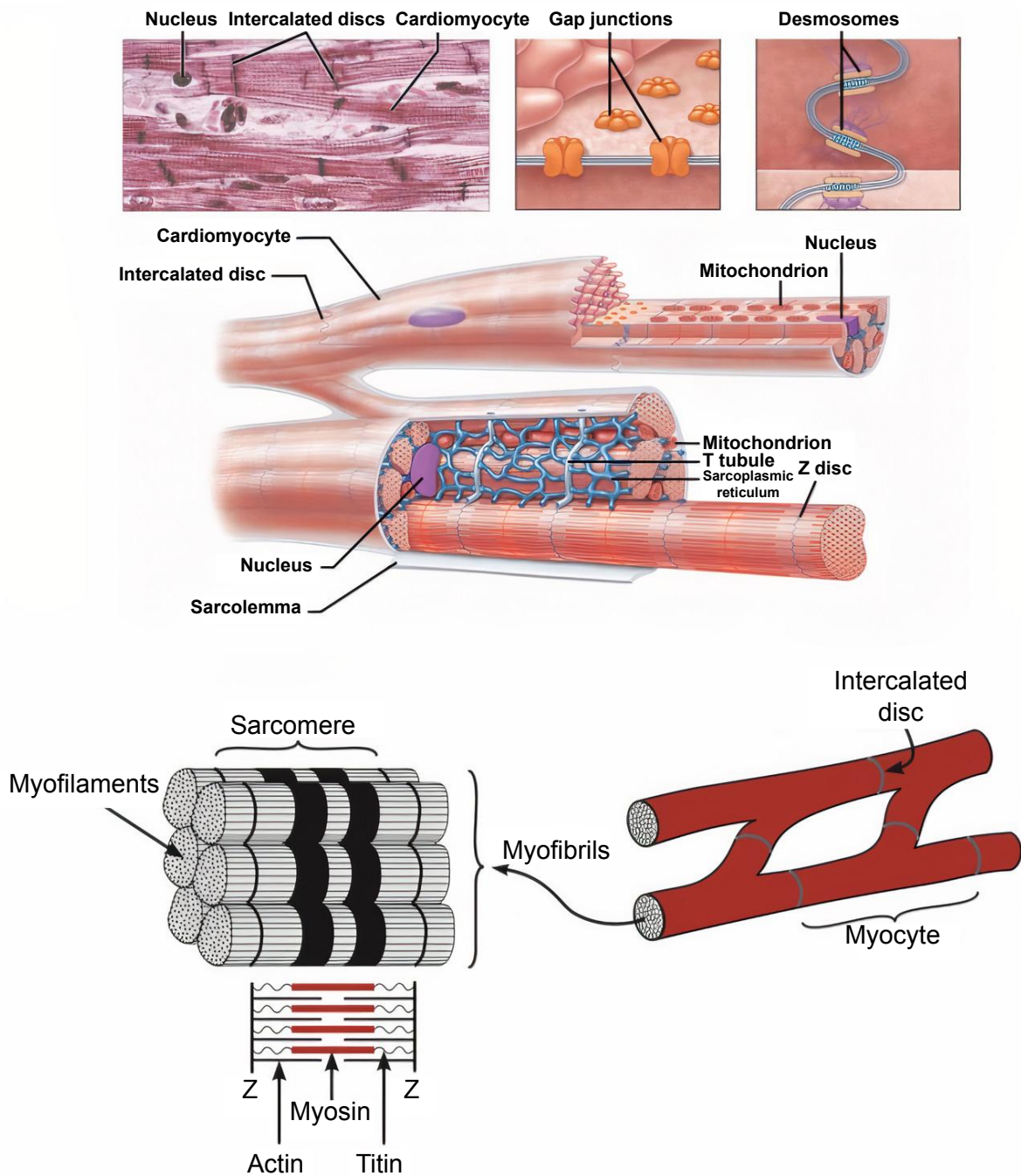
Figure 1.3: Internal structure of cardiomyocytes (image adapted from [87]).

and both types of cells are involved in the development of fibrosis in injured cardiac tissue.

- Extracellular matrix and collagen: they furnish the passive mechanical properties of cardiac tissue. The extracellular matrix occupies an important role in muscle development and maintainance of the functional integrity of the myocardium. The collagen network surrounds single myocytes instead.

- Gap junctions: they are essentially ionic channels with a length of about 2-12 nm and a diameter of about 2 nm, used to interconnect myocytes mostly end-to-end (longitudinal gap junctions), but also laterally (transversal gap junctions).

- Cardiac stem cells: they regulate myocytes turnover and play a role in myocardial recovery after injury.

We depict in Fig. 1.3 the microscopic elements that constitute a single cardiomyocyte.

## 1.3 THE CONDUCTION SYSTEM OF THE HEART

At the microscopic scale, the contraction of cardiac cells, as in other muscle cells, is initiated by an electrical activation due to an action potential (AP) [138]. The AP is generated by the interaction of inward and outward ionic currents that pass through the cardiac cells membrane. Indeed, depolarizing transitory currents raise the transmembrane potential of the excitable cells from its resting value, which ranges between -90 and -60 mV, to slightly positive values [35]. After that, repolarizing currents return the transmembrane potential to its resting value. These ionic currents cause variations in the concentration of several ionic species. The most important one in the initiation of cardiac contraction is given by the intracellular calcium concentration $[Ca^{2+}]_i$ [87].

AP propagates from one cell to its neighbors through gap junctions, i.e. intercellular low-resistance ionic channels. This allows the stimulus to travel through the whole cardiac tissue from one cell to another. Indeed, cardiomyocytes are arranged in sheets of fibers. The gap junctions are located for the most part, although not exclusively, in the longitudinal direction of the fibers, resulting in preferential lines of propagation for the electric signal [35].

Differently from skeletal muscle cells, cardiac cells can activate themselves autonomously, independently of a nervous stimulus [35]. The electrical activity of the heart starts at the so called sinoatrial node (SAN), a group of cardiac pacemaker cells located on the top of the RA [83]. The cells of the SAN have the fastest spontaneous depolarization speed of the cardiac conduction system and therefore they control the cardiac frequency in normal conditions. The autonomic nervous system and the endocrine system present a connection with the SAN cells, because they can modulate both beat-to-beat and long-term variations of the cardiac frequency [72]. In normal conditions, these cells generate an AP that propagates throughout the RA. Then, thanks to the Bachmann's
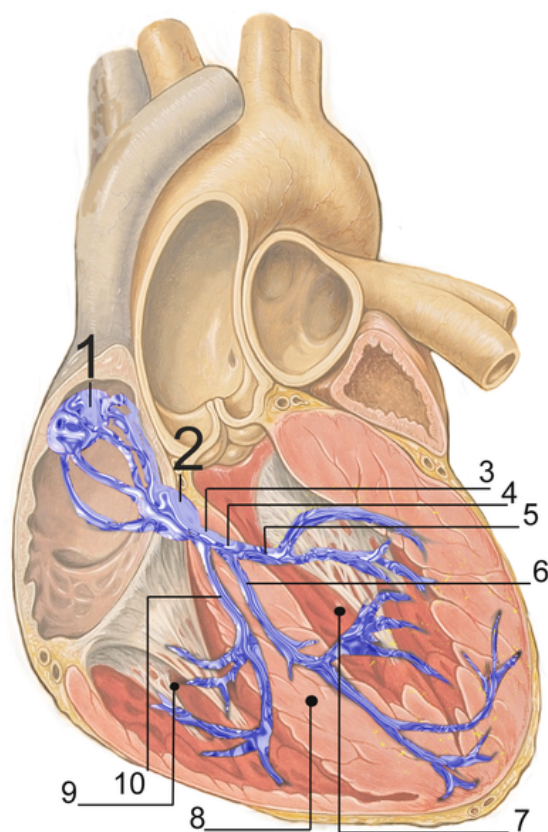
Figure 1.4: Heart conduction system (image taken from [199]). 1. Sinoatrial node. 2. Atrioventricular node. 3. Bundle of His. 4. Left bundle branch. 5. Left posterior fascicle. 6. Left anterior fascicle. 7. Left ventricle 8. Ventricular septum. 9. Right ventricle. 10. Right bundle branch.

bundle and some other preferential lines of trasmission, the AP reaches the LA. Both atria are stimulated in such a way that they will contract in a coordinated and physiological manner [83]. The activation front reaches the atrioventricular node (AVN), located in the central conjunction area between atria and ventricles, where, precisely, the interatrial septum and interventricular septum meet. The cells of the AVN have a relatively slow conduction velocity (CV) and they are responsible for the major part of the normal conduction delays between atrial and ventricular contractions. Such delays are properly timed to optimize the atrial pump activity and to protect the ventricles from early stimulation [83]. The AVN conducts the AP through the nonexcitable atrioventricular septum and activates the specialized fibers of the bundle of His and the Purkinje network. This network spreads as a tree-like left and right bundle branches that end on the endocardial surface of the ventricles [165]. These Purkinje terminations transmit the AP to the ventricular walls, which propagates throughout the ventricles and induces ventricular contraction. The electrical activation of the LV, which is the largest cardiac chamber among the four that are present, normally starts at the interventricular septum. On the other hand, the RV normally contracts shortly after the LV [35, 165]. The whole heart conduction system is depicted in Fig. 1.4.
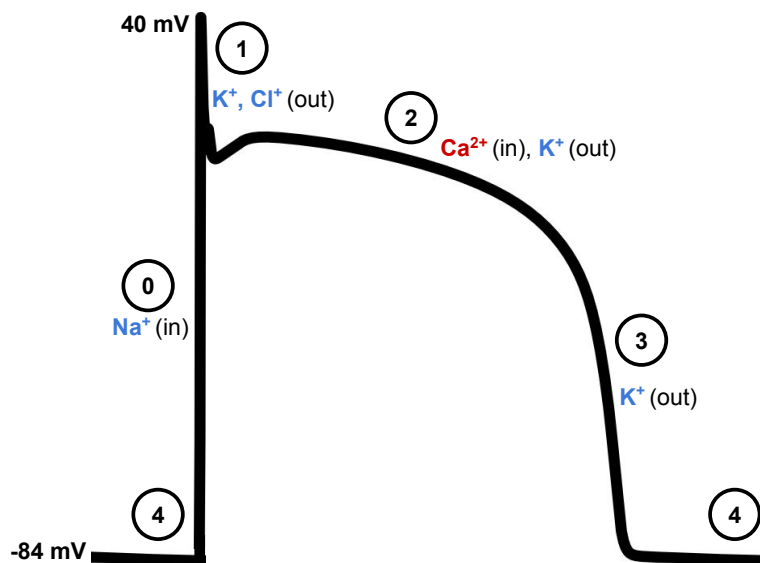
Figure 1.5: Example of ventricular AP with its phases: ∅ (depolarization or upstroke), 1 (peak or notch), 2 (plateau), 3 (repolarization or recovery), 4 (resting). Intracellular calcium concentration $[Ca^{2+}]_i$ plays a major role in heart contraction [19]. Image taken from [24].

## 1.4 THE ACTION POTENTIAL

As the focus of this thesis is on the ventricular part of the heart, we analyze the main phases of a ventricular AP in normal conditions (as reported in Figure 1.5) [35]:

- Phase ∅: myocytes undergo a rapid depolarization due to the opening of the fast $Na^+$ channels. This causes a rapid increase in the membrane conductance, and thus a rapid influx of $Na^+$ ions into the cell, the $I_{Na}$ current, through sodium channels.

- Phase 1: inactivation of the fast $Na^+$ channels. The transient net outward current causing the small downward deflection of the AP is due to $K^+$ and $Cl^-$ ions carried by the $I_{to1}$ and $I_{to2}$ currents, respectively.

- Phase 2: plateau created by a balance between the inward movement of calcium ions $Ca^{2+}$, the $I_{Ca}$ current through L-type calcium channels, and the outward movement of potassium ions $K^+$, contributing to the $I_{Ks}$ current through the slow delayed rectifier potassium channels. The sodium-calcium exchanger current $I_{Na,Ca}$ and the sodium/potassium pump current $I_{Na,K}$ also play minor roles during this phase.

- Phase 3: rapid repolarization phase of the AP, when the L-type $Ca^{2+}$ channels close while the slow delayed rectifier $K^+$ channels ($I_{Ks}$) are still open. This ensures a net outward current, corresponding to negative change in membrane potential, thus allowing more types of $K^+$ channels to open. These are primarily the rapid delayed rectifier $K^+$ channels ($I_{Kr}$ current)
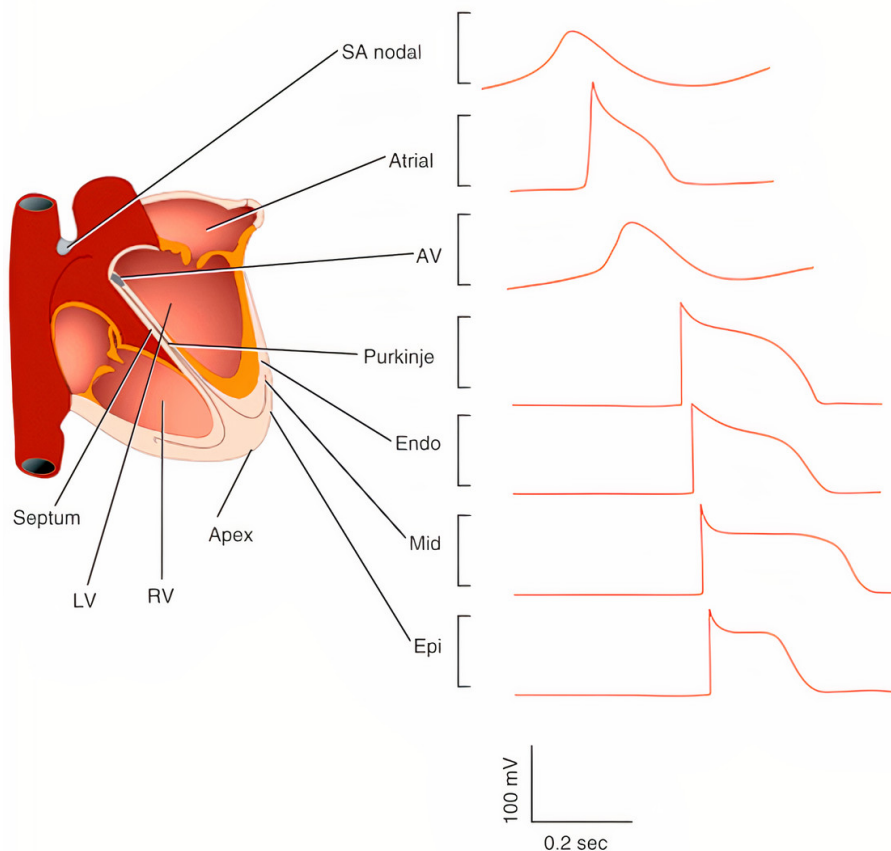
Figure 1.6: Heterogeneity of cardiac APs in different regions of the heart (image taken from [109]).

and the inwardly rectifying K$^+$ current I$_{K1}$. This net outward, positive current causes the cell to repolarize. The delayed rectifier K$^+$ channels close when the membrane potential is restored to about -84 mV, while I$_{K1}$ is maintained throughout phase 4, contributing to set the resting membrane potential.

- Phase 4: resting phase, where the transmembrane potential remains at the resting value of about -84 mV until it is stimulated again by an external electrical activity.

We underline that the cardiac AP is different moving from one region of the heart to another one, as can be seen in Fig. 1.6. Its shape, the duration of the different phases, and also the total AP duration (APD), change from the epicardial to the endocardial zone, from atria to ventricles.
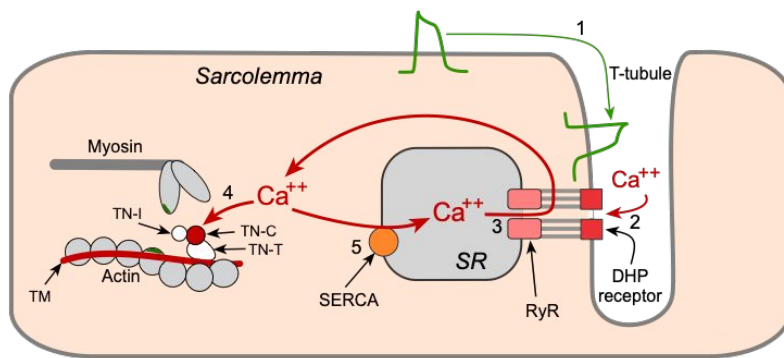
Figure 1.7: Action of $[Ca^{2+}]_i$ in the contraction process (image taken from [87]).

## 1.5 EXCITATION-CONTRACTION COUPLING

In this section, we focus on the role of intracellular calcium concentration $[Ca^{2+}]_i$ in cardiac active mechanics. This ionic species influences the pacemaking at the level of the SAN and the contraction of the whole cardiac tissue [35].

Intracellular calcium concentration increases during the first phases of the AP because of the flux of ions coming from the extracellular space through the specialized long lasting (L-type) channels. Moreover, there is a subsequent release of calcium from the terminal cistarnae in the sarcoplasmic reticulum, according to the calcium induced-calcium release mechanism [87]. Crossbridge dynamics, i.e. contraction of the cardiomyocytes, is initiated by this change of the intracellular calcium concentration. At this point, $[Ca^{2+}]_i$ ions bind to troponin-C in the thin filaments, which leads to the detachment of troponin regulatory complex to the binding site in actin and to the binding of the head of myosin to actin. Consequently, thin and thick filaments of the sarcomeres, which are the smallest functional units in cardiomyocytes (see Fig. 1.3), start to slide past each other. In this way, the individual sarcomeres shorten, and the whole cell contracts.

The contraction of the cell continues as long as the cytosolic calcium concentration remains high enough. Intracellular calcium concentration starts to decrease in the last part of the AP, due to the ions leak through the calcium pump, the Na-Ca exchanger and the binding to cytosolic proteins ($[Ca^{2+}]_i$ buffers) inside the sarcolemma. In this phase, some of the free ions are also trapped by an adenosine triphosphate dependent calcium pump. Calcium starts to dissociate from the binding sites and the troponin complexes bind again to the actin fibers. The sarcomeres return then to their initial length and the cell relaxes. The entire process is synthesized in Fig 1.7.

## 1.6 WIGGERS DIAGRAM

The Wiggers diagram is a standard plot used in cardiac physiology to illustrate the coordinated effects of electrophysiology, mechanics and hemodynamics in a healthy human heart [107]. It presents time on the X-axis and the following possible values on the Y-axis:
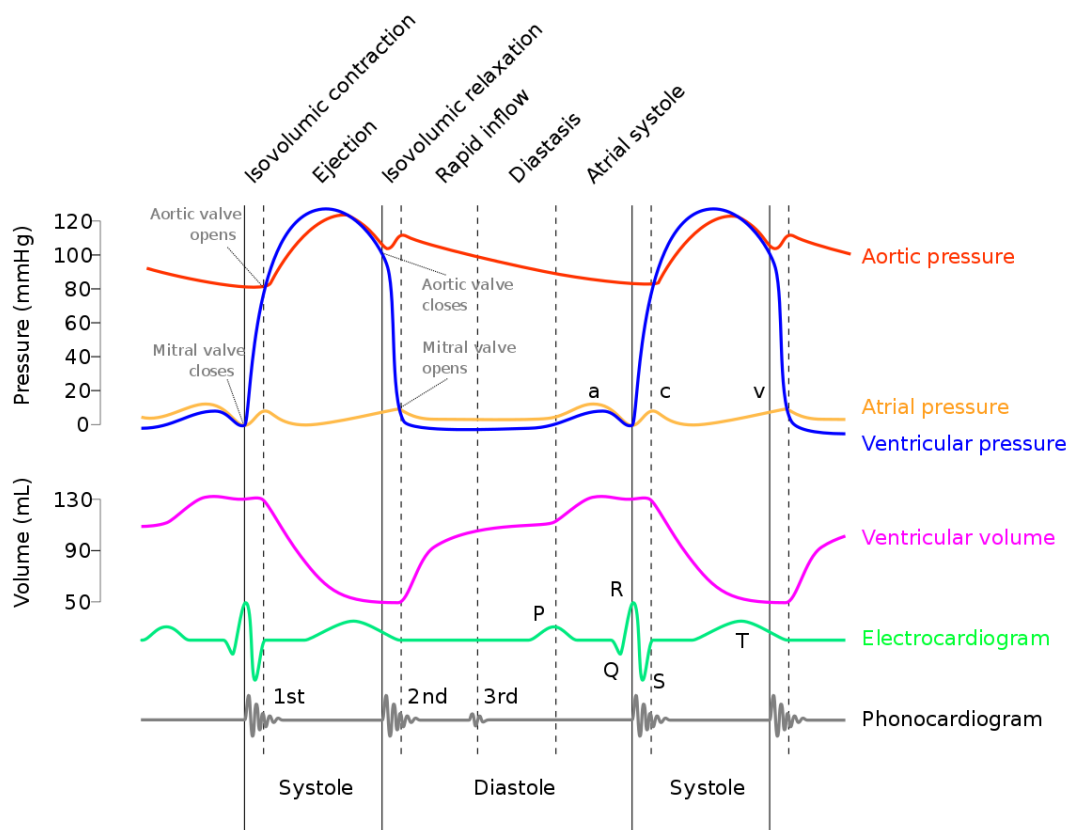
Figure 1.8: Typical Wiggers diagram for the left heart (image taken from [201]).

- Blood pressure (specifically aortic pressure, ventricular pressure, atrial pressure).

- Ventricular volume.

- Electrocardiogram (ECG), which is a recording of the electrical activity of the heart over a period of time using electrodes placed on the skin.

- Phonocardiogram, which is a plot that shows all the sounds made by the heart. It is recorded with a machine called phonocardiograph.

The Wiggers diagram clearly illustrates the coordinated variation of these values as the heart beats. Specifically, the entire cardiac cycle is divided into the following different phases:

- Atrial contraction or ventricular filling phase: the MV is opened and the blood flows into the LV.

- Isovolumetric contraction phase: the MV is closed. The LV pressure increases while the LV volume remains approximately constant.

- Rapid and slow ventricular ejection phase: the AV is opened, whereas the MV is closed. The LV is contracting and pumping blood towards the aorta.
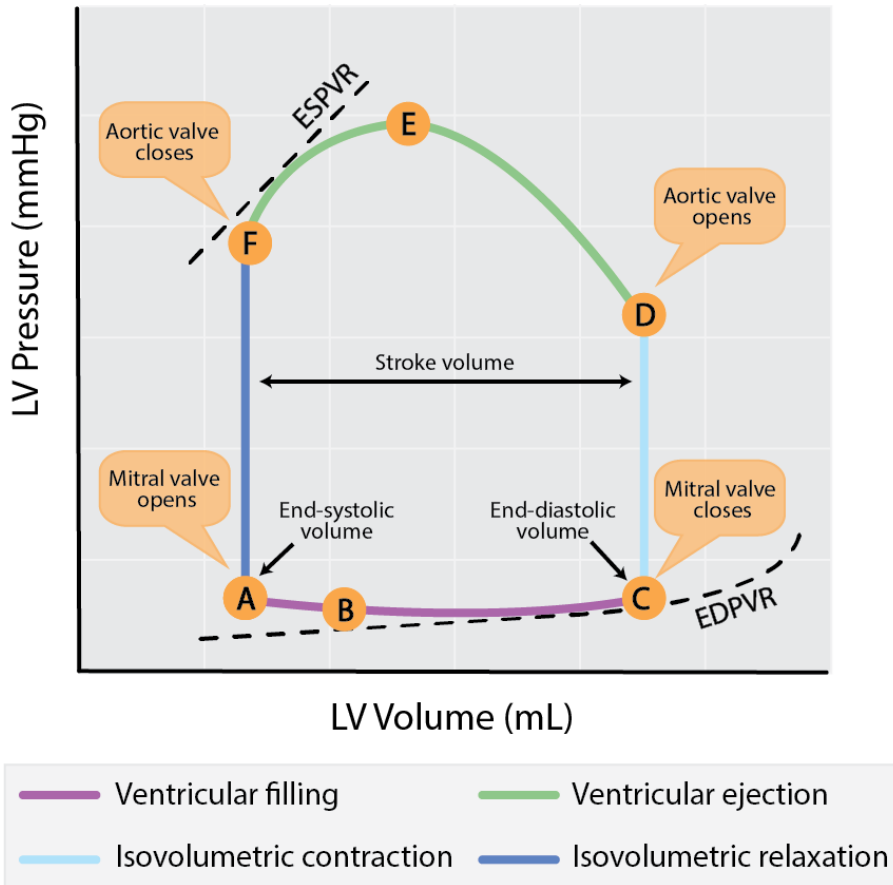
Figure 1.9: Example of PV loop. From A to B: early ventricular filling phase. From B to C: late ventricular filling phase. From C to D: isovolumetric contraction phase. From D to E: early ventricular ejection phase. From E to F: late ventricular ejection phase. From F to A: isovolumetric relaxation phase. Image taken from [23].

- Isovolumetric relaxation phase: both the MV and the AV are closed. The LV pressure decreases while the LV volume remains approximately constant.

- Rapid inflow phase: the MV opens again, the blood flows again into the LV and the cycle repeats itself.

For the sake of simplicity, the cardiac cycle has been presented hereabove for the left part of the heart, but the same phases holds also for the right part.

The Wiggers diagram is illustrated in Fig. 1.8. By looking at the physiological aortic pressure over time, we notice that it is approximately equal to 80 mmHg until the rapid ventricular ejection phase occurs. When the blood is pushed towards the aorta, it rises to almost 120 mmHg. Then, it comes back to the original value during the relaxation phase [107]. In the LV pressure diagram, there is a significant gradient during the isovolumetric contraction phase, because when the ventricle contracts, the pressure exterted in the blood pool builds up and approximately reaches 120 mmHg. After that, we observe a pressure drop when the ventricle stops to contract, i.e. during the isovolumetric relaxation phase [107]. Due to the reduced thickness and contractility properties of the atria, we do not notice significant variations in the atrial pressure wave during the cardiac

cycle. Indeed, this value slightly increases during the ventricular filling phase only.

The LV volume drops during the ventricular ejection phase, because the blood is pumped out from the LV and moves towards the aorta. The volume starts to increase slowly when the MV opens again, so that the LV starts to receive blood from the LA once again. Regarding the cardiac cycle, we distinguish systolic phases, when the heart (or a part of it) is contracting, and diastolic ones, when the heart (or a part of it) is relaxing.

As it can be seen in Fig 1.9, LV pressure and volume can be also represented in the so called pressure-volume (PV) loop, where the time dependency is somehow neglected [23]. Three out of four phases, namely isovolumetric contraction, ventricular ejection and isovolumetric relaxation, are dominated by active mechanics and excitation-contraction coupling. Only in the latter phase, i.e. ventricular filling, passive mechanics plays a significant role. Specifically, it dictates the so called end-diastolic pressure volume relationship. Indeed, we refer to end-diastolic volume (EDV) and end-diastolic pressure (EDP) to indicate the maximum blood pool volume reached by the ventricle during relaxation, along with the corresponding internal pressure [23]. On the other hand, end-systolic volume (ESV) and end-systolic pressure (ESP) represent the minimum blood pool volume of the ventricle, i.e. at the end of contraction, and the corresponding pressure [23].

There are several indicators commonly used in the clinical setting to characterize the heart function. One of these is the stroke volume (SV), which quantifies the amount of blood that is pumped every heartbeat:

$$SV = EDV - ESV \tag{1.1}$$

Then, there is also the ejection fraction (EF), which is given by the SV normalized by the EDV and accounts for the variability in size between patients:

$$EF = \frac{SV}{EDV}100 \tag{1.2}$$

In humans, EF tipically ranges between 50% and 80%. Lower values are generally sign of heart failure or other pathological conditions [52]. The average SV of a healthy adult is about 80 mL, with an EDV of 130 mL [107]. In the next sections we detail how electrophysiology, mechanics and hemodynamics may be altered in pathological scenarios. In particular, the focus of this thesis is on patients with ICM.

## 1.7 CARDIAC ARRHYTHMIAS

Arrhythmias are heart rhythm disorders in which the heartbeat is irregular [203]. The term bradycardia expresses the pathological condition in which the HR is slower than normal, i.e. 60 to 100 heartbeats per minute (in adults, at rest) [104]. On the contrary, tachycardia leads to faster HRs, which can go significantly over 100 heartbeats per minute (in adults, at rest) [104]. Arrhythmias are initiated by an abnormal AP generation/propagation. Sometimes, they manifest
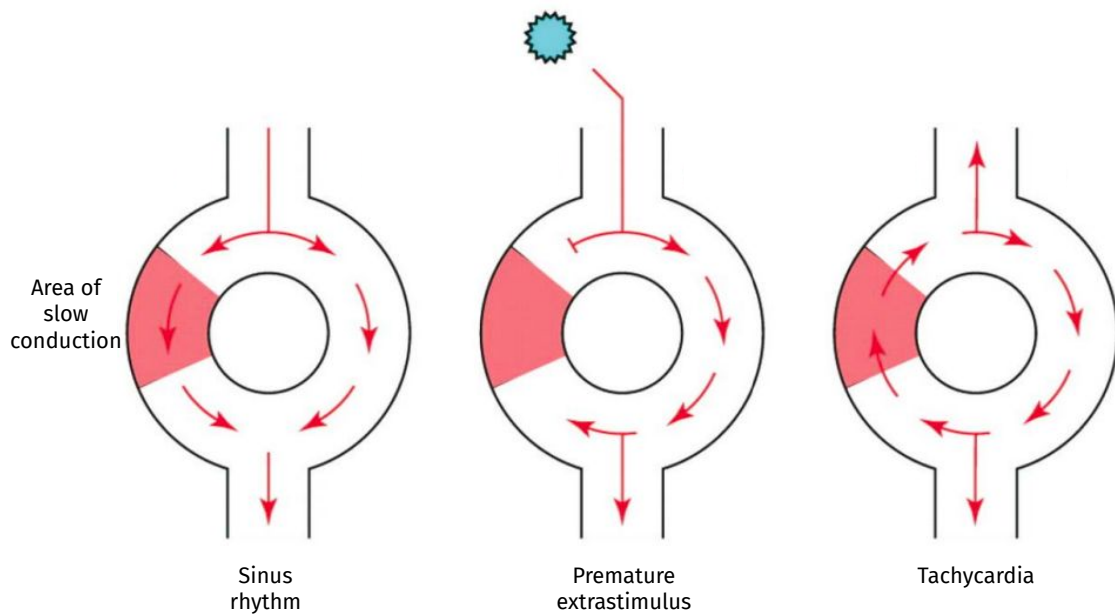
Figure 1.10: Example of reentry circuit due to slow conduction areas. Starting from SR (left), a premature stimulus arrives while the slow pathway is still in the effective refractory period (ERP), i.e. in the time period in which a new AP cannot be elicited (center). The electric signal travels back once the ERP ends and initiates a circular path (right). Image adapted from [67].

in the form of reentries, where the AP travels in a circular path under the appearance of a self-exciting wavefront [203]. Furthermore, it is easier for the AP wavefront to deviate from the SR behavior in presence of areas of slow conduction (as in Fig. 1.10). Reentries may be dangerous, especially if they are frequent and persistent. They may be hemodynamically stable or unstable. Especially in the latter case, the capability of the heart to exert its pumping function might be significantly compromised. Finally, they can also degenerate into a chaotic state called fibrillation, where the pathways continuously change their size and location. Severe tachycardias and fibrillations are associated with SCD [90].

Arrhythmias can be observed both in atria and ventricles, but the most dangerous ones are generally associated with ventricles [90]. From the clinical perspective, according to the specific pathogenesis of the patient, arrhythmias are treated by using drugs, such as beta blockers, or by surgery. In the latter case, cardiac ablation or implantable cardioverter-defibrillators are employed, especially for patients that underwent infarction [97, 102, 169, 202].

## 1.8 ISCHEMIC CARDIOMYOPATHY

ICM is the most common type of dilated cardiomyopathy and it is one of the most frequent causes of heart failure [48, 106, 121]. It mostly affects the LV and it impairs the ability of the heart to efficiently pump blood in the circulation system.
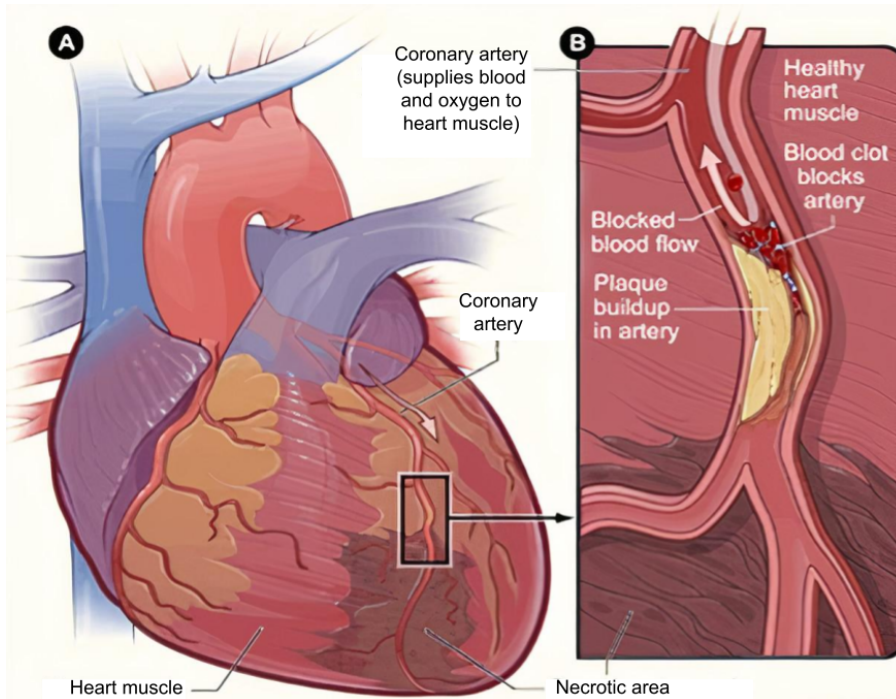
Figure 1.11: Myocardial infarction in the ventricular part of the heart (A) generated by a blood clot in the coronary artery (B). The infarcted area is no longer perfused and is subjected to electromechanical remodeling. Indeed, the loss of myocytes due to blood flow obstruction is generally replaced by collageneous scar tissue, which is very stiff and non-conductive. Peri-infarct areas around the necrotic zones, which are also called grey zones, are generally present. Grey zones own intermediate myocardial properties between scars and non-remodelled regions. Image adapted from [4].

Myocardial infarction (see Fig. 1.11) leads to an enlargement of the blood pool volume, i.e. an increase of ESV, EDV and EDP. Both SV and EF significantly reduce, along with the mean arterial pressure (MAP). Healthy, peri-infarct and infarct zones are liable for short-term and long-term remodeling of the electrophysiological behavior, involving modifications in the restitution curves of CV, APD and ERP. Ischemic regions are also known to become stiffer and thinner than full healthy tissue, with either a low or a strong impairment in their contractility function. The LV pathophysiological remodeling has a significant impact on flow rates across the heart valves, pressures and volumes ranges of LA, RA, RV, systemic and pulmonary circulation. This also implies relevant metabolic changes in the whole body [170].

Patients with ICM present different symptoms including shortness of breath, fatigue, inability to exercise and dizziness [48, 106, 121]. Moreover, the presence of fibrous tissue and slow conduction areas eases the generation of irregular heart rhythms, which are generally more dangerous and more frequent than the ones observed in non-ICM patients [169]. These electric abnormalities are called VT and can be either hemodynamically stable or unstable. In some dangerous cases, they may also degenerate yielding VF. These arrhythmias, if severe and not properly treated, may induce palpitations, fainting or possibly SCD.

# CARDIAC ELECTROMECHANICAL MODELS

In this chapter, we introduce the mathematical models that have been used in this thesis to study cardiac electromechanics in human ventricles [61, 131, 147, 162]. Then, we explain the numerical methods that are employed to accurately and efficiently solve this mathematical problem [45, 131, 148, 161]. With respect to other electromechanical models available in the literature [8, 37, 60, 65, 128, 158, 173, 187, 195], our mathematical and numerical model features several novelties.

- We propose a 3D-ØD closed-loop electromechanical model suitable for LVs with ICM. Our mathematical model accounts for space heterogeneity in the electromechanical properties of both cardiac cells and tissue (Secs. 2.1 and 2.2).

- We derive a balance of mechanical energy for both the ØD closed-loop cardiocirculatory model and the 3D-ØD coupled problem (Sec. 2.3).

- We introduce novel numerical schemes for the discretization of the 3D-ØD model of cardiac electromechanics. We develop reliable and scalable inter-grid transfer operators to capture the significant spatial-scale separation between electrophysiology and mechanics. Moreover, our strategy allows for numerical simulations of any type of arrhythmia (Sec. 2.4).

## 2.1 MATHEMATICAL MODELS

We consider a computational domain $\Omega_0 \subset \mathbb{R}^3$, representing the 3D region occupied by an LV in reference (i.e. stress-free) configuration (Fig. 2.1) [147, 148]. We split the boundary of $\Omega_0$ into endocardium ($\Gamma_0^{\text{endo}}$), epicardium ($\Gamma_0^{\text{epi}}$) and ventricular base ($\Gamma_0^{\text{base}}$), namely the artificial boundary located where the LV geometry is cut.

We consider a multiphysics and multiscale model of cardiac electromechanics made of five different blocks (henceforth denoted as core models) plus a coupling condition. The core models are associated with the different physical phenomena concurring – at different spatial and temporal scales – at the heart function. They correspond to the propagation of the AP ($\mathscr{E}$) [34, 35, 132], ions dynamics ($\mathscr{I}$) [25, 99, 186], active contraction of cardiomyocytes ($\mathscr{A}$) [142, 143, 152, 153, 155], tissue mechanics ($\mathscr{M}$) [70, 115] and blood circulation ($\mathscr{C}$) [20, 76]. Finally, the volume conservation condition ($\mathscr{V}$) enables to consistently couple ($\mathscr{M}$) and ($\mathscr{C}$) core models. In Fig. 2.2 we depict the electric analog circuit corresponding to our ØD circulation model, along with the coupling with a 3D electromechanical description of the LV.
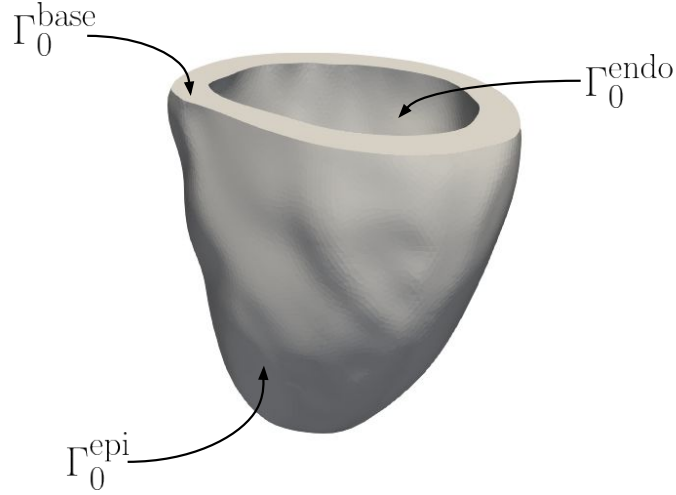
Figure 2.1: Representation of boundaries $\Gamma_0^{\text{epi}}$, $\Gamma_0^{\text{base}}$ and $\Gamma_0^{\text{endo}}$ of the domain $\Omega_0$, given by the Zygote Solid 3D LV [80], which represents the LV of the 50th percentile of a healthy caucasian male in the U.S., reconstructed from a high resolution computed tomography scan.

### 2.1.1 Electrophysiology $(\mathcal{E})$–$(\mathcal{I})$

We model the electrophysiological process by means of the monodomain equation, a diffusion-reaction PDE that describes the electric properties of cardiac muscle cells, assuming the same anisotropy ratios between the intracellular and extracellular spaces [35]. It is a homogenized continuum model, which means that it is used to capture average properties of many cardiomyocytes, and not the behavior of single cells. We couple the monodomain equation with the TTP06 ionic model, because we focus on the human LV [186]. This model permits to describe the microscopic details of the single cardiomyocyte in a physiological manner [35].

The electrophysiological model reads:

$$
\begin{cases}
J\chi_m \left[ C_m \dfrac{\partial u}{\partial t} + \mathcal{I}_{\text{ion}}(u, \boldsymbol{w}, \boldsymbol{z}) + \mathcal{I}_{\text{SAC}}(u, \mathbf{F}) \right] & \text{in } \Omega_0 \times (0, T], \\
\quad = \nabla \cdot (J\mathbf{F}^{-1}\mathbf{D}\mathbf{F}^{-T}\nabla u) + J\chi_m \mathcal{I}_{\text{app}}(t) \\
\dfrac{\partial \boldsymbol{w}}{\partial t} - \mathbf{H}(u, \boldsymbol{w}) = 0 & \text{in } \Omega_0 \times (0, T], \\
\dfrac{\partial \boldsymbol{z}}{\partial t} - \mathbf{G}(u, \boldsymbol{w}, \boldsymbol{z}) = 0 & \text{in } \Omega_0 \times (0, T], \\
\left( J\mathbf{F}^{-1}\mathbf{D}\mathbf{F}^{-T}\nabla u \right) \cdot \mathbf{N} = 0 & \text{on } \partial\Omega_0 \times (0, T], \\
u = u_0, \ \boldsymbol{w} = \boldsymbol{w}_0, \ \boldsymbol{z} = \boldsymbol{z}_0 & \text{in } \Omega_0 \times \{0\}.
\end{cases}
\tag{2.1}
$$

$\Omega_0 \subset \mathbb{R}^3$ is the computational domain, $T > 0$ is the final time. $C_m$ is the total membrane capacitance and $\chi_m$ is the area of cell membrane per tissue volume. $u$ is the dimensionless transmembrane potential, vector $\boldsymbol{w} = \{w_1, w_2, ..., w_k\}$ expresses k recovery (or gating) variables, which play the role of probability
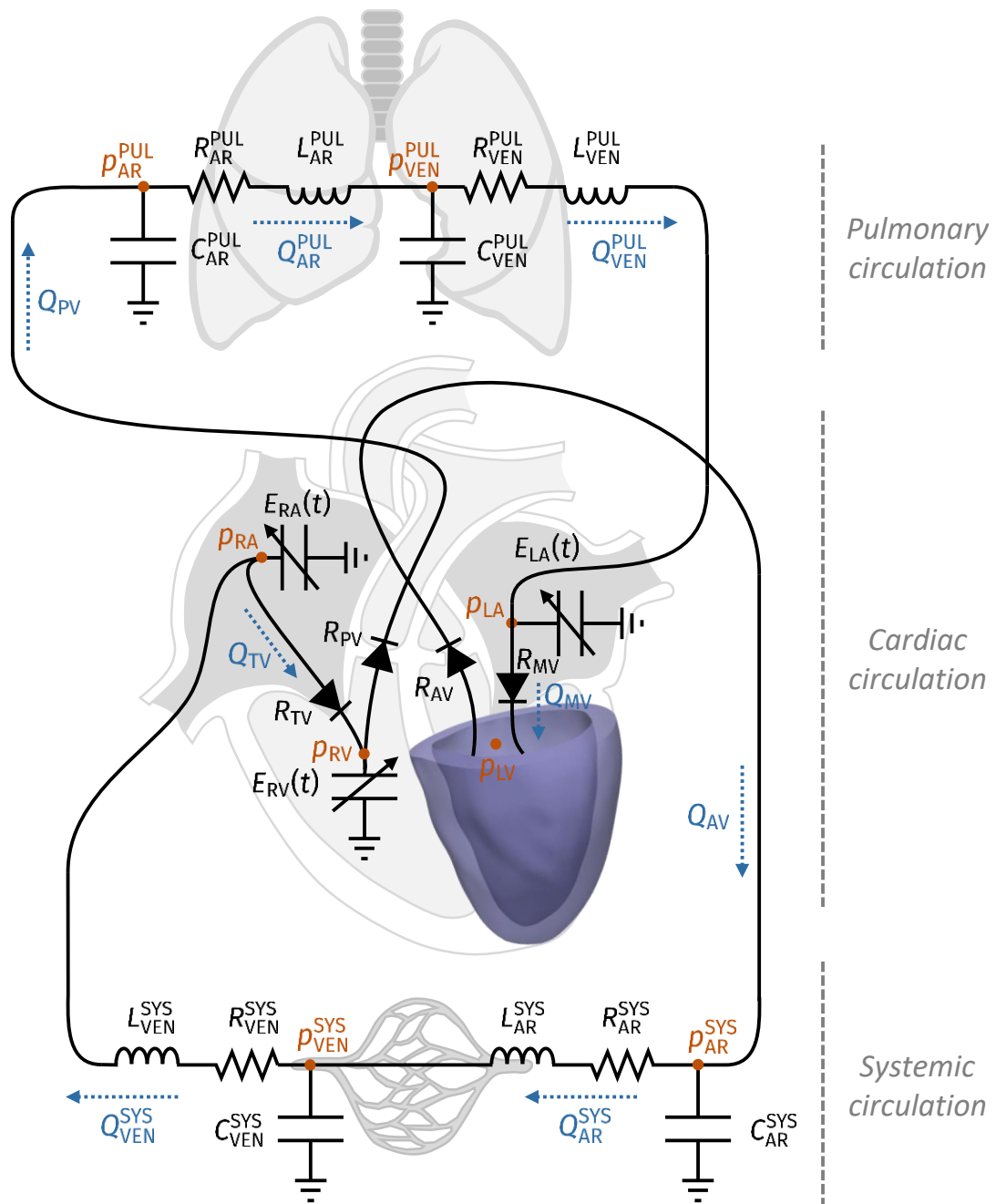
Figure 2.2: 3D-∅D coupling between the 3D LV electromechanical model and the ∅D circulation model. The state variables corresponding to pressures and fluxes are depicted in orange and blue, respectively. The LV geometry may possibly present ICM [162].
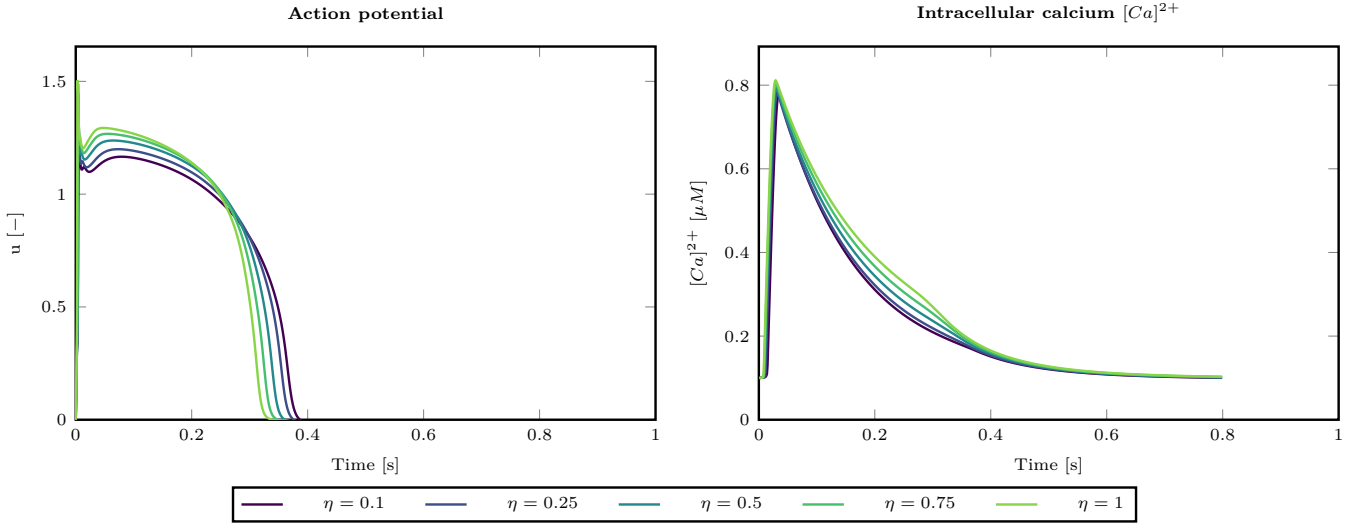
Figure 2.3: Dimensionless AP (left) and intracellular calcium concentration $[Ca^{2+}]_i$ (right) for different values of $\eta = \eta(x)$ (TTP06 model, epicardium). $\eta = 1$ corresponds to healthy tissue, whereas $\eta \in \{0.1, 0.25, 0.5, 0.75\}$ defines different peri-infarct zones.

density functions and model the fraction of open ionic channels across the membrane of a single cell, and vector $z = \{z_1, z_2, ..., z_m\}$ defines m concentration variables of specific ionic species such as calcium $[Ca^{2+}]_i$, which plays a major role in heart contraction and mechanical activation. $\mathcal{I}_{app}(t)$ is an external applied current, which simulates in our case the behavior of the Purkinje network [151, 190]. Indeed we use it to trigger the AP in specific points of the myocardium. $\mathcal{I}_{ion}(u, w, z)$ is the feedback from the cellular scale into the tissue one, and strictly depends on the chosen ionic model. A Neumann boundary condition is applied all over the boundary and defines the condition of electrically isolated domain. $\mathbf{H}(u, w)$ and $\mathbf{G}(u, w, z)$ keep into account the specific features of the TTP06 ionic model [186].

The diffusion tensor is given by:

$$\mathbf{D} = \eta\sigma_l \frac{\mathbf{Ff}_0 \otimes \mathbf{Ff}_0}{|\mathbf{Ff}_0|^2} + \eta\sigma_t \frac{\mathbf{Fs}_0 \otimes \mathbf{Fs}_0}{|\mathbf{Fs}_0|^2} + \eta\sigma_n \frac{\mathbf{Fn}_0 \otimes \mathbf{Fn}_0}{|\mathbf{Fn}_0|^2}, \quad (2.2)$$

being $\mathbf{f}_0$ the vector field expressing fiber direction, $\mathbf{s}_0$ the vector field related to sheet direction and $\mathbf{n}_0$ the vector field that indicates the sheet-normal, or equivalently crossfiber, direction [130]. Longitudinal, transversal and normal conductivities are expressed by $\sigma_l, \sigma_t, \sigma_n \in \mathbb{R}^+$, respectively [157]. As a novel contribution, we introduce a parameter $\eta = \eta(x)$ that takes into account the effect of ischemic regions both at the macroscopic scale and at the microscopic one. With respect to the latter point, $G_{Na}(x)$, $G_{CaL}(x)$, $G_{kr}(x)$ and $G_{ks}(x)$ conductances of the TTP06 ionic model [186] vary in space according to the following laws:

$$G_{Na}(x) = \left[0.38 + \frac{10}{9}(\eta(x) - 0.1)0.62\right] G_{Na},$$

$$G_{CaL}(\boldsymbol{x}) = \left[0.31 + \frac{10}{9}(\eta(\boldsymbol{x}) - 0.1)0.69\right]G_{CaL},$$

$$G_{kr}(\boldsymbol{x}) = \left[0.30 + \frac{10}{9}(\eta(\boldsymbol{x}) - 0.1)0.70\right]G_{kr},$$

$$G_{ks}(\boldsymbol{x}) = \left[0.20 + \frac{10}{9}(\eta(\boldsymbol{x}) - 0.1)0.80\right]G_{ks},$$

where $G_{Na}$, $G_{CaL}$, $G_{kr}$ and $G_{ks}$ are defined as in [186]. We can potentially consider a continuum of grey zones using linear interpolation, for $\eta(\boldsymbol{x}) \in [0.1, 1]$, going from the full healthy case ($\eta(\boldsymbol{x}) = 1$) to the grey zone described in [6] ($\eta(\boldsymbol{x}) = 0.1$), where $G_{Na}$, $G_{CaL}$, $G_{kr}$ and $G_{ks}$ conductances are reduced to 38%, 31%, 30% and 20% of their physiological values, respectively. We model scars as myocardial regions where no evolution of both the transmembrane potential and all ionic variables occur, where therefore Eq. (2.1) is not actually solved. We report in Fig. 2.3 the evolution over time of the transmembrane potential u and the intracellular calcium concentration $[Ca^{2+}]_i$ for different values of the parameter $\eta$. Moving from $\eta(\boldsymbol{x}) = 1$ to $\eta(\boldsymbol{x}) = 0.1$ leads to a reduced upstroke and a longer plateau of the AP. This parameter $\eta$ will be also introduced in Secs. 2.1.2 and 2.1.3 for mechanical activation and passive mechanics, respectively.

By indicating $\mathbf{X}$ and $\mathbf{x}$ as the reference and deformed coordinates respectively, we introduce the deformation tensor $\mathbf{F} = \mathbf{I} + \frac{\partial \mathbf{d}}{\partial \mathbf{X}}$ and its determinant $J = \det(\mathbf{F})$, which are needed to perform the mechano-electric coupling [183]. Indeed, we model the so called MEFs [41, 73]. The geometry-mediated MEFs incorporate the effects of displacement $\mathbf{d}$ on the cardiac tissue, while other physiological processes act at the level of single cardiomyocytes [95, 184]. Among them, some examples are selective (e.g. $K^+$-permeable) or nonselective SACs and intracellular calcium $[Ca^{2+}]_i$ binding to sarcolemmal buffers, the latter requiring more sophisticated ventricular ionic models [14, 180]. In this thesis we model nonselective SACs by means of the following formulation [95]:

$$\mathfrak{I}_{SAC}(u, \mathbf{F}) = G_s(|\mathbf{F}\mathbf{f}_0| - 1)_+(u - u_{rev}), \tag{2.3}$$

where $G_s$ and $u_{rev}$ represent the conductance of the channels and the reversal potential, respectively. SACs may alter the shape of the AP by lengthening or shortening its duration (APD) and by generating higher resting potentials. This may induce EADs or DADs and premature excitation. Both geometry-mediated MEFs and nonselective SACs are generally known to be pro-arrhythmic in pathological scenarios, because they increase the likelihood of having extra stimuli during cardiac contraction and relaxation [184].

In some of the numerical simulations that will be presented in Chap. 4, we consider Eq. (2.1) with several degrees of complexity to assess similarities and differences in the outcomes of the electromechanical simulations, both in SR and during VT, for the different configurations, which are reported in Tab. 2.1. In particular, the choice of three different mathematical models for the geometry-mediated MEFs, namely ($\mathscr{E}_{gMEF\text{-}minimal}$), ($\mathscr{E}_{gMEF\text{-}enhanced}$) and ($\mathscr{E}_{gMEF\text{-}full}$), is motivated by the numerous formulations of this type of feedback that can be found

| Model name | Equation |
|---|---|
| $(\mathscr{E})$ | $\chi_m \left[ C_m \dfrac{\partial u}{\partial t} + \mathcal{I}_{ion}(u, w) \right] - \nabla \cdot (\mathbf{D_I} \nabla u) = \chi_m \mathcal{I}_{app}(t)$ |
| $(\mathscr{E}_{\text{gMEF-minimal}})$ | $\chi_m \left[ C_m \dfrac{\partial u}{\partial t} + \mathcal{I}_{ion}(u, w) \right] - \nabla \cdot (J\mathbf{F}^{-1} \mathbf{D_I} \mathbf{F}^{-T} \nabla u) = \chi_m \mathcal{I}_{app}(t)$ |
| $(\mathscr{E}_{\text{gMEF-enhanced}})$ | $\chi_m \left[ C_m \dfrac{\partial u}{\partial t} + \mathcal{I}_{ion}(u, w) \right] - \nabla \cdot (J\mathbf{F}^{-1} \mathbf{D} \mathbf{F}^{-T} \nabla u) = \chi_m \mathcal{I}_{app}(t)$ |
| $(\mathscr{E}_{\text{gMEF-full}})$ | $J\chi_m \left[ C_m \dfrac{\partial u}{\partial t} + \mathcal{I}_{ion}(u, w) \right] - \nabla \cdot (J\mathbf{F}^{-1} \mathbf{D} \mathbf{F}^{-T} \nabla u) = J\chi_m \mathcal{I}_{app}(t)$ |
| $(\mathscr{E}_{\text{SAC}})$ | $\chi_m \left[ C_m \dfrac{\partial u}{\partial t} + \mathcal{I}_{ion}(u, w) + \mathcal{I}_{SAC}(u, \mathbf{F}) \right] - \nabla \cdot (\mathbf{D_I} \nabla u) = \chi_m \mathcal{I}_{app}(t)$ |
| $(\mathscr{E}_{\text{gMEF-full, SAC}})$ | $J\chi_m \left[ C_m \dfrac{\partial u}{\partial t} + \mathcal{I}_{ion}(u, w) + \mathcal{I}_{SAC}(u, \mathbf{F}) \right] - \nabla \cdot (J\mathbf{F}^{-1} \mathbf{D} \mathbf{F}^{-T} \nabla u) = J\chi_m \mathcal{I}_{app}(t)$ |

Table 2.1: Modeling choices for the monodomain equation. $\mathbf{D_I}$ indicates the conductivity tensor in Eq. (2.2) with $\mathbf{F} = \mathbf{I}$.

in the literature [32, 38, 95, 137]. Indeed, we range from minimal to complete inclusion of geometry-mediated MEFs in the monodomain equation. Nevertheless, unless otherwise stated, we employ model ($\mathscr{E}_{\text{gMEF-minimal}}$) for cardiac electrophysiology.

### 2.1.2 *Mechanical activation* ($\mathscr{A}$)

Mechanical activation bridges electrophysiology and passive mechanics. There are two approaches in literature, namely the active stress [94, 140] and the active strain [2, 3]. With the former technique, the underlying hypothesis is that an active force is generated by the myocardium, whereas in the latter case an active deformation is prescribed to the cardiac tissue.

*Active stress* ($\mathscr{A}_{\text{stress}}$)

Heart contraction is the result of mechano-chemical interactions among the contractile proteins actin and myosin, taking place at the scale of the sarcomeres, the fundamental contractile unit of the cardiac muscle [19, 30, 83, 142]. To model such complex mechanisms, we consider either the model proposed in [140] or the one reported in [142], denoted as RDQ18 and RDQ20-MF, respectively.

We anticipate that these two byophysically detailed active stress models do not foresee the use of $\eta(x)$. Both RDQ18 and RDQ20-MF models receive different intracellular calcium waves $[Ca^{2+}]_i$ from ($\mathscr{E}$)–($\mathscr{I}$) according to the specific area

of the myocardium (scar, grey zone or healthy) and provide physiological values of active tension in all cases. Indeed, they can properly handle the active force generation processes in very different physiological scenarios.

RDQ18     This model is based on a biophysically detailed description of the sarcomeric proteins with an explicit representation of the cooperative nearest neighboring interactions, responsible for the high sensitivity of the cardiac contractile apparatus to changes in calcium concentration, which is one of the ionic species modelled by the TTP06 ionic model. Thanks to the spatially-explicit representation of the sarcomere filaments, the RDQ18 model also incorporates the feedback of the sarcomere shortening, resulting from the muscle contraction, on the force generation mechanism itself. This is of outmost importance since the regulation due to the sarcomere length (SL) constitutes the microscopical basis of the well-known Frank-Starling mechanism at the macroscale level; in practice, higher EDVs translate into higher SVs [83].

The RDQ18 model is given by the following system of ODEs:

$$
\begin{cases}
\dfrac{\partial \mathbf{s}}{\partial t} = \mathbf{K}(\mathbf{s}, [Ca^{2+}]_i, SL) & \text{in } \Omega_0 \times (0, T], \\
\mathbf{s}(0) = \mathbf{s}_0 & \text{in } \Omega_0 \times \{0\},
\end{cases}
\tag{2.4}
$$

where the vector $\mathbf{s}$ collects the variables of the RDQ18 model and $\mathbf{K}$ is a suitable function defined in [140] (we remark that $\mathbf{K}$ does not involve derivatives of $\mathbf{s}$ with respect to the spatial variable). Within a multiscale framework, the RDQ18 model is ideally set at every point of the computational domain $\Omega_0$. The input variable $[Ca^{2+}]_i$ is provided by the TTP06 ionic model in each point of the domain, while SL is given by the solution of the mechanical model through the fourth invariant $\mathcal{I}_{4f} = \mathbf{F}\mathbf{f}_0 \cdot \mathbf{F}\mathbf{f}_0$, as we will explain in Sec. 2.1.3.

The output of the RDQ18 model is the permissivity $P \in [0, 1]$, obtained as a function of the states $\mathbf{s}$ (i.e. $P = G(\mathbf{s})$, where $G$ is a linear function defined in [140]). The permissivity represents the fraction of contractile units being in the force-generating state. Hence, the effective active tension is given by $T_a = T_a^{max} P$, where $T_a^{max}$ denotes the tension generated when all the contractile units are generating forces (i.e. for $P = 1$).

The RDQ18 model accurately describes the microscopic force generation mechanisms. This accuracy results in a higher computational cost compared to phenomenological models typically used for multiscale simulations (see e.g. [94, 110]). To overcome this issue, in the multiscale model of electromechanics we take advantage of the model based on ANNs presented in [143]. This model is a fast surrogate of the RDQ18 model, i.e. the FOM model, learned from a collection of pre-computed simulations obtained with the RDQ18 model itself, thanks to the Machine Learning algorithm that we proposed in [141]. Such ROM is written in the same form of Eq. (2.4). However, the state vector $\mathbf{s}$ of ANN-based model only contains two variables, instead of more than 2000 variables as in the FOM model. This significantly reduces the computational costs associated with its numerical approximation (both in terms of CPU time and memory storage),

at the price of only a small approximation, as the overall relative error between the results of the FOM and of the ROM is of the order of $10^{-3}$ [143]. In this way we obtain an excellent trade-off between computational cost and biophysical accuracy of the results.

RDQ20-MF   This model denotes the mean-field version of the one proposed in [142] and stands for an upgrade of the RDQ18 model. Similarly to RDQ18 and unlike most of the models that have been used in the literature in the past [94, 110, 150], RDQ20-MF is not based on a phenomenological description of force generation, but on a biophysically accurate description of regulatory and contractile proteins and their dynamics. Thanks to suitable dimensionality reduction techniques, the dynamics of stochastic processes underlying both chemical and mechanical microscale transitions are described in only 20 ODEs (that is $\mathbf{s}(t) \in \mathbb{R}^{20}$). The computational cost of this model is thus comparable to that of phenomenological models, while providing a biophysical description that is consistent with the level of detail and mechanistic understanding of the ionic model to which it is coupled.

The inputs of the RDQ20-MF model are the intracellular calcium concentration $[Ca^{2+}]_i$ coming from $(\mathcal{E})$–$(\mathcal{I})$, the sarcomere length SL and its time derivative (the latter allows to account for the so-called force-velocity relationship [84]), which is not considered in the RDQ18 model. Variable SL is still obtained by using the fourth invariant $\mathcal{I}_{4f} = \mathbf{F}\mathbf{f}_0 \cdot \mathbf{F}\mathbf{f}_0$, which measures the tissue stretch in the fiber direction, as will be better explained in Sec. 2.1.3. Finally, the output of the RDQ20-MF model is the active tension generated at the microscale, that can be obtained as $T_a(\mathbf{s}, SL)$.

*Active strain* $(\mathscr{A}_{\text{strain}})$

We consider a phenomenological law that keeps into account the local shortening of the fibers $\gamma_f$ at the macroscopic level [11, 61, 152, 155]. Myocardial displacement $\mathbf{d}$ and concentration of intracellular calcium ions $[Ca^{2+}]_i$ play an important role in the time evolution of $\gamma_f$.

The phenomenological law reads:

$$
\begin{cases}
\dfrac{\partial \gamma_f}{\partial t} - \eta \dfrac{\varepsilon}{g([Ca^{2+}]_i)} \Delta \gamma_f = \eta \dfrac{1}{g([Ca^{2+}]_i)} \Phi([Ca^{2+}]_i, \gamma_f, \mathbf{d}) & \text{in } \Omega_0 \times (0, T], \\
\nabla \gamma_f \cdot \mathbf{N} = 0 & \text{on } \partial\Omega_0 \times (0, T], \\
\gamma_f = 0 & \text{in } \Omega_0 \times \{0\},
\end{cases}
\tag{2.5}
$$

where $g([Ca^{2+}]_i) = \mu_A([Ca^{2+}]_i)^2$, $\Phi([Ca^{2+}]_i, \gamma_f, \mathbf{d}) = \alpha H_{[Ca^{2+}]_{i,o}}([Ca^{2+}]_i)([Ca^{2+}]_i -$

$[Ca^{2+}]_{i,o})^2 R_{FL}(\mathcal{I}_{4f}) + \displaystyle\sum_{j=1}^{5} (-1)^j (j+1)(j+2)\mathcal{I}_{4f}\gamma_f^j$ is the active force and $R_{FL}(\mathcal{I}_{4f})$ is

a truncated Fourier series expressing the sarcomere force-length relationship [66]. Both $\alpha$ and $\mu_A$ should be calibrated according to the specific case under

investigation. The active deformation is computed by exploiting the following orthotropic form [3]:

$$\mathbf{F}_A = \mathbf{I} + \gamma_f \mathbf{f}_0 \otimes \mathbf{f}_0 + \gamma_s \mathbf{s}_0 \otimes \mathbf{s}_0 + \gamma_n \mathbf{n}_0 \otimes \mathbf{n}_0, \tag{2.6}$$

where $\mathbf{s}_0$ and $\mathbf{n}_0$ represent sheets and their normal direction respectively, with $\gamma_s$ and $\gamma_n$ corresponding to local shortening or elongation [13, 117]:

$$\gamma_n = \bar{k}' \left( \bar{k}_{endo} \frac{\lambda - \lambda_{epi}}{\lambda_{endo} - \lambda_{epi}} + \bar{k}_{epi} \frac{\lambda - \lambda_{endo}}{\lambda_{epi} - \lambda_{endo}} \right) \left( \frac{1}{\sqrt{1 + \gamma_f}} - 1 \right), \tag{2.7}$$

$$\gamma_s = \frac{1}{(1 + \gamma_f)(1 + \gamma_n)} - 1. \tag{2.8}$$

Here $\lambda$ represents a transmural coordinate, varying from $\lambda_{endo}$ at the endo-cardium to $\lambda_{epi}$ at the epicardium, which permits to have a transversely non-homogeneous thickening of the left ventricular wall. $\gamma_s$ set like (2.8) yields to $\det(\mathbf{F}_A) = 1$. Due to its phenomenological nature, here it is necessary to use the coefficient $\eta = \eta(\mathbf{x})$ to keep into account the effects of scars ($\eta(\mathbf{x}) = 0$), grey zones ($\eta(\mathbf{x}) \in [0.1, 1)$) and healthy tissue ($\eta(\mathbf{x}) = 1$). The reduced value of $\eta(\mathbf{x})$ for grey zones defines a lower peak value of $\gamma_f$ during the cardiac cycle and induces slower activation and deactivation with respect to the healthy case. These outcomes are obtained by reducing the effects of the forcing term and the diffusion term in Eq. 2.5, respectively.

### 2.1.3  *Mechanics ($\mathcal{M}$)*

We describe the dynamics of the tissue displacement $\mathbf{d}$ by the momentum con-servation equation (see e.g. [115]):

$$\begin{cases} \rho_s \dfrac{\partial^2 \mathbf{d}}{\partial t^2} - \nabla \cdot \mathbf{P} = 0 & \text{in } \Omega_0 \times (0, T], \\ \mathbf{P}\mathbf{N} + \mathbf{K}^{epi}\mathbf{d} + \mathbf{C}^{epi} \dfrac{\partial \mathbf{d}}{\partial t} = 0 & \text{on } \Gamma_0^{epi} \times (0, T], \\ \mathbf{P}\mathbf{N} = -p_{LV}(t)\, J\mathbf{F}^{-T}\mathbf{N} & \text{on } \Gamma_0^{endo} \times (0, T], \\ \mathbf{P}\mathbf{N} = p_{LV}(t)|J\mathbf{F}^{-T}\mathbf{N}|\mathbf{v}^{base} & \text{on } \Gamma_0^{base} \times (0, T]. \end{cases} \tag{2.9}$$

In the active stress framework, the Piola-Kirchhoff stress tensor $\mathbf{P} = \mathbf{P}(\mathbf{d}, T_a)$ is a function of displacement $\mathbf{d}$ and active tension $T_a$. On the other hand, $\mathbf{P} = \mathbf{P}(\mathbf{d}, \gamma_f)$ in the active strain approach. In both cases, the Piola-Kirchhoff stress tensor incorporates both passive and active mechanics of the cardiac tissue.

Under the hyperelasticity assumption, once the strain energy density function $\mathcal{W} : \text{Lin}^+ \to \mathbb{R}$ is introduced, the passive part of the Piola-Kirchhoff stress tensor is always obtained as $\frac{\partial \mathcal{W}(\mathbf{F})}{\partial \mathbf{F}}$. Several models are available in literature to describe the anisotropic nature of the myocardium, such as the Guccione [69, 70] or the

Holzapfel-Ogden laws [77]. Thanks to its lower computational cost and the limited number of parameters that makes the calibration phase straightforward, the Guccione constitutive law is nowadays more used in the context of patient-specific electromechanical modeling [60, 173]. The strain energy function of this model reads [69, 70]:

$$
\begin{aligned}
\mathcal{W} = \mathcal{W}(\mathbf{F}) &= \frac{\overline{C}}{2}\left(e^Q - 1\right) \\
Q &= b_{ff}E_{ff}^2 + b_{ss}E_{ss}^2 + b_{nn}E_{nn}^2 \\
&+ b_{fs}\left(E_{fs}^2 + E_{sf}^2\right) + b_{fn}\left(E_{fn}^2 + E_{nf}^2\right) + b_{sn}\left(E_{sn}^2 + E_{ns}^2\right).
\end{aligned}
\tag{2.10}
$$

$E_{ab} = \mathbf{E}a_0 \cdot b_0$ for $a, b \in \{f, s, n\}$ are the entries of $\mathbf{E} = \frac{1}{2}(\mathbf{C} - \mathbf{I})$, i.e the Green-Lagrange strain energy tensor. $\mathbf{C} = \mathbf{F}^\mathsf{T}\mathbf{F}$ represents the right Cauchy-Green deformation tensor. $\overline{C}$ is defined as follows:

$$
\overline{C} = C[\eta + (1-\eta)4.56] \qquad \eta \in [0, 1],
\tag{2.11}
$$

being $C$ a coefficient fitted from experiments [70].

As in cardiac electrophysiology and mechanical activation (Secs. 2.1.1 and 2.1.2, respectively), we assign $\eta = 1$ to healthy tissue, $\eta \in [0.1, 1)$ represents grey zones, and $\eta = 0$ defines scar regions. In this way, we model a stiffer myocardium for infarcted areas. We introduce a convex term $\mathcal{W}_{vol}(J) = \frac{B}{2}(J-1)\log(J)$ into the energy function $\mathcal{W}$, such that $J = 1$ is its global minimum. This term sets a nearly-incompressible constraint, i.e. it penalizes large variations of volume [33, 49, 207]. $B \in \mathbb{R}^+$ is the bulk modulus, which has a role in the torsion mechanism of the ventricle and enforces the incompressibility constraint [61, 161].

When $(\mathscr{A}_{stress})$ is employed, the full Piola-Kirchhoff tensor reads:

$$
\mathbf{P} = \mathbf{P}(\mathbf{d}, T_a) = \frac{\partial \mathcal{W}(\mathbf{F})}{\partial \mathbf{F}} + T_a \frac{\mathbf{F}\mathbf{f}_0 \otimes \mathbf{f}_0}{\sqrt{\mathcal{I}_{4f}}},
\tag{2.12}
$$

where the first term stands as the passive part, while the latter as the active one. The active tension $T_a$ is provided by the force generation model (in our case, either RDQ18 or RDQ20-MF). $\mathcal{I}_{4f} = \mathbf{F}\mathbf{f}_0 \cdot \mathbf{F}\mathbf{f}_0$ is a measure of the tissue stretch along the fiber direction.

In $(\mathscr{A}_{strain})$, in addition to the reference configuration $\Omega_0$ and the deformed one $\Omega$, we introduce an intermediate state $\hat{\Omega}$, which represents the active part of the deformation [2, 3, 111, 152]. The $2^{\mathrm{nd}}$ order tensor $\mathbf{F}_A$ maps $\Omega_0$ into $\hat{\Omega}$, whereas the $\mathbf{F}_E$ tensor transforms $\hat{\Omega}$ into $\Omega$. We finally reach the multiplicative decomposition of $\mathbf{F} = \mathbf{F}_E\mathbf{F}_A$. The full Piola-Kirchhoff tensor $\mathbf{P}$ reads:

$$
\mathbf{P} = \mathbf{P}(\mathbf{d}, \gamma_f) = \det(\mathbf{F}_A)\mathbf{P}_E\mathbf{F}_A^{-\mathsf{T}}, \qquad \mathbf{P}_E = \frac{\partial \mathcal{W}(\mathbf{C}_E, J)}{\partial \mathbf{F}_E}.
\tag{2.13}
$$

For additional details on the final form of tensor $\mathbf{P} = \mathbf{P}(\mathbf{d}, \gamma_f)$, we refer to [61].

To model the interaction of the LV with the pericardium [129, 174], we impose at the epicardial boundary $\Gamma_0^{\mathrm{epi}}$ the generalized Robin boundary condition $\mathbf{PN} + \mathbf{K}^{\mathrm{epi}}\mathbf{d} + \mathbf{C}^{\mathrm{epi}}\frac{\partial \mathbf{d}}{\partial t} = \mathbf{0}$, by defining the following tensors:

$$\mathbf{K}^{\mathrm{epi}} = K_\perp^{\mathrm{epi}}(\mathbf{N} \otimes \mathbf{N}) + K_\parallel^{\mathrm{epi}}(\mathbf{I} - \mathbf{N} \otimes \mathbf{N}),$$
$$\mathbf{C}^{\mathrm{epi}} = C_\perp^{\mathrm{epi}}(\mathbf{N} \otimes \mathbf{N}) + C_\parallel^{\mathrm{epi}}(\mathbf{I} - \mathbf{N} \otimes \mathbf{N}),$$

where the constants $K_\perp^{\mathrm{epi}}$, $K_\parallel^{\mathrm{epi}}$, $C_\perp^{\mathrm{epi}}$, $C_\parallel^{\mathrm{epi}} \in \mathbb{R}^+$ are local values of stiffness and viscosity of the epicardial tissue in the normal or tangential directions, respectively. At the base $\Gamma_0^{\mathrm{base}}$, we set the energy-consistent boundary condition $\mathbf{PN} = p_{\mathrm{LV}}(t)\,|J\mathbf{F}^{-\mathsf{T}}\mathbf{N}|\,\mathbf{v}^{\mathrm{base}}$, originally proposed in [143], that provides an explicit expression for the stresses located at the artificial boundary $\Gamma_0^{\mathrm{base}}$, where we have defined the vector:

$$\mathbf{v}^{\mathrm{base}} = \frac{\int_{\Gamma_0^{\mathrm{endo}}} J\mathbf{F}^{-\mathsf{T}}\mathbf{N}\,d\Gamma_0}{\int_{\Gamma_0^{\mathrm{base}}} |J\mathbf{F}^{-\mathsf{T}}\mathbf{N}|\,d\Gamma_0}.$$

This formulation allows to straightforwardly couple the 3D mechanical model with a ØD model of the whole circulatory system in an energetically consistent manner [147]. At the endocardium $\Gamma_0^{\mathrm{endo}}$, the boundary condition $\mathbf{PN} = -p_{\mathrm{LV}}(t)\,J\mathbf{F}^{-\mathsf{T}}\mathbf{N}$ accounts for the pressure $p_{\mathrm{LV}}(t)$ exerted by the blood contained in the ventricular chamber, modeled through the ØD closed-loop circulation model.

As anticipated, the mechanical model $(\mathcal{M})$ introduces a feedback on both $(\mathscr{A}_{\mathrm{stress}})$ and $(\mathscr{A}_{\mathrm{strain}})$ via $\mathcal{I}_{4f}$. For the two force generation models of $(\mathscr{A}_{\mathrm{stress}})$, $\mathbf{d}$ determines the local sarcomere length SL. More precisely, since sarcomeres are aligned with the muscle fibers $\mathbf{f}_0$, the local sarcomere length SL is given as $SL = SL_0\sqrt{\mathcal{I}_{4f}}$, where $SL_0$ denotes the sarcomere length at rest. To recover the SL field, we consider solving the following differential problem [147]:

$$\begin{cases} -\delta_{SL}^2 \Delta SL + SL = SL_0\sqrt{\mathcal{I}_{4f}} & \text{in } \Omega_0 \times (0, T), \\ \delta_{SL}^2 \nabla SL \cdot \mathbf{N} = 0 & \text{on } \partial\Omega_0 \times (0, T), \end{cases} \tag{2.14}$$

where $\delta_{SL}$ is a regularization parameter, whose aim is that of making the field SL smoother across the computational domain $\Omega_0$, by preventing sharp spatial variations across scales smaller than $\delta_{SL}$.

### 2.1.4 *Blood circulation ($\mathscr{C}$)*

To model the hemodynamics of the whole circulatory network, we consider a lumped parameters closed-loop model [147], inspired by previous models available in literature [20, 76]. Systemic and pulmonary circulations are modeled with resistance-inductance-capacitance (RLC) circuits, one for the arterial part and the other one for the venous part. The four chambers are modeled by time-varying elastance elements, whereas the four valves are represented as non-ideal diodes. Our ØD closed-loop circulation model reads:

$$
\begin{cases}
\dfrac{dV_{LA}(t)}{dt} = Q_{VEN}^{PUL}(t) - Q_{MV}(t), & \text{(2.15a)} \\[2mm]
\dfrac{dV_{LV}(t)}{dt} = Q_{MV}(t) - Q_{AV}(t), & \text{(2.15b)} \\[2mm]
\dfrac{dV_{RA}(t)}{dt} = Q_{VEN}^{SYS}(t) - Q_{TV}(t), & \text{(2.15c)} \\[2mm]
\dfrac{dV_{RV}(t)}{dt} = Q_{TV}(t) - Q_{PV}(t), & \text{(2.15d)} \\[2mm]
C_{AR}^{SYS}\dfrac{dp_{AR}^{SYS}(t)}{dt} = Q_{AV}(t) - Q_{AR}^{SYS}(t), & \text{(2.15e)} \\[2mm]
C_{VEN}^{SYS}\dfrac{dp_{VEN}^{SYS}(t)}{dt} = Q_{AR}^{SYS}(t) - Q_{VEN}^{SYS}(t), & \text{(2.15f)} \\[2mm]
C_{AR}^{PUL}\dfrac{dp_{AR}^{PUL}(t)}{dt} = Q_{PV}(t) - Q_{AR}^{PUL}(t), & \text{(2.15g)} \\[2mm]
C_{VEN}^{PUL}\dfrac{dp_{VEN}^{PUL}(t)}{dt} = Q_{AR}^{PUL}(t) - Q_{VEN}^{PUL}(t), & \text{(2.15h)} \\[2mm]
\dfrac{L_{AR}^{SYS}}{R_{AR}^{SYS}}\dfrac{dQ_{AR}^{SYS}(t)}{dt} = -Q_{AR}^{SYS}(t) - \dfrac{p_{VEN}^{SYS}(t) - p_{AR}^{SYS}(t)}{R_{AR}^{SYS}}, & \text{(2.15i)} \\[2mm]
\dfrac{L_{VEN}^{SYS}}{R_{VEN}^{SYS}}\dfrac{dQ_{VEN}^{SYS}(t)}{dt} = -Q_{VEN}^{SYS}(t) - \dfrac{p_{RA}(t) - p_{VEN}^{SYS}(t)}{R_{VEN}^{SYS}}, & \text{(2.15j)} \\[2mm]
\dfrac{L_{AR}^{PUL}}{R_{AR}^{PUL}}\dfrac{dQ_{AR}^{PUL}(t)}{dt} = -Q_{AR}^{PUL}(t) - \dfrac{p_{VEN}^{PUL}(t) - p_{AR}^{PUL}(t)}{R_{AR}^{PUL}}, & \text{(2.15k)} \\[2mm]
\dfrac{L_{VEN}^{PUL}}{R_{VEN}^{PUL}}\dfrac{dQ_{VEN}^{PUL}(t)}{dt} = -Q_{VEN}^{PUL}(t) - \dfrac{p_{LA}(t) - p_{VEN}^{PUL}(t)}{R_{VEN}^{PUL}}, & \text{(2.15l)}
\end{cases}
$$

being $t \in (0, T]$, where:

$$p_{LV}(t) = p_{EX}(t) + E_{LV}(t) \left( V_{LV}(t) - V_{0,LV} \right), \tag{2.16a}$$

$$p_{LA}(t) = p_{EX}(t) + E_{LA}(t) \left( V_{LA}(t) - V_{0,LA} \right), \tag{2.16b}$$

$$p_{RV}(t) = p_{EX}(t) + E_{RV}(t) \left( V_{RV}(t) - V_{0,RV} \right), \tag{2.16c}$$

$$p_{RA}(t) = p_{EX}(t) + E_{RA}(t) \left( V_{RA}(t) - V_{0,RA} \right), \tag{2.16d}$$

$$Q_{MV}(t) = \frac{p_{LA}(t) - p_{LV}(t)}{R_{MV}(p_{LA}(t), p_{LV}(t))}, \tag{2.16e}$$

$$Q_{AV}(t) = \frac{p_{LV}(t) - p_{AR}^{SYS}(t)}{R_{AV}(p_{LV}(t), p_{AR}^{SYS}(t))}, \tag{2.16f}$$

$$Q_{TV}(t) = \frac{p_{RA}(t) - p_{RV}(t)}{R_{TV}(p_{RA}(t), p_{RV}(t))}, \tag{2.16g}$$

$$Q_{PV}(t) = \frac{p_{RV}(t) - p_{AR}^{PUL}(t)}{R_{PV}(p_{RV}(t), p_{AR}^{PUL}(t))}, \tag{2.16h}$$

with $t \in (0, T]$. In this model, $p_{LA}(t)$, $p_{RA}(t)$, $p_{LV}(t)$, $p_{RV}(t)$, $V_{LA}(t)$, $V_{RA}(t)$, $V_{LV}(t)$ and $V_{RV}(t)$ refer to pressures and volumes in the cardiac chambers (LA, RA, LV and RV, respectively). The variables $Q_{MV}(t)$, $Q_{AV}(t)$, $Q_{TV}(t)$ and $Q_{PV}(t)$ indicate the flow rates through the valves. Moreover, $p_{AR}^{SYS}(t)$, $Q_{AR}^{SYS}(t)$, $p_{VEN}^{SYS}(t)$ and $Q_{VEN}^{SYS}(t)$ express pressures and flow rates of the systemic circulation (arterial and venous). Similarly, $p_{AR}^{PUL}(t)$, $Q_{AR}^{PUL}(t)$, $p_{VEN}^{PUL}(t)$ and $Q_{VEN}^{PUL}(t)$ define pressures and flow rates of the pulmonary circulation (arterial and venous). $p_{EX}(t)$ represents the pressure exerted outside the heart by the surrounding organs and respiration. For the sake of simplicity, we consider $p_{EX}(t) = 0$. Time varying $E_{LA}(t)$, $E_{LV}(t)$, $E_{RA}(t)$, $E_{RV}(t)$ are the analytically prescribed elastances of the four cardiac chambers calibrated on a physiological basis, with values ranging from $E_{LA}^{pass}$, $E_{LV}^{pass}$, $E_{RA}^{pass}$, $E_{RV}^{pass}$ – when the chambers are at rest – to $(E_{LA}^{pass} + E_{LA}^{act,max})$, $(E_{LV}^{pass} + E_{LV}^{act,max})$, $(E_{RA}^{pass} + E_{RA}^{act,max})$, $(E_{RV}^{pass} + E_{RV}^{act,max})$ – when the chambers are fully contracted. Finally, $R_{MV}(p_1, p_2)$, $R_{AV}(p_1, p_2)$, $R_{TV}(p_1, p_2)$ and $R_{PV}(p_1, p_2)$ define the behavior of valves as diodes, according to the following relationship:

$$R_i(p_1, p_2) = \begin{cases} R_{min}, & \text{if} \quad p_1 < p_2 \\ R_{max}, & \text{if} \quad p_1 \geqslant p_2 \end{cases} \quad \text{for} \quad i \in \{MV, AV, TV, PV\},$$

where $p_1$ and $p_2$ denote the pressures ahead and behind the valve leaflets with respect to the flow direction, whereas $R_{min}$ and $R_{max}$ are the minimum and maximum resistance of the valves. For an idealized valve, one would have $R_{min} = 0$ and $R_{max} = +\infty$ instead. By setting $R_{min} > 0$, one has dissipation of mechanical energy taking place when the blood flows through the opened valve; we set $R_{max} < +\infty$ sufficiently large so that blood leakage when the valve is closed is negligible.

Hereafter, for the sake of brevity, Eqs. (2.15)–(2.16) will be expressed in the following compact form:

$$
\begin{cases}
\dfrac{d\mathbf{c}_1(t)}{dt} = \mathbf{Z}(t, \mathbf{c}_1(t), \mathbf{c}_2(t)) & t \in (0, T], \\
\mathbf{c}_2(t) = \mathbf{W}(t, \mathbf{c}_1(t)) & t \in (0, T], \\
\mathbf{c}_1(0) = \mathbf{c}_{1,0}, \\
\mathbf{c}_2(0) = \mathbf{W}(0, \mathbf{c}_1(0)),
\end{cases}
\tag{2.17}
$$

where:

$$
\mathbf{c}_1(t) = (V_{LA}(t), V_{LV}(t), V_{RA}(t), V_{RV}(t), p_{AR}^{SYS}(t), p_{VEN}^{SYS}(t), p_{AR}^{PUL}(t), p_{VEN}^{PUL}(t),
$$
$$
Q_{AR}^{SYS}(t), Q_{VEN}^{SYS}(t), Q_{AR}^{PUL}(t), Q_{VEN}^{PUL}(t))^{\mathsf{T}},
$$
$$
\mathbf{c}_2(t) = (p_{LV}(t), p_{LA}(t), p_{RV}(t), p_{RA}(t), Q_{MV}(t), Q_{AV}(t), Q_{TV}(t), Q_{PV}(t))^{\mathsf{T}};
$$

$\mathbf{Z}(t, \mathbf{c}_1(t), \mathbf{c}_2(t))$ collects the whole right hand side of Eq. (2.15), while $\mathbf{c}_2(t) = \mathbf{W}(t, \mathbf{c}_1(t))$ stands as a compact notation for Eq. (2.16), rewritten in explicit form with respect to the variable $\mathbf{c}_2$.

### 2.1.5 3D-ØD coupling ($\mathscr{V}$)

In Eq. (2.17) each cardiac chamber is modeled as a time-varying elastance element, that is a ØD simplified model. In this thesis, we employ this ØD circulation model in conjunction with the 3D LV model given by ($\mathscr{E}$)–($\mathscr{I}$)–($\mathscr{A}$)–($\mathscr{M}$). With this goal, we remove from the circulation model the time-varying elastance element associated with the LV, and we replace it with the 3D electromechanical model. Hence, the PV relationship between $p_{LV}$ and $V_{LV}$ is no longer prescribed by Eq. (2.16a), but by the resolution of the 3D electromechanical model. The resulting 3D–ØD coupled model (depicted in Fig. 2.2) must satisfy at each time $t \in (0, T)$ the coupling condition $V_{LV}^{\varnothing D}(\mathbf{c}_1(t)) = V_{LV}^{3D}(\mathbf{d}(t))$, that we denote by ($\mathscr{V}$), where $V_{LV}^{\varnothing D}(\mathbf{c}_1(t)) = V_{LV}(t)$ represents the LV volume in the ØD circulation model. $V_{LV}^{3D}(\mathbf{d}(t))$ represents the LV volume in the 3D model and it is computed as:

$$
V_{LV}^{3D}(\mathbf{d}(t)) = \int_{\Gamma_0^{endo}} J(t) \left( (\mathbf{h} \otimes \mathbf{h}) (\mathbf{x} + \mathbf{d}(t) - \mathbf{b}) \right) \cdot \mathbf{F}^{-\mathsf{T}}(t) \mathbf{N} \, d\Gamma_0,
$$

where $\mathbf{h}$ is a vector orthogonal to the LV centerline (i.e. lying on the LV base) [147]. Subtracting to the space coordinate $\mathbf{x} + \mathbf{d}(t)$ that of a point $\mathbf{b}$, lying inside the LV, improves the accuracy of the formula when the ventricular base changes its orientation.

Having introduced an additional scalar constraint, i.e. ($\mathscr{V}$), we expect an additional unknown: it is in fact $p_{LV}$, which is not determined by Eq. (2.16a) anymore. Rather, it acts as a Lagrange multiplier enforcing the constraint ($\mathscr{V}$).

Hence, we define the "reduced" vector $\widetilde{\mathbf{c}}_2$ such that $\mathbf{c}_2^\top = (p_{LV}, \widetilde{\mathbf{c}}_2^\top)$, so that we can rewrite Eqs. (2.16a)–(2.16h) as $\widetilde{\mathbf{c}}_2(t) = \widetilde{\mathbf{W}}(t, \mathbf{c}_1(t), p_{LV}(t))$. This allows to write the "reduced" version of Eq. (2.17) as ($\mathscr{C}$), where we have defined:

$$
\widetilde{\mathbf{Z}}(t, \mathbf{c}_1, p_{LV}) := \mathbf{Z}\left(t, \mathbf{c}_1, \begin{pmatrix} p_{LV} \\ \widetilde{\mathbf{W}}(t, \mathbf{c}_1, p_{LV}) \end{pmatrix}\right).
$$

### 2.1.6 *Windkessel model ($\mathscr{W}$)*

In some cases, either to simplify the mathematical model or to ease 3D-ØD parameters tuning in patient-specific LVs, we will use a 2-element windkessel afterload model. This model defines the evolution in time of variables $p_{LV}(t)$ and $V_{LV}(t)$ only, and it is extensively presented in [61, 161], along with its numerical discretization. For the sake of completeness, we report here below its equation:

$$
C \frac{dp_{LV}(t)}{dt} = -\frac{p_{LV}(t)}{R} - \frac{dV_{LV}(t)}{dt}, \tag{2.18}
$$

with $t \in (0, T]$. $C, R > 0$ are two parameters representing the capacitance and the resistance of the electric circuit that mimics the blood flowing in the aorta.

### 2.2 REFERENCE CONFIGURATION AND INITIAL DISPLACEMENT

In the mechanics model ($\mathscr{M}$), the stress-strain relationship is referred to the natural stress-free configuration $\Omega_0$. However, the cardiac chambers are subject to loads during the cardiac cycle (i.e., non zero forces are applied to the boundary at every $t \in (0, T)$).

Let us denote by $\widetilde{\Omega}$ the medical image used to generate the LV. This configuration surely presents residual stresses, since an internal pressure $p_{LV} \neq 0$ is acting at every stage of the heartbeat. Therefore, in the preprocessing stage, we need to recover the reference configuration $\Omega_0$ from $\widetilde{\Omega}$.

Our strategy to initialize the numerical simulation is sketched in Fig. 2.4. As a first step, starting from the geometry acquired from medical imaging $\widetilde{\Omega}$, we recover the stress-free reference configuration $\Omega_0$ by virtually deflating the LV previously subject to an internal pressure $\widetilde{p}$. Then, as a second step, we inflate the LV again, by applying the EDP $p_{ED}$ at the endocardium. In the next sections we give the mathematical details behind these two steps.

### 2.2.1 *Recovering the reference configuration*

We assume that the configuration $\widetilde{\Omega}$ occurs during diastole, where typically the medical image is acquired: the LV is loaded by a small pressure $p_{LV} = \widetilde{p}$ and only a residual active tension $T_a = \widetilde{T}_a > 0$ acts. By adopting a quasi-static assumption (motivated by the relatively slow movement of the myocardium
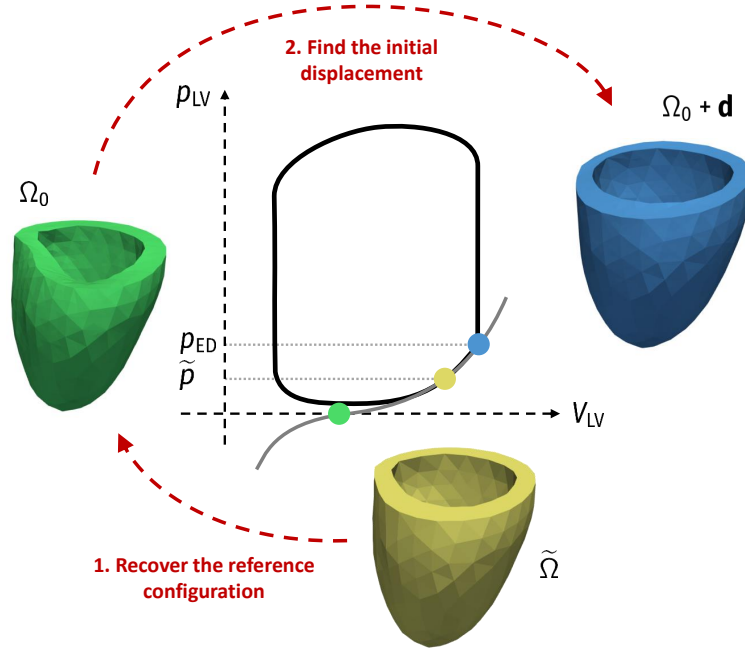
Figure 2.4: Sketch of the strategy used to initialize the simulation. The grey line represents the so–called Klotz curve [88], that is the PV relationship of the relaxed ventricle. The black line represents the PV loop of the LV.

during the final part of diastole), the tissue displacement is given by the solution of the following differential problem: find $\mathbf{d}$ such that

$$
\begin{cases}
\nabla \cdot \mathbf{P} = 0 & \text{in } \Omega_0, \\
\mathbf{P}\mathbf{N} + \mathbf{K}^{\text{epi}}\mathbf{d} = \mathbf{o} & \text{on } \Gamma_0^{\text{epi}}, \\
\mathbf{P}\mathbf{N} = p_{\text{LV}} |J\mathbf{F}^{-\mathsf{T}}\mathbf{N}| \, \mathbf{v}^{\text{base}} & \text{on } \Gamma_0^{\text{base}}, \\
\mathbf{P}\mathbf{N} = -p_{\text{LV}} J\mathbf{F}^{-\mathsf{T}}\mathbf{N} & \text{on } \Gamma_0^{\text{endo}}.
\end{cases}
\tag{2.19}
$$

Eq. (2.19) is derived from $(\mathscr{M})$ by setting to zero the time-dependent terms. We recall that $\mathbf{P} = \mathbf{P}(\mathbf{d}, T_a)$ with the active stress approach, while $\mathbf{P} = \mathbf{P}(\mathbf{d}, \gamma_f)$ with the active strain formulation. For the sake of simplicity, the reference configuration procedure will be formulated in the active stress framework by employing $T_a$ and $\widetilde{T}_a$, even if similar considerations hold for the active strain approach (with $\gamma_f$ and $\widetilde{\gamma}_f$). Thus, to recover the coordinate $\mathbf{x}_0$ of the configuration $\Omega_0$ we need to solve the following inverse problem: find the domain $\Omega_0$ such that, if we displace $\mathbf{x}_0$ by the solution $\mathbf{d} = \mathbf{d}_{\text{eq}}(\mathbf{x}_0, p_{\text{LV}}, T_a)$ of Eq. (2.19) obtained for $p_{\text{LV}} = \widetilde{p}$ and $T_a = \widetilde{T}_a$, we get the coordinate $\widetilde{\mathbf{x}}$ of the domain $\widetilde{\Omega}$ (i.e. $\widetilde{\mathbf{x}} = \mathbf{x}_0 + \mathbf{d}$). In Sec. 2.5 we present an algorithm for its numerical solution.

### 2.2.2 *Finding the initial displacement*

After the recovery of the reference configuration $\Omega_0$, we set $p_{LV} = p_{ED}$. Then, we solve again Eq. (2.19). In this manner, we obtain the end-diastolic configuration of the LV, i.e. $\mathbf{d}_{ED}$. Hence, we set $\mathbf{d}_0 = \mathbf{d}_{ED}$ in Eq. (2.9).

## 2.3 BALANCE OF MECHANICAL ENERGY

We derive a balance of the mechanical energy for the whole cardiovascular system. In particular, we analyze how mechanical energy is injected, dissipated and transferred in the different compartments of the heart and in both systemic and pulmonary circulation. In Sec. 2.3.1, we consider the ØD closed-loop circulation model ($\mathscr{C}$) introduced in Sec. 2.1.4. In Sec. 2.3.2 we focus on the coupled 3D-ØD model ($\mathscr{M}$)–($\mathscr{V}$)–($\mathscr{C}$).

### 2.3.1 *Energy balance for the ØD model*

To define the terms associated with the work performed by the cardiac chambers, we write $E_i(t) = E_i^{\text{pass}} + E_i^{\text{act}}(t)$ (for $i \in \{LA, LV, RA, RV\}$), where $E_i^{\text{pass}}$ is the passive elastance of the tissue (i.e. the elastance when the tissue is not activated) and $E_i^{\text{act}}$ is instead the active component of the elastance.

**Definition 1.** *We define the total mechanical energy of the whole ØD cardiocirculatory model as:*

$$
\begin{aligned}
\mathcal{M}(t) = {}& \mathcal{E}_{LA}(t) + \mathcal{E}_{LV}(t) + \mathcal{E}_{RA}(t) + \mathcal{E}_{RV}(t) \\
& + \mathcal{E}_{AR}^{SYS}(t) + \mathcal{E}_{VEN}^{SYS}(t) + \mathcal{E}_{AR}^{PUL}(t) + \mathcal{E}_{VEN}^{PUL}(t) \\
& + \mathcal{K}_{AR}^{SYS}(t) + \mathcal{K}_{VEN}^{SYS}(t) + \mathcal{K}_{AR}^{PUL}(t) + \mathcal{K}_{VEN}^{PUL}(t),
\end{aligned}
$$

*where, for $i \in \{LA, LV, RA, RV\}$, $j \in \{AR, VEN\}$ and $k \in \{SYS, PUL\}$:*

- $\mathcal{E}_i(t) = \dfrac{1}{2} E_i^{\text{pass}} \left(V_i(t) - V_{o,i}\right)^2$ *is the elastic energy stored by a cardiac chamber;*

- $\mathcal{E}_j^k(t) = \dfrac{1}{2} C_j^k \left(p_j^k(t)\right)^2$ *is the elastic energy stored in the vascular network, due to vessels compliance;*

- $\mathcal{K}_j^k(t) = \dfrac{1}{2} L_j^k \left(Q_j^k(t)\right)^2$ *is the kinetic energy related to the blood flow inertia.*

We provide now a deeper explanation of the definition of $\mathcal{E}_j^k$. Let us consider, as an example, $\mathcal{E}_{AR}^{SYS}$. We notice that $Q_{AV}(t) - Q_{AR}^{SYS}(t)$ is the net blood flux passing through the arterial systemic network. Hence, by denoting with $V_{AR}^{SYS}(t)$ the blood volume stored in the arterial systemic network, we have:

$$
\frac{dV_{AR}^{SYS}(t)}{dt} = Q_{AV}(t) - Q_{AR}^{SYS}(t).
$$

By comparing the latter equation to Eq. (2.15e) we get:

$$p_{AR}^{SYS}(t) = \frac{1}{C_{AR}^{SYS}} \left( V_{AR}^{SYS}(t) - V_{0,AR}^{SYS} \right),$$

where $V_{0,AR}^{SYS}$ is the blood volume stored within the arterial systemic network when the pressure is null. In conclusion, we have:

$$\mathcal{E}_{AR}^{SYS}(t) = (2\, C_{AR}^{SYS})^{-1} \left( V_{AR}^{SYS}(t) - V_{0,AR}^{SYS} \right)^2,$$

where $1/C_{AR}^{SYS}$ is the arterial systemic network elastance (the inverse of the compliance), coherently with the definition of $\mathcal{E}_{LA}$.

**Definition 2.** *We define the power generated by active contraction, due to ATP consumption occurring at the cellular level, as:*

$$\Pi^{act}(t) = \Pi_{LA}^{act}(t) + \Pi_{LV}^{act}(t) + \Pi_{RA}^{act}(t) + \Pi_{RV}^{act}(t),$$

*where $\Pi_i^{act}(t) = -E_i^{act}(t) \left( V_i(t) - V_{0,i} \right) \frac{dV_i}{dt}(t)$ is the power exerted by the active contraction of a cardiac chamber (for $i \in \{LA, LV, RA, RV\}$),*

**Definition 3.** *We define the power dissipated within the 0D circulation model by viscous forces (e.g. the blood flows through the valves and the vascular network) as:*

$$\Pi^{diss}(t) = \Pi_{MV}(t) + \Pi_{AV}(t) + \Pi_{TV}(t) + \Pi_{PV}(t)$$
$$+ \Pi_{AR}^{SYS}(t) + \Pi_{VEN}^{SYS}(t) + \Pi_{AR}^{PUL}(t) + \Pi_{VEN}^{PUL}(t).$$

*where:*

- *the power dissipated by the blood flux through the cardiac valves is given by:*

$$\Pi_{MV}(t) = -\frac{(p_{LA}(t) - p_{LV}(t))^2}{R_{MV}(p_{LA}(t), p_{LV}(t))}, \qquad \Pi_{AV}(t) = -\frac{\left(p_{LV}(t) - p_{AR}^{SYS}(t)\right)^2}{R_{AV}(p_{LV}(t), p_{AR}^{SYS}(t))},$$

$$\Pi_{TV}(t) = -\frac{(p_{RA}(t) - p_{RV}(t))^2}{R_{TV}(p_{RA}(t), p_{RV}(t))}, \qquad \Pi_{PV}(t) = -\frac{\left(p_{RV}(t) - p_{AR}^{PUL}(t)\right)^2}{R_{PV}(p_{RV}(t), p_{AR}^{PUL}(t))};$$

$$(2.20)$$

- *$\Pi_j^k(t) = -R_j^k \left( Q_j^k(t) \right)^2$, that is the power dissipated by the arterial systemic network (for $j \in \{AR, VEN\}$ and $k \in \{SYS, PUL\}$).*

We remark that all the terms in Eq. (2.20) are nonpositive.

**Definition 4.** *We define the power due to the action of the external pressure $p_{EX}$ on the myocardium as:*

$$\Pi^{ex}(t) = \Pi_{LA}^{ex}(t) + \Pi_{LV}^{ex}(t) + \Pi_{RA}^{ex}(t) + \Pi_{RV}^{ex}(t),$$

*where $\Pi_i^{ex}(t) = -p_{EX}(t) \frac{dV_i}{dt}(t)$ is the power exerted by the external pressure $p_{EX}(t)$ acting on a cardiac chamber (for $i \in \{LA, LV, RA, RV\}$).*

We have the following result.

**Proposition 1.** *The solution of Eq. (2.17) for the whole 0D circulation model satisfies the energy balance:*

$$\frac{d}{dt}\mathcal{M}(t) = \Pi^{act}(t) + \Pi^{diss}(t) + \Pi^{ex}(t), \tag{2.21}$$

*whose terms are introduced in Defs. 1–4.*

*Proof.* To derive Eq. (2.21) we consider, as illustrative examples, a representative cardiac chamber, a cardiac valve and a vascular branch. Indeed, similar computations hold for the other chambers, valves and vascular compartments.
*Energy balance of the cardiac chambers.* Let us consider the LA. By multiplying Eq. (2.16b) by $\frac{dV_{LA}(t)}{dt}$ and thanks to Eq. (2.15a), we get:

$$p_{LA}(t)(Q_{VEN}^{PUL}(t) - Q_{MV}(t)) = \frac{d}{dt}\mathcal{E}_{LA}(t) - \Pi_{LA}^{act}(t) - \Pi_{LA}^{ex}(t). \tag{2.22}$$

*Energy balance of the cardiac valves.* From (2.16e) we obtain:

$$(p_{LA}(t) - p_{LV}(t))Q_{MV}(t) = -\Pi_{MV}(t). \tag{2.23}$$

Similar considerations hold for the other valves.
*Energy balance of the peripheral blood reservoirs.* By multiplying the first equation of (2.15e) by $p_{AR}^{SYS}(t)$, we get:

$$p_{AR}^{SYS}(t)Q_{AV}(t) - p_{AR}^{SYS}(t)Q_{AR}^{SYS}(t) = \frac{d}{dt}\mathcal{E}_{AR}^{SYS}(t) \tag{2.24}$$

*Energy balance of the peripheral blood conducting system.* By multiplying (2.15i) by $R_{AR}^{SYS}Q_{AR}^{SYS}(t)$, we get:

$$p_{AR}^{SYS}(t)Q_{AR}^{SYS}(t) - p_{VEN}^{SYS}(t)Q_{AR}^{SYS}(t) = \frac{d}{dt}\mathcal{K}_{AR}^{SYS}(t) - \Pi_{AR}^{SYS}(t). \tag{2.25}$$

*Total balance.* By proceeding as above for the other cardiac chambers, valves and vascular branches, and summing up the resulting equations, we obtain Eq. (2.21). This completes the proof. □

Each of the four terms of Eq. (2.21) represents the result of the sum of different contributions, associated with the four chambers, the four valves and the different compartments of the vascular network (systemic and pulmonary, arterial and venous). The total work performed in a time interval $[0, T]$ is obtained by integrating the corresponding power over time, according to the following definition.

**Definition 5.** *Let us consider a time horizon $T > 0$. The total work performed by active and dissipative forces in the time interval $[0, T]$ are defined as:*

$$W^{act} = \int_0^T \Pi^{act}(t)\, dt, \qquad W^{diss} = \int_0^T \Pi^{diss}(t)\, dt,$$

*respectively.*

When the heart rhythm has reached a periodic regime, it carries out its function alongside a cyclical path. In this case, the work balance of the following proposition holds.

**Proposition 2.** *Let us suppose that* $p_{EX}(t)$ *is constant in time. Then, periodic solutions of Eq. (2.17) (i.e. with* $\mathbf{c}_1(0) = \mathbf{c}_1(T)$*) satisfy:*

$$W^{\text{act}} + W^{\text{diss}} = 0. \tag{2.26}$$

*Proof.* We integrate the energy balance of Eq. (2.21) over a cardiac cycle $[0, T]$. Thanks to the periodicity assumption, the contribution of the mechanical energy term $\mathcal{M}$ is null. Moreover, it is easy to show that the term $\Pi^{\text{ex}}(t)$ is conservative and hence its contribution over $[0, T]$ is also zero. $\qquad\square$

Therefore, when the heart is functioning in a periodic regime, the work performed by the contraction of the four chambers balances the energy dissipated by the four valves and by the blood flux through the systemic and pulmonary circulations.

### 2.3.2 *Energy balance for the 3D-0D coupled model*

For the sake of simplicity, we derive this part of the energy balance within the active stress approach, i.e. $\mathbf{P} = \mathbf{P}(\mathbf{d}, T_a)$.

3D LV ENERGY BALANCE  By multiplying the first equation of $(\mathcal{M})$ by $\frac{\partial \mathbf{d}}{\partial t}$ and integrating over $\Omega_0$ we obtain:

$$\int_{\Omega_0} \rho_s \frac{\partial^2 \mathbf{d}}{\partial t^2} \cdot \frac{\partial \mathbf{d}}{\partial t} \, d\mathbf{x} + \int_{\Omega_0} \mathbf{P}(\mathbf{d}, T_a) : \nabla \left( \frac{\partial \mathbf{d}}{\partial t} \right) \, d\mathbf{x} = \int_{\partial\Omega_0} \mathbf{P}(\mathbf{d}, T_a)\mathbf{N} \cdot \frac{\partial \mathbf{d}}{\partial t} \, d\Gamma_0. \tag{2.27}$$

By substituting the boundary conditions of $(\mathcal{M})$ into (2.27), we obtain the following energy balance for the 3D LV model:

$$\frac{d}{dt}\mathcal{K}_{\text{LV,3D}}(t) + \frac{d}{dt}\mathcal{E}_{\text{LV,3D}}(t) = \Pi^{\text{act}}_{\text{LV,3D}}(t) + \Pi^{\text{diss}}_{\text{LV,3D}}(t) + \Pi^{\text{press}}_{\text{LV,3D}}(t). \tag{2.28}$$

This relation reveals the mutual balance of:

- the kinetic energy associated with the motion of the LV:

$$\mathcal{K}_{\text{LV,3D}}(t) = \frac{1}{2} \int_{\Omega_0} \rho_s \left| \frac{\partial \mathbf{d}}{\partial t} \right|^2 \, d\mathbf{x};$$

- the elastic energy internally stored by the LV muscle and by the elastic components of the surrounding tissues:

$$\mathcal{E}_{\text{LV,3D}}(t) = \int_{\Omega_0} \mathcal{W}(\mathbf{F}) \, d\mathbf{x} + \frac{1}{2} \int_{\Gamma_0^{\text{epi}}} \left[ K_\perp^{\text{epi}} |\mathbf{d} \cdot \mathbf{N}|^2 + K_\parallel^{\text{epi}} |(\mathbf{I} - \mathbf{N} \otimes \mathbf{N})\mathbf{d}|^2 \right] \, d\Gamma_0,$$

where the displacement at the epicardium is split into the normal $|\mathbf{d} \cdot \mathbf{N}|$ and tangent $|(\mathbf{I} - \mathbf{N} \otimes \mathbf{N})\mathbf{d}|$ component;

- the power exerted by the active contraction of the LV:

$$\Pi_{\text{LV,3D}}^{\text{act}}(t) = - \int_{\Omega_0} T_a \frac{\mathbf{F}\mathbf{f}_0 \otimes \mathbf{f}_0}{\sqrt{\mathcal{J}_{4f}}} : \nabla\left(\frac{\partial \mathbf{d}}{\partial t}\right) d\mathbf{x},$$

- the power dissipated by the interaction with the pericardium:

$$\Pi_{\text{LV,3D}}^{\text{diss}}(t) = - \int_{\Gamma_0^{\text{epi}}} \left[ C_\perp^{\text{epi}} \left| \frac{\partial \mathbf{d}}{\partial t} \cdot \mathbf{N} \right|^2 + C_\parallel^{\text{epi}} \left| (\mathbf{I} - \mathbf{N} \otimes \mathbf{N}) \frac{\partial \mathbf{d}}{\partial t} \right|^2 \right] d\Gamma_0 \leqslant 0,$$

which is a nonpositive term;

- the power exchanged with the blood contained in the LV cavity, by means of the action of pressure $p_{\text{LV}}(t)$ on the endocardium:

$$\Pi_{\text{LV,3D}}^{\text{press}}(t) = p_{\text{LV}}(t) \left[ \int_{\Gamma_0^{\text{endo}}} J\mathbf{F}^{-\mathsf{T}}\mathbf{N} \cdot \frac{\partial \mathbf{d}}{\partial t} d\Gamma_0 - \int_{\Gamma_0^{\text{base}}} |J\mathbf{F}^{-\mathsf{T}}\mathbf{N}| \frac{\partial \mathbf{d}}{\partial t} d\Gamma_0 \cdot \mathbf{v}^{\text{base}} \right].$$

As in [143], the term in square brackets corresponds to the time derivative of the LV volume, that is $\Pi_{\text{LV,3D}}^{\text{press}}(t) = p_{\text{LV}}(t)\frac{d}{dt}V_{\text{LV}}^{\text{3D}}(\mathbf{d}(t))$. Then, in virtue of the coupling condition $(\mathcal{V})$ and Eq. (2.15b), we obtain $\Pi_{\text{LV,3D}}^{\text{press}}(t) = p_{\text{LV}}(t)(Q_{\text{MV}}(t) - Q_{\text{AV}}(t))$.

TOTAL ENERGY BALANCE  By setting $p_{\text{EX}}(t) \equiv 0$, i.e. by neglecting the effect of the pressure exerted by the surronding organs, and by replacing the energy balance of the ØD LV model with Eq. (2.28), we obtain again Eq. (2.21), where the total mechanical energy is now:

$$\begin{aligned}
\mathcal{M}(t) = {}& \mathcal{E}_{\text{LA}}(t) + \mathcal{E}_{\text{LV,3D}}(t) + \mathcal{E}_{\text{RA}}(t) + \mathcal{E}_{\text{RV}}(t) \\
& + \mathcal{E}_{\text{AR}}^{\text{SYS}}(t) + \mathcal{E}_{\text{VEN}}^{\text{SYS}}(t) + \mathcal{E}_{\text{AR}}^{\text{PUL}}(t) + \mathcal{E}_{\text{VEN}}^{\text{PUL}}(t) \\
& + \mathcal{K}_{\text{AR}}^{\text{SYS}}(t) + \mathcal{K}_{\text{VEN}}^{\text{SYS}}(t) + \mathcal{K}_{\text{AR}}^{\text{PUL}}(t) + \mathcal{K}_{\text{VEN}}^{\text{PUL}}(t) + \mathcal{K}_{\text{LV,3D}}(t)
\end{aligned} \tag{2.29}$$

and the power of active contraction and the total dissipated power ($\Pi^{\text{diss}}(t) \geqslant 0$) are:

$$\Pi^{\text{act}}(t) = \Pi_{\text{LA}}^{\text{act}}(t) + \Pi_{\text{LV,3D}}^{\text{act}}(t) + \Pi_{\text{RA}}^{\text{act}}(t) + \Pi_{\text{RV}}^{\text{act}}(t);$$

$$\begin{aligned}
\Pi^{\text{diss}}(t) = {}& \Pi_{\text{MV}}(t) + \Pi_{\text{AV}}(t) + \Pi_{\text{TV}}(t) + \Pi_{\text{PV}}(t) \\
& + \Pi_{\text{AR}}^{\text{SYS}}(t) + \Pi_{\text{VEN}}^{\text{SYS}}(t) + \Pi_{\text{AR}}^{\text{PUL}}(t) + \Pi_{\text{VEN}}^{\text{PUL}}(t) + \Pi_{\text{LV,3D}}^{\text{diss}}(t),
\end{aligned}$$

respectively; here $\Pi^{\text{ex}}(t) \equiv 0$. We remark that Prop. 2 applies also to this case. Finally, we conclude that the 3D-ØD coupled model satisfies the principle of conservation of mechanical energy. This result is achieved thanks to the energy-consistent boundary conditions imposed at the LV base; see Eq. (2.9). If other boundary conditions – such as homogeneous Neumann conditions – are imposed at the base instead, the relationship $\Pi_{\text{LV,3D}}^{\text{press}}(t) = p_{\text{LV}}(t)\frac{d}{dt}V_{\text{LV}}^{\text{3D}}(\mathbf{d}(t))$ may not hold and the balance of Eq. (2.21) would not be satisfied.

We notice that, compared to the fully ØD case, the 3D electromechanical model shows two additional terms, namely $\mathcal{K}_{\text{LV,3D}}(t)$ and $\Pi^{\text{diss}}_{\text{LV,3D}}$, respectively accounting for the kinetic energy of the LV and for the dissipation associated with the interaction of $\Gamma^{\text{epi}}_0$ with surrounding tissues. Indeed, both features are not included in the ØD circulation model, in which cardiac chambers are modeled quasistatically.

### 2.3.3 *Quantitative analysis of cardiac energetics*

In Fig. 2.5 we report all the energy and power terms over a characteristic steady-state cardiac cycle obtained with a numerical simulation of the ØD circulation model. For this simulation we employ the parameters reported in [147, 148], with $E^{\text{act,max}}_{\text{LV}} = 2.75 \, \text{mmHg} \, \text{mL}^{-1}$ and $E^{\text{pass}}_{\text{LV}} = 0.08 \, \text{mmHg} \, \text{mL}^{-1}$. Fig. 2.5 (top-left) displays the time evolution of the terms of Eq. (2.21). We notice that, while the energy input ($\Pi^{\text{act}}$) occurs in a short time interval of nearly $100 \, \text{ms}$ (during systole), energy dissipation ($\Pi^{\text{diss}}$) takes place throughout the entire duration of the heartbeat. As a matter of fact, mechanical energy $\mathcal{M}$ plays a dominant role. Moreover, it is initially accumulated and then it is gradually dissipated as the blood flows through systemic and pulmonary circulations.

Fig. 2.5 (top-right, bottom-left, bottom-right) illustrate the details of the three terms $\mathcal{M}$, $\Pi^{\text{act}}$ and $\Pi^{\text{diss}}$, showing how they split into the various subterms during the different phases of the heartbeat. Specifically, we notice that the chamber that contributes the most to the work generation is the LV, followed by the RV, while the atria only contribute – albeit to a small extent – around $t = 0.8 \, \text{s}$, during the atrial systole. The large part of mechanical energy and of dissipated power are associated with the systemic arterial circulation, as this branch of the circulatory network is located downstream the LV, the chamber carrying out most of the mechanical work. We remark that a non-negligible dissipation of energy also takes place across the open valves, due to the high-speed blood flow across the valvular orifices.

Our model allows to estimate the daily production of mechanical work of the heart. This is obtained by multiplying the number of seconds in a day times the average generated power, given by:

$$\overline{\Pi}^{\text{act}} = \frac{1}{T} \int_0^T \Pi^{\text{act}}(t) \, dt.$$

Applying this formula to the results of the simulation considered in Fig. 2.5, we obtain a daily work production of $182.5 \, \text{kJ}$, of which $155.9 \, \text{kJ}$ attributable to the LV, $24.8 \, \text{kJ}$ to the RV and only $1.8 \, \text{kJ}$ to the atria.

In the daily clinical practice, the work generated by the myocardium is instead estimated through simple relationships [81, 114]. In this regard, our model offers a tool to estimate the validity of these approaches. A commonly used formula [81] is:

$$\overline{\Pi}^{\text{act}} \simeq \overline{p^{\text{SYS}}_{\text{AR}}} \frac{SV}{T_{\text{beat}}}, \tag{2.30}$$
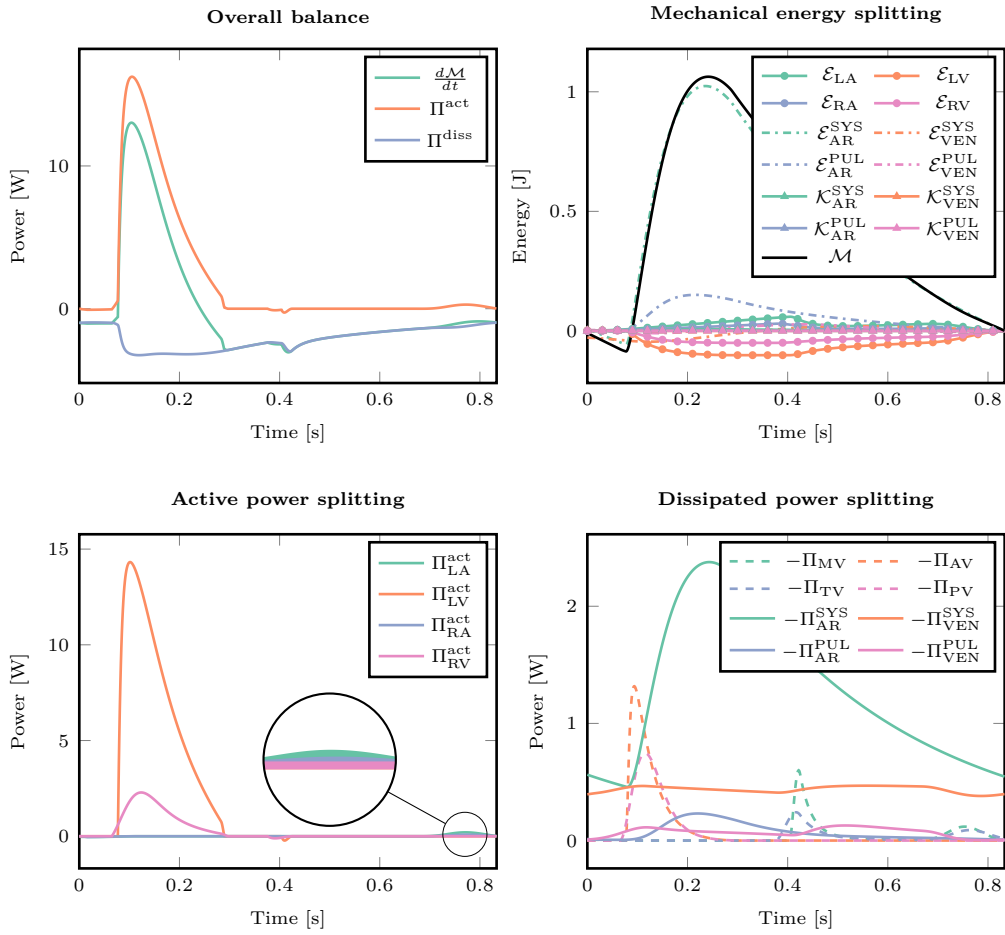
Figure 2.5: Time evolution of both power and energy terms ($\mathcal{M}$, $\mathcal{E}$, $\mathcal{K}$, $\Pi^{\mathrm{act}}$, $\Pi^{\mathrm{diss}}$) of the ∅D circulation model. We consider a single heartbeat in a periodic regime.

where $\overline{p_{AR}^{SYS}}$ denotes the average systemic arterial pressure (corresponding to the wrist average blood pressure), SV is the stroke volume and $T_{beat}$ is the heartbeat period. By applying (2.30) to the results of the above simulation, we obtain a daily work generation of 152.4 kJ. Hence (2.30) underestimates the mechanical work by 16%. As a matter of fact, (2.30) only refers to the work done by the LV (which is, instead, approximated up to an error of only 2%). The large part of the error is thus attributable to the work performed by the RV, which is not accounted for in (2.30).

In common clinical practice, then, $\overline{p_{AR}^{SYS}}$ is not directly measured, but it is estimated as $\overline{p_{AR}^{SYS}} = 1/3\,p_{max} + 2/3\,p_{min}$, where $p_{max}$ and $p_{min}$ are the maximum (systolic) and minimum (diastolic) arterial pressures (see e.g. [114]). With this further approximation, we obtain an estimated daily work of 138.8 kJ, which represents 1.3% of an ideal intake of calories of an healthy adult male (i.e. 33.15 kcal out of approximately 2500 kcal). This underestimates the LV work by 11% and the total work of the myocardium by 24%.

## 2.4 NUMERICAL DISCRETIZATION

In this thesis, we develop two schemes for the numerical discretization of the 3D-ØD coupled problem of cardiac electromechanics and cardiovascular circulation. These two numerical schemes are both sketched in Figs. 2.6 and 2.7. We use partitioned strategies that allow to separate and properly manage the space and time scales related to cardiac electromechanics, by considering different space and time resolutions according to the characteristic scale of each core model. These two schemes are thus segregated (i.e. the different core models are solved sequentially), exploit intergrid transfer operators (as different mesh sizes are employed for the different core models) and are staggered (as different time steps are used for the different core models) [147, 148, 161]. For these reasons, we refer to them as SIS schemes [131].

We first update the variables of ($\mathscr{I}$) and ($\mathscr{E}$), then the variables of ($\mathscr{A}$) and finally, after updating the unknowns of ($\mathscr{M}$) or ($\mathscr{M}$)–($\mathscr{V}$), respectively, we update the ones of ($\mathscr{W}$) or ($\mathscr{C}$), respectively.

Space discretization is based on the FEM [136]. We consider a fine representation of the computational domain for both ($\mathscr{I}$) and ($\mathscr{E}$) models, whereas a coarser one is employed for both ($\mathscr{A}$) and ($\mathscr{M}$). This is motivated by the requirement of a higher resolution for ($\mathscr{I}$) and ($\mathscr{E}$), due to the sharp wavefronts characterizing electrophysiological solutions, whereas both ($\mathscr{A}$) and ($\mathscr{M}$) feature larger spatial scales [32, 37, 161]. Moreover, the nonlinearities of ($\mathscr{M}$) warrants for the use of a coarser space discretization to make the numerical solution less computationally demanding. The SIS1 scheme deals with non-nested tetrahedral meshes among the different core models and exploits the RL-RBFs to effectively transfer information among the different grids [161]. Non-nested meshes are more flexible to accommodate geometrical heterogeneity and to be tuned to different local accuracy requirements. Moreover, they can be generated in a completely independent fashion for electrophysiology and mechanics. On
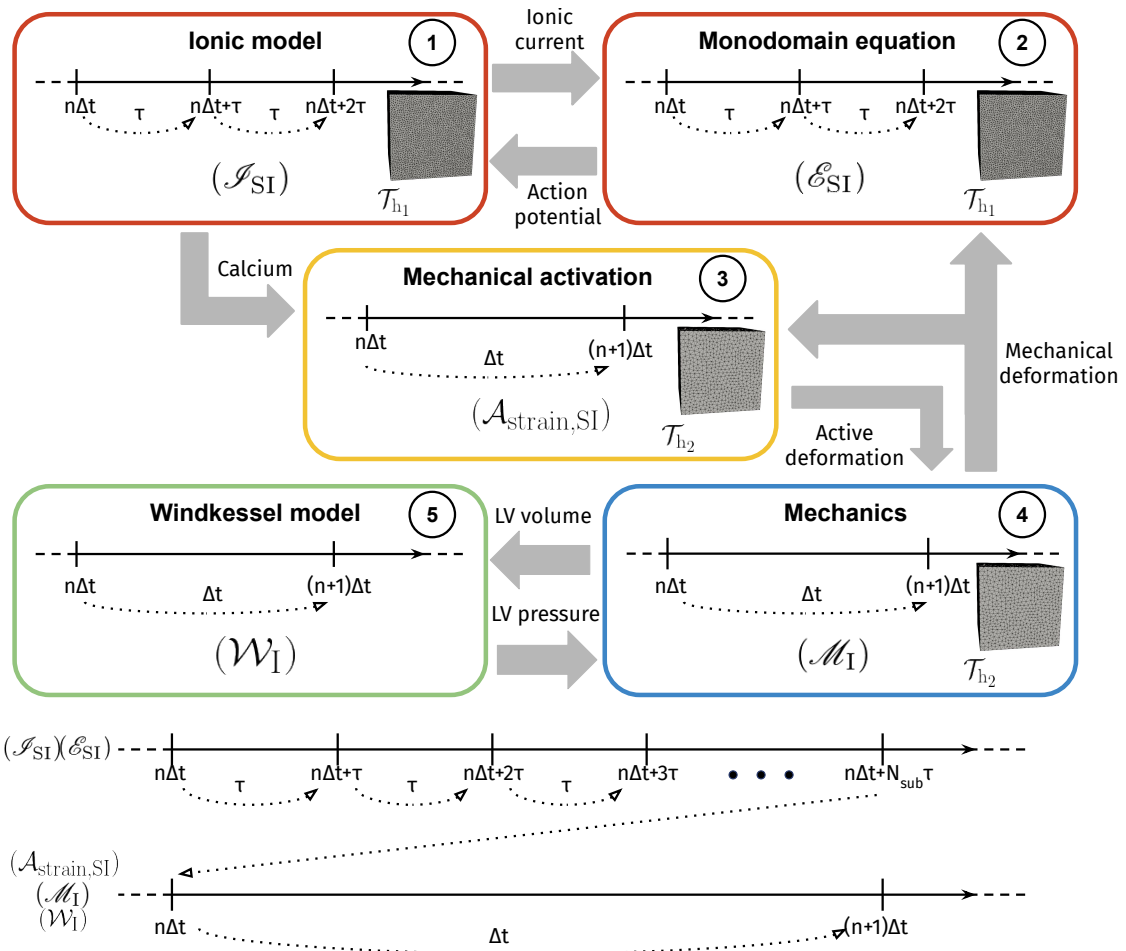
Figure 2.6: SIS1 numerical scheme. This approach has been tested with the active strain only and without the closed-loop circulation model.
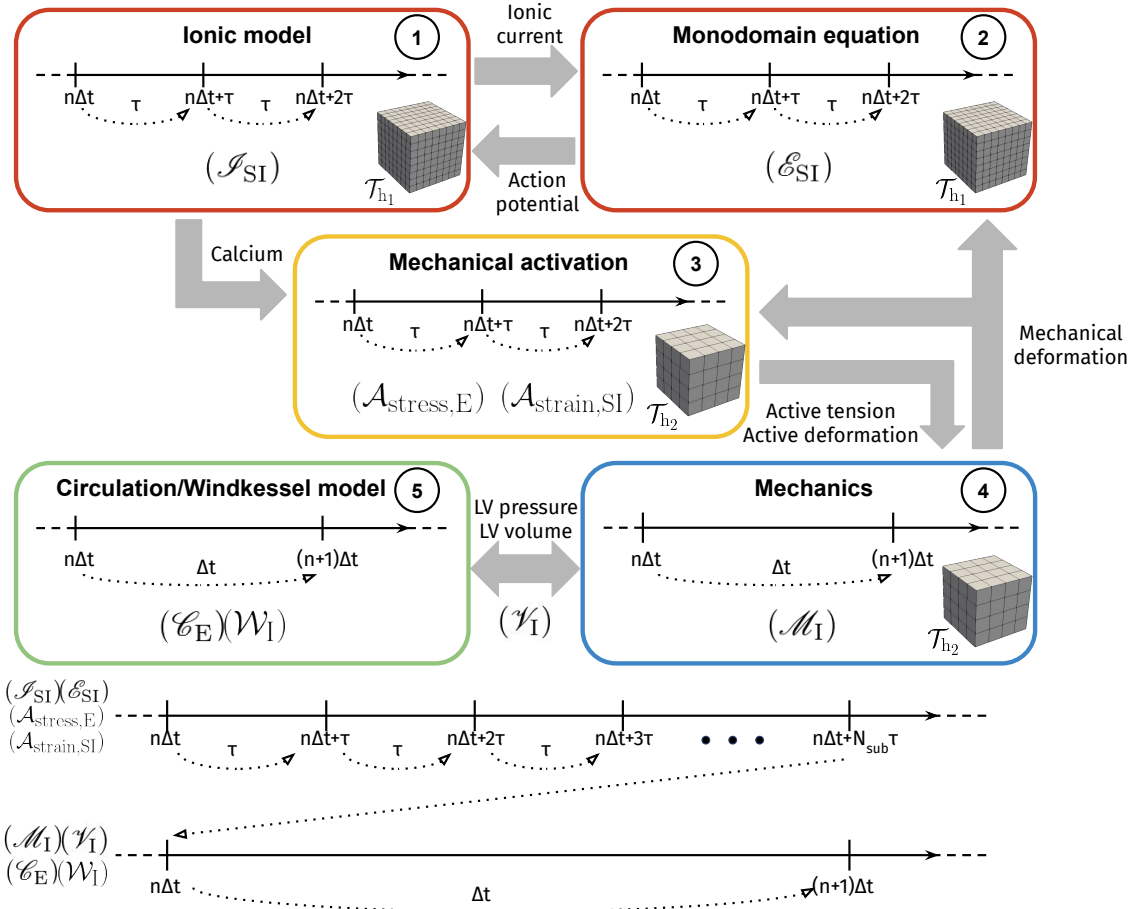
Figure 2.7: SIS2 numerical scheme. This approach has been tested with both the active stress and the active strain frameworks. We also consider the windkessel model and the whole cardiocirculatory model.

the other hand, the original implementation of RL-RBFs enables the use of first order polynomials only [46]. The SIS2 scheme works with nested hexahedral meshes only, but it has the capability to transfer scalar and vector fields with any polynomial degree [148]. This option gives the possibility to perform high-order electromechanical simulations [148].

Regarding time discretization, we consider Finite Difference schemes (backward differentiation formulas, known as BDF) [136] and a staggered strategy based on the Godunov splitting scheme [64]. This approach introduces a first order splitting error and does not undermine the stability of the numerical scheme [148, 161]. For electrophysiology, we employ a semi-implicit scheme, that we denote by $(\mathscr{I}_{SI})$–$(\mathscr{E}_{SI})$, where SI stands for semi-implicit. Mechanical activation is solved with an explicit method in time for the active stress framework $(\mathscr{A}_{stress,E})$, whereas a semi-implicit time solver is in place for the active strain approach $(\mathscr{A}_{strain,SI})$. Mechanics $(\mathscr{M}_I)$ is instead implicitly discretized in time, due to the fact that the highly nonlinear (exponential) terms of the strain energy function $\mathcal{W}$ would need a restriction on the time step in both the semi-implicit and explicit contexts. Finally, we employ an explicit Euler method for the circulation model, indicated as $(\mathscr{C}_E)$, while the windkessel model $(\mathscr{W}_I)$ is solved by means of the implicit Euler method. SIS1 scheme employs two different time steps, a smaller one for electrophysiology and a bigger one for activation, mechanics and the windkessel model. On the other hand, SIS2 scheme uses a shorter time step for electrophysiology and activation and a longer one for mechanics and circulation. Indeed, mechanical activation, which is relatively inexpensive from the computational viewpoint, can be flexibly adapted to consider either the same time step of electrophysiology or the one coming from mechanics without compromising accuracy [131, 147, 148, 161].

In the SIS2 scheme, we develop a strategy to perform the 3D-ØD coupling $(\mathscr{V})$ between $(\mathscr{M})$ and $(\mathscr{C})$, at the numerical level, within a segregated setting. Specifically, we solve the 3D mechanical problem under a volumetric constraint coming from the ØD circulation model. The cavity pressure acts as Lagrange multiplier associated with this constraint. Thus, we obtain a saddle-point problem that we address, at the algebraic level, by means of a Schur complement reduction.

### 2.4.1 *Intergrid transfer operators*

In this section, we present two intergrid transfer operators that have the capability to interpolate in a fast and accurate manner both scalar and vector fields between different meshes defined on the same computational domain. Indeed, we deal with systems of PDEs and ODEs whose solution components represent different physical variables, and we want to use either non-nested or nested grids on LVs to represent these different numerical variables. Specifically, in our fully-coupled electromechanical model, as will be detailed in Sec. 2.4.2, we need to transfer the scalar field $[Ca^{2+}]_i$ from $(\mathscr{I})$ (fine scale) towards $(\mathscr{A})$ (coarse scale) and the vector field **d** from $(\mathscr{M})$ (coarse scale) towards $(\mathscr{E})$ (fine scale).

The first interpolation strategy is based on RL-RBF and has been employed for non-nested tetrahedral meshes for piecewise linear scalar and vector fields [161]. The second intergrid transfer operator works with nested hexahedral meshes and enables the use of different Finite Elements for different core models [148].

*Non-nested meshes*

Our aim is to "transfer" the values of a certain function from one mesh to another one. For this reason, we present our intergrid transfer operator based on RL-RBF in the most general framework. We exploit several properties of RBF to perform the interpolation task by considering a general function $f$ and by following the idea developed in [46].

Let $f : \mathbb{R}^3 \to \mathbb{R}^d$ be a scalar (d=1) or possibly a vector field (d>1) in the 3D setting. Given a set of M nodes $\Xi = \{\xi_m\}_{m=1}^M$ in $\mathbb{R}^3$, we define an interpolant $\Pi_f(\boldsymbol{x})$ (with $\boldsymbol{x} \in \mathbb{R}^3$) of the general field $f$ by means of RBF in the following way:

$$\Pi_f(\boldsymbol{x}) = \sum_{m=1}^M \gamma_m^f \pi(\|\boldsymbol{x} - \xi_m\|, r), \tag{2.31}$$

with $\{\gamma_m^f\}_{m=1}^M$ representing a set of interpolation weights. RBFs are denoted by $\pi(\cdot, r)$, which can be either globally or locally supported according to the choice of the radius $r$. We use Beckert & Wendland RBF:

$$\pi(\|\boldsymbol{x}\|, r) = \left(1 - \frac{\|\boldsymbol{x}\|}{r}\right)^4 \left(1 + 4\frac{\|\boldsymbol{x}\|}{r}\right),$$

which are locally supported. Other options, involving also globally supported basis functions, are available as well [26, 51]. We introduce an interpolation matrix $\boldsymbol{\Phi}^{int} \in \mathbb{R}^{M \times M}$ such that:

$$\Phi_{i,j}^{int} = \pi(\|\xi_i - \xi_j\|, r) \quad \text{with} \quad i, j = 1, ..., M.$$

We call $f_\Xi$ the evaluation of the field $f$ in all the M interpolation nodes that belong to the set $\Xi$. The interpolation constraint is algebraically expressed as follows:

$$\boldsymbol{\Phi}^{int}\boldsymbol{\gamma}^f = f_\Xi, \tag{2.32}$$

with $\boldsymbol{\gamma}^f = \{\gamma_m^f\}_{m=1}^M$ solution of linear system (2.32).

Both fields $f$ and $\Pi_f(\boldsymbol{x})$ assume the same value at the interpolation nodes, i.e. $\Pi_f(\xi_m) = f(\xi_m)$ with m = 1, ..., M. The choice of local RBF leads to a sparse matrix $\boldsymbol{\Phi}^{int}$. At this point, once $\Pi_f(\boldsymbol{x})$ is determined, we can evaluate the interpolant on a set $\Lambda = \{\lambda_n\}_{n=1}^N$ of N different points with respect to the interpolation nodes contained in $\Xi$:

$$\Pi_f(\lambda_n) = \sum_{m=1}^M \gamma_m^f \pi(\|\lambda_n - \xi_m\|, r). \tag{2.33}$$

In our application $\Xi$ and $\Lambda$ will be two different sets of nodes of two independent triangulations of the computational domain $\Omega \subset \mathbb{R}^3$ where the interpolant $\Pi_f(\cdot)$ is defined.

We introduce a matrix $\boldsymbol{\Phi}^{\text{eval}} \in \mathbb{R}^{N \times M}$ such that:

$$\boldsymbol{\Phi}_{i,j}^{\text{eval}} = \pi(\|\boldsymbol{\lambda}_i - \boldsymbol{\xi}_j\|, r) \quad \text{for} \quad i = 1, ..., N \quad \text{and} \quad j = 1, ..., M.$$

This sparse matrix is used to determine $\mathbf{f}_\Lambda$, i.e. to evaluate the RBF interpolant $\Pi_f$ on $\Lambda$:

$$\mathbf{f}_\Lambda = \boldsymbol{\Phi}^{\text{eval}} \boldsymbol{\gamma}^f = \boldsymbol{\Phi}^{\text{eval}} (\boldsymbol{\Phi}^{\text{int}})^{-1} \mathbf{f}_\Xi. \tag{2.34}$$

To obtain a smoother interpolant that is able to interpolate exactly any constant field and that is accurate for small values of the radius $r$ [46], we rescale $\Pi_f(\boldsymbol{x})$ by the interpolant $\Pi_g(\boldsymbol{x})$ of the constant function $g(\boldsymbol{x}) = 1$, which assumes a value equal to one at each interpolation point:

$$\overline{\Pi}_f(\boldsymbol{x}) = \frac{\Pi_f(\boldsymbol{x})}{\Pi_g(\boldsymbol{x})} = \frac{\sum_{m=1}^M \gamma_m^f \pi(\|\boldsymbol{x} - \boldsymbol{\xi}_m\|, r)}{\sum_{l=1}^M \gamma_l^g \pi(\|\boldsymbol{x} - \boldsymbol{\xi}_l\|, r)}. \tag{2.35}$$

We formulate in this way RL-RBF. Algebraically, the interpolation problem associated with (2.35) can be written in the following form:

$$\boldsymbol{\Phi}^{\text{int}} \boldsymbol{\gamma}^f = \mathbf{f}_\Xi, \tag{2.36}$$

$$\boldsymbol{\Phi}^{\text{int}} \boldsymbol{\gamma}^g = \mathbf{1}_\Xi, \tag{2.37}$$

where $\boldsymbol{\gamma}^g = \{\gamma_m^g\}_{m=1}^M$ and $\mathbf{1}_\Xi$ vector of ones on the interpolation nodes defined in $\Xi$. Linear systems (2.36) and (2.37) are solved separately. The evaluation of interpolant $\overline{\Pi}_f$ at a specific point $\boldsymbol{x}$ is:

$$\overline{\Pi}_f(\boldsymbol{x}) = \frac{\boldsymbol{\Phi}^{\text{eval}} (\boldsymbol{\Phi}^{\text{int}})^{-1} \mathbf{f}_\Xi}{\boldsymbol{\Phi}^{\text{eval}} (\boldsymbol{\Phi}^{\text{int}})^{-1} \mathbf{1}_\Xi}, \tag{2.38}$$

where $(\boldsymbol{\Phi}^{\text{eval}})^{\mathsf{T}} \in \mathbb{R}^M$ is such that $(\boldsymbol{\Phi}^{\text{eval}})_j^{\mathsf{T}} = \pi(\|\boldsymbol{x} - \boldsymbol{\xi}_j\|, r)$.

To take into account the distribution of mesh points on the two tetrahedral grids, we define an adaptive strategy to select the radius of the support for Beckert & Wendland basis functions by means of the number of links that a certain vertex of the mesh has with the surrounding neighborhood. In this way we exploit the structure of the mesh to build a variable and local support of the RBF that keeps into account the level of refinement of the mesh in each region of the computational domain. For more details about this technique we refer to [46]. In Fig. 2.8, we see the differences between the approach based on the number of links and the one with a fixed radius. A number of links equal to 1 is sufficient to obtain a good interpolated solution and has been used hereafter.

In [161], we also propose a numerical test for elliptic PDEs with known exact solution, to show the accuracy and the reliability of this operator. Both scalar
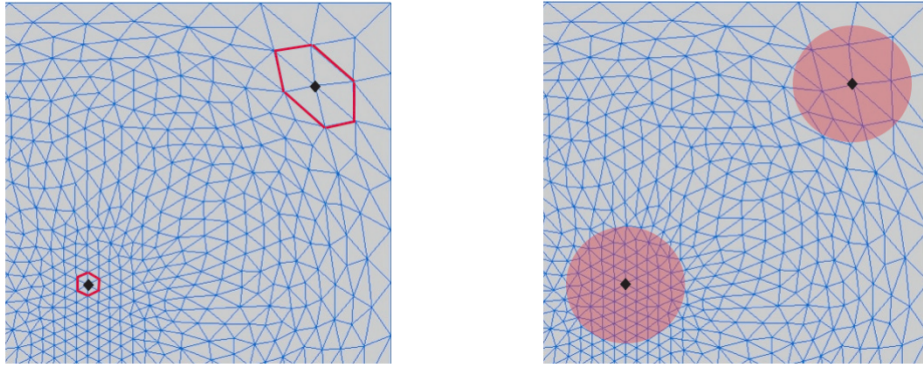
Figure 2.8: Support of the RBF, which is chosen either according to the number of links (left) or within a fixed radius (right), for an unstructured grid (image taken from [46]).

and vector fields are interpolated among structured, nested unstructured and non-nested unstructured grids. We perform strong scalability tests and a convergence analysis of both $L^2$ and $H^1$ errors. The computational time scales almost linearly with the number of CPUs. Finally, we also recover the order of convergence that we expect theoretically (i.e 1 for the $H^1$ norm error and 2 for the $L^2$ norm error) for each mesh combination.

*Nested meshes*

We implement an intergrid transfer operator between nested grids that can be generalized to the case of locally-refined non-conforming nested grids. All the numerical details about this strategy can be found in [1]. Briefly, we build an efficient and scalable interpolation data structure on top of the intergrid transfer operator that enables to evaluate the feedback coming from $(\mathscr{E})$ at the quadrature nodes defined on the mesh used for $(\mathscr{M})$ (and vice-versa), regardless of the polynomial degree that is used to discretize the two different models. This entails a high level of numerical flexibility: different Finite Element degrees, as well as different levels of mesh refinement, can be effortlessly selected to tune the computational efficiency on the desired accuracy.

### 2.4.2 *Space discretization*

We consider either two non-nested tetrahedral meshes (SIS1 scheme) or two nested hexahedral meshes (SIS2 scheme) $\mathcal{T}_{h_1}$ and $\mathcal{T}_{h_2}$ of the computational domain $\Omega_0$, represented by an LV in the reference configuration. $\mathcal{T}_{h_1}$ has been generated either independently from $\mathcal{T}_{h_2}$ (SIS1 scheme) or by uniformly refining $\mathcal{T}_{h_2}$ according to an octree structure (SIS2 scheme) [1, 29], i.e. by recursively splitting each parent element of $\mathcal{T}_{h_2}$ into eight sub-elements for a prescribed number of times, i.e. until the desired geometrical detail is reached. Here $h_1$ and $h_2$ (with $h_1 < h_2$) represent the mesh sizes, which are computed as the mean of the maximum diameter of each element.

We denote by $N_u$, $N_{w,z}$, $N_s$ or $N_{\gamma_f}$ and $N_d$ the number of degrees of freedom (DOFs, that is the number of variables) for the dimensionless transmembrane potential, gating and concentration variables, mechanical activation variables for either the active stress or the active strain, and displacement, respectively. We denote the set of tensor-products of polynomials with degree smaller than or equal to r over a mesh element K as either $\mathbb{P}_r(K)$ (SIS1 scheme) or $\mathbb{Q}_r(K)$ (SIS2 scheme), and we introduce the finite dimensional spaces:

$$\mathcal{X}_{h_1}^r = \{v \in C^0(\overline{\Omega}_0) : v|_K \in \mathbb{P}_r(K) \vee v|_K \in \mathbb{Q}_r(K) \ \ \forall K \in \mathcal{T}_{h_1}\},$$

$$\mathcal{X}_{h_2}^s = \{v \in C^0(\overline{\Omega}_0) : v|_K \in \mathbb{P}_s(K) \vee v|_K \in \mathbb{Q}_s(K) \ \ \forall K \in \mathcal{T}_{h_2}\},$$

for $r, s \geqslant 1$. We remark that when the SIS1 scheme is employed, r=s=1 for all core models, while $r \neq s$ is allowed for the SIS2 scheme.

We adopt the following notation. We denote by, e.g., $\mathbf{d}_{h_1}(t) \approx \mathbf{d}(t)$ the semi-discretized Finite Element approximation of the variable $\mathbf{d}(t)$, defined over the computational mesh $\mathcal{T}_{h_1}$. On the other hand, we denote by $\underline{\mathbf{d}}_{h_1}(t)$ the vector collecting the DOFs associated with $\mathbf{d}_{h_1}(t)$. Finally, we denote by $\underline{\mathbf{d}}_{h_1}^n \simeq \underline{\mathbf{d}}_{h_1}(t^n)$ the vector collecting the DOFs of the fully discretized Finite Element problem.

*Monodomain equation*

The set of basis functions for $\mathcal{X}_{h_1}^r$ with $N_u = \dim(\mathcal{X}_{h_1}^r)$ is given by $\{\phi_i\}_{i=1}^{N_u}$. The semi-discretized formulation of the monodomain equation reads: find $u_{h_1}(t) \in \mathcal{X}_{h_1}^r$ for all $t \in (0, T]$ such that:

$$
\begin{aligned}
\chi_m &\left[ \int_{\Omega_0} C_m J_{h_1} \dot{u}_{h_1}(t) \phi_i \, d\Omega_0 + \int_{\Omega_0} J_{h_1} \widetilde{\mathcal{J}}_{ion}(u_{h_1}(t), \boldsymbol{w}_{h_1}(t), \boldsymbol{z}_{h_1}(t)) \phi_i \, d\Omega_0 \right.\\
&\left. + \int_{\Omega_0} J_{h_1} \widetilde{\mathcal{J}}_{SAC}(u_{h_1}(t), \mathbf{F}_{h_1}(\mathbf{d}_{h_1}(t))) \phi_i \, d\Omega_0 \right] \\
&+ \int_{\Omega_0} (J_{h_1} \mathbf{F}_{h_1}^{-1}(\mathbf{d}_{h_1}(t)) \widetilde{\mathbf{D}} \mathbf{F}_{h_1}^{-T}(\mathbf{d}_{h_1}(t)) \nabla u_{h_1}(t)) \cdot \nabla \phi_i \, d\Omega_0 \\
&= \chi_m \int_{\Omega_0} J_{h_1} \widetilde{\mathcal{J}}_{app}(t) \phi_i \, d\Omega_0 \quad \forall i = 1, ..., N_u,
\end{aligned}
$$
(2.39)

with $u_{h_1}(0) = \sum_{j=1}^{N_u} (u_0, \phi_j)_{L^2(\Omega_0)} \phi_j$. The functions $\boldsymbol{w}_{h_1}(t)$ and $\boldsymbol{z}_{h_1}(t)$ are the semi-discretized versions of the gating variables and of the concentration variables, whereas $u_{h_1}(t) = \sum_{j=1}^{N_u} u_{j,h_1}(t) \phi_j$ is the Finite Element solution that approximates $u = u(t)$. The tensor $\mathbf{F}_{h_1}$ is the interpolated deformation tensor, obtained through the following procedures:

- SIS1 scheme: RL-RBF are employed for the interpolation of $\mathbf{d}_{h_2}$, which is obtained from $(\mathcal{M})$. The interpolant $\bar{\Pi}_{\mathbf{d}}(\mathbf{x})$ is built on $\mathcal{T}_{h_2}$ and it is used to obtain $\mathbf{d}_{h_1}$ on $\mathcal{T}_{h_1}$ by following the procedure explained in Sec. 2.4.1 and by exploiting formula (2.35). Then, we get $\mathbf{F}_{h_1} = \mathbf{I} + \nabla \mathbf{d}_{h_1}$ through the adaptation of the Zienkiewicz-Zhu gradient recovery method [208, 209] to the tensor case. This method is known to be efficient and superconvergent.

If $\mathbf{F}_{h_1}$ is assembled without a proper gradient recovery technique, the AP may become unstable during systole, i.e. when the deformation is higher [161].

- SIS2 scheme: the gradient of the numerical solution $\mathbf{d}_{h_2}$ to problem ($\mathcal{M}$) (i.e. $\nabla \mathbf{d}_{h_2}$) is recovered on $\mathcal{T}_{h_2}$ by means of an $L^2$ projection [1]. Then, our intergrid transfer operator between nested meshes and arbitrary Finite Element spaces is employed to interpolate $\nabla \mathbf{d}_{h_2}$ from $\mathcal{T}_{h_2}$ to $\mathcal{T}_{h_1}$. This interpolant exploits the evaluations of the basis functions on the quadrature nodes distributed on the two grids [148]. In this way, we obtain $\nabla \mathbf{d}_{h_1}$. Finally, $\mathbf{F}_{h_1} = \mathbf{I} + \nabla \mathbf{d}_{h_1}$ is assembled on $\mathcal{T}_{h_1}$. If $\mathbf{d}_{h_1}$ is obtained from $\mathbf{d}_{h_2}$ directly, i.e. without passing from the space gradient, the AP may become unstable during systole, i.e. when the deformation is higher [148].

We highlight that for both the numerical schemes, it is important to use gradient recovery strategies to assemble MEFs in an accurate manner.

At this point, we rewrite Eq. (2.39) as a system of nonlinear ODEs by setting $\underline{\mathbf{u}}_{h_1}(t) = \{u_{j,h_1}(t)\}_{j=1}^{N_u}$:

$$\begin{cases} \chi_m \left[ C_m \mathcal{M} \dot{\underline{\mathbf{u}}}_{h_1}(t) + \mathbf{I}_{ion}(\underline{\mathbf{u}}_{h_1}(t), \underline{\mathbf{w}}_{h_1}(t), \underline{\mathbf{z}}_{h_1}(t)) + \mathbf{I}_{SAC}(\underline{\mathbf{u}}_{h_1}(t), \underline{\mathbf{d}}_{h_1}(t)) \right] \\ \quad + \mathcal{K}(\underline{\mathbf{d}}_{h_1}(t)) \underline{\mathbf{u}}_{h_1}(t) = \chi_m \mathbf{I}_{app}(t) \qquad\qquad\qquad\qquad\qquad \forall t \in (0, T], \\ \underline{\mathbf{u}}_{h_1}(0) = \underline{\mathbf{u}}_{0,h_1}, \end{cases}$$
$$(2.40)$$

where we have defined the following matrices

$$\mathcal{M}_{ij} = \int_{\Omega_0} J_{h_1} \phi_j \phi_i \, d\Omega_0, \quad \mathcal{K}_{ij}(\underline{\mathbf{d}}_{h_1}(t)) = \int_{\Omega_0} (J_{h_1} \mathbf{F}_{h_1}^{-1} \widetilde{\mathbf{D}} \mathbf{F}_{h_1}^{-T} \nabla \phi_j) \cdot \nabla \phi_i \, d\Omega_0,$$

and the following vectors

$$\left( \mathbf{I}_{ion}(\underline{\mathbf{u}}_{h_1}(t), \underline{\mathbf{w}}_{h_1}(t), \underline{\mathbf{z}}_{h_1}(t)) \right)_i = \int_{\Omega_0} J_{h_1} \widetilde{\mathcal{I}}_{ion}(u_{h_1}(t), w_{h_1}(t), z_{h_1}(t)) \phi_i \, d\Omega_0,$$

$$\left( \mathbf{I}_{SAC}(\underline{\mathbf{u}}_{h_1}(t), \underline{\mathbf{d}}_{h_1}(t)) \right)_i = \int_{\Omega_0} J_{h_1} \widetilde{\mathcal{I}}_{SAC}(u_{h_1}(t), \mathbf{F}_{h_1}(d_{h_1}(t))) \phi_i \, d\Omega_0,$$

$$\left( \mathbf{I}_{app}(t) \right)_i = \int_{\Omega_0} J_{h_1} \widetilde{\mathcal{I}}_{app}(t) \phi_i \, d\Omega_0.$$

For the evaluation of the nonlinear term $\mathbf{I}_{ion}(\underline{\mathbf{u}}_{h_1}(t), \underline{\mathbf{w}}_{h_1}(t), \underline{\mathbf{z}}_{h_1}(t))$, three strategies are available [122, 125, 126]. In this thesis, we use the so-called ionic current interpolation (ICI) approach, which yields a faster assembly of the ionic term [91]. By denoting with $\{\mathbf{x}_q^K\}_{q=1}^{N_q}$ and $\{\omega_q^K\}_{q=1}^{N_q}$ the quadrature nodes and weights of

a generic mesh element of $K \in \mathcal{T}_{h_1}$, the term $\mathbf{I}_{\mathrm{ion}}(\underline{\mathbf{u}}_{h_1}(t), \underline{\mathbf{w}}_{h_1}(t), \underline{\mathbf{z}}_{h_1}(t))$ is firstly evaluated at the DOFs and then interpolated at the quadrature nodes:

$$\int_{\Omega_0} J_{h_1} \widetilde{\mathcal{J}}_{\mathrm{ion}}(u_{h_1}(t), \boldsymbol{w}_{h_1}(t), \boldsymbol{z}_{h_1}(t)) \phi_i \, d\Omega_0$$

$$\approx \sum_{K \in \mathcal{T}_{h_1}} \left( \sum_{q=1}^{N_q} \sum_{j=1}^{N_u} J_{j,h_1} \widetilde{\mathcal{J}}_{\mathrm{ion}} \left( u_{j,h_1}(t), \boldsymbol{w}_{j,h_1}(t) z_{j,h_1}(t) \right) \phi_j(\mathbf{x}_q^K) \phi_i(\mathbf{x}_q^K) \omega_q^K \right). \quad (2.41)$$

*Ionic model*

The ionic model under consideration is a system of 18 ODEs (12 for the gating variables, 6 for the concentration variables), which indirectly depends on the space variable over the mesh $\mathcal{T}_{h_1}$ through the transmembrane potential $u$. The semi-discrete formulation can be written as follows:

$$\begin{cases} \underline{\dot{\boldsymbol{w}}}_{h_1}(t) = \overline{\mathbf{H}}(\underline{\mathbf{u}}_{h_1}(t), \underline{\boldsymbol{w}}_{h_1}(t)) & \forall t \in (0, T], \\ \underline{\dot{\boldsymbol{z}}}_{h_1}(t) = \overline{\mathbf{G}}(\underline{\mathbf{u}}_{h_1}(t), \underline{\boldsymbol{w}}_{h_1}(t), \underline{\boldsymbol{z}}_{h_1}(t)) & \forall t \in (0, T], \\ \underline{\boldsymbol{w}}_{h_1}(0) = \underline{\boldsymbol{w}}_{0,h_1}, \\ \underline{\boldsymbol{z}}_{h_1}(0) = \underline{\boldsymbol{z}}_{0,h_1}. \end{cases} \quad (2.42)$$

*Mechanical activation*

ACTIVE STRESS The semi-discrete formulation, which is written on $\mathcal{T}_{h_2}$, reads:

$$\begin{cases} \underline{\dot{\mathbf{s}}}_{h_2}(t) = \overline{\mathbf{K}}(\underline{\mathbf{s}}_{h_2}(t), ([\underline{\mathbf{Ca}^{2+}}]_{i,h_2}(t), \underline{\mathbf{SL}}_{h_2}(t), \underline{\dot{\mathbf{SL}}}_{h_2}(t))^\mathsf{T}) & \forall t \in (0, T], \\ \underline{\mathbf{s}}_{h_2}(0) = \underline{\mathbf{s}}_{0,h_2}. \end{cases} \quad (2.43)$$

where $[\underline{\mathbf{Ca}^{2+}}]_{i,h_2}(t)$ is obtained by interpolating the intracellular calcium concentration of the TTP06 model from $\mathcal{T}_{h_1}$ to $\mathcal{T}_{h_2}$. $\underline{\dot{\mathbf{SL}}}_{h_2}(t)$ is present only in the RDQ20-MF model. The operator $\overline{\mathbf{K}}$ represents the element-wise application of either the ANN associated with the RDQ18 model or the RDQ20-MF model [140, 143]. On the other hand, $SL_{h_2}(t)$ is obtained by solving:

$$\begin{cases} \left( SL_{h_2}(t) - SL_0 \sqrt{\mathcal{J}_{4f,h_2}(t)} \right) - \delta_{SL}^2 \Delta SL_{h_2}(t) = 0 & \text{in } \Omega_0 \times (0, T) \\ \delta_{SL}^2 \nabla SL_{h_2}(t) \cdot \mathbf{N}_{h_2} = 0 & \text{on } \partial\Omega_0 \times (0, T) \end{cases} \quad (2.44)$$

where $\mathcal{J}_{4f,h_2}(t) = \mathbf{F}_{h_2}(t)\mathbf{f}_0 \cdot \mathbf{F}_{h_2}(t)\mathbf{f}_0$. Finally, $T_{a,h_2}(t)$ denotes the semi-discretized active tension, obtained by evaluating the function $T_a = T_a^{\max} G(\mathbf{s})$ at the nodes.

ACTIVE STRAIN The Galerkin formulation related to the equation for $\gamma_f$ reads: given $\mathbf{d}_{h_2}(t)$ and the interpolated intracellular calcium concentration $[Ca^{2+}]_{i,h_2}(t)$

of the TTP06 model from $\mathfrak{T}_{h_1}$ to $\mathfrak{T}_{h_2}$, find $\gamma_{f,h_2}(t) \in \mathfrak{X}_{h_2}^r$ for all $t \in (0, T]$ such that

$$\int_{\Omega_0} \dot{\gamma}_{f,h_2}(t)\phi_i d\Omega_0 + \varepsilon \int_{\Omega_0} \frac{1}{g([Ca^{2+}]_{i,h_2}(t))} \nabla\gamma_{f,h_2}(t) \cdot \nabla\phi_i d\Omega_0$$

$$-\int_{\Omega_0} \frac{1}{g([Ca^{2+}]_{i,h_2}(t))} \Phi([Ca^{2+}]_{i,h_2}(t), \gamma_{f,h_2}(t), \mathbf{d}_{h_2}(t))\phi_i d\Omega_0 = 0 \quad \forall i = 1, ..., N_{\gamma_f},$$

(2.45)

with $\gamma_{f,h_2}(0) = \sum_{j=1}^{N_{\gamma_f}} (\gamma_{f,0}, \phi_j)_{L^2(\Omega_0)}\phi_j$. By introducing the proper matrices, the following system of ODEs is obtained:

$$\begin{cases} \mathcal{M}\underline{\dot{\gamma}}_{f,h_2}(t) + \varepsilon\mathcal{K}([\underline{\mathbf{Ca^{2+}}}]_{i,h_2}(t))\underline{\gamma}_{f,h_2}(t) \\ + \mathbf{\Phi}([\underline{\mathbf{Ca^{2+}}}]_{i,h_2}(t), \underline{\gamma}_{f,h_2}(t), \underline{\mathbf{d}}_{h_2}(t)) = 0 \quad \forall t \in (0, T], \\ \underline{\gamma}_{f,h_2}(0) = \underline{\gamma}_{f,0,h_2}. \end{cases}$$

(2.46)

*Mechanics*

We denote by $[\mathfrak{X}_{h_2}^s]^3$ the finite dimensional subspace of vector valued functions and by $\{\phi_i\}_{i=1}^{N_d}$ its basis. The semi-discretized version of $(\mathscr{M})$ reads: given $T_{a,h_2}(t)$ from active stress (equivalently, $\gamma_{f,h_2}(t)$ from active strain), find $\mathbf{d}_{h_2} = \mathbf{d}_{h_2}(t) \in [\mathfrak{X}_{h_2}^s]^3$ for all $t \in (0, T]$ such that

$$\int_{\Omega_0} \rho_s \ddot{\mathbf{d}}_{h_2}(t) \cdot \phi_i \, d\Omega_0 + \int_{\Omega_0} \mathbf{P} : \nabla\phi_i d\Omega_0$$

$$+ \int_{\Gamma_0^{epi}} \left[ (\mathbf{N}_{h_2} \otimes \mathbf{N}_{h_2}) \left( K_\perp^{epi}\mathbf{d}_{h_2}(t) + C_\perp^{epi}\dot{\mathbf{d}}_{h_2}(t) \right) \right.$$

$$\left. + (\mathbf{I} - \mathbf{N}_{h_2} \otimes \mathbf{N}_{h_2}) \left( K_\parallel^{epi}\mathbf{d}_{h_2}(t) + C_\parallel^{epi}\dot{\mathbf{d}}_{h_2}(t) \right) \right] \cdot \phi_i \, d\Gamma_0$$

$$= -p_{LV}(t)\int_{\Gamma_0^{endo}} J_{h_2}\mathbf{F}_{h_2}^{-T}\mathbf{N}_{h_2} \cdot \phi_i \, d\Gamma_0 + p_{LV}(t)\int_{\Gamma_0^{base}} |J_{h_2}\mathbf{F}_{h_2}^{-T}\mathbf{N}_{h_2}|\mathbf{v}_{h_2}^{base} \cdot \phi_i \, d\Gamma_0$$

$$\forall i = 1, ..., N_d,$$

(2.47)

being $\mathbf{P} = \mathbf{P}(\mathbf{d}_{h_2}(t), T_{a,h_2}(t))$ for active stress and $\mathbf{P} = \mathbf{P}(\mathbf{d}_{h_2}(t), \gamma_{f,h_2}(t))$ for active strain, $\mathbf{d}_{h_2}(0) = \sum_{j=1}^{N_d}(\mathbf{d}_0, \phi_j)_{[L^2(\Omega_0)]^3}\phi_j$, $\dot{\mathbf{d}}_{h_2}(0) = \sum_{j=1}^{N_d}(\dot{\mathbf{d}}_0, \phi_j)_{[L^2(\Omega_0)]^3}\phi_j$, with

$$\mathbf{v}_{h_2}^{base} = \frac{\int_{\Gamma_0^{endo}} J_{h_2}\mathbf{F}_{h_2}^{-T}\mathbf{N}_{h_2} \, d\Gamma_0}{\int_{\Gamma_0^{base}} |J_{h_2}\mathbf{F}_{h_2}^{-T}\mathbf{N}_{h_2}| \, d\Gamma_0}.$$

The corresponding algebraic formulation reads:

$$
\begin{cases}
\rho_s \mathcal{M}\ddot{\underline{\mathbf{d}}}_{h_2}(t) + \mathcal{F}\dot{\underline{\mathbf{d}}}_{h_2}(t) + \mathcal{G}\underline{\mathbf{d}}_{h_2}(t) + \mathbf{S} = p_{LV}(t)\,\mathbf{p}(\underline{\mathbf{d}}_{h_2}(t)) \\
\hspace{8cm} \forall t \in (0, T], \\
\underline{\mathbf{d}}_{h_2}(0) = \underline{\mathbf{d}}_{0,h_2}, \quad \dot{\underline{\mathbf{d}}}_{h_2}(0) = \dot{\underline{\mathbf{d}}}_{0,h_2},
\end{cases}
$$

(2.48)

with:

$$
\mathbf{S}_i = \int_{\Omega_0} \mathbf{P} : \nabla \boldsymbol{\phi}_i \, d\Omega_0,
$$

$$
\mathcal{F}_{ij} = \int_{\Gamma_0^{epi}} \left[ (\mathbf{N}_{h_2} \otimes \mathbf{N}_{h_2}) C_\perp^{epi} + (\mathbf{I} - \mathbf{N}_{h_2} \otimes \mathbf{N}_{h_2}) C_\parallel^{epi} \right] \boldsymbol{\phi}_j \cdot \boldsymbol{\phi}_i \, d\Gamma_0,
$$

$$
\mathcal{G}_{ij} = \int_{\Gamma_0^{epi}} \left[ (\mathbf{N}_{h_2} \otimes \mathbf{N}_{h_2}) K_\perp^{epi} + (\mathbf{I} - \mathbf{N}_{h_2} \otimes \mathbf{N}_{h_2}) K_\parallel^{epi} \right] \boldsymbol{\phi}_j \cdot \boldsymbol{\phi}_i \, d\Gamma_0,
$$

$$
\mathbf{p}_i(\underline{\mathbf{d}}_{h_2}(t)) = - \int_{\Gamma_0^{endo}} J_{h_2} \mathbf{F}_{h_2}^{-T} \mathbf{N}_{h_2} \cdot \boldsymbol{\phi}_i \, d\Gamma_0 + \int_{\Gamma_0^{base}} |J_{h_2} \mathbf{F}_{h_2}^{-T} \mathbf{N}_{h_2}| \mathbf{v}_{h_2}^{base} \cdot \boldsymbol{\phi}_i \, d\Gamma_0,
$$

where $\underline{\mathbf{d}}_{h_2}(t) = \{\mathbf{d}_{j,h_2}(t)\}_{j=1}^{N_d}$. Eqs. (2.39), (2.42), (2.45) and (2.47) provide a splitted semi-discretization of the entire electromechanical model.

### 2.4.3 *Time discretization*

With the aim of developing a staggered strategy, we introduce two time steps $\Delta t$ and $\tau = \Delta t / N_{sub}$, being $N_{sub} \in \mathbb{N}$ a number of intermediate substeps that is set a priori. For the SIS1 scheme, the longer time step $\Delta t$ is used for $(\mathscr{A}_{strain,SI})$, $(\mathscr{W}_I)$ and $(\mathscr{M}_I)$, whereas the shorter time step $\tau$ is employed for $(\mathscr{I}_{SI})$–$(\mathscr{E}_{SI})$. For the SIS2 scheme, we consider $\Delta t$ for $(\mathscr{M}_I)/(\mathscr{M}_I)$–$(\mathscr{V}_I)$ and $(\mathscr{W}_I)/(\mathscr{C}_E)$, while $\tau$ is needed for $(\mathscr{I}_{SI})$–$(\mathscr{E}_{SI})$ and $(\mathscr{A}_{stress,E})/(\mathscr{A}_{strain,SI})$ [131, 161].

*Electrophysiology*

For the sake of simplicity, even though we can employ high-order time schemes for cardiac electrophysiology [130], we introduce the time discretization of problem $(\mathscr{I}_{SI})$–$(\mathscr{E}_{SI})$ by means of the BDF1 scheme.

In particular, once we set $t^{n+\frac{m}{N_{sub}}} = t^n + m\tau$, for $m = 1, ..., N_{sub}$, problem $(\mathscr{I}_{SI})$–$(\mathscr{E}_{SI})$ from $t^n$ to $t^{n+1}$ reads as follows:

- We find $\underline{\boldsymbol{w}}_{h_1}^{n+\frac{m}{N_{sub}}}$ and $\underline{\boldsymbol{z}}_{h_1}^{n+\frac{m}{N_{sub}}}$ defined on $\mathcal{T}_{h_1}$ by solving:

$$
\begin{cases}
\dfrac{1}{\tau}\underline{\boldsymbol{w}}_{h_1}^{n+\frac{m}{N_{sub}}} = \dfrac{1}{\tau}\underline{\boldsymbol{w}}_{h_1}^n + \overline{\mathbf{H}}(\underline{\mathbf{u}}_{h_1}^n, \underline{\boldsymbol{w}}_{h_1}^{n+\frac{m}{N_{sub}}}), \\[3mm]
\dfrac{1}{\tau}\underline{\boldsymbol{z}}_{h_1}^{n+\frac{m}{N_{sub}}} = \dfrac{1}{\tau}\underline{\boldsymbol{z}}_{h_1}^n + \overline{\mathbf{G}}(\underline{\mathbf{u}}_{h_1}^n, \underline{\boldsymbol{w}}_{h_1}^n, \underline{\boldsymbol{z}}_{h_1}^n).
\end{cases}
$$

(2.49)

We adopt here the first order IMEX scheme proposed in [148]. Specifically, we employ an explicit treatment of the ionic concentrations to avoid the solution of a nonlinear system (such choice does not compromise the stability of the scheme, thanks to the non-stiff dynamics of concentrations), and an implicit treatment of the gating variables, because of the severe CFL condition on the time step induced by an explicit scheme. We notice that, thanks to the linear dynamics of the gating variables, such implicit handling does not require the solution of a system of linear or nonlinear equations.

- We interpolate $\underline{\mathbf{d}}_{h_2}^n$ on the fine mesh $\mathcal{T}_{h_1}$ once per time step $\Delta t$, at $t = t^n$. We use $\underline{\mathbf{z}}_{h_1}^{n+\frac{m}{N_{sub}}}$ from (2.49) and $\underline{\mathbf{d}}_{h_1}^n$ to find $\underline{\mathbf{u}}_{h_1}^{n+\frac{m}{N_{sub}}}$ over $\mathcal{T}_{h_1}$ by solving:

$$
\left( \chi_m C_m \frac{1}{\tau} \mathcal{M} + \mathcal{K}(\underline{\mathbf{d}}_{h_1}^n) + \chi_m \mathbf{I}_u^{ion}\left( \underline{\mathbf{u}}_{h_1}^n, \underline{\mathbf{z}}_{h_1}^{n+\frac{m}{N_{sub}}} \right) + \chi_m \mathbf{I}_u^{SAC}\left( \underline{\mathbf{u}}_{h_1}^n, \underline{\mathbf{d}}_{h_1}^n \right) \right) \underline{\mathbf{u}}_{h_1}^{n+\frac{m}{N_{sub}}} =
$$
$$
\chi_m C_m \frac{1}{\tau} \mathcal{M} \underline{\mathbf{u}}_{h_1}^n - \chi_m \tilde{\mathbf{I}}^{ion}\left( \underline{\mathbf{u}}_{h_1}^n, \underline{\mathbf{z}}_{h_1}^{n+\frac{m}{N_{sub}}} \right) + \chi_m \mathbf{I}_{app}\left( t^{n+\frac{m}{N_{sub}}} \right).
$$

(2.50)

$\mathbf{I}_u^{ion}$ is the derivative of the terms of $\mathbf{I}_{ion}$ that linearly depends on $\underline{\mathbf{u}}_{h_1}$, $\mathbf{I}_u^{SAC}$ is the derivative of the $\mathbf{I}_{SAC}$ term that linearly depends on $\underline{\mathbf{u}}_{h_1}$, $\tilde{\mathbf{I}}^{ion}$ collects all the other terms.

*Mechanical activation*

As already stated, the time discretization of mechanical activation for the two SIS schemes is different. Both approaches can be used and prove to be accurate [148, 161].

SIS1 SCHEME   Once $[\underline{\mathbf{Ca}}^{2+}]_{i,h_2}^{n+1}$, coming from (2.49), is interpolated on the coarse mesh $\mathcal{T}_{h_2}$, find $\underline{\boldsymbol{\gamma}}_{f,h_2}^{n+1}$ by solving:

$$
\left( \frac{1}{\tau} \mathcal{M} + \varepsilon \mathcal{K}([\underline{\mathbf{Ca}}^{2+}]_{i,h_2}^{n+1}) + \boldsymbol{\Phi}_{\gamma_f}(\underline{\boldsymbol{\gamma}}_{f,h_2}^n, \underline{\mathbf{d}}_{h_2}^n, [\underline{\mathbf{Ca}}^{2+}]_{i,h_2}^{n+1}) \right) \underline{\boldsymbol{\gamma}}_{f,h_2}^{n+1}
$$
$$
= \frac{1}{\tau} \mathcal{M} \underline{\boldsymbol{\gamma}}_{f,h_2}^n - \boldsymbol{\Phi}_s(\underline{\boldsymbol{\gamma}}_{f,h_2}^n, \underline{\mathbf{d}}_{h_2}^n, [\underline{\mathbf{Ca}}^{2+}]_{i,h_2}^{n+1}).
$$

(2.51)

SIS2 SCHEME   In the active stress framework, once $[\underline{\mathbf{Ca}}^{2+}]_{i,h_2}^{n+\frac{m}{N_{sub}}}$, coming from (2.49), is interpolated on the coarse mesh $\mathcal{T}_{h_2}$, we find $\underline{\mathbf{s}}_{h_2}^{n+\frac{m}{N_{sub}}}$ by solving:

$$
\underline{\mathbf{s}}_{h_2}^{n+\frac{m}{N_{sub}}} = \underline{\mathbf{s}}_{h_2}^n + \tau \overline{\mathbf{K}}(\underline{\mathbf{s}}_{h_2}^n, ([\underline{\mathbf{Ca}}^{2+}]_{i,h_2}^{n+\frac{m}{N_{sub}}}, \underline{\mathbf{SL}}_{h_2}^n, \underline{\dot{\mathbf{SL}}}_{h_2}^n)^\top).
$$

(2.52)

where $\underline{\mathbf{SL}}^n_{h_2}$ is obtained by solving problem (2.44). We remark that $\underline{\dot{\mathbf{SL}}}^n_{h_2}$ is neglected for the RDQ18 model.

Alternatively, in the active strain framework, we find $\underline{\gamma}^{n+\frac{m}{N_{sub}}}_{f,h_2}$ by solving:

$$
\begin{aligned}
&\left( \frac{1}{\tau}\mathcal{M} + \varepsilon\mathcal{K}([\mathbf{Ca^{2+}}]^{n+\frac{m}{N_{sub}}}_{i,h_2}) + \boldsymbol{\Phi}_{\gamma_f}(\underline{\gamma}^n_{f,h_2}, \mathbf{d}^n_{h_2}, [\mathbf{Ca^{2+}}]^{n+\frac{m}{N_{sub}}}_{i,h_2}) \right) \underline{\gamma}^{n+\frac{m}{N_{sub}}}_{f,h_2} \\
&= \frac{1}{\tau}\mathcal{M}\underline{\gamma}^n_{f,h_2} - \boldsymbol{\Phi}_s(\underline{\gamma}^n_{f,h_2}, \mathbf{d}^n_{h_2}, [\mathbf{Ca^{2+}}]^{n+\frac{m}{N_{sub}}}_{i,h_2}).
\end{aligned}
\tag{2.53}
$$

*Mechanics*

After having solved (2.49), (2.50), (2.51) or (2.52)/(2.53) and (2.55), we treat $(\mathcal{M}_I)$–$(\mathscr{V}_I)$ at $t^{n+1}$ by updating $\underline{\mathbf{d}}^{n+1}_{h_2}$ and $p^{n+1}_{LV}$ with the following system:

$$
\begin{cases}
\left( \rho_s\frac{1}{\Delta t^2}\mathcal{M} + \frac{1}{\Delta t}\mathcal{F} + \mathcal{G} \right) \underline{\mathbf{d}}^{n+1}_{h_2} + \mathbf{S} \\
\qquad = \rho_s\frac{2}{\Delta t^2}\mathcal{M}\underline{\mathbf{d}}^n_{h_2} - \rho_s\frac{1}{\Delta t^2}\mathcal{M}\underline{\mathbf{d}}^{n-1}_{h_2} + \frac{1}{\Delta t}\mathcal{F}\underline{\mathbf{d}}^n_{h_2} + p^{n+1}_{LV}\mathbf{p}(\underline{\mathbf{d}}^n_{h_2}, \underline{\mathbf{d}}^{n+1}_{h_2}), \\
V^{3D}_{LV}(\underline{\mathbf{d}}^{n+1}_{h_2}) = V^{0D}_{LV}(\mathbf{c}^n_1).
\end{cases}
\tag{2.54}
$$

Eq. (2.54) is a nonlinear saddle-point problem. In Sec. 2.4.4 we provide details about its numerical approximation at the algebraic level.

An alternative approach for the numerical discretization of 3D cardiac electromechanics would be employing implicit monolithic schemes, which are known to be stable and accurate, but at the same time they present constraints in the choice of the time steps and they are characterized by high computational costs [61, 161]. Indeed, we can only use one time step and one mesh with a monolithic approach. Therefore, we are forced to choose a small time step and a fine representation of the computational domain due to the requirements of cardiac electrophysiology. Our approach is instead accurate and computationally efficient, thanks to the flexibility in the choice of both space and time resolution among the different core models.

*Circulation*

Finally, we find $\mathbf{c}^{n+1}_1$ with the forward Euler method:

$$
\mathbf{c}^{n+1}_1 = \mathbf{c}^n_1 + \tau\widetilde{\mathbf{Z}}\left( t^n, \mathbf{c}^n_1, p^{n+1}_{LV} \right).
\tag{2.55}
$$

### 2.4.4 *Algorithm for the numerical resolution of Eq. (2.54)*

We approximate the solution of Eq. (2.54) by means of a quasi-Newton strategy [136], as we proposed in [143]. Specifically, in the computation of the Jacobian matrix, we neglect the derivative of the nonlocal term $\mathbf{v}^{base}_{h_2}$ in the pressure variable, and we update the Jacobian at each time step, but not through the iterations of Newton's loop. By moving all the terms in Eq. (2.54) to the left

hand side and by rewriting its first and second line as $\mathbf{r}_\mathbf{d}^{n+1}(\underline{\mathbf{d}}_{h_2}^{n+1}, p_{LV}^{n+1}) = \mathbf{0}$ and $r_p^{n+1}(\underline{\mathbf{d}}_{h_2}^{n+1}) = 0$, respectively, the quasi-Newton algorithm reads as follows:

- We set $\underline{\mathbf{d}}_{h_2}^{n+1,0} = \underline{\mathbf{d}}_{h_2}^{n}$ and $p_{LV}^{n+1,0} = p_{LV}^{n}$.

- For $j = 0, 1, \dots$, until a convergence criterion is not fulfilled, we solve the following linear system:

$$
\begin{pmatrix} J_{\mathbf{d},\mathbf{d}}^{n+1} & J_{\mathbf{d},p}^{n+1} \\ J_{p,\mathbf{d}}^{n+1} & 0 \end{pmatrix} \begin{pmatrix} \Delta\underline{\mathbf{d}}_{h_2}^{n+1,j} \\ \Delta p_{LV}^{n+1,j} \end{pmatrix} = - \begin{pmatrix} \mathbf{r}_\mathbf{d}^{n+1,j} \\ r_p^{n+1,j} \end{pmatrix}, \tag{2.56}
$$

where $J_{\mathbf{d},\mathbf{d}}^{n+1} \simeq \frac{\partial}{\partial\underline{\mathbf{d}}}\mathbf{r}_\mathbf{d}^{n+1}(\underline{\mathbf{d}}_{h_2}^{n}, p_{LV}^{n})$ (wherein we neglected the derivative with respect to the nonlocal term $\mathbf{v}_{h_2}^{base}$), $J_{\mathbf{d},p}^{n+1} = \frac{\partial}{\partial p}\mathbf{r}_\mathbf{d}^{n+1}(\underline{\mathbf{d}}_{h_2}^{n}, p_{LV}^{n})$, $J_{p,\mathbf{d}}^{n+1} = \frac{\partial}{\partial\underline{\mathbf{d}}}r_p^{n+1}(\underline{\mathbf{d}}_{h_2}^{n})$, $\mathbf{r}_\mathbf{d}^{n+1,j} = \mathbf{r}_\mathbf{d}^{n+1}(\underline{\mathbf{d}}_{h_2}^{n+1,j}, p_{LV}^{n+1,j})$ and $r_p^{n+1,j} = r_p^{n+1}(\underline{\mathbf{d}}_{h_2}^{n+1,j})$.

- We update $\underline{\mathbf{d}}_{h_2}^{n+1,j+1} = \underline{\mathbf{d}}_{h_2}^{n+1,j} + \Delta\underline{\mathbf{d}}_{h_2}^{n+1,j}$ and $p_{LV}^{n+1,j+1} = p_{LV}^{n+1,j} + \Delta p_{LV}^{n+1,j}$.

- When the convergence criterion is satisfied, we set $\underline{\mathbf{d}}_{h_2}^{n+1} = \underline{\mathbf{d}}_{h_2}^{n+1,j}$ and $p_{LV}^{n+1} = p_{LV}^{n+1,j}$.

From the algebraic viewpoint, we solve the saddle-point problem (2.56) via Schur complement reduction [18]. Specifically, we solve the two linear systems:

$$
J_{\mathbf{d},\mathbf{d}}^{n+1}\mathbf{v}^{n+1,j} = \mathbf{r}_\mathbf{d}^{n+1,j}, \qquad J_{\mathbf{d},\mathbf{d}}^{n+1}\mathbf{w}^{n+1,j} = J_{\mathbf{d},p}^{n+1}
$$

and we set:

$$
\Delta p_{LV}^{n+1,j} = \frac{r_p^{n+1,j} - J_{p,\mathbf{d}}^{n+1}\mathbf{v}^{n+1,j}}{J_{p,\mathbf{d}}^{n+1}\mathbf{w}^{n+1,j}}, \quad \Delta\underline{\mathbf{d}}_{h_2}^{n+1,j} = -\left(\mathbf{v}^{n+1,j} + \mathbf{w}^{n+1,j}\Delta p_{LV}^{n+1,j}\right). \tag{2.57}
$$

We remark that, thanks to the reuse of the Jacobian matrix throughout the Newton loop, $\mathbf{w}^{n+1,j}$ becomes independent of $j$ and thus it does not need to be recomputed at each iteration. Our scheme only involves the following operations: for each time step, we assemble the matrix $J_{\mathbf{d},\mathbf{d}}^{n+1}$ and the vectors $J_{p,\mathbf{d}}^{n+1}$ and $J_{\mathbf{d},p}^{n+1}$ and we solve the linear system $J_{\mathbf{d},\mathbf{d}}^{n+1}\mathbf{w}^{n+1,0} = J_{\mathbf{d},p}^{n+1}$; at each Newton iteration, we only need to solve the linear system $J_{\mathbf{d},\mathbf{d}}^{n+1}\mathbf{v}^{n+1,j} = \mathbf{r}_\mathbf{d}^{n+1,j}$ and perform a couple of matrix-vector multiplications and a vector-vector sum of Eq. (2.57). We later show, through several numerical simulations, that this approach is numerically stable. Even more importantly, our scheme is appropriate for the whole heartbeat, as it does not require adaptations according to the specific cardiac phase [148, 162].

Moreover, our approach allows for a segregated solution of the 3D-ØD coupled model, which is instead typically solved through a monolithic strategy [76]. As a matter of fact, segregated schemes available in literature that couple a mechanical problem with a model describing the dynamics of a fluid (even when described through a ØD circulation model) generally fail when the fluid domain

is fully enclosed by the solid structure, because the incompressibility constraint of the fluid is no longer satisfied after the structure update [76]. This is known as balloon dilemma and affects also cardiac chambers, when either coupled with a 3D circulation model – within a fluid-structure interaction framework [12, 68] – or with a ØD one. To overcome it, the 3D-ØD cardiac circulation models available in literature rely either on a monolithic solution of the two models, where the ØD and 3D models are simultaneously discretized as a unique system and then typically solved by a Newton method [76] or iterative methods that progressively update the cavity pressures and the solid displacement, until convergence is reached. For instance, in [86], the authors proposed a method where the cavity pressure is initially estimated by extrapolating from previous time steps. Then, the cavity compliance (i.e. $\partial V / \partial p$, where $p$ and $V$ are the cavity pressure and volume, respectively) is estimated by finite differences and is used to update the pressure until the blood flux of the 3D model matches that of the ØD model within a prescribed tolerance. Similarly, in [45, 61], during the isovolumic phases, the cavity pressure is iteratively updated by a fixed point scheme. However, convergence of this scheme depends upon a relaxation parameter, whose optimal value needs to be manually assessed from case to case [61].

With our approach, instead, the mechanical 3D model ($\mathcal{M}$) and the circulation ØD model ($\mathcal{C}$) are solved in both a segregated and a staggered manner. Indeed, we do not solve the ($\mathcal{M}$) model simultaneously to the ($\mathcal{C}$) model, but coupled to the volume-consistency condition ($\mathcal{V}$) instead. In this way we end up with the saddle-point problem (2.54). Thanks to the above algorithm, finally, at each Newton iteration, we only need to solve a linear system involving the Jacobian matrix of the ($\mathcal{M}$) problem and to perform a couple of matrix-vector operations.

## 2.5 RECOVERING THE REFERENCE STRESS-FREE CONFIGURATION

Here we present the algorithm for recovering the reference configuration $\Omega_0$ from the deformed configuration $\widetilde{\Omega}$, knowing that the latter is obtained from the former by applying a pressure $\widetilde{p}$ and an active tension $\widetilde{T}_a$. The steady state version of the PDE for cardiac mechanics is reported in Eq. (2.19). In what follows, we denote by $\mathbf{d} = \mathbf{d}_{eq}(\mathbf{x}_0, p_{LV}, T_a)$ the equilibrium solution of Eq. (2.19) obtained on the computational domain of coordinate $\mathbf{x}_0$. Hence, our aim is finding a coordinate $\mathbf{x}_0$ such that $\mathbf{x}_0 + \mathbf{d}_{eq}(\mathbf{x}_0, p_{LV}, T_a) = \widetilde{\mathbf{x}}$.

### 2.5.1 *Algorithm for the recovery of the reference configuration*

A representation of this algorithm is shown in Fig. 2.9. We start by setting the coordinate of the reference configuration $\mathbf{x}_0$ equal to the coordinate of the deformed one (i.e. $\mathbf{x}_0^{(0)} = \widetilde{\mathbf{x}}$). Then, we solve the elastostatic problem of Eq. (2.19), and we get the displacement $\mathbf{d}^{(0)} = \mathbf{d}_{eq}(\mathbf{x}_0^{(0)}, p_{LV}, T_a)$ (Fig. 2.9, top-left). Since, when the configuration $\widetilde{\Omega}$ is recorded the active tension $\widetilde{T}_a$ is almost zero, in
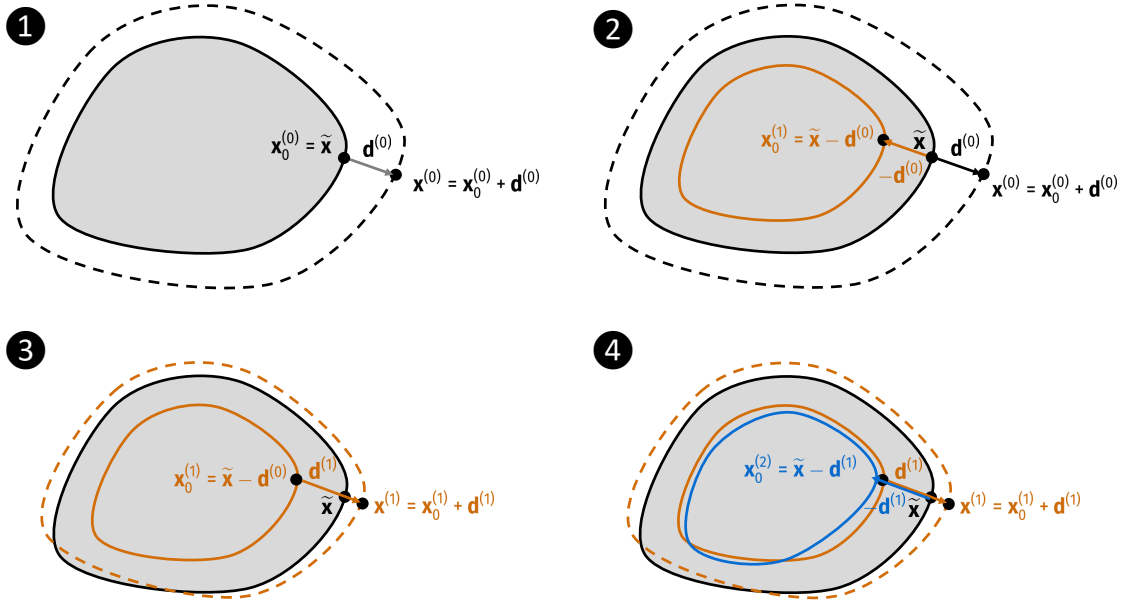
Figure 2.9: Representation of the basic version of the fixed-point algorithm (see Algorithm 1).

the deformed configuration $\mathbf{x}^{(0)} = \mathbf{x}_0^{(0)} + \mathbf{d}^{(0)}$ the ventricle is inflated compared to the configuration $\widetilde{\mathbf{x}}$. Thus, with the aim of correcting the mismatch between $\mathbf{x}^{(0)}$ and $\widetilde{\mathbf{x}}$, we deflate the ventricle by setting $\mathbf{x}_0^{(1)} = \mathbf{x}_0^{(0)} + (\widetilde{\mathbf{x}} - \mathbf{x}^{(0)}) = \widetilde{\mathbf{x}} - \mathbf{d}^{(0)}$ (Fig. 2.9, top-right). Then, we proceed by iterating the above steps. More precisely, for $k \geqslant 1$, we compute $\mathbf{d}^{(k)} = \mathbf{d}_{eq}(\mathbf{x}_0^{(k)}, p_{LV}, T_a)$ (Fig. 2.9, bottom-left) and we set $\mathbf{x}_0^{(k+1)} = \widetilde{\mathbf{x}} - \mathbf{d}^{(k)}$ (Fig. 2.9, bottom-right), stopping when the difference between two consecutive iterations is sufficiently small.

The procedure is reported in Algorithm 1, where STEADYSTATEMECHANICS denotes the function that solves problem (2.19) on the geometry with coordinates $\mathbf{x}_0$. The latter function solves the nonlinear system by means of the Newton method. In case the Newton iterations do not reach convergence (according to a criterion based both on the residual and on the difference between two consecutive iterations), it returns a flag to indicate failure of the algorithm. More precisely, the function signature reads:

$$(\texttt{converged\_SSM}, \mathbf{d}) = \text{STEADYSTATEMECHANICS}(\mathbf{x}_0, p_{LV}, T_a)$$

where, if convergent, `converged_SSM` is true and $\mathbf{d} = \mathbf{d}_{eq}(\mathbf{x}_0, p_{LV}, T_a)$, while in case of non convergence `converged_SSM` is false and $\mathbf{d}$ is not used.

Algorithm 1 can be interpreted as a fixed-point iteration scheme. Indeed, the fixed-point $\mathbf{x}_0$ of the map defined by the Algorithm 1 iteration satisfies $\mathbf{x}_0 = \widetilde{\mathbf{x}} - \mathbf{d}_{eq}(\mathbf{x}_0, p_{LV}, T_a)$. The fixed-point iterations of Algorithm 1 are sketched in Fig. 2.10. The solution is obtained as the intersection between the line $\widetilde{\mathbf{x}} = \mathbf{x}_0 + \mathbf{d}$ and the manifold $\mathbf{d} = \mathbf{d}_{eq}(\mathbf{x}_0, p_{LV}, T_a)$. The algorithm proceeds iteratively in the space $(\mathbf{x}_0, \mathbf{d})$: the first variable is updated by the fixed-point iterations (horizontal axis of Fig. 2.10), while the second variable is updated by Newton iterations (vertical axis of Fig. 2.10).

**Algorithm 1** Reference configuration recovery (basic version)

**parameters:** $k_{max}, \epsilon_{tol}$
**output:** `converged_RCB`, $\mathbf{x}_0$

**procedure** REFERENCECONFIGURATIONBASE($\widetilde{\mathbf{x}}, \widetilde{p}, \widetilde{T}_a$)
    $\mathbf{x}_0^{(0)} \leftarrow \widetilde{\mathbf{x}}$
    **for** $k = 0, \dots, k_{max}$ **do**
        $(\texttt{converged\_SSM}, \mathbf{d}^{(k)}) \leftarrow$ STEADYSTATEMECHANICS($\mathbf{x}_0^{(k)}, \widetilde{p}, \widetilde{T}_a$)
        **if not** `converged_SSM` **then**
            **return** (false, **0**)                       ▷ Newton method does not converge.
        **end if**
        $\mathbf{x}^{(k)} \leftarrow \mathbf{x}_0^{(k)} + \mathbf{d}^{(k)}$
        **if** $\|\mathbf{x}^{(k)} - \widetilde{\mathbf{x}}\| \leqslant \epsilon_{tol}\|\mathbf{d}^{(k)}\|$ **then**
            **return** (true, $\mathbf{x}_0^{(k)}$)                     ▷ Fixed-point converged.
        **end if**
        $\mathbf{x}_0^{(k+1)} \leftarrow \widetilde{\mathbf{x}} - \mathbf{d}^{(k)}$                    ▷ Fixed-point update.
    **end for**
    **return** (false, **0**)                 ▷ Maximum number of iterations reached.
**end procedure**
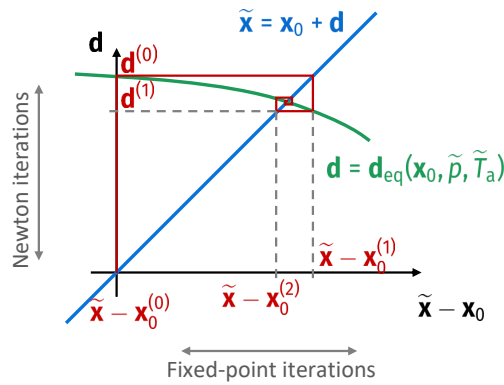


Figure 2.10: Representation of the basic version of the reference configuration algorithm (Algorithm 1).
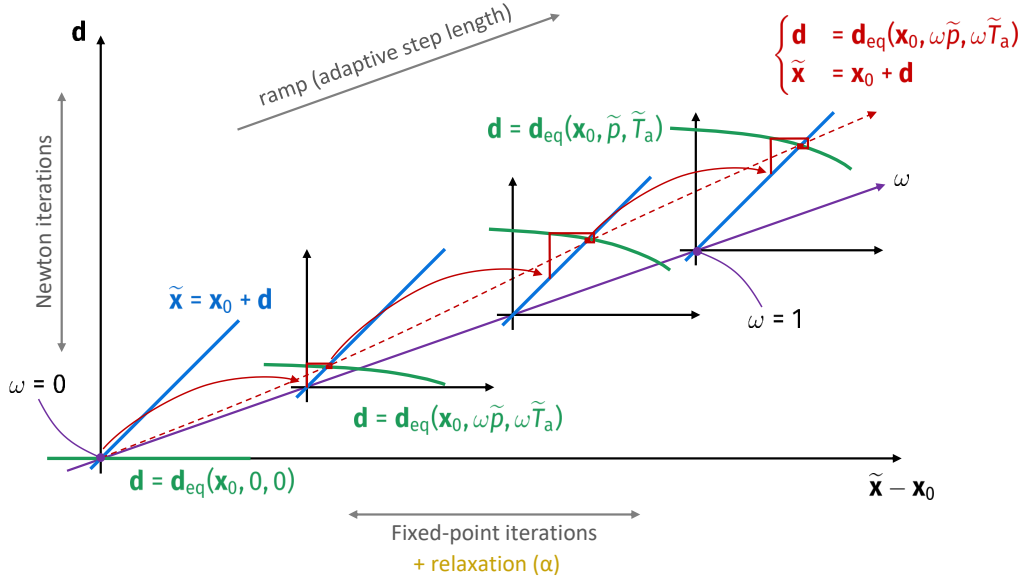
Figure 2.11: Representation of the enhanced version of the reference configuration recovery algorithm (see Algorithms 2 and 3).

However, the implementation shown in Algorithm 1 has several limitations when applied to realistic heart geometries and to nonlinear constitutive laws, such as in the case of cardiac mechanics. In fact, both the Newton method employed in SteadyStateMechanics and the fixed-point scheme employed in ReferenceConfigurationBase do not converge if the initial guess is not "sufficiently" close to the solution. In particular, our experience revealed that the attraction basin of the fixed-point iterations scheme gets smaller and smaller as the value of $p_{LV}$ grows, which makes Algorithm 1 unsuitable for realistic cardiac geometries.

We improved Algorithm 1 by increasing its robustness from several points of view. We propose in Algorithm 2 the enhanced version of Algorithm 1. We introduced a relaxation parameter $\alpha \in (0, 1]$ in the fixed-point iteration, by rewriting it as $x_0^{(k)} \leftarrow x_0^{(k-1)} + \alpha(\widetilde{x} - x^{(k-1)})$. We update $\alpha$ adaptively as written in Algorithm 3: in case of non-convergence of the Newton iterations, we repeat the last fixed-point iteration for a smaller value of $\alpha$; in case of convergence, we increase it in the next iteration. Moreover, the fixed-point iterations are nested inside an outer loop, in which we progressively increase the value of $p_{LV}$ and $T_a$ until the target value $\widetilde{p}$ and $\widetilde{T}_a$ is reached (continuation method). In this outer loop, we adaptively change the step $\omega^{(k)}$, by decreasing it in case of failure of the inner fixed-point loop and by increasing it in case of success.

We remark that after each failure of either SteadyStateMechanics or FixedPoint function, we reset the value of $d$ to the last solution of Eq. (2.19). This ensures the success of such continuation strategy, by which we move in the space $(x_0, d, \omega)$ staying close to the intersection of the curves $d = \widetilde{x} - x_0$ and $d = d_{eq}(x_0, \omega p_{LV}, \omega T_a)$ (see Fig. 2.11).

---

**Algorithm 2** Reference configuration recovery (enhanced version)

---

**parameters:** $k_{max}, \epsilon_{tol}^{ramp}, \epsilon_{tol}^{final}, \gamma_\omega^+, \gamma_\omega^-, \Delta\omega_{max}$
**output:** converged_RC, $\mathbf{x}_0$

**procedure** REFERENCECONFIGURATION($\widetilde{\mathbf{x}}, \widetilde{p}, \widetilde{T}_a$)
    $\mathbf{x}_0^{(0)} \leftarrow \widetilde{\mathbf{x}}$
    $\omega^{(0)} \leftarrow 0$
    $\Delta\omega \leftarrow \Delta\omega_{max}$
    **for** $k = 0, \dots, k_{max}$ **do**
        $\omega^{(k)} \leftarrow \min(\omega^{(k-1)} + \Delta\omega, 1)$
        **if** $\omega^{(k)} = 1$ **then**
            $\epsilon_{tol} \leftarrow \epsilon_{tol}^{final}$
        **else**
            $\epsilon_{tol} \leftarrow \epsilon_{tol}^{ramp}$
        **end if**
        (converged_FP, $\mathbf{x}_0^{(k)}$) $\leftarrow$ FIXEDPOINT($\widetilde{\mathbf{x}}, \omega^{(k)}\widetilde{p}, \omega^{(k)}\widetilde{T}_a\mathbf{x}_0^{(k-1)}, \epsilon_{tol}$)
        **if** converged_FP **then**
            **if** $\omega^{(k)} = 1$ **then**
                **return** (true, $\mathbf{x}_0^{(k)}$)                  ▷ Ramp converged.
            **end if**
            $\Delta\omega \leftarrow \min(\gamma_\omega^+ \Delta\omega, \Delta\omega_{max})$
        **else**
            $\Delta\omega \leftarrow \gamma_\omega^- \Delta\omega$
        **end if**
    **end for**
    **return** (false, $\mathbf{0}$)          ▷ Maximum number of iterations reached.
**end procedure**

---

---

**Algorithm 3** Inner fixed-point loop of the reference configuration recovery algorithm

---

**parameters:** $k_{max}, \alpha_{min}, \alpha_{max}, \gamma_\alpha^+, \gamma_\alpha^-$
**output:** converged_FP, $\mathbf{x}_0$

**procedure** FIXEDPOINT($\widetilde{\mathbf{x}}, p_{LV}, T_a, \mathbf{x}_0, \epsilon_{tol}$)
    $\mathbf{x}_0^{(0)} \leftarrow \mathbf{x}_0$
    $\alpha \leftarrow \alpha_{max}$
    (converged_SSM, $\mathbf{d}^{(0)}$) $\leftarrow$ STEADYSTATEMECHANICS($\mathbf{x}_0^{(0)}, p_{LV}, T_a$)
    **if not** converged_SSM **then**
        **return** (false, $\mathbf{0}$)
    **end if**
    **for** $k = 0, \ldots, k_{max}$ **do**
        $\mathbf{x}_0^{(k)} \leftarrow \mathbf{x}_0^{(k-1)} + \alpha(\widetilde{\mathbf{x}} - \mathbf{x}^{(k-1)})$              $\triangleright$ Fixed-point update.
        (converged_SSM, $\mathbf{d}^{(k)}$) $\leftarrow$ STEADYSTATEMECHANICS($\mathbf{x}_0^{(k)}, \widetilde{p}, \widetilde{T}_a$)
        **if** converged_SSM **then**
            $\mathbf{x}^{(k)} \leftarrow \mathbf{x}_0^{(k)} + \mathbf{d}^{(k)}$
            **if** $\|\mathbf{x}^{(k)} - \widetilde{\mathbf{x}}\| \leqslant \epsilon_{tol}\|\mathbf{d}^{(k)}\|$ **then**
                **return** (true, $\mathbf{x}_0^{(k)}$)              $\triangleright$ Fixed-point converged.
            **end if**
            $\alpha \leftarrow \min(\gamma_\alpha^+ \alpha, \alpha_{max})$
        **else**
            $\alpha \leftarrow \max(\gamma_\alpha^- \alpha, \alpha_{min})$
        **end if**
    **end for**
    **return** (false, $\mathbf{0}$)         $\triangleright$ Maximum number of iterations reached.
**end procedure**

---

### 2.5.2 *Projection of the reference configuration from a coarser mesh*

The procedure to recover the reference configuration (Algorithm 2) requires to numerically solve the elastostatic problem of Eq. (2.19) multiple times, until the fixed point algorithm converges. According to our experience, this procedure can be very computationally demanding in cardiac applications, especially if realistic human heart geometries and fine representations of the computational domain need to be considered. To overcome this issue, the reference configuration recovery algorithm can be run on a coarser mesh compared to the couple of nested meshes $\mathcal{T}_{h_2}$-$\mathcal{T}_{h_1}$ used for the electromechanical model with the SIS2 scheme. A natural choice can be to exploit once again the efficient hierarchical octree structure, but starting from a coarser level $h_3$, generating accordingly the triad of nested meshes $\mathcal{T}_{h_3}$-$\mathcal{T}_{h_2}$-$\mathcal{T}_{h_1}$. However, a further level of coarsening would imply a loss of geometric accuracy that is propagated also into the finer couple of meshes $\mathcal{T}_{h_2}$-$\mathcal{T}_{h_1}$, affecting the electromechanical model.

For this reason, we propose a projection technique which enables to map to the reference configuration $\Omega_0$ from a coarser non-nested mesh. This mesh named $\mathcal{T}_{\widetilde{h}_3}$ can be independently generated with a mesh size $\widetilde{h}_3$ such that $h_3 < \widetilde{h}_3 < h_2$. Such strategy provides the advantages of having more flexibility on the choice of the mesh size $\widetilde{h}_3$ and of preserving the geometric accuracy for the electromechanical meshes $\mathcal{T}_{h_2}$-$\mathcal{T}_{h_1}$.

The complete procedure consists of the following steps:

1. generate two non-nested computational meshes $\mathcal{T}_{h_2}$ and $\mathcal{T}_{\widetilde{h}_3}$ from the deformed configuration $\widetilde{\Omega}$, i.e. the one reconstructed from the medical images, such that $h_2 < \widetilde{h}_3$. The former is characterized by the target mesh size for the mechanical simulation.

2. solve the reference configuration recovery (Algorithm 2) on the coarser mesh $\mathcal{T}_{\widetilde{h}_3}$, obtaining the displacement field $\mathbf{d}_{\widetilde{h}_3}$;

3. project the displacement $\mathbf{d}_{\widetilde{h}_3}$ on the finer mesh $\mathcal{T}_{h_2}$ obtaining the field $\widehat{\mathbf{d}}_{h_2}$, which approximates the displacement $\mathbf{d}_{h_2}$, i.e. the one that would be computed if the reference configuration recovery (Algorithm 2) is applied directly on the finer mesh $\mathcal{T}_{h_2}$;

4. move each vertex of the mesh $\mathcal{T}_{h_2}$ according to $\mathbf{x}_0 = \widetilde{\mathbf{x}} - \widehat{\mathbf{d}}_{h_2}$, recovering the computational mesh $\mathcal{T}_{h_2}$ that describes the reference configuration $\Omega_0$;

5. hierarchically refine $\mathcal{T}_{h_2}$ to generate the fine mesh $\mathcal{T}_{h_1}$ for the electrophysiology.

We remark that the projection step 3 is necessary despite both $\mathcal{T}_{h_2}$ and $\mathcal{T}_{\widetilde{h}_3}$ describe the same domain $\widetilde{\Omega}$. Indeed, in practice, their boundaries do not match, since they are independent polygonal surfaces made of piecewise linear elements. Thus, some vertices of $\mathcal{T}_{h_2}$ can lie outside $\mathcal{T}_{\widetilde{h}_3}$, as illustrated in the 2D
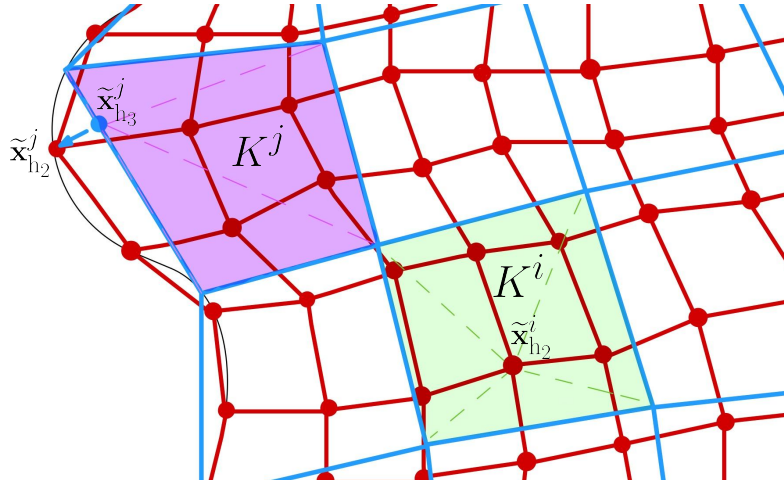
Figure 2.12: A sketch of the projection procedure from a coarse mesh $\mathcal{T}_{\widetilde{h}_3}$ (in blue) into a finer mesh $\mathcal{T}_{h_2}$ (in red): on the internal points $\widetilde{\mathbf{x}}_{h_2}^i \in \mathcal{T}_{h_2}$ we recover the value exploiting the basis functions of the element $K^i \in \mathcal{T}_{h_3}$ (in green); on the external points $\widetilde{\mathbf{x}}_{h_2}^j \in \mathcal{T}_{h_2}$ we project the value of the closest point $\widetilde{\mathbf{x}}_{h_3}^j \in \mathcal{T}_{\widetilde{h}_3}$ evaluated on the closest element $K^j \in \mathcal{T}_{\widetilde{h}_3}$ (in purple).

sketch of Fig. 2.12. As a consequence, to recover $\widehat{\mathbf{d}}_{h_2}$ in all the vertices of the mesh $\mathcal{T}_{h_2}$, we proceed in a different way if these vertices lie inside or outside $\mathcal{T}_{\widetilde{h}_3}$. In particular:

- for the internal vertices – denoted as $\widetilde{\mathbf{x}}_{h_2}^i$, $i = 0, 1, 2, \ldots$ – it is sufficient to find the element $K^i \in \mathcal{T}_{h_3}$ such that $K^i \ni \widetilde{\mathbf{x}}_{h_2}^i$ and evaluate $\mathbf{d}_{h_3}(\widetilde{\mathbf{x}}_{h_2}^i)$ exploiting its Finite Element expansion on $K^i$ (see Fig. 2.12, green element);

- conversely, for each external point – denoted as $\widetilde{\mathbf{x}}_{h_2}^j$, $j = 0, 1, 2, \ldots$ – more sub-steps are necessary, (see Fig. 2.12, purple element):

  1. we find the closest element $K^j \in \mathcal{T}_{\widetilde{h}_3}$ from the external point $\widetilde{\mathbf{x}}_{h_2}^j$;

  2. on $K^j$ we find the closest point $\widetilde{\mathbf{x}}_{h_3}^j$ to $\widetilde{\mathbf{x}}_{h_2}^j$;

  3. we evaluate $\mathbf{d}_{h_3}(\widetilde{\mathbf{x}}_{h_3}^j)$ projecting the resulting value into the external point $\widetilde{\mathbf{x}}_{h_2}^j$.

From the implementation point of view, this projection is performed by exploiting the VTK library [166]. VTK filtering utilities allow to locate all internal points, which are the majority, in a really fast way. Moreover, the VTK library is efficient in performing closest points interpolation, leading to a very fast projection procedure. However, we remark that the hierarchical octree structure [1, 29] still remains more effective for electromechanical simulations, where the exchange of information between (nested) meshes occurs at each time step. Indeed, the projection presented here is intended to be a single pre-processing step to

be performed before the non-stationary electromechanical simulation when the SIS2 scheme is employed.

## 2.6 METHODS

For the implementation of the SIS1 scheme, we use LifeV [96], a C++ open-source Finite Element library. The mathematical models and the numerical methods regarding the SIS2 scheme are implemented in life$^x$ (https://lifex.gitlab.io/lifex), a high-performance C++ library developed within the iHEART project and based on the deal.II (https://www.dealii.org) Finite Element core [7].

For the preprocessing phase, which covers mesh generation, tagging procedure and interpolation of clinical data, we exploit a recently proposed tool for cardiac geometries [53]. This tool is based on VMTK - the Vascular Modelling Toolkit [5, 178].

All the numerical simulations that will be presented in the next chapters are performed on three HPC facilities available at MOX for the iHEART project. The first cluster is endowed with 8 Intel Xeon Platinum 8160 processors, for a total of 192 computational cores and a total amount of 1.5TB of available RAM. The second cluster contains 160 computational cores (5 nodes endowed with Intel Xeon E5-4610 v2, 2.3GHz) and 1.2TB of available RAM. Finally, the third cluster is made of 100 computational cores (5 nodes endowed with Intel Xeon E5-2640 v4, 2.4GHz) and 384GB of available RAM.

To trigger the electric signal in the LV, we apply a current $\widetilde{\mathcal{J}}_{app}(\mathbf{x}, t)$ with either a cubic or a gaussian distribution in space and a peak value $\widetilde{\mathcal{J}}_{app}^{max}$, for a duration of $t_{app}$. Even if we do not model the Purkinje network explicitly [151, 190], the activation pattern that we obtain from $\widetilde{\mathcal{J}}_{app}(\mathbf{x}, t)$ is known to provide physically acceptable results [61]. According to the specific numerical simulation, we apply either different stimuli or a single stimulus that mimics a pacing protocol. The former approach is normally used for SR simulations, while the latter is usually employed to induce VT [138].

There are several rule-based techniques to generate the fiber, sheet and cross-fiber distributions [16, 50, 130, 153] for both idealized and patient-specific LVs. In this thesis, we use the Bayer-Blake-Plank-Trayanova algorithm [16, 130] to get $\mathbf{f}_0$, $\mathbf{s}_0$ and $\mathbf{n}_0$ vector fields for our geometries. In particular, fiber direction rotates clockwise throughout the ventricular wall from $60°$ at the endocardium to $-60°$ at the epicardium, whereas transversal fiber direction varies transmurally from $-20°$ at the endocardium to $20°$ at the epicardium.

# 3

NUMERICAL RESULTS IN PHYSIOLOGICAL CONDITIONS

In this chapter, we present electromechanical simulations in SR on LVs without ICM. In this way, we prove the capability of our mathematical approach to effectively simulate physiological scenarios.

## 3.1 IDEALIZED LEFT VENTRICLE

We start by showing a numerical simulation of a full heartbeat ($T = 0.8\,s$) in the electromechanical framework, by considering an idealized LV.

We depict the meshes in Figs. 3.1 and 3.2. Their details are provided in Tab. 3.1. We employ the SIS1 scheme, which enables the use of different independent grids, even though we have to use $\mathbb{P}_1$ Finite Elements to numerically approximate the core models, so that the unknowns are actually computed on the vertices of each tetrahedron. The time step for electrophysiology is $\tau = 50\,\mu s$, whereas the one for activation, mechanics and windkessel model is $\Delta t = 5\tau = 250\,\mu s$. All the parameters used in the electromechanical model can be found in Appendix A.1.1.

Differently from all the other numerical simulations of this thesis, here and in Sec. 4.1.1 we apply the so called prestress technique instead of the reference configuration recovery method (Sec. 2.2 and Sec. 2.5) to properly take into account the internal stresses of the myocardium at the beginning of the electromechanical simulation [61]. Indeed, we compute a distribution of stresses such that the reference geometry is in equilibrium with the blood pressure $p_{LV}$ at the end of the diastolic phase. We perform an additive decomposition of tensor $\mathbf{P} = \mathbf{P}(\mathbf{d}) + \mathbf{P}_0$, where the prestress tensor $\mathbf{P}_0$ is determined to ensure a null displacement $\mathbf{d}_0$ in correspondance of the initial pressure at the endocardium. For more information about this technique we refer to [61].

In Fig. 3.3 we observe the evolution in space and time of the transmembrane potential $V$, activation variable $\gamma_f$ and total displacement magnitude $|\mathbf{d}|$ over one entire heartbeat. Even if the electrophysiogical mesh is fine, we should use a smaller value of $h_{mean}$ to describe all the space scales properly and to have a convergent velocity of the wavefront [17]. The activation is slightly delayed with

| Core models | Number of elements | Number of vertices | $h_{mean}$ |
|---|---|---|---|
| Electrophysiology | 1'002'886 | 170'009 | 1.2 mm |
| Activation and mechanics | 119'419 | 21'928 | 3 mm |

Table 3.1: Information about the two meshes of an idealized LV with the corresponding number of elements, number of vertices and average edge length.
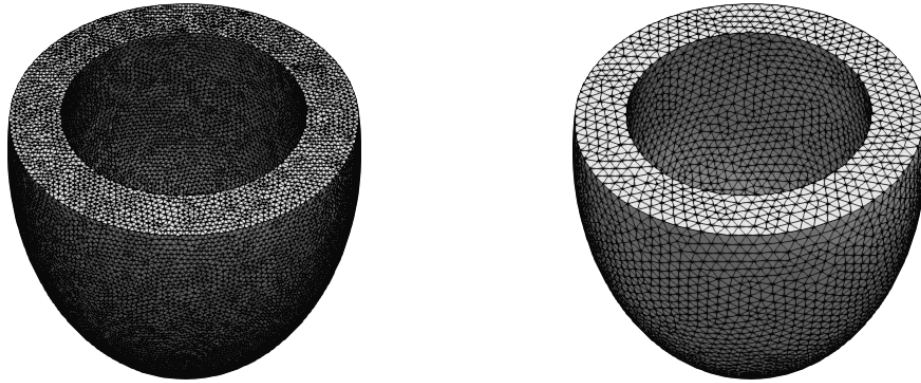
Figure 3.1: View from above of the meshes for the idealized LV for electrophysiology (left), activation and mechanics (right).
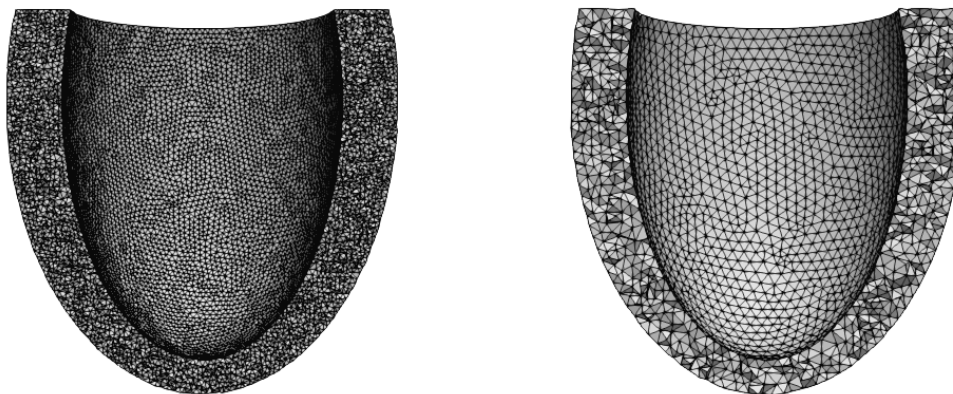


Figure 3.2: Cut front view of the meshes for the idealized LV for electrophysiology (left), activation and mechanics (right).

respect to the propagation of the AP because it is driven by the calcium concentration, that evolves in time slower than the transmembrane potential. The myocardial tissue undergoes a significant thickening, which is in accordance with experimental observations [139]. A high value of the bulk modulus B permits to obtain a significant torsion of the LV and to impose the quasi-incompressibility constraint [61]. With the choice of parameters for the Robin boundary condition at the epicardium in the mechanical problem (2.9), we are able to properly keep into account the effect of the pericardium [129]: in this way we can reduce the movement of the apex while increasing the one of the base.

The PV loop is depicted in Fig. 3.4. Even if a comparison with in-vivo measurements would be meaningless, due to the fact that we are dealing with an ideal-
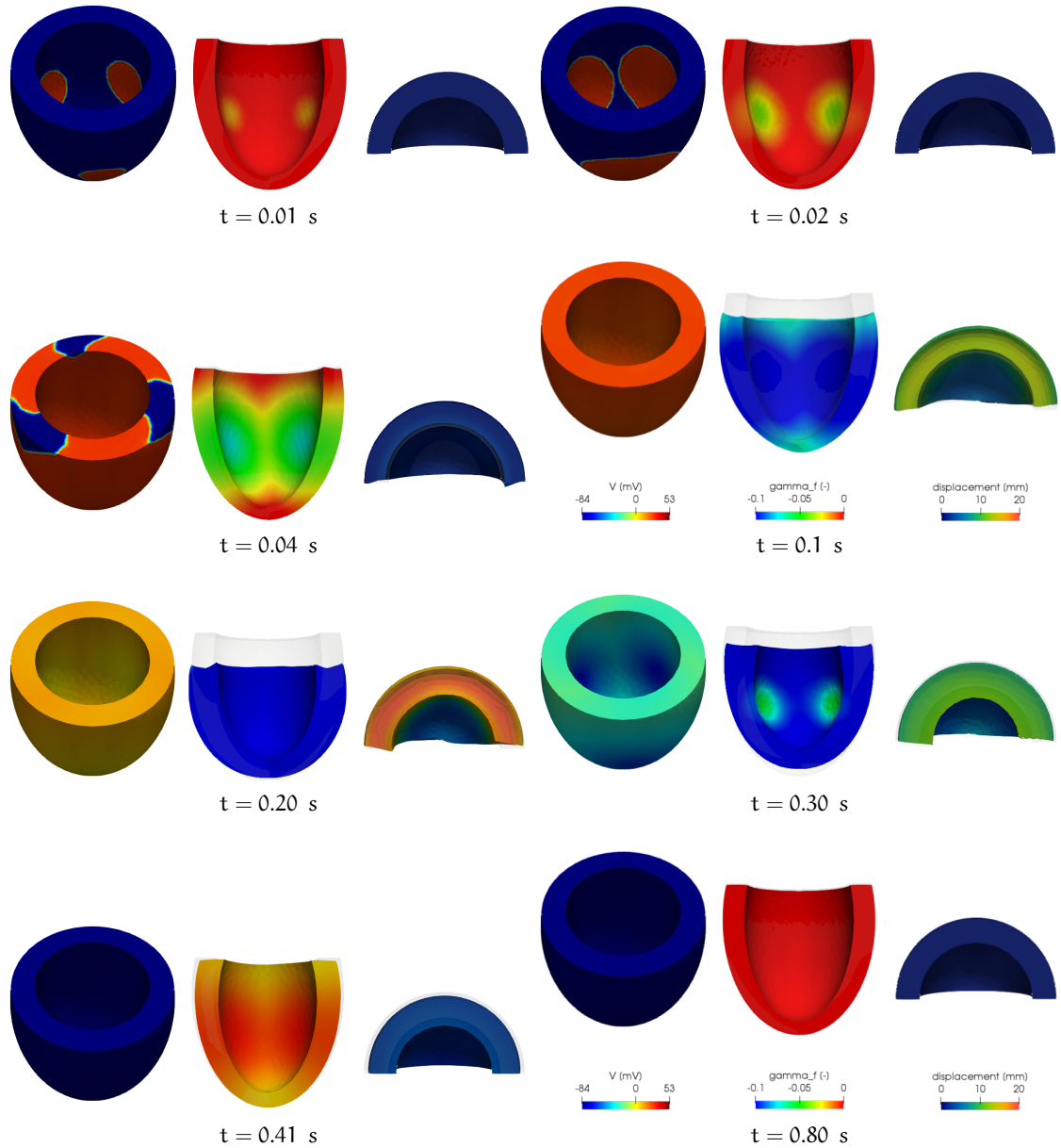
Figure 3.3: Evolution of the transmembrane potential V, $\gamma_f$ and $|\mathbf{d}|$ in the idealized LV over the time. The second and the third views of each picture are warped by the displacement vector.

ized framework, we can state that the PV loop developed over the simulation is in accordance with those observed experimentally [154], at least qualitatively.

Finally, with reference to [61], we have also performed this numerical simulation in a monolithic fashion, by considering only the first isochoric phase, for a total time $T = 50\,\mathrm{ms}$. In this case we are forced to use the time step of electrophysiology (here $\tau = \Delta t = 50\,\mu s$) also for both activation and mechanics, due to the fact that AP and calcium dynamics require a higher resolution in time. For what concerns space discretization, we are again forced to use only the mesh of electrophysiology (here the one of the first row in Tab. 3.1), even if we do not
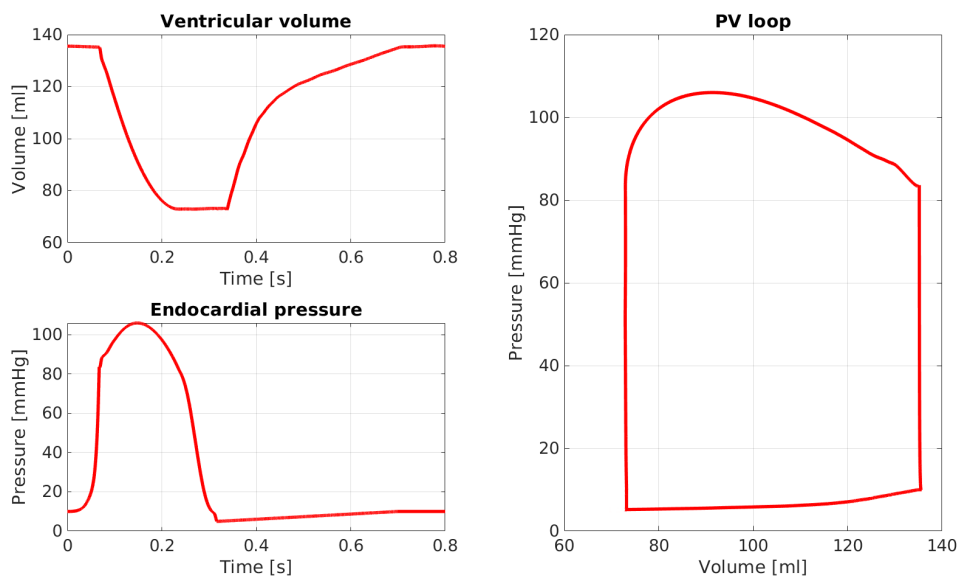
Figure 3.4: Ventricular volume and endocardial pressure over time (left) with PV loop (right) for the idealized LV.

| Numerical scheme | Electrophysiology | Activation | Mechanics | Interpolation |
|---|---|---|---|---|
| Monolithic | 0.47 s | 0.30 s | 8.2 s | - |
| SIS1 | 0.48 s | 0.24 s | 3.1 s | 2.4 s |

Table 3.2: Comparison between monolithic and SIS1 schemes in terms of CPU times dedicated to the assembly stages of the block matrices corresponding to the different physics. These results are referred to time $t = 30\,\text{ms}$ of the simulation, during the systolic phase.

need such a high number of elements for the mechanical problem. In Tab. 3.2, we report the time needed to perform one single time step with both monolithic and SIS1 approaches in a parallel framework. We place ourselves in the worst scenario where we consider a time step for the SIS1 scheme in which we have to solve the whole electromechanical problem and interpolate both calcium concentration and displacement vector. This does not occur for all the time steps of the numerical simulation. We see that the use of two different time steps and two different meshes, which is allowed by our RL-RBF intergrid transfer operator, yields a significant gain with respect to the monolithic strategy. Monolithic schemes are indeed not competitive in terms of performance with respect to segregated ones. With the SIS1 approach we observe a 10x speed-up in the computational time with respect to [61]. Given the scalability properties of RL-RBF [46, 161], this speed-up holds for different combinations in number of cores and mesh resolution. The interpolation process does not present a bottleneck for the numerical simulations even when a very large number of cores is employed and no load balancing issues have been observed. Morever, the SIS1 scheme also guarantees a proper and accurate capture of both the time and space scales

Time: 0.030000 s
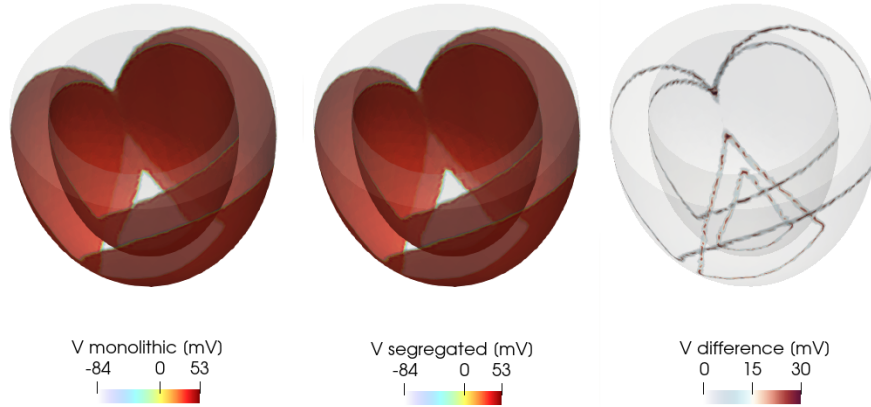


Figure 3.5: Comparison between monolithic and SIS1 schemes for the transmembrane potential V over the computational domain at a certain time step (t = 30 ms). We also provide in the third view the pointwise difference in absolute value between the transmembrane potentials of the two schemes, i.e. $|V_{\text{monolithic}}(\boldsymbol{x}) - V_{\text{segregated}}(\boldsymbol{x})|$.

Time: 0.030000 s
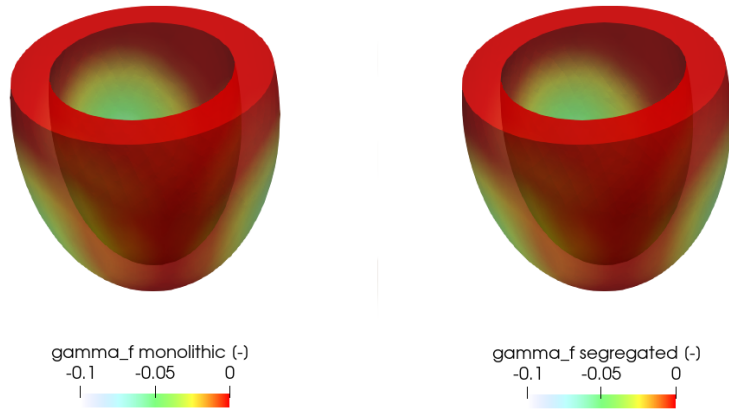


Figure 3.6: Comparison between monolithic and SIS1 schemes for $\gamma_{\text{f}}$ over the computational domain at t = 30 ms.

of this multiphysics problem. Indeed, in Figs. 3.5 and 3.6, we observe small differences in the velocity of propagation of the wavefronts. This little discrepancy is due to the splitting error of the segregated scheme, to the small error in space introduced by the interpolation process, and finally to the larger time step used for activation and mechanics. The same conclusions hold also for the electrophysiological problem, due to the feedback that involves the deformation tensor **F**.

|  | Number of elements | Number of vertices | $h_{mean}$ |
|---|---|---|---|
| **Mesh1** | | | |
| Electrophysiology | 1'008'896 | 1'046'641 | 1 mm |
| Activation/Mechanics | 15'764 | 19'099 | 4 mm |
| **Mesh2** | | | |
| Electrophysiology | 2'590'464 | 2'663'817 | 0.75 mm |
| Activation/Mechanics | 40'476 | 47'529 | 3 mm |
| **Mesh3** | | | |
| Electrophysiology | 8'939'776 | 9'116'741 | 0.5 mm |
| Activation/Mechanics | 139'684 | 159'149 | 2 mm |

Table 3.3: Details of the Zygote LV meshes used for the numerical results reported in Sec. 3.2. Two nested meshes are generated for each of the three configurations (Mesh1, Mesh2, and Mesh3): the finer - used for the electrophysiological model - is obtained by recursively splitting each element of the coarser - adopted for both the activation and mechanical models.

## 3.2 REALISTIC LEFT VENTRICLE

We now present some numerical simulations of cardiac electromechanics with the SIS2 scheme by considering the Zygote LV [80] in SR.

We list in Tab. 3.3 the three configurations of the nested computational meshes under consideration, from the coarsest (Mesh1) to the finest one (Mesh3). In all the cases, we employ for the electrophysiological problem a mesh size that is four times smaller than the one of the mechanical problem.

In terms of numerical results, we first provide a grid sensitivity study, by considering increasingly refined meshes, i.e. Mesh1, Mesh2 and Mesh3. Then, we show that our mathematical model can generate several scenarios according to the chosen parameter sets: specifically, we vary preload, afterload and contractility, and we evaluate the effects of these changes on the PV loops of the LV. We also depict activation maps generated by means of either $\mathbb{Q}_1$ or $\mathbb{Q}_2$ elements for electrophysiology and only $\mathbb{Q}_1$ elements for activation and mechanics: in this way we show that our intergrid transfer operator can handle different Finite Element spaces for different core models.

All the parameters related to the electromechanical model are reported in Appendix A.1.2. We use a time step $\tau = 50\,\mu s$ for electrophysiology and activation, and $\Delta t = 5\tau = 250\,\mu s$ for mechanics.

### 3.2.1 *Mesh sensitivity*

We run electromechanical simulations for several heartbeats (T = 4 s) on Mesh1, Mesh2 and Mesh3 of Tab. 3.3 to study how the numerical results vary with the space discretization. Given the negligible impact of MEFs in SR (see Chap. 4) and for the sake of simplicity, we consider model ($\mathscr{E}$) for cardiac electrophysiol-
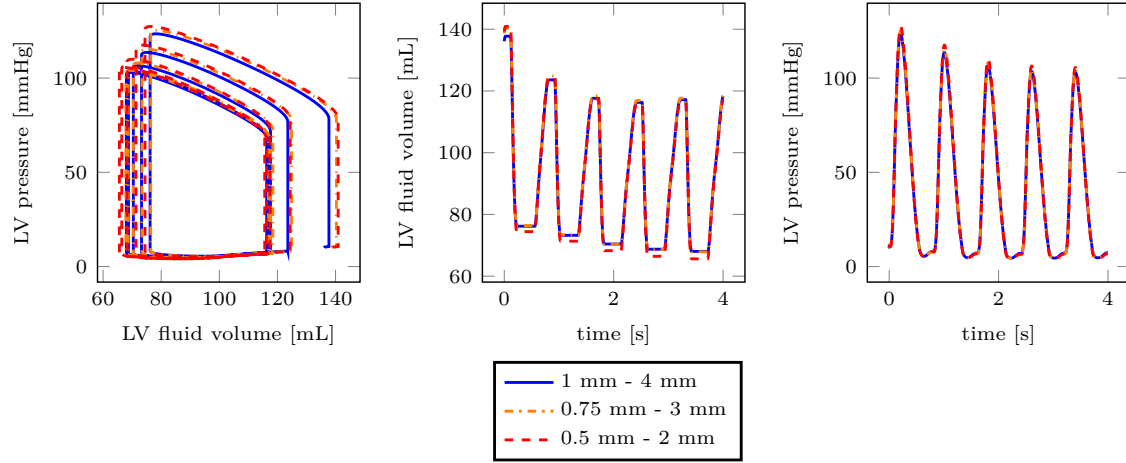
Figure 3.7: Pressure and volume transients over time and PV loops related to the Zygote LV, considering different mesh resolutions (Mesh1, Mesh2, Mesh3 of Tab. 3.3) and $\mathbb{Q}_1$ Finite Element spaces.

ogy. In Fig. 3.7 we display the PV loop and the evolution in time of pressure and volume for the three proposed mesh settings. These numerical results are not only influenced by the average diameter $h_{mean}$ [8], but also by the effective number of DOFs. Under the assumption of properly distributed mesh elements, the number of DOFs itself can potentially be an indicator to evaluate the accuracy of the space discretization for cardiac simulations, unifying numerical approximations coming from different mesh elements and different techniques, such as FEM, Spectral Element Methods and Isogeometric Analysis [24, 127, 136].

In Fig. 3.8 we display the activation maps for the Mesh1 setting in Tab. 3.3. We use either $\mathbb{Q}_1$ or $\mathbb{Q}_2$ Finite Elements for electrophysiology, and $\mathbb{Q}_1$ for both activation and mechanics. We show one numerical simulation with $\mathbb{Q}_2$ Finite Elements for electrophysiology to underline that our mathematical discretization can be extended to high-order methods, which are known to be more suitable than standard FEM for wave propagation problems [24, 127]. We observe that the activation map resulting from $\mathbb{Q}_2$ Finite Elements features slightly more pronounced anisotropy of the isochrones. Indeed, the additional DOFs provided by $\mathbb{Q}_2$ elements allow to better outline the different roles of conductivities $\sigma_l$, $\sigma_t$ and $\sigma_n$, as shown in [130].

### 3.2.2 *Variations in preload, afterload and contractility*

We test the response of our electromechanical model to some scenarios of clinical interest. The parameters of the baseline simulation are reported in [148]. Starting from this setting, we consider three physiologically relevant scenarios, aimed at investigating the effects of changes in preload, afterload and myocardial contractility, respectively. In all the cases, we simulate several heartbeats, until when we reach a periodic regime. However, we report only the PV loops related to the last cycle.
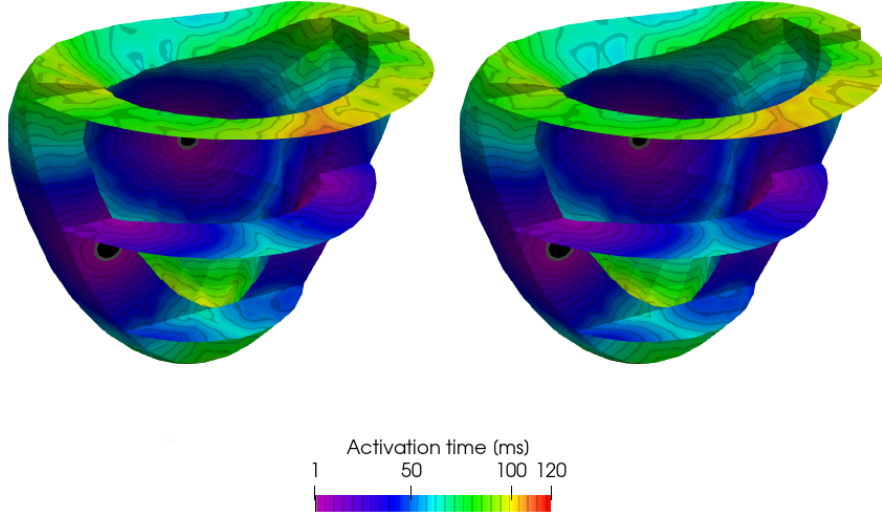
Figure 3.8: Activation times on the Zygote LV considering different Finite Element spaces ($\mathbb{Q}_1$, 1'046'641 DOFs, on the left, and $\mathbb{Q}_2$, 8'211'745 DOFs, on the right) for electrophysiology.

*Stresses computation*

We define the following indicator to evaluate the components of the mechanical stress:

$$S_{ab} = (\mathbf{Pa}_o) \cdot \frac{\mathbf{Fb}_o}{|\mathbf{Fb}_o|}, \tag{3.1}$$

where $a, b \in \{f, s, n\}$ indicate the fiber ($f$), the sheet ($s$) and the crossfiber ($n$) direction respectively. The metric $S_{ab}$ measures the stress component in the **b** direction (where $\mathbf{b} = \frac{\mathbf{Fb}_o}{|\mathbf{Fb}_o|}$ denotes the direction $\mathbf{b}_0$ in the current configuration) across a surface normal to the direction $\mathbf{a}_o$. Hence, we refer to axial stresses when $a = b$, to shear stresses when $a \neq b$. We remark that in the active stress framework, **P** incorporates an additive decomposition between the passive and the active terms, the latter coming from the active tension $T_a$. On the other hand, in the active strain approach, **F** is defined by a multiplicative decomposition between the passive and the active components of the deformation tensor, the latter coming from the $\gamma_f$ variable.

Even though a possible strategy to handle the computation of the stress tensor would be to solve an $L^2$-projection problem [148], we represent each component as a piecewise constant ($\mathbb{Q}_0$) Finite Element vector, where the average of the values over the quadrature points of each cell is associated with the only local DOF corresponding to the cell centroid. Since the stresses are only processed for visualization purposes, our strategies turns out to be very efficient while not hampering the accuracy of the computation.

*Baseline simulation*

In Fig. 3.9 we report the time evolution of both the transmembrane potential V and the displacement magnitude $|\mathbf{d}|$ in the Zygote LV, by considering the first heartbeat of the numerical simulation. We use Mesh2 in Tab. 3.3. We compute the initial displacement $\mathbf{d}_0$ by inflating $\Omega_0$ until the desired EDP is reached. We accomplish this task by performing a pressure ramp on the quasi-static approximation of the mechanical problem, i.e. Eq. (2.19).

In Fig. 3.10 we depict the axial stresses $S_{ff}$, $S_{ss}$ and $S_{nn}$, whereas in Fig. 3.11 we show the shear stresses $S_{fs}$, $S_{fn}$ and $S_{sf}$. We observe that $S_{ff}$ has a dominant role with respect to $S_{ss}$ and $S_{nn}$, especially during ejection (i.e. the second part of systole) and isovolumetric relaxation (i.e. early diastole). The same considerations hold for the shear stresses components involving the fiber field $f$.

*Test Case 1*

We change the ventricles preload (i.e. their EDP) by modifying the value of the atrial contractility with respect to the baseline setting. More precisely, we consider the two cases when $E_{LA}^{act,max}$ and $E_{RA}^{act,max}$ are respectively increased and decreased by 50%. As shown in Fig. 3.12, the larger the atrial contractility, the more blood is injected in the ventricle, thus increasing preload. Moreover, our electromechanical model predicts a larger SV for a larger preload. This is consistent with the so-called Frank-Starling effect, a self-regulatory mechanism that guarantees the balance between venous return and cardiac output [83].

*Test Case 2*

We investigate the effects of changing the resistance of the arterial circulation. This mimics the situation of a patient affected by diseases associated with hypertension, such as arteriosclerosis, or to the effect of vasodilator-vasoconstrictor drugs. Starting from the baseline setting, we perform two additional simulations where we respectively increase and decrease by 15% the value of $R_{AR}^{SYS}$. In both cases, we modify the value of $C_{AR}^{SYS}$ accordingly, so that the product $R_{AR}^{SYS}C_{AR}^{SYS}$, corresponding to the characteristic time constant of the arterial system, is preserved. The results in Fig. 3.12 show that an increase of the arterial resistance yields larger values of both the AV opening pressure and the maximal LV pressure (hypertensive effect).

*Test Case 3*

We consider the response of our electromechanical model to either positive or negative changes to inotropic state of the muscle, whose effect is that of increasing and, respectively, decreasing the myocardial contractility. Specifically, starting from the baseline, we first increment and then decrement the atrial contractility ($E_{LA}^{act,max}$ and $E_{RA}^{act,max}$) and the ventricular contractility ($T_a^{max}$ and $E_{RV}^{act,max}$) by 35%. The results in Fig. 3.12 show that an increase in myocardial

$t = 0.03\,\text{s}$        $t = 0.06\,\text{s}$

$t = 0.25\,\text{s}$        $t = 0.375\,\text{s}$

$t = 0.42\,\text{s}$        $t = 0.45\,\text{s}$

$t = 0.60\,\text{s}$        $t = 0.80\,\text{s}$
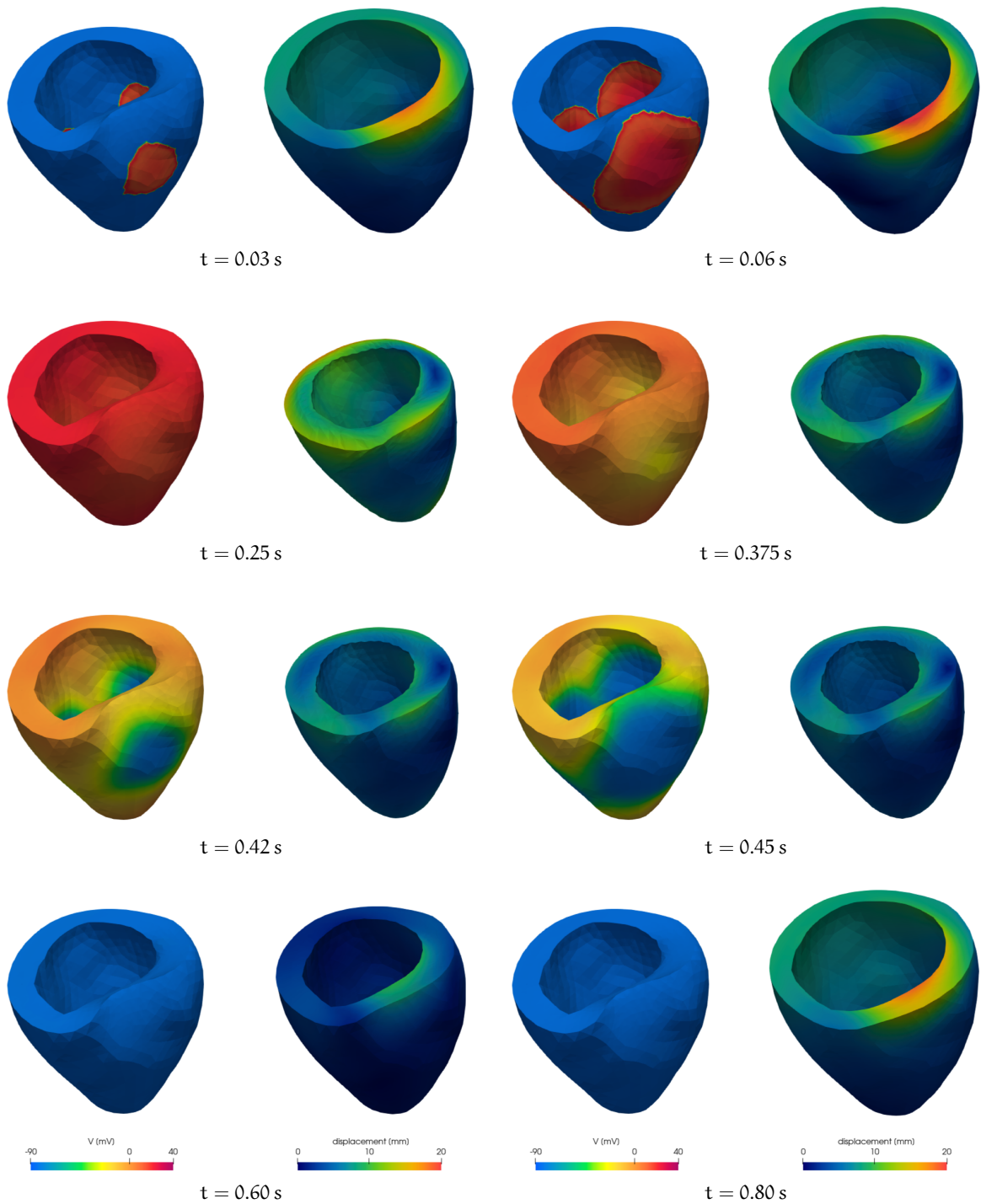
Figure 3.9: Evolution of the transmembrane potential V and the displacement magnitude $|\mathbf{d}|$ in the Zygote LV over time. The right view of each picture is warped by the displacement vector. Conversely, the transmembrane potential V is displayed on the reference configuration $\Omega_0$.
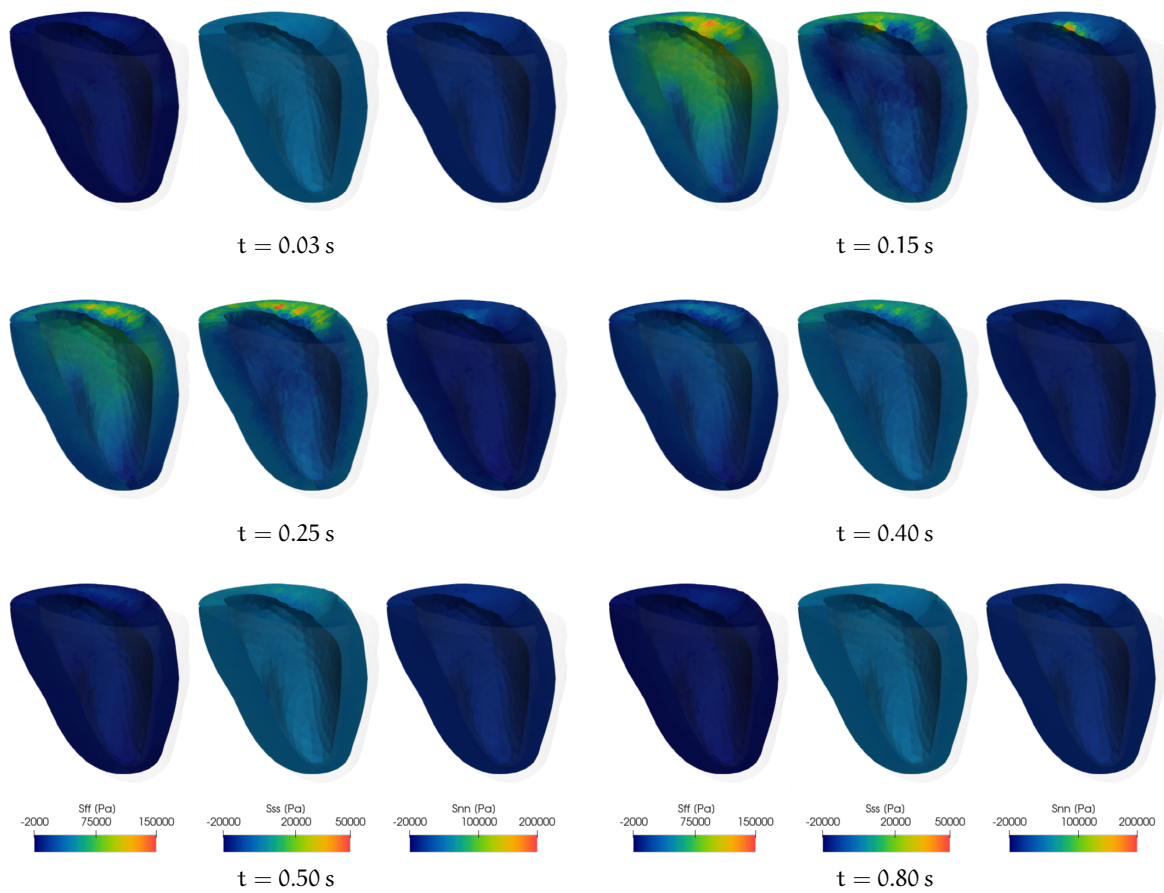
Figure 3.10: Evolution of $S_{ff}$, $S_{ss}$, $S_{nn}$ during the first heartbeat of the numerical simulation.
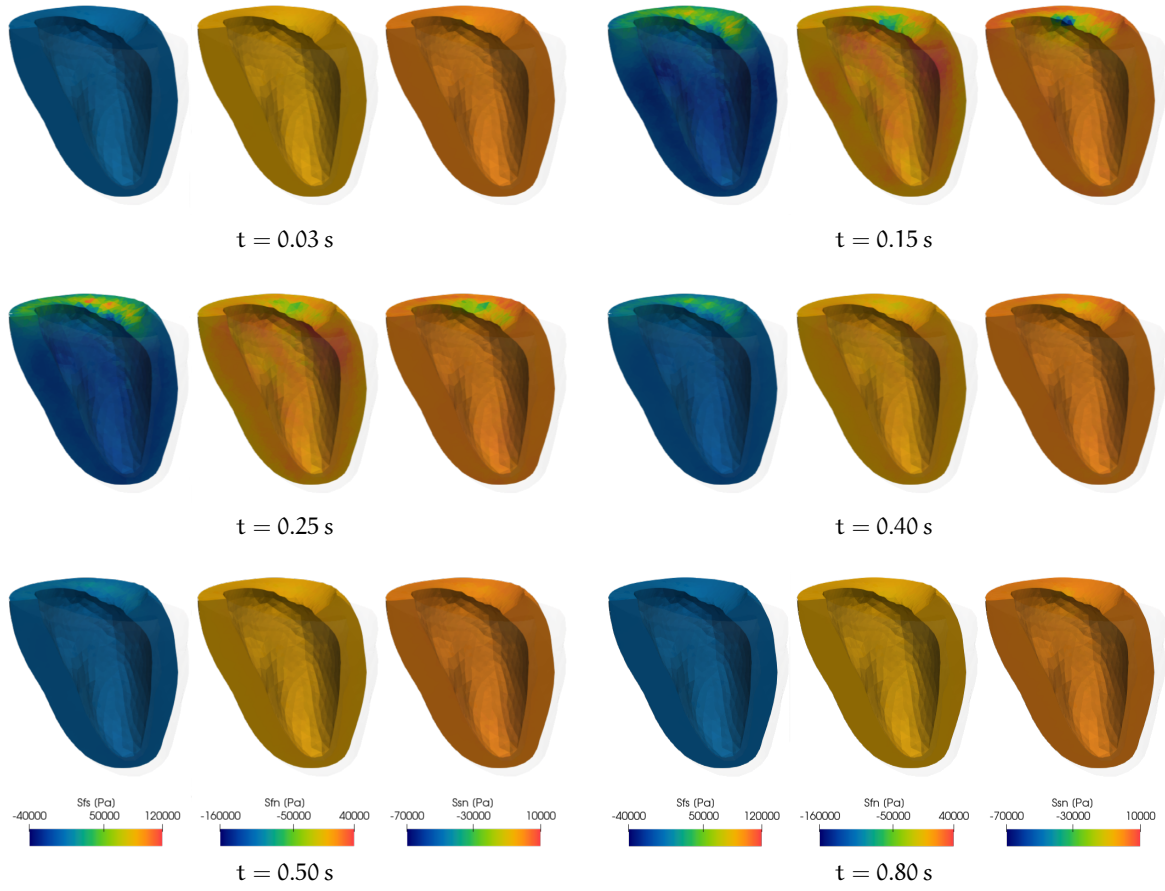
Figure 3.11: Evolution of $S_{fs}$, $S_{fn}$ and $S_{sn}$ during the first heartbeat of the numerical simulation.
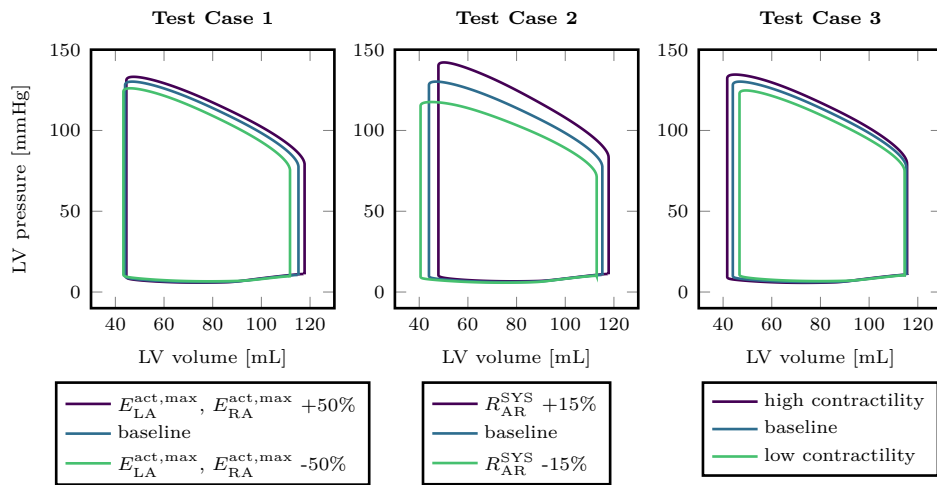


Figure 3.12: LV PV loops obtained in the three Test cases of Sec. 3.2.2 compared with baseline.

contractility generates an increase of both the maximal LV pressure and the SV, but it does not affect preload. As a matter of fact, the EDP is unaltered.

## 3.3 DISCUSSION

In Sec. 3.1 we show the effectiveness of our SIS1 scheme to simulate the electromechanical activity of an idealized LV in physiological conditions, where the PV loop qualitatively resembles the ones observed experimentally [154]. The SIS1 scheme makes use of an intergrid transfer operator based on RL-RBF to accurately and efficiently interpolate the intracellular calcium concentration $[Ca^{2+}]_i$ and the deformation tensor $\mathbf{F}$ between the very different non-nested meshes employed for electrophysiology and mechanics. Indeed, non-nested grids are more flexible to accommodate geometrical heterogeneity and to be tuned to different local accuracy requirements. The use of two different meshes and time steps entails a significant speed-up in the numerical resolution of this multifield coupled problem with respect to the monolithic approach, which is slower and more memory-demanding while leading to similar levels of accuracy [146, 161]. To the best of our knowledge, only techniques involving nested grids and first-order Finite Elements have been used in the context of cardiac electromechanics [32, 37]. Moreover, proofs of scalability are not provided and comparisons in terms of computational costs are lacking. The SIS1 scheme and the numerical simulations presented in Sec. 3.1 fill this gap by enabling the use of completely independent meshes and by providing comparisons with a monolithic strategy in terms of computational times and accuracy [161].

On the other hand, in Sec. 3.2 we consider our SIS2 scheme, in which we employ another parallel and flexible intergrid transfer operator that permits to interpolate the numerical solution of a core model between nested meshes and among possibly different Finite Element spaces [1]. This scheme accounts for the coupling of a 3D electromechanical model with a ØD circulation model in a fully segregated manner while avoiding the balloon dilemma [76] – which affects segregated schemes wherein the displacement update is not aware of the incompressibility constraint of the enclosed fluid, thus possibly leading to the failure of the scheme [12, 68] – by the introduction of a volumetric constraint on the numerical solution of the mechanical problem. In this way, the cavity pressure can be reinterpreted as a Lagrange multiplier associated with the constraint, that enforces the coupling between the ØD circulation model and the 3D electromechanical model. At the algebraic level, we end up with a saddle-point problem, that we solve by means of Schur complement reduction [18].

In the active stress model we replaced a biophysically detailed, but computationally demanding, subcellular model of active force generation by a surrogate model, based on an ANN [143]. This model, which is based on a Machine Learning approach from a collection of pre-computed simulations, allows to accurately reproduce the results of the FOM model by reducing by a factor of 1'000 the number of internal variables [141, 143]. In this way we obtain a very

favorable trade-off between the biophysical accuracy of the results and the computational cost of our numerical simulations.

We consider electromechanical simulations on the Zygote LV where we vary different parameters of the mathematical model to affect preload, afterload and contractility, thus investigating its response for situations of clinical interest. Our mathematical model correctly reproduces the increase of SV as a consequence of increased preload, coherently with the Frank-Starling law [83], thus guaranteeing the matching between the venous return and the cardiac output. We also present a numerical test where we use different polynomial orders for the electrophysiological variables, on one hand, and for the activation and the mechanical ones, on the other hand.

# NUMERICAL RESULTS IN PATHOLOGICAL CONDITIONS

In this chapter, we present electromechanical simulations for LVs with ICM, both in SR and under VT. We show that our mathematical framework enables the investigation of severe pathological scenarios, including arrhythmias.

## 4.1 PATIENT-SPECIFIC LEFT VENTRICLES WITH ISCHEMIC CARDIOMYOPA-THY

We consider two patient-specific LVs with ICM in which both the geometry and the distribution of the ischemic regions are mapped from Late Gadolinium Enhancement Magnetic Resonance Imaging (LGE-MRI). We employ the SIS1 scheme for SR simulations on the first LV, whereas we use the SIS2 scheme to perform SR and VT simulations on the second LV. Thanks to the availability of more clinical data, we develop a personalized computational model on the second patient by manually calibrating some electromechanical parameters in the mathematical model. All clinical data reported in this section were appropriately de-identified and acquired for a retrospective study in accordance with the Johns Hopkins Institutional Review Board.

### 4.1.1 *First geometry*

| Core models | Number of elements | Number of vertices | $h_{mean}$ |
|---|---|---|---|
| Electrophysiology | 3'584'356 | 605'480 | 0.8 mm |
| Activation and mechanics | 448'044 | 81'243 | 2.0 mm |

Table 4.1: Information about the two meshes of the first patient-specific LV with ICM with the corresponding number of elements, number of vertices and average edge length.

We display the distribution of scars, grey zones and healthy areas over the myocardium of the first LV in Fig. 4.1. This heterogeneity translates into different electromechanical properties. The prestress technique described in Sec. 3.1 is still in place to properly initialize the numerical simulation [61]. We illustrate the two unstructured and independent grids employed for the electromechanical simulation in Figs. 4.2 and 4.3. By combining these figures with the information reported in Tab. 4.1, we notice that the SIS1 scheme allows for a significant space scales separation between electrophysiology and mechanics even in complex patient-specific cases.

In Figs. 4.5 and 4.6 we show the evolution in time of both $\gamma_f$ and $\mathbf{d}$ over one heartbeat. The distribution of infarct, peri-infarct and healthy regions is interpo-
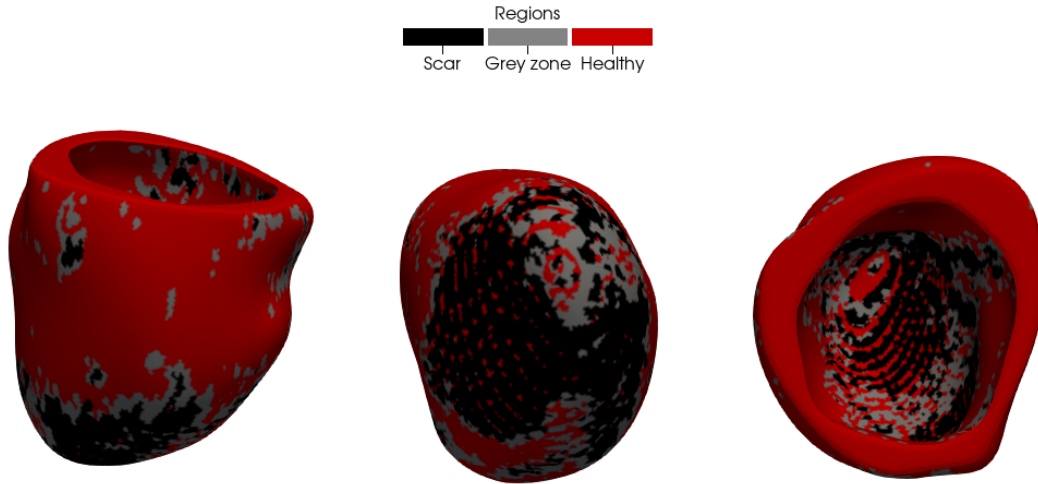
Figure 4.1: First patient-specific LV with ICM: distribution of scars (black), grey zones (grey) and non-remodeled regions (red) over the myocardium.
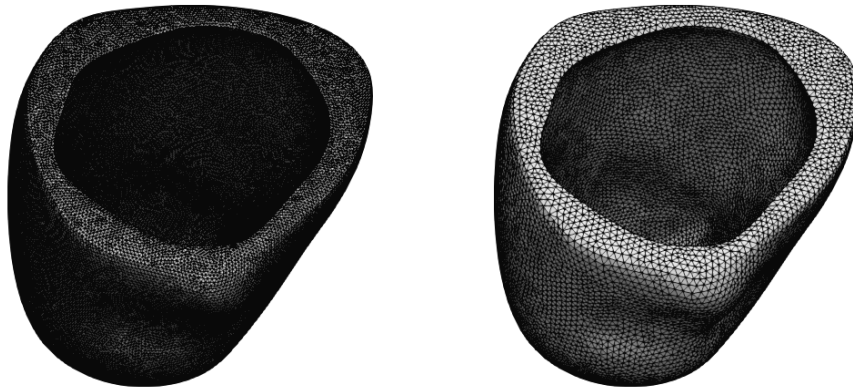


Figure 4.2: View from above of the first patient-specific LV with ICM meshes for electrophysiology (left), activation and mechanics (right).
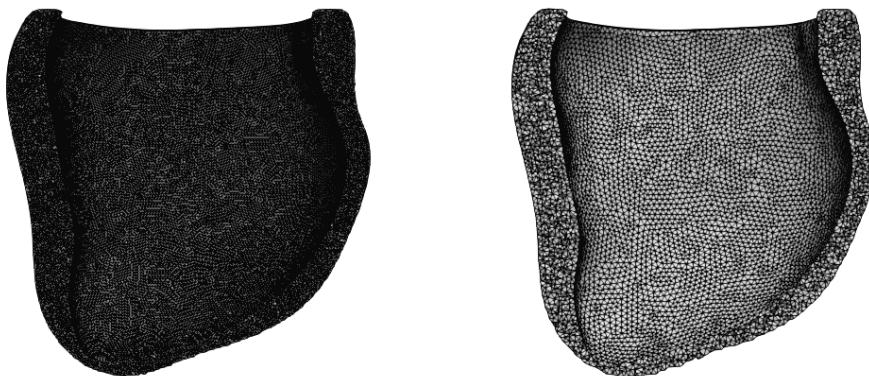


Figure 4.3: Cut front view of the first patient-specific LV with ICM meshes for electrophysiology (left), activation and mechanics (right).

lated on the coarser mesh. We observe a different thickening of the cardiac tissue according to the specific area of the LV. Dense scars, which mostly occupy the
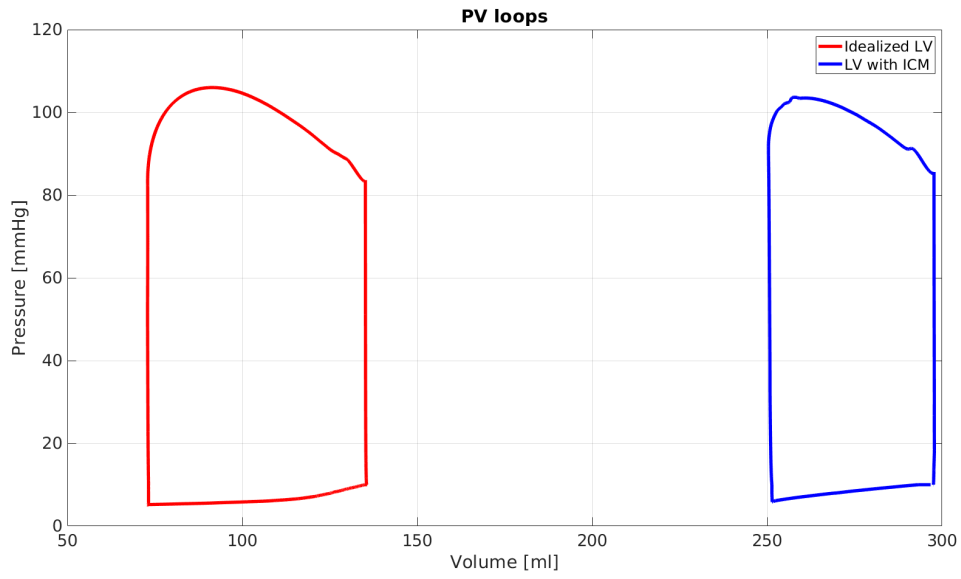
Figure 4.4: Comparison between the PV loops of the idealized LV of Sec. 3.1 and the first patient-specific LV with ICM.



$$t = 0 \ s \qquad\qquad t = 0.15 \ s$$

$$t = 0.25 \ s \qquad\qquad t = 0.35 \ s$$

$$t = 0.44 \ s \qquad\qquad t = 0.70 \ s$$
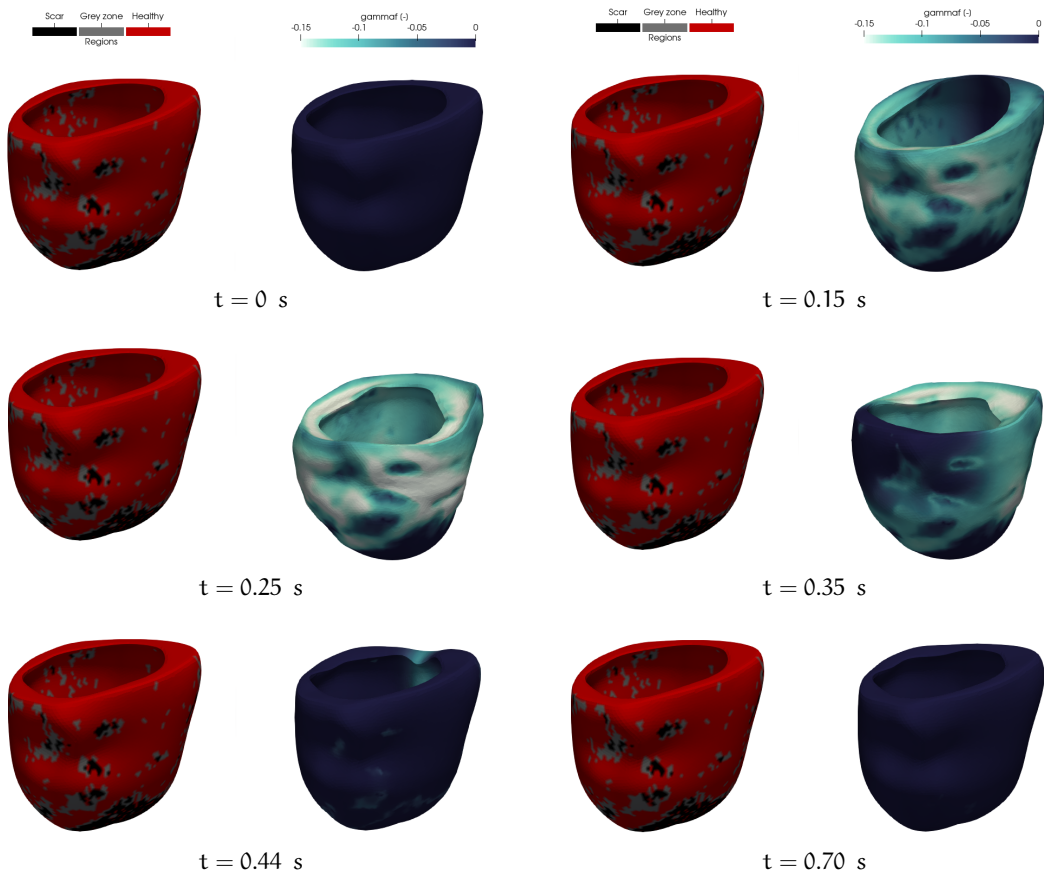
Figure 4.5: Evolution of $\gamma_f$ over the time for the first patient-specific LV with ICM. The left view synthesizes the ischemic regions distribution on the coarser mesh. The right view of each picture is warped by the displacement vector.
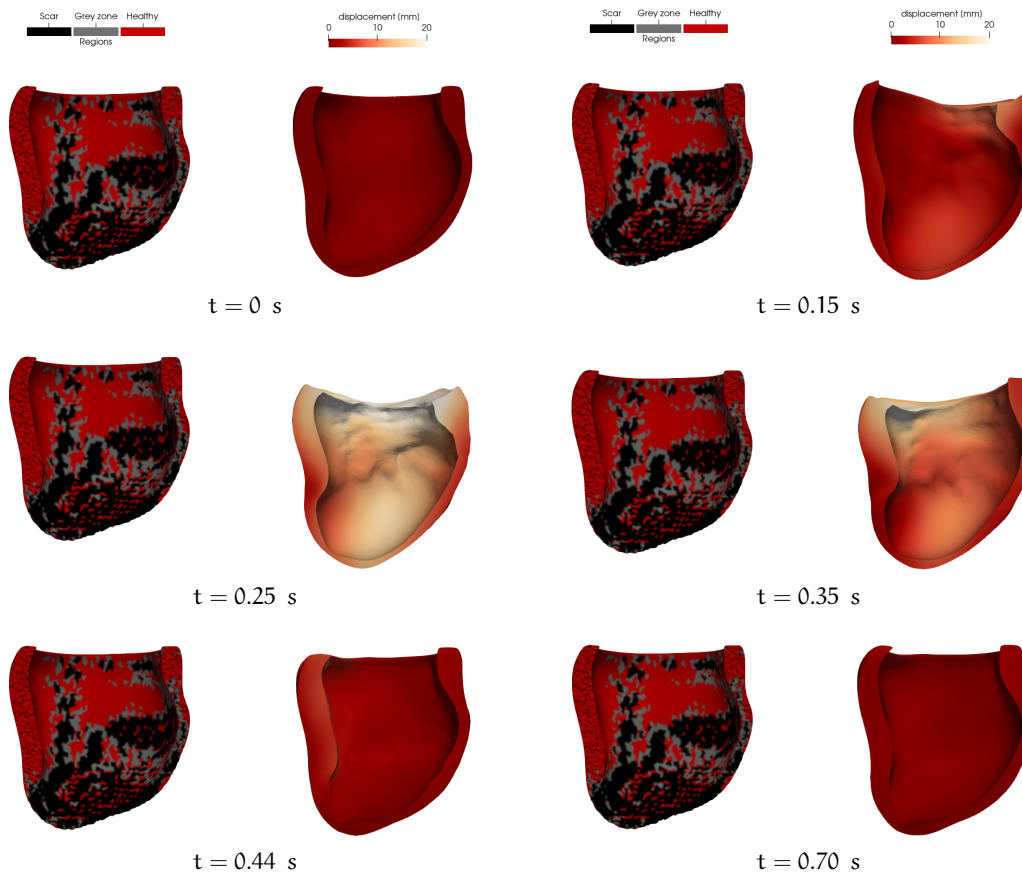
Figure 4.6: Evolution of **d** over the time for the first patient-specific LV with ICM. The left view synthesizes the ischemic regions distribution on the coarser mesh. The right view of each picture is warped by the displacement vector.

lower part of the LV, do not present any electrophysiological activity and do not contract. Grey zones show intermediate electromechanical properties between scars and healthy regions.

In Fig. 4.4, we depict the PV loop of this patient-specific LV. We see that, compared to an idealized LV, which resembles physiological conditions, the PV loop of an ICM patient significantly moves towards the right and manifests a lower SV. This is motivated by the electromechanical remodeling that is determined by ICM over a long period of time.

We stress that, for this specific numerical simulation, due to the lack of clinical data, the parameters of the electromechanical model are not calibrated for the patient at hand. Indeed, we reuse the parametrization of the electromechanical model that is proposed in [161]. For this reason, the PV loop only provides qualitative indications of what is generally observed in ICM patients.

### 4.1.2 *Second geometry*

We depict the geometric model of the second patient-specific LV in Fig. 4.7. We use the Segment cardiac image analysis software package [74] to segment the
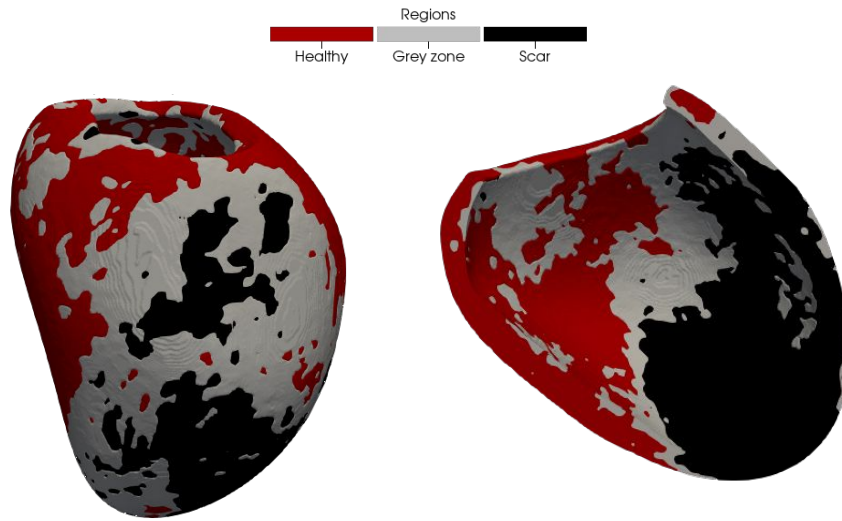
Figure 4.7: Second patient-specific LV with ICM: distribution of scars (black), grey zones (grey) and non-remodeled regions (red) over the myocardium. Volumetric view (left) and cut view (right).

| Parameter | Value |
|-----------|-------|
| EF | 13 % |
| SV | 39 mL |
| HR | 57 |
| MAP | 80 mmHg |
| SBP | 110 mmHg |
| DBP | 69 mmHg |

Table 4.2: Patient-specific data for the second LV with ICM. EF, SV and HR have been retrieved from Cine MRI, while MAP, SBP and DBP where observed by means of a sphygmomanometer.

Cine Magnetic Resonance Imaging (MRI) of the patient. From this segmentation, we retrieve the volume of the LV blood pool over time, SV, EF and HR. We also collected some pressure data, namely MAP, systolic blood pressure (SBP) and diastolic blood pressure (DBP), by using a sphygmomanometer before the clinical trial. All these information are reported in Tab. 4.2.

The geometry is tetrahedralized by using elements of average edge length equal to $0.35\,\text{mm}$. We show the tetrahedral mesh and the tags for base, epicardium and endocardium in Fig. 4.8. Meshing and ischemic region mapping from imaging are performed with the commercial software Materialise Mimics [105]. On the other hand, VMTK is used to generate the corresponding hexahedral mesh and to downsample it to the desired resolution employed in the numerical simulations (average element diameter $h_{\text{mean}} = 1.5\,\text{mm}$, 638'048 elements and 692'535 vertices). We also use VMTK to accurately map the ischemic
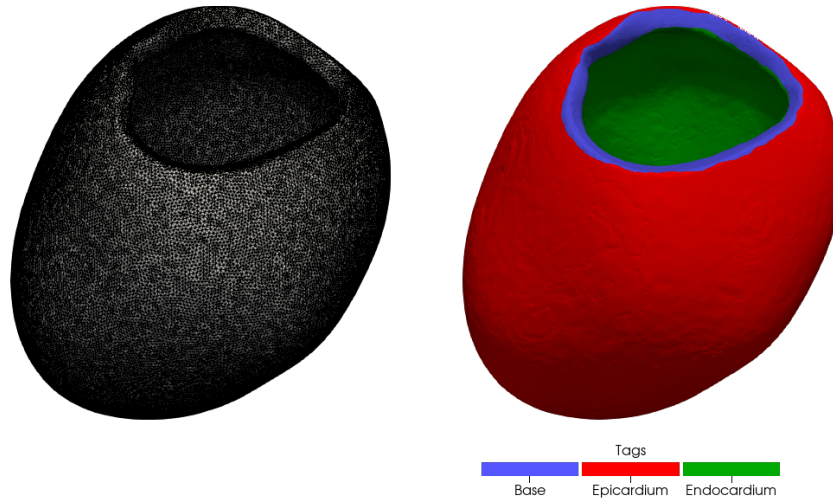
Figure 4.8: Initial tetrahedral mesh (left) and distribution of tags over the myocardium (right) for the second patient-specific LV with ICM.

region distribution from the original high resolution mesh to the downsampled one, after computing the reference configuration, as shown in Fig. 4.9.

We compute the reference configuration of this patient-specific LV by solving the inverse problem proposed in [147, 148], which is also reported in Sec. 2.2 and Sec. 2.5. In this way, we get the geometry in a stress-free condition, as if the blood was completely removed from the LV. Accounting for the heterogeneous coefficient $\eta = \eta(x)$ in Eqs. (2.1), (2.5) and (2.9) has a clear influence on the numerical solution of this inverse problem, as shown in Fig. 4.10 [162].

We report the setup of all the numerical simulations of this section in Tab. 4.3. We will present personalized numerical results in the context of cardiac electrophysiology and cardiac electromechanics, both in SR and during VT, for a patient-specific LV with ICM. Despite the complete SIS2 scheme would be beneficial, we do not consider different mesh resolutions for electrophysiology and mechanics but rather use a mesh that balances numerical accuracy and computational efficiency for both models. In this way, we have a fully consistent geometrical representation of these complex patient-specific ischemic regions, which is certainly important to define, to the best of our knowledge, the first individualized computational model of the electromechanical activity in a human LV with ICM.

*Sinus rhythm*

We run several numerical simulations in SR (Tab. 4.3, code ①) to perform the calibration of the parameters of our electromechanical model. In particular, we manually tuned $\mu_A$ for active strain, $K_\perp^{epi}$, $K_\parallel^{epi}$, $C_\perp^{epi}$ and $C_\parallel^{epi}$ for mechanics, resistance $R$ and capacitance $C$ of the 2-element windkessel model. We do not calibrate the passive mechanics parameters related to the Guccione constitutive law. Indeed, we are unable to fit a Klotz curve for this patient-specific case [88]. We reuse the same parametrization provided in [156] on failing swine hearts.

| Code | Type | Software | $h_{mean}$ | Time step | Stimulation protocol [s] |
|---|---|---|---|---|---|
| ① | Electromechanics (SR) | $\texttt{life}^{\text{x}}$ (hexahedral meshes) | 1.5 mm | $\tau = 5 \cdot 10^{-5}$ s (20$\tau$ for mechanics) | - |
| ② | Electrophysiology (VT) | CARP (tetrahedral meshes) | 0.35 mm | $\tau = 2.5 \cdot 10^{-5}$ s | [0, 0.45, 0.90, 1.35, 1.80, 2.25, 2.54, 2.82] |
| ③ | Electrophysiology (VT) | $\texttt{life}^{\text{x}}$ (hexahedral meshes) | 1.5 mm | $\tau = 5 \cdot 10^{-5}$ s | [0, 0.45, 0.76, 1.04] |
| ④ | Electromechanics (VT, pathological parametrization) | $\texttt{life}^{\text{x}}$ (hexahedral meshes) | 1.5 mm | $\tau = 5 \cdot 10^{-5}$ s (20$\tau$ for mechanics) | [0, 0.45, 0.76, 1.04] |
| ⑤ | Electromechanics (VT, healthy parametrization) | $\texttt{life}^{\text{x}}$ (hexahedral meshes) | 1.5 mm | $\tau = 5 \cdot 10^{-5}$ s (20$\tau$ for mechanics) | [0, 0.45, 0.76, 1.04] |

Table 4.3: Setup for all the numerical simulations of Sec. 4.1.2. The pacing point is the same for each stimulation protocol. The parameters of the electromechanical model can be found in Appendix A.2.2.
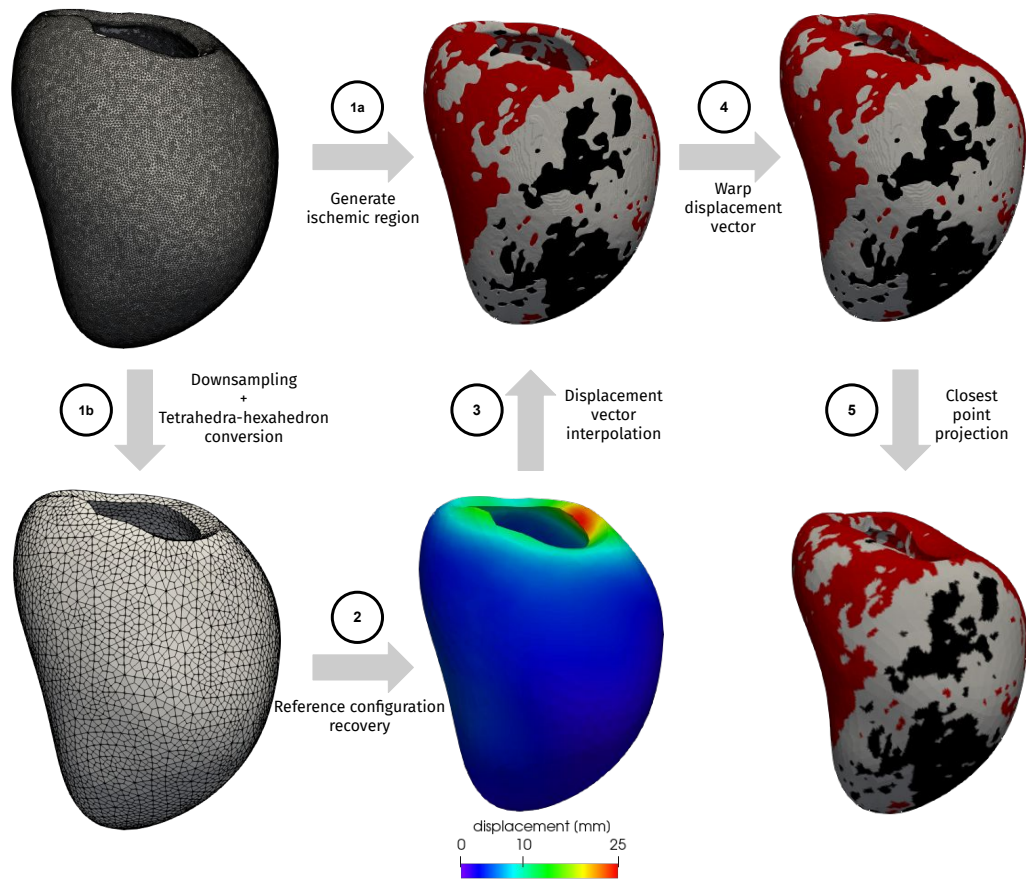
Figure 4.9: Preprocessing phase for the second patient-specific LV with ICM. The ischemic regions are mapped on the high resolution tetrahedral mesh (step 1a). Then, downsampling and conversion to hexahedral elements are performed (step 1b). We compute the reference configuration on the latter mesh (step 2). The displacement vector is accurately and efficiently interpolated on the high resolution mesh with the ischemic regions, by using the interpolant proposed in [148] (step 3). Finally, we warp the tetrahedral mesh with the interpolated reference configuration displacement (step 4) and we perform closest point projection of the ischemic regions distribution on the hexahedral mesh used in our numerical simulations (step 5).

We remind that the reference configuration recovery is repeated for each new set of parameters. We report in Appendix A.2.2 the final configuration that we used for the SR simulation. In Fig. 4.11 we depict the evolution of $\gamma_f$ and displacement magnitude $|\mathbf{d}|$ over different time steps of the numerical simulation. We highlight the heterogeneity in the activation of the myocardium, that leads to different contractility according to the specific region. Dense scars, which approximately occupy half of the LV, do not contract. Displacement magnitude $|\mathbf{d}|$ is again dominant at the base, so that the LV is pushed towards the apex. Moreover, even if we do not perform a quantitative strain analysis, we get a qualitative match between the displacement field observed from our numerical simulation and the one coming from Cine MRI.

In Fig. 4.12, we show the evolution of the LV volume over time for the patient, along with the PV loop. We provide a good quantitative match with Cine
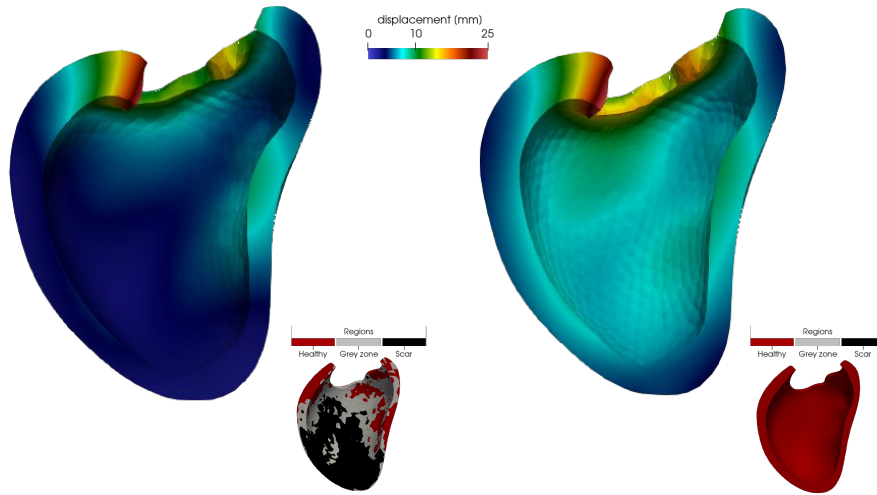
Figure 4.10: Reference configuration recovery for the second patient-specific LV with ICM. We depict the displacement to reach the unstressed geometry $\Omega_0$ in case the ischemic regions distribution is imported (left) or when fully healthy conditions are considered (right). Scars, which are mostly localized at the apex, prevent the unloading for part of the myocardium.

MRI for the evolution of blood pool volume over time, as well as for all values reported in Tab. 4.2. Indeed, even if we do not have at our disposal the evolution of the LV pressure over time, we also provide a match with the three available pointwise pressure measurements (i.e. MAP, SBP and DBP). Moreover, we underline the major differences with respect to a reference healthy PV loop (baseline simulation in [148]). The presence of ICM significantly dilates the LV over the years. As a consequence, the PV loop moves to the right and both EDV and ESV increase. The EDP is generally higher with ICM, whereas the pressure peak is lower. Indeed, the capability of the LV to push blood into the aorta is strongly impaired. This coincides with smaller contractility and reduced EF.

*Ventricular tachycardia*

We induced a VT by repeatedly stimulating the LV at one specific location. We run an electrophysiological simulation with the software package CARP (CardioSolv LLC) [191, 193] on the original tetrahedral mesh ($h_{mean} = 0.35\,\text{mm}$) and we induced a sustained VT by following the strategy proposed in [6] (Tab. 4.3, code ②). Then, we run an electrophysiological simulation with the life$^x$ library on the hexahedral mesh ($h_{mean} = 1.5\,\text{mm}$). We reproduce a similar activation map between the two numerical simulations, as shown in Fig 4.13.

Next, we induce a sustained VT in the life$^x$ electrophysiological simulation by using a shorter stimulation protocol (Tab. 4.3, code ③). While the VT observed in CARP has a basis cycle length BCL $\approx 0.390\,\text{s}$, the one resulting from life$^x$ shows a BCL $\approx 0.420\,\text{s}$. This may be motivated by the use of different stimulation protocols, different mesh elements (tetrahedron vs. hexahedron) and different average mesh sizes ($0.35\,\text{mm}$ vs. $1.5\,\text{mm}$). In particular, given the same biophysical parametrizations, the mesh resolution has a significant impact on

Figure 4.11: Evolution in SR of $\gamma_f$ and displacement magnitude $|\mathbf{d}|$ for the second patient-specific LV with ICM (Tab. 4.3, code ①). Each picture is warped by the displacement vector.

the effective CVs [204]. The use of a shorter stimulation protocol and a coarser mesh resolution for the electrophysiological simulation performed in $\texttt{life}^{\times}$ are dictated by the complexity of the electromechanical simulations that we run. Indeed, to ensure maximum comparability of the results, electrophysiological and electromechanical simulations in $\texttt{life}^{\times}$ (Tab. 4.3, codes ①, ③ ④, ⑤) must run by employing the same numerical settings. The electrophysiological simulation performed in CARP stands as a reference solution, thanks to the fine space and time discretization that we adopted.

At this point, we run an electromechanical simulation under VT (Tab. 4.3, code ④) by using the multiphysics model parameters reported in Appendix A.2.2.
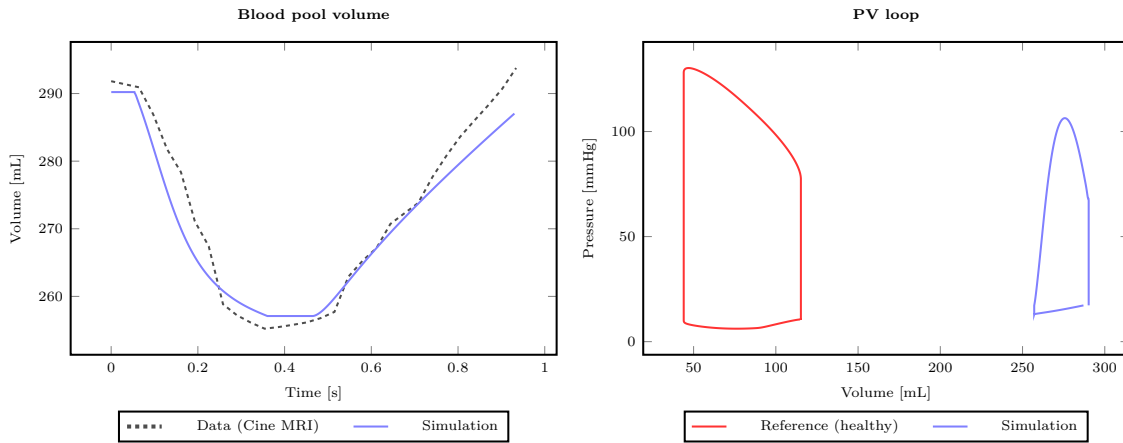
Figure 4.12: Electromechanical simulation of the second patient-specific LV with ICM (Tab. 4.3, code ①): blood pool volume over time (left) and PV loop (right). We highlight the comparison with clinical data and a reference healthy LV (taken from [148]).
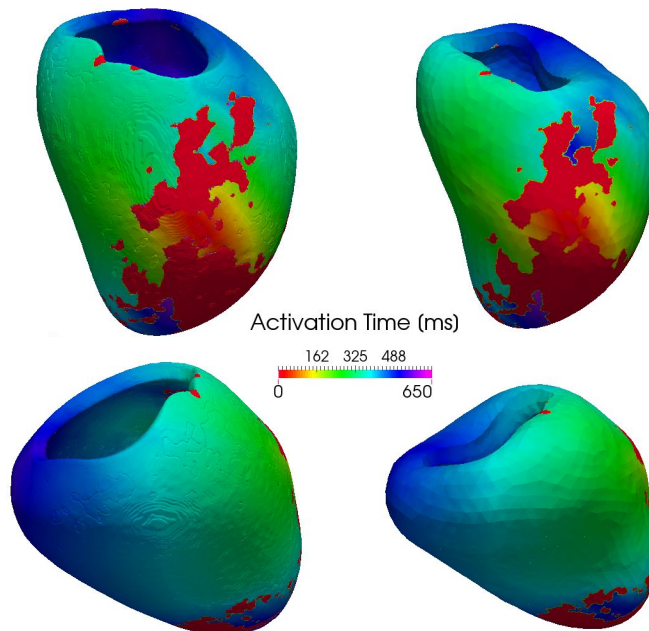


Figure 4.13: Activation time for the second patient-specific LV with ICM. Numerical simulations from CARP (left, Tab. 4.3, code ②) and life$^\text{x}$ (right, Tab. 4.3, code ③). We use a tetrahedral mesh ($h_{mean} = 0.35$ mm) in CARP. We consider the reference configuration, meshed with hexahedral elements ($h_{mean} = 1.5$ mm), in life$^\text{x}$. Only minor differences in terms of activation times can be observed between the two cases.

More specifically, for the ØD circulation model, we consider the pathological parametrization reported in Tab. A.9, with steady state initial conditions obtained after running the ØD model in SR for 100 heartbeats.

In Fig. 4.14 we compare the electrophysiological simulation (Tab. 4.3, code ③) with the electromechanical one (Tab. 4.3, code ④), by depicting the distribution of the transmembrane potential over time. In the time interval before the VT is triggered, no major differences between the two numerical simulations are observed. On the other hand, after the VT is induced, its morphology around
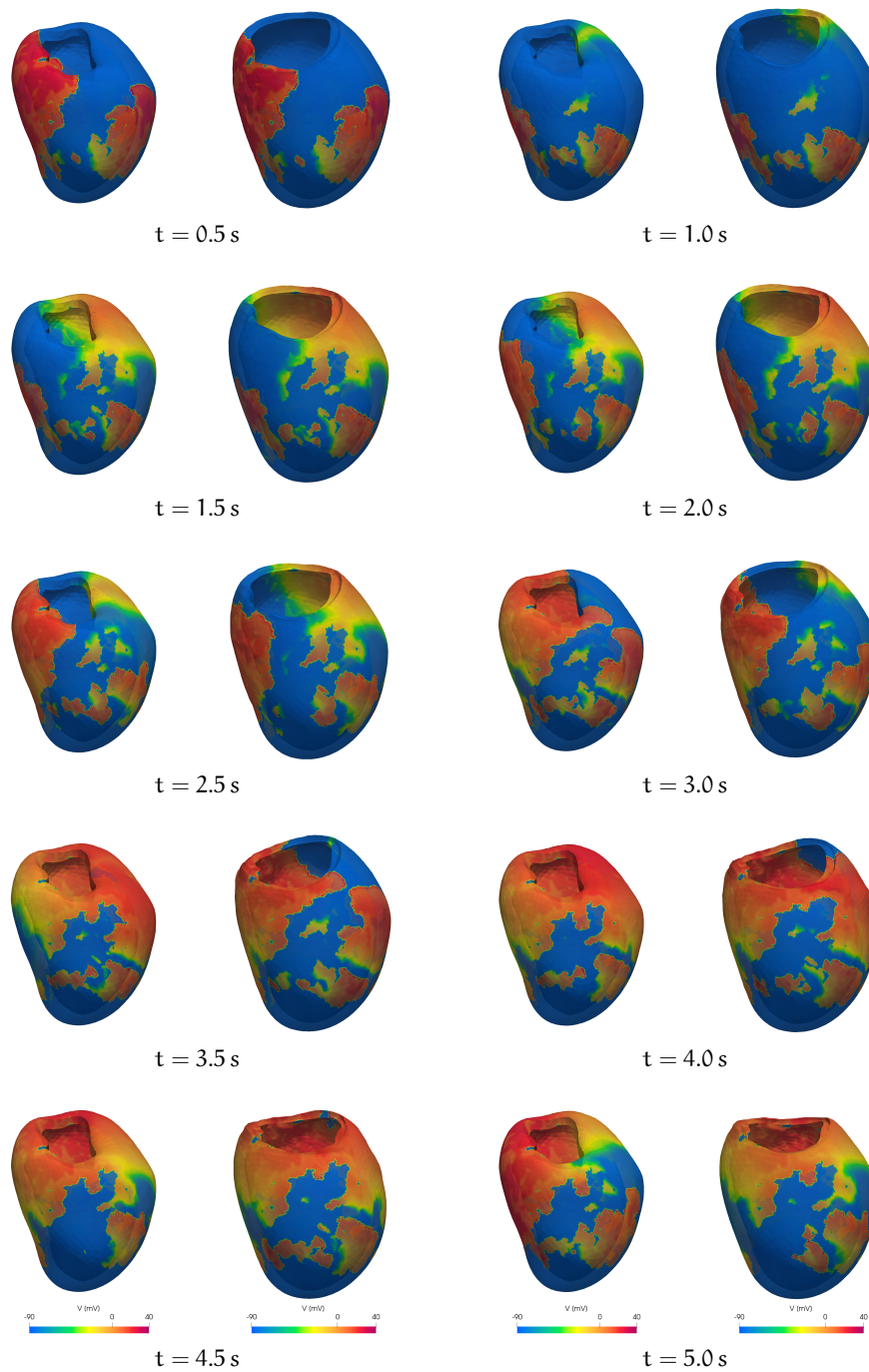
Figure 4.14: Propagation of the transmembrane potential V during VT for the second patient-specific LV with ICM. Electrophysiological simulation (left, Tab. 4.3, code ③) runs on the geometry retrieved from LGE-MRI (i.e. without reference configuration recovery). Electromechanical simulation (right, Tab. 4.3, code ④) is warped by the displacement vector.
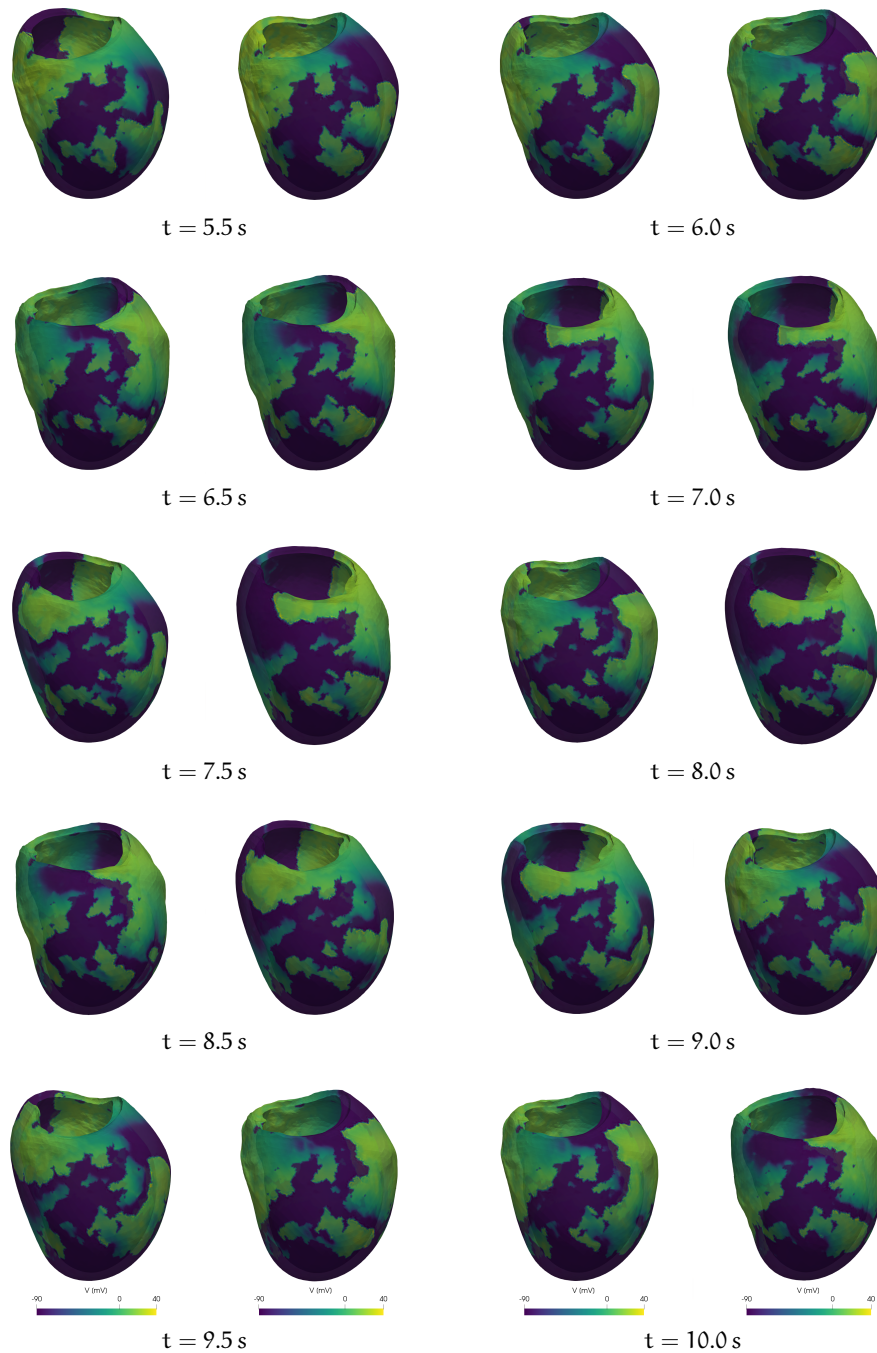
Figure 4.15: Propagation of the transmembrane potential V during VT for the second patient-specific LV with ICM. We depict two electromechanical simulations with a healthy parametrization of the circulation model (left, Tab. 4.3, code ⑤) and a pathological one (right, Tab. 4.3, code ④). The geometry is warped by the displacement vector in both cases.
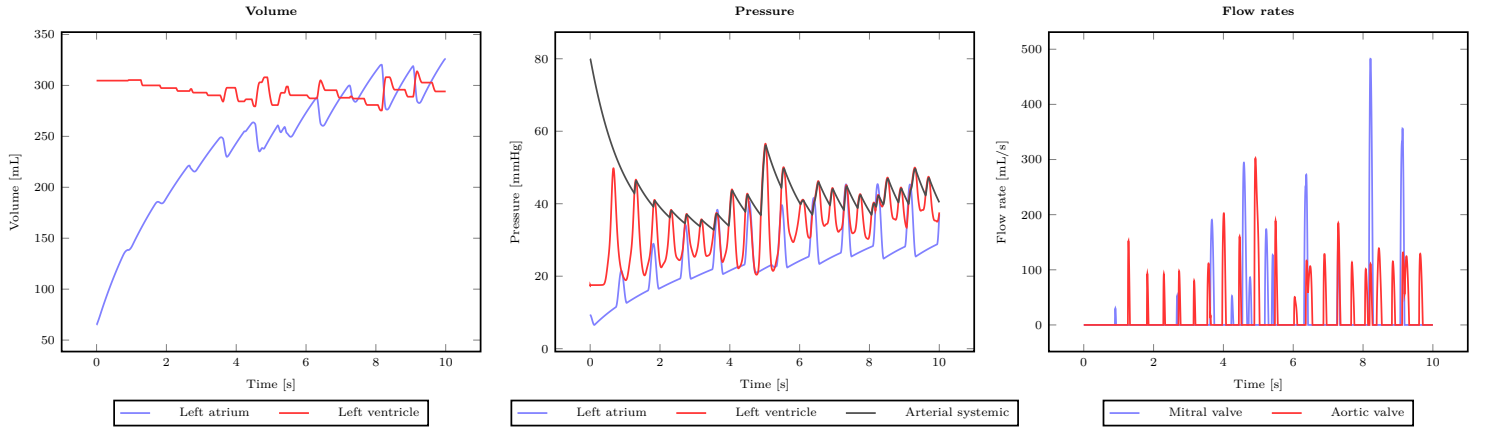
Figure 4.16: Electromechanical simulation of VT for the second patient-specific LV with ICM and a healthy parametrization of the circulation model (Tab. 4.3, code ⑤): blood pool volume over time for the ØD LA and the 3D LV (left), pressure over time for the LA, the LV and the arterial systemic part of the cardiovascular system (center), flow rates of the MV and the AV (right).
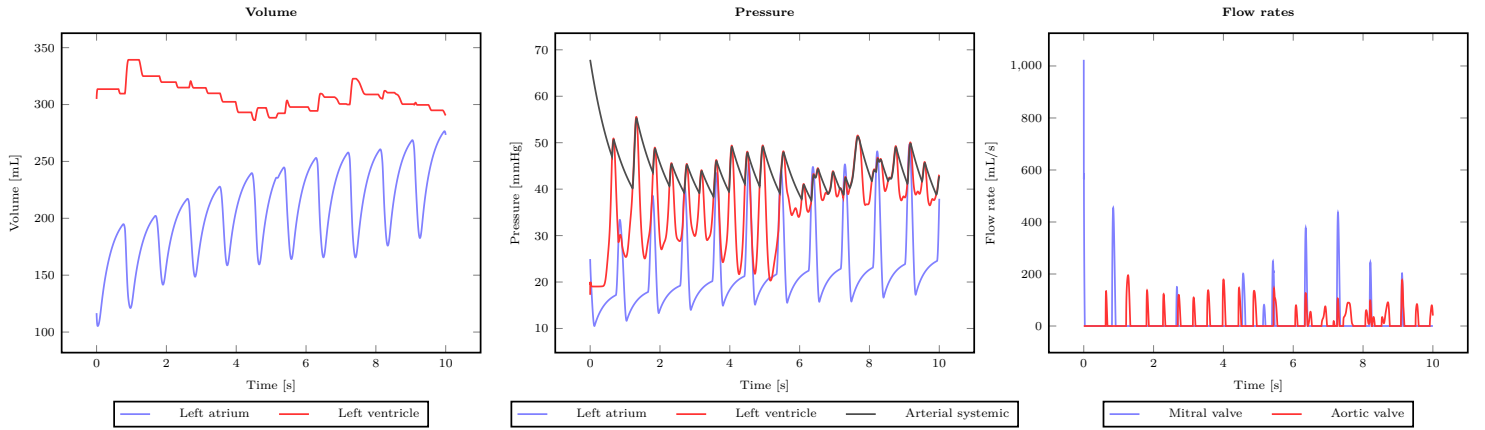


Figure 4.17: Electromechanical simulation of VT for the second patient-specific LV with ICM and a pathological parametrization of the circulation model (Tab. 4.3, code ④): blood pool volume over time for the ØD LA and the 3D LV (left), pressure over time for the LA, the LV and the arterial systemic part of the cardiovascular system (center), flow rates of the MV and the AV (right).

the isthmus significantly changes, as well as the CV of the electric signal. Indeed, the basis cycle length slightly increases, going to BCL ≈ 0.440 s. Moreover, given a certain stimulation point and a certain sequence of S1-S2-S3 stimuli, we also conclude that in this case, if a VT is observed by considering electrophysiology only, a VT is also inducible by considering electromechanics.

We also compare two electromechanical simulations which are performed by using a very different parametrization for the ØD circulation model: the first one (Tab. 4.3, code ⑤), resembles the activity of a heart without infarction (Tab. A.8), whereas the second one (Tab. 4.3, code ④) defines a pathological cardiovascular system with an infarcted heart (Tab. A.9). For further details about the two settings, we refer to Appendix A.2.2.

In Fig. 4.15 we highlight that different parametrizations of the circulation model induce differents activation patterns and consequently different displacement fields. Nevertheless, we employ the very same sequence of S1-S2-S3 stimuli to induce the VT. In Figs. 4.16 and 4.17 we illustrate the behavior of LA pressure and volume, LV pressure and volume, arterial systemic pressure, MV and AV flow rates, during VT. We highlight that pressures in the aorta and in the LV are either dropping or oscillating on unsustainable levels for the cardiovascular system. Indeed, the LV is not able to push blood into the circulation system and the blood pool volume presents small variations over time. On the other hand, both LA pressure and volume are increasing during VT. In particular, due to electric isolation between atria and ventricles, the LA is assumed to follow the SR pacing during the simulated VT, which lasts for $10\,\mathrm{s}$. Moreover, the flow rates of both MV and AV indicate that, even if no regurgitation occurs, there is no proper synchronization between the different cardiac chambers. For this reason, the left heart function is highly compromised. Finally, the PV loop of the LV is not stabilizing over a certain limit cycle that would not cause its impairment. For this reason, we can classify the VT as hemodynamically unstable regardless the parametrization of the ØD circulation model. This VT is critical for the patient and it may lead to SCD.

## 4.2 ZYGOTE LEFT VENTRICLE

We present electromechanical simulations to evaluate the effects of MEFs by considering the geometric model of the Zygote LV in Fig. 4.18, which is endowed with an idealized distribution of ischemic regions made by two scars and two different types of grey zones. We consider different modeling choices for the monodomain equation, as reported in Tab. 2.1.

We introduce a fine geometrical description (1'987'285 DOFs, 1'926'912 cells, $h_{\mathrm{mean}} \approx 0.86\,\mathrm{mm}$) for cardiac electrophysiology to accurately capture the electric propagation due to fine-scale phenomena arising from the continuum modeling of the cellular level, especially with the aim of reproducing and properly address arrhythmias [162]. On the other hand, cardiac mechanics allows a lower space resolution (35'725 DOFs, 30'108 cells, $h_{\mathrm{mean}} \approx 3.3\,\mathrm{mm}$). This eases its numerical solution, which is computationally demanding given the intrinsic high degree of nonlinearity, especially for the assembling phase [161].

We start from a baseline simulation with model ($\mathscr{E}$), in which we obtain a stable VT. Then, we compare the effects of different geometry-mediated MEFs, i.e. models ($\mathscr{E}$), ($\mathscr{E}_{\mathrm{gMEF\text{-}minimal}}$), ($\mathscr{E}_{\mathrm{gMEF\text{-}enhanced}}$) and ($\mathscr{E}_{\mathrm{gMEF\text{-}full}}$). We also study the impact of different parametrizations for SACs, i.e. ($\mathscr{E}_{\mathrm{SAC}}$), with respect to ($\mathscr{E}$). Finally, we evaluate the combined effects of geometry-mediated MEFs and non-selective SACs. The values of the parameters that we use to get these numerical results are reported in Appendix A.2.3.
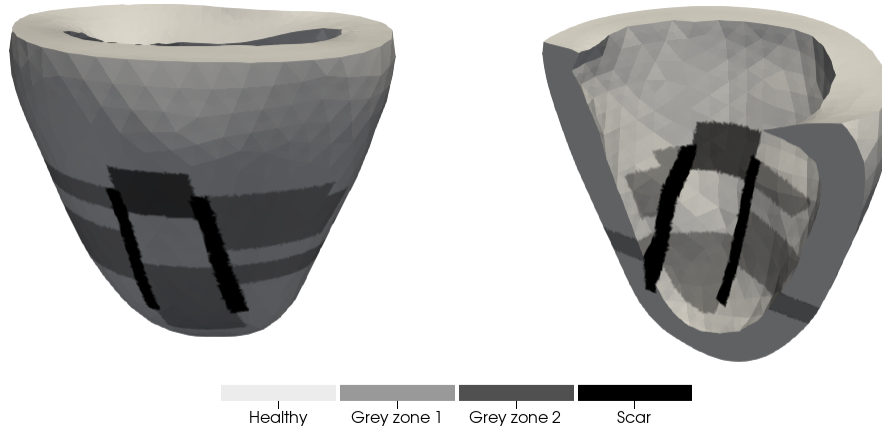
Figure 4.18: Zygote LV with an idealized distribution of scars (black), grey zones (grey) and non-remodeled regions (white) over the myocardium. Volumetric view (left) and cut view (right). The first type of grey zone corresponds to $\eta = 0.2$, while on the second one $\eta = 0.1$ is prescribed.

### 4.2.1  *Baseline simulation*

We depict in Fig. 4.19 the evolution of the transmembrane potential and the displacement magnitude for the baseline electromechanical simulation, where all MEFs are fully neglected (model ($\mathscr{E}$) in Tab. 2.1). We induce a sustained VT with a figure-of-eight pattern around the isthmus, which is laterally bordered by scars, that act as conduction blocks.

In Fig. 4.20, we compare the PV loop over different heartbeats for the baseline simulation under VT with a reference healthy PV loop in SR obtained by removing scars and grey zones. We observe that the contractility increases while the SV decreases. The EF remains approximately the same and indeed we approach a steady state in which the electromechanical function is not impaired.

VT associated with ischemia is known to perturb the normal isovolumetric processes and to influence the end systolic/diastolic pressure volume relationship. Simultaneously, a phenomenon called incomplete relaxation may occur, especially when the VT does not leave enough time for the uncoupling of all the actin-myosin bonds between two consecutive contraction phases [15]. The occurrence of this phenomenon is illustrated in Fig. 4.21, where we depict the time evolution of the minimum, maximum and average active stress in the computational domain $\Omega_0$ for a reference healthy case in SR and the baseline simulation under VT. Specifically, in the healthy case there is always a time interval between two consecutive heartbeats (precisely, during ventricular diastole) in which the active stress is virtually zero in the LV. In the VT case, instead, the cardiac muscle is never fully relaxed, thus not allowing the LV to complete its emptying. All these details are properly captured by our electromechanical model thanks to its biophysical accuracy.
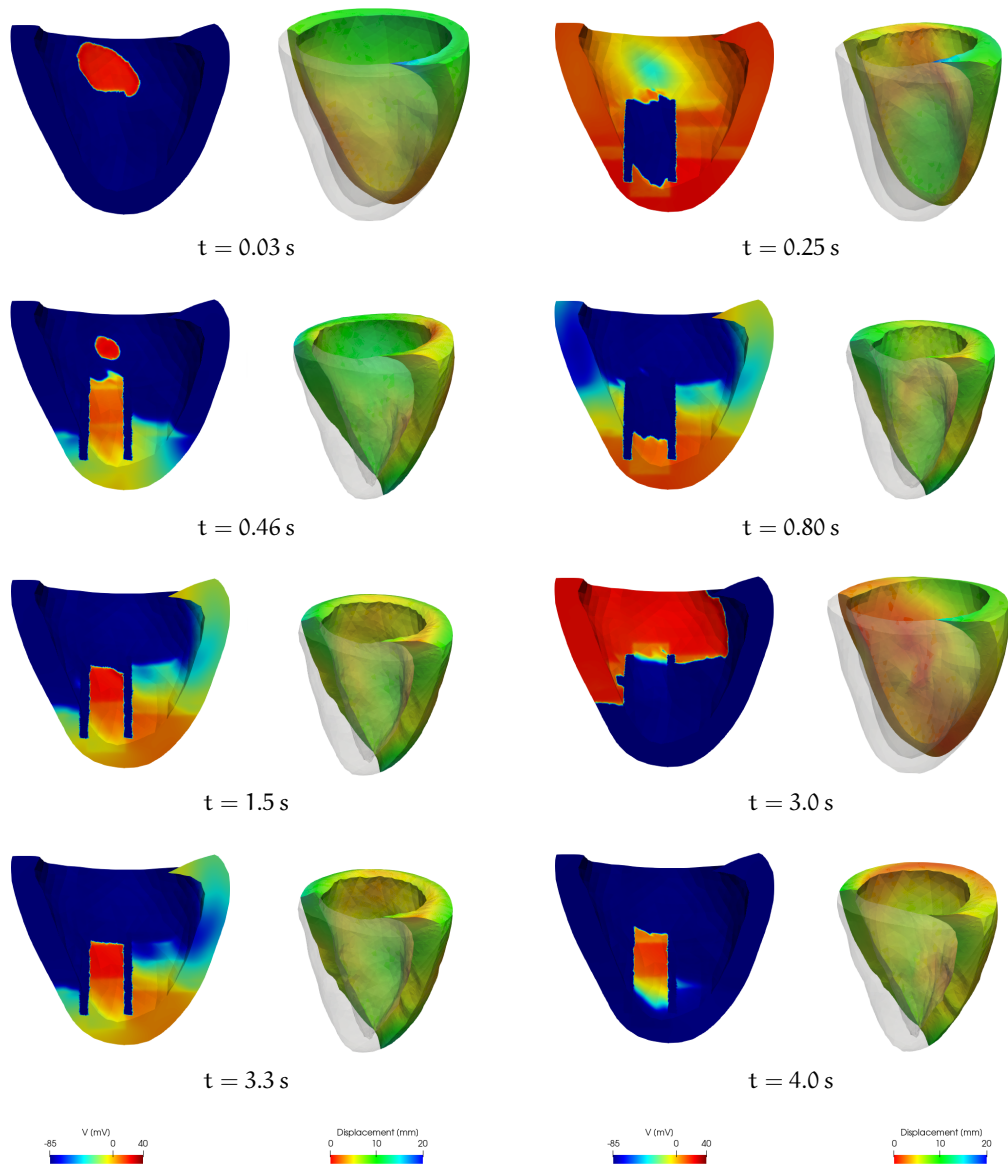
Figure 4.19: Time evolution of the transmembrane potential V (left) and displacement magnitude |**d**| (right) for the Zygote LV with an idealized distribution of ischemic regions. Each picture on the right side is warped by the displacement vector **d**. MEFs are neglected, i.e. we use model ($\mathscr{E}$).
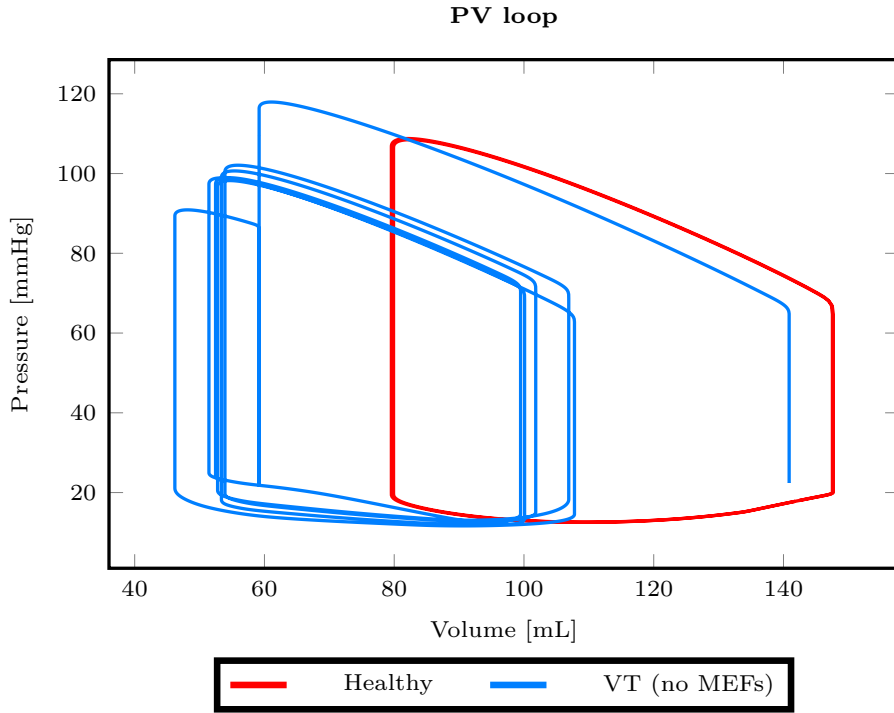
**PV loop**

Figure 4.20: Comparison between a reference healthy PV loop in SR (red, Appendix A.2.3, heart-beat period equal to 0.8 s) and the one obtained in the baseline simulation under VT for t ∈ [0, 4] s (light blue). We underline that here we induce a hemodynamically tolerated VT.
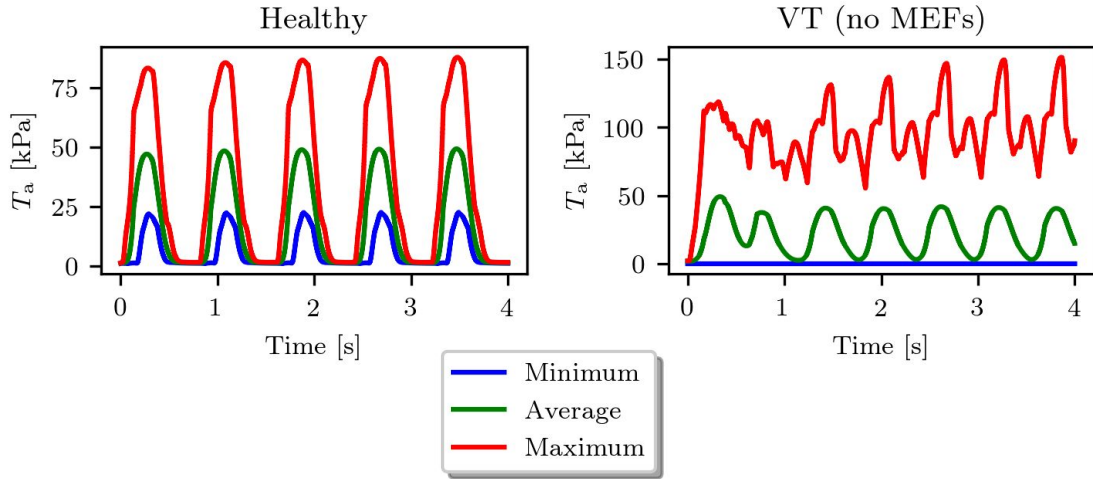


Figure 4.21: Minimum, average and maximum active tension $T_a$ over time for a reference healthy case in SR (left, Appendix A.2.3, heartbeat period equal to 0.8 s) and the baseline simulation under VT (right). We see that incomplete relaxation occurs during VT.

### 4.2.2 *Effects of geometry-mediated MEFs*

We consider four different modeling choices for the geometry-mediated MEFs, namely $(\mathscr{E})$, $(\mathscr{E}_{\text{gMEF-minimal}})$, $(\mathscr{E}_{\text{gMEF-enhanced}})$ and $(\mathscr{E}_{\text{gMEF-full}})$ in Tab. 2.1, while

$(\mathcal{E})$ $(\mathcal{E}_{\text{gMEF-minimal}})$ $(\mathcal{E}_{\text{gMEF-enhanced}})$ $(\mathcal{E}_{\text{gMEF-full}})$

$t = 0.20\,\text{s}$

$t = 0.45\,\text{s}$

$t = 2.4\,\text{s}$

$t = 4.0\,\text{s}$

V (mV)

-85   0   40
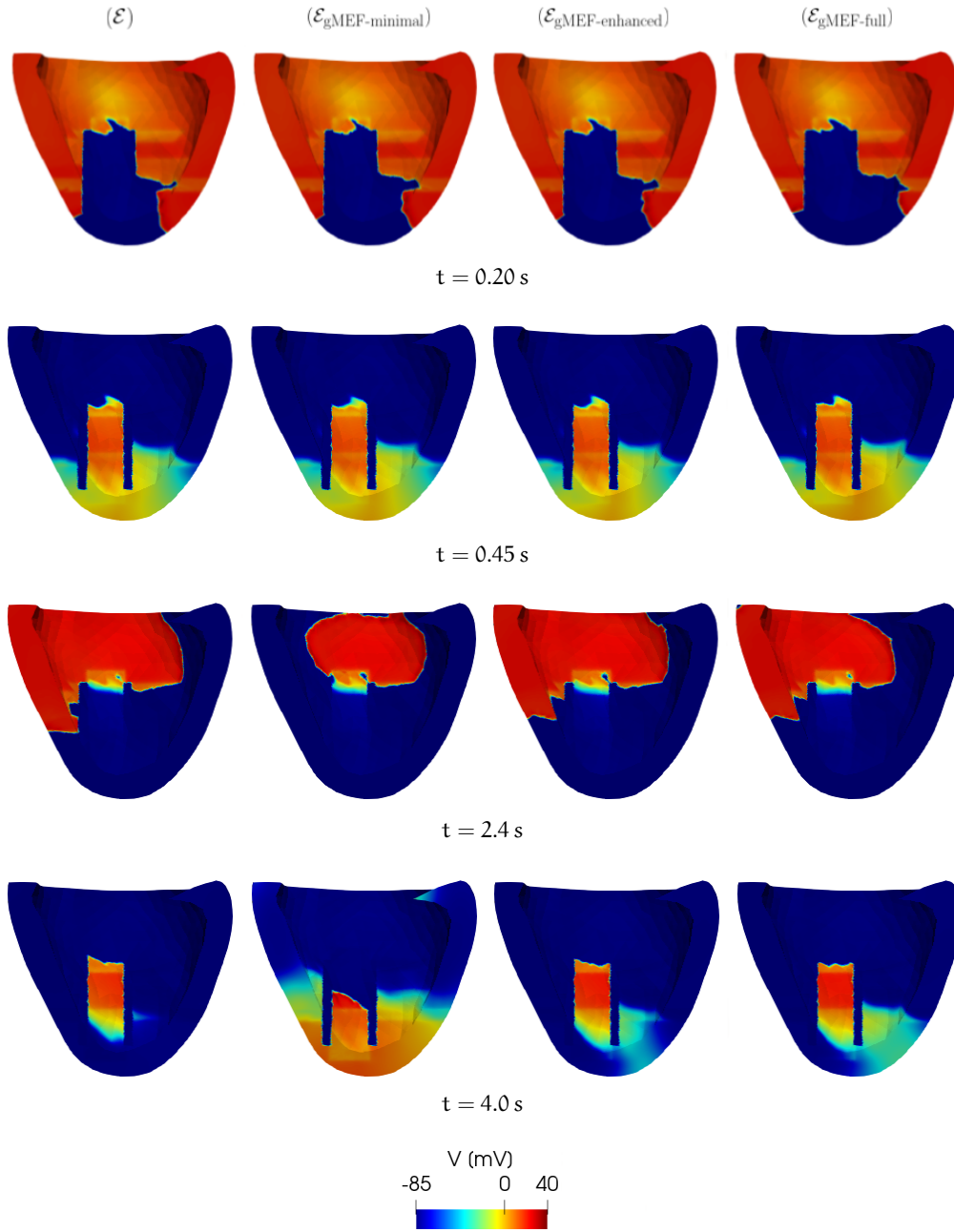
Figure 4.22: Comparison among different models for geometry-mediated MEFs in terms of transmembrane potential V.
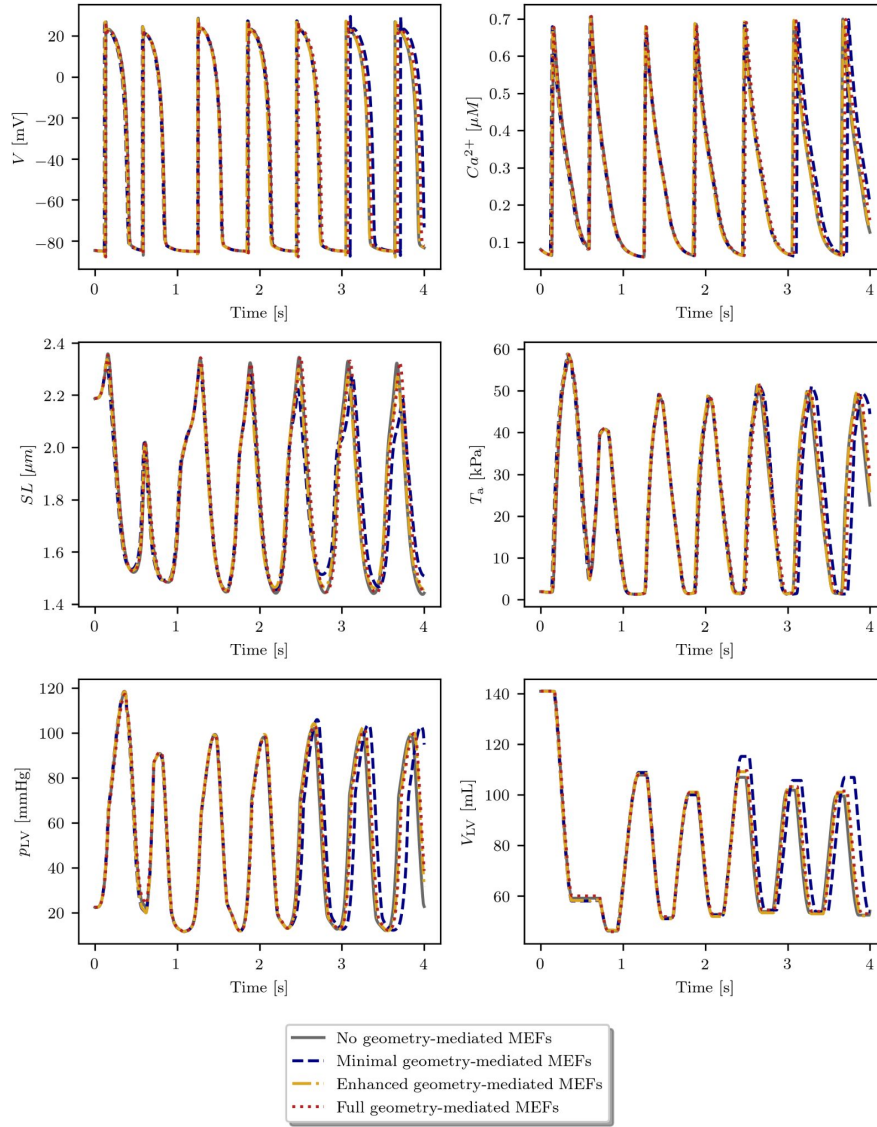
Figure 4.23: Pointwise values of transmembrane potential $V$, intracellular calcium concentration $[Ca^{2+}]_i$, sarcomere length SL, active tension $T_a$, pressure $p_{LV}$ and volume $V_{LV}$ over time for $(\mathscr{E})$, $(\mathscr{E}_{gMEF\text{-}minimal})$, $(\mathscr{E}_{gMEF\text{-}enhanced})$ and $(\mathscr{E}_{gMEF\text{-}full})$.

for the moment we completely neglect the impact of SACs. We perform four different electromechanical simulations by employing these four different formulations for the monodomain equation.

We illustrate in Fig. 4.22 the development of transmembrane potential $V$ over time. We observe minor differences in AP propagation among $(\mathscr{E})$, $(\mathscr{E}_{gMEF\text{-}enhanced})$ and $(\mathscr{E}_{gMEF\text{-}full})$. These differences, as it can be seen for $t = 4$ s, are mainly focused on the depolarization wave and occur during VT. Moreover, by looking at Tab. 4.4, we notice that the VT BCL is very similar among these three models. Indeed, the BCL is approximately equal to $0.60$ s, which is long if compared to more dangerous VT and justifies a stable ventricular excitation.

| Model | $(\mathcal{E})$ | $(\mathcal{E}_{\text{gMEF-minimal}})$ | $(\mathcal{E}_{\text{gMEF-enhanced}})$ | $(\mathcal{E}_{\text{gMEF-full}})$ |
|---|---|---|---|---|
| BCL | 0.60 s | 0.65 s | 0.61 s | 0.60 s |

Table 4.4: BCL for different modeling choices of geometry-mediated MEFs. Model $(\mathcal{E}_{\text{gMEF-minimal}})$ significantly changes BCL with respect to $(\mathcal{E})$, $(\mathcal{E}_{\text{gMEF-enhanced}})$, $(\mathcal{E}_{\text{gMEF-full}})$.

| Model | VT type |
|---|---|
| $(\mathcal{E})$ | Stable (BCL = 0.60 s) |
| $(\mathcal{E}_{\text{SAC}})$, $G_s = 100\,s^{-1}$, $V_{\text{rev}} = -70\,mV$ | Stable (BCL = 0.60 s) |
| $(\mathcal{E}_{\text{SAC}})$, $G_s = 100\,s^{-1}$, $V_{\text{rev}} = -35\,mV$ | Stable (BCL = 0.60 s) |
| $(\mathcal{E}_{\text{SAC}})$, $G_s = 100\,s^{-1}$, $V_{\text{rev}} = 0\,mV$ | Unstable (BCL$_{\text{avg}} = 0.50\,s$) |
| $(\mathcal{E}_{\text{SAC}})$, $G_s = 50\,s^{-1}$, $V_{\text{rev}} = 0\,mV$ | Stable (BCL = 0.60 s) |

Table 4.5: VT classification for different SACs parametrizations. The unstable VT has a BCL that ranges from 0.43 s to 0.58 s.

On the other hand, $(\mathcal{E}_{\text{gMEF-minimal}})$ entails major changes in VT BCL, which increases from 0.60 s (for model $(\mathcal{E})$) to 0.65 s, and alters CV, that significantly decreases.

These observations are in agreement with Fig. 4.23, where the electrophysiological, mechanical and hemodynamic variables retrieved in a random point of the computational domain are shifted forward in time during VT for $(\mathcal{E}_{\text{gMEF-minimal}})$, while $(\mathcal{E})$, $(\mathcal{E}_{\text{gMEF-enhanced}})$ and $(\mathcal{E}_{\text{gMEF-full}})$ show a very similar pattern. This is also motivated by the change in the VT exit site, as it can be seen from Fig. 4.22 for t = 2.4 s. This phenomenon is particularly evident from the plot of sarcomere length over time (Fig. 4.23), which also presents different peak values for $(\mathcal{E}_{\text{gMEF-minimal}})$ and $t \gtrsim 2.4$ s. Finally, we notice that wave stability is not affected by geometry-mediated MEFs. Indeed, the VT always remains hemodynamically stable in the four different cases.

### 4.2.3 *Effects of SACs*

In this section, we fully neglect the effects of geometry-mediated MEFs and we focus on different parametrizations for SACs in terms of $G_s$ and $V_{\text{rev}}$. We also compare the outcomes of $(\mathcal{E}_{\text{SAC}})$ with the ones of $(\mathcal{E})$ to outline similarities and differences.

We notice from Fig. 4.24 that both APD and wave stability are affected by SACs parametrizations. Indeed, by combining the 3D information with the
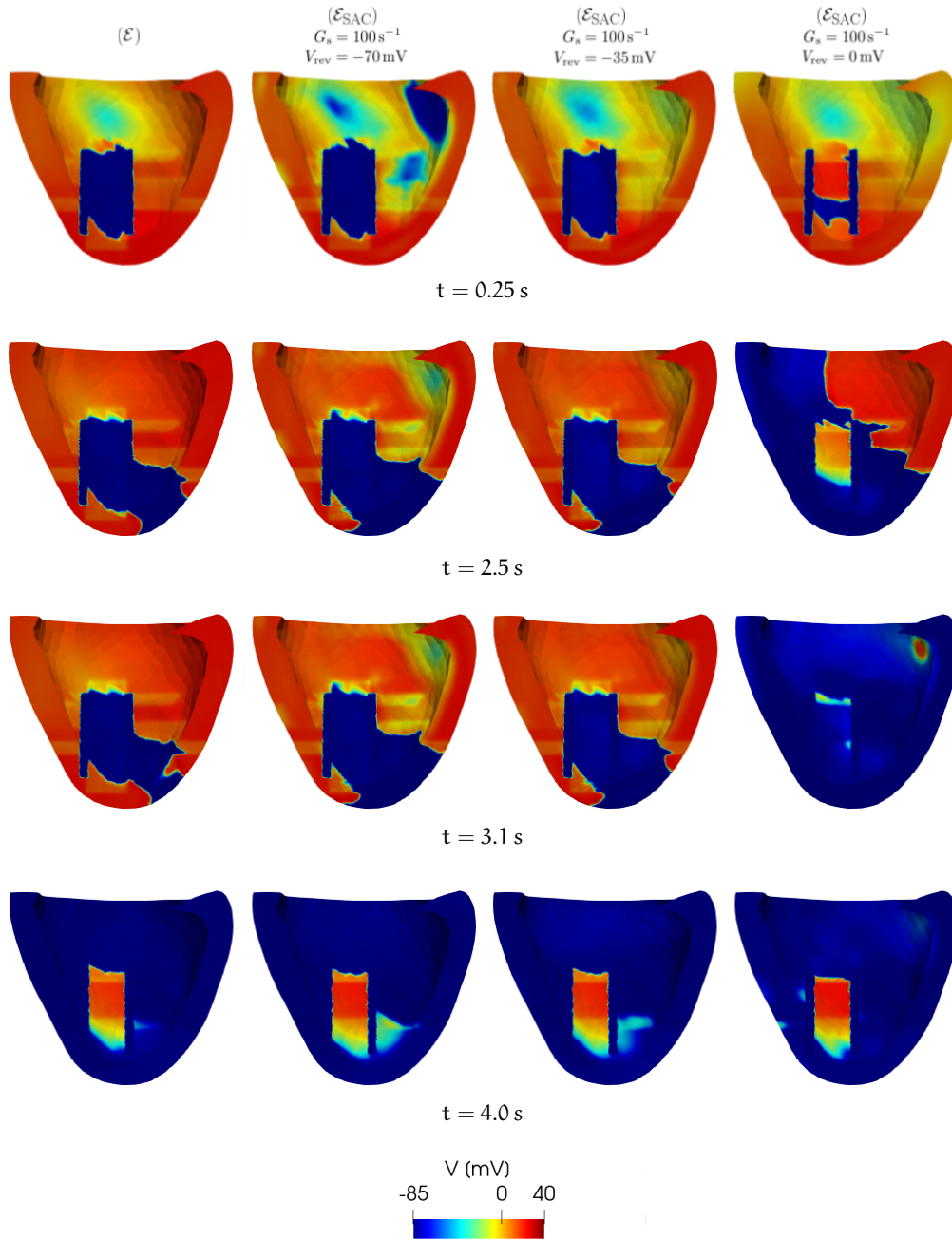
Figure 4.24: Comparison between model $(\mathcal{E})$ and model $(\mathcal{E}_{\mathrm{SAC}})$, for different values of $V_{\mathrm{rev}}$ ($G_{\mathrm{s}} = 100\,\mathrm{s}^{-1}$).
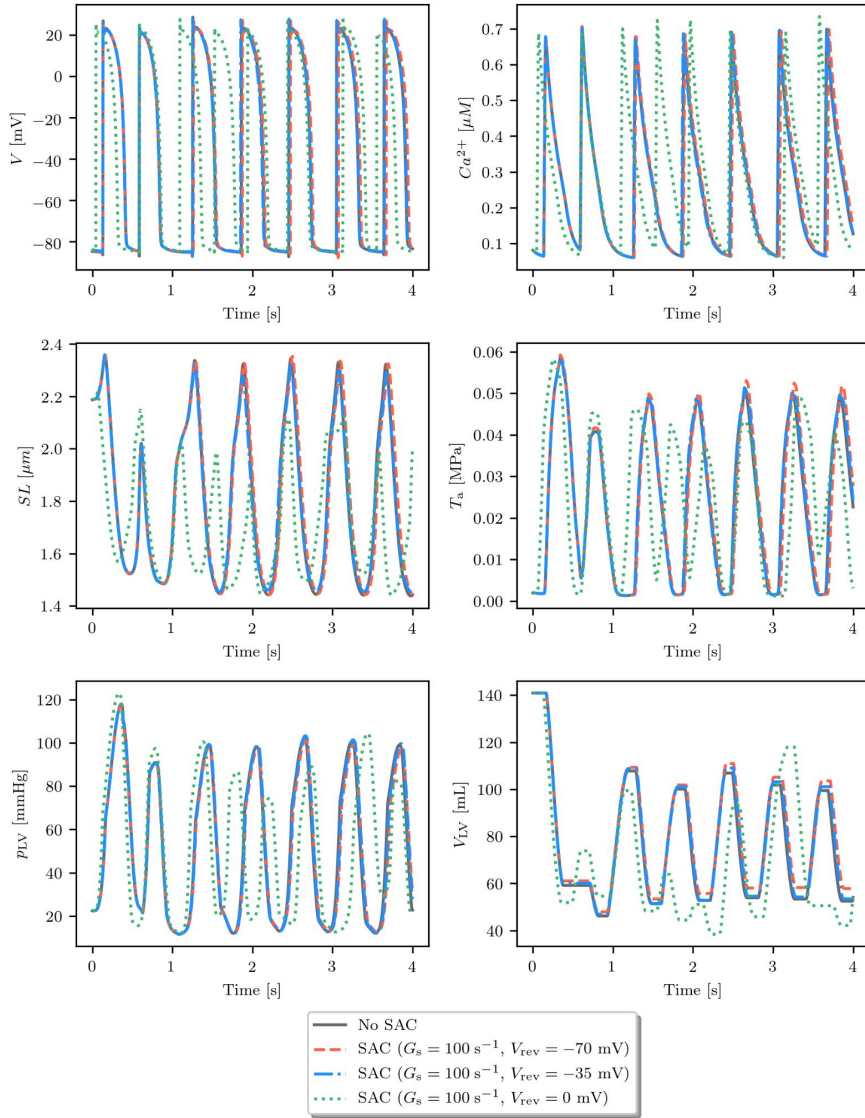
Figure 4.25: Pointwise values of transmembrane potential $V$, intracellular calcium concentration $[Ca^{2+}]_i$, sarcomere length $SL$, active tension $T_a$, pressure $p_{LV}$ and volume $V_{LV}$ over time for $(\mathscr{E})$ and $(\mathscr{E}_{SAC})$ with different choices of $V_{rev}$ ($G_s = 100\,s^{-1}$).

pointwise evaluations of Fig. 4.25, we discover that there is one choice of the parameters, namely $G_s = 100\,s^{-1}$ and $V_{rev} = 0\,mV$, that converts the VT from stable to unstable. The instability derives from an extra stimulus that is completely driven by contraction, which occurs in the superior-right part of the ventricle. This extra stimulus changes the VT morphology, along with its BCL, which is not the same over time.

By considering data of Tab. 4.5, we observe that the VT BCL remains the same when there is no stability transition. Moreover, from the hemodynamic perspective, the onset of different types of arrhythmias is driven by the combined effects of $G_s$ and $V_{rev}$. Indeed, in Fig. 4.25 we see that given $G_s$, different
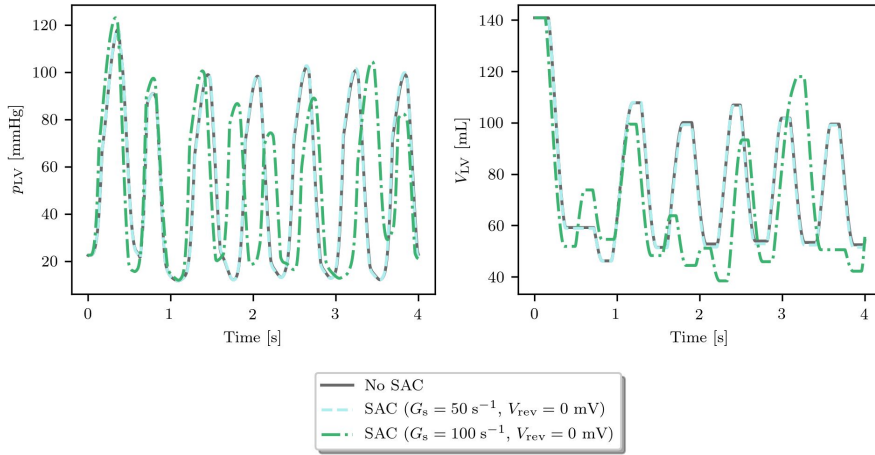
Figure 4.26: Pointwise values of pressure $p_{LV}$ and volume $V_{LV}$ over time for $(\mathscr{E})$ and $(\mathscr{E}_{SAC})$ with different choices of $G_s$ ($V_{rev} = 0\,mV$).

| Model | VT type |
|---|---|
| $(\mathscr{E})$ | Stable ($0.60\,s$) |
| $(\mathscr{E}_{SAC})$, $G_s = 100\,s^{-1}$, $V_{rev} = 0\,mV$ | Unstable ($BCL_{avg} = 0.50\,s$) |
| $(\mathscr{E}_{gMEF\text{-}full,\,SAC})$, $G_s = 100\,s^{-1}$, $V_{rev} = 0\,mV$ | Unstable ($BCL_{avg} = 0.47\,s$) |

Table 4.6: VT classification for combinations of geometry-mediated MEFs and nonselective SACs. The unstable VT related to $(\mathscr{E}_{SAC})$ has a BCL that ranges from $0.43\,s$ to $0.58\,s$. The unstable VT related to $(\mathscr{E}_{gMEF\text{-}full,\,SAC})$ has a BCL that ranges from $0.44\,s$ to $0.50\,s$.

$V_{rev}$ may change wave stability. On the other hand, in Fig. 4.26 we show that different $G_s$ may affect wave stability, with $V_{rev}$ fixed a priori.

### 4.2.4 *Combined effects of geometry-mediated MEFs and SACs*

We also evaluate the combined effects of geometry-mediated MEFs and non-selective SACs for an unstable VT. Once SACs parametrization is fixed, we notice that switching between no formulation (i.e. $(\mathscr{E}_{SAC})$) to full formulation (i.e. $(\mathscr{E}_{gMEF\text{-}full,\,SAC})$) of geometry-mediated MEFs entails significant differences. In particular, from Fig. 4.27 we see that $(\mathscr{E}_{gMEF\text{-}full,\,SAC})$ triggers the extra stimuli faster than $(\mathscr{E}_{SAC})$. As we can see from Fig. 4.28, the VT remains unstable but both pressure and volume traces over time are very different from each other for $(\mathscr{E}_{SAC})$ and $(\mathscr{E}_{gMEF\text{-}full,\,SAC})$. From Tab. 4.6, we infer that the VT BCL for $(\mathscr{E}_{gMEF\text{-}full,\,SAC})$ is lower than the one of $(\mathscr{E}_{SAC})$. This potentially defines a more dangerous VT. Finally, in Fig. 4.29 we highlight the joint contributions of electrophysiology, mechanics and hemodynamics in the $(\mathscr{E}_{gMEF\text{-}full,\,SAC})$ coupled model.
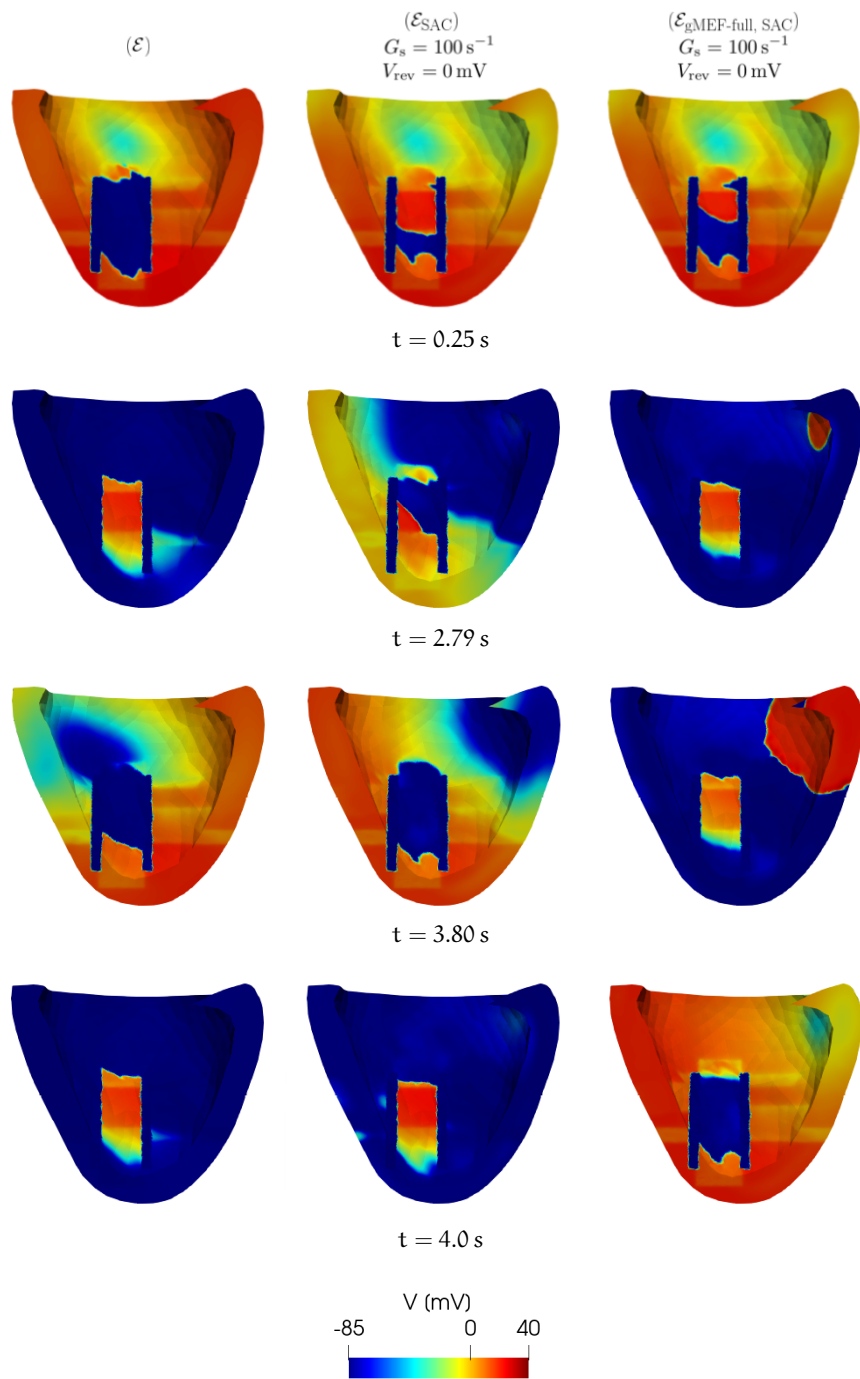
Figure 4.27: Comparison among models $(\mathscr{E})$, $(\mathscr{E}_{\mathrm{SAC}})$ and $(\mathscr{E}_{\mathrm{gMEF\text{-}full,\ SAC}})$.
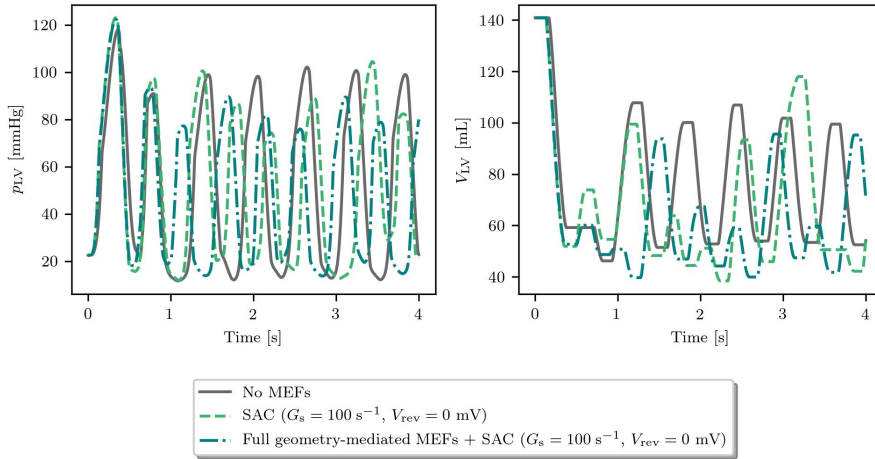
Figure 4.28: Pointwise values of pressure $p_{LV}$ and volume $V_{LV}$ over time for $(\mathscr{E})$, $(\mathscr{E}_{SAC})$ $(G_s = 100\,s^{-1}, V_{rev} = 0\,mV)$ and $(\mathscr{E}_{gMEF\text{-}full, SAC})$ $(G_s = 100\,s^{-1}, V_{rev} = 0\,mV)$.

## 4.3 DISCUSSION

In Sec. 4.1.1 we provide a numerical test to assess the applicability of the SIS1 scheme to patient-specific LVs with ICM. We keep a very good separation of space-time scales in terms of mesh sizes and time steps. The coefficient $\eta = \eta(x)$ permits to use different parametrizations for infarct, peri-infarct and non-remodelled zones inside the electromechanical model. The PV loop qualitatively resembles the one of an ICM patient with heart remodeling and severely reduced EF.

In Sec. 4.1.2 we present a personalized computational model of the electromechanical activity in the LV of a patient with ICM, both in SR and VT. We manually personalize model parameters by means of numerical simulations in SR to fit the available clinical data. Then, we successfully induce a sustained VT and we study its effects by combining electrophysiological, mechanical and hemodynamic observations. To the best of our knowledge, this is the first time in which a VT is analyzed by means of an electromechanical model in a patient-specific ventricle with ICM. All the numerical results in Sec. 4.1.2 are obtained with the SIS2 scheme.

Again, our mathematical parametrization incorporates the heterogeneous distribution of scars, grey zones and non-remodeled regions of human ventricles. Differently from previous works in literature [6, 133], we model both electrophysiological and mechanical properties. While prior state-of-the-art electromechanical simulations seek to model both normal function and pathological conditions, including heart failure [173], or the impact of drugs [101], only the SR case is addressed and tissue heterogeneity of the myocardium is not kept into account over the entire electromechanical model. The coupling with a closed-loop system and the numerical scheme developed in this thesis allow for the effective numerical simulation of VT. Indeed, this approach does not discrimi-
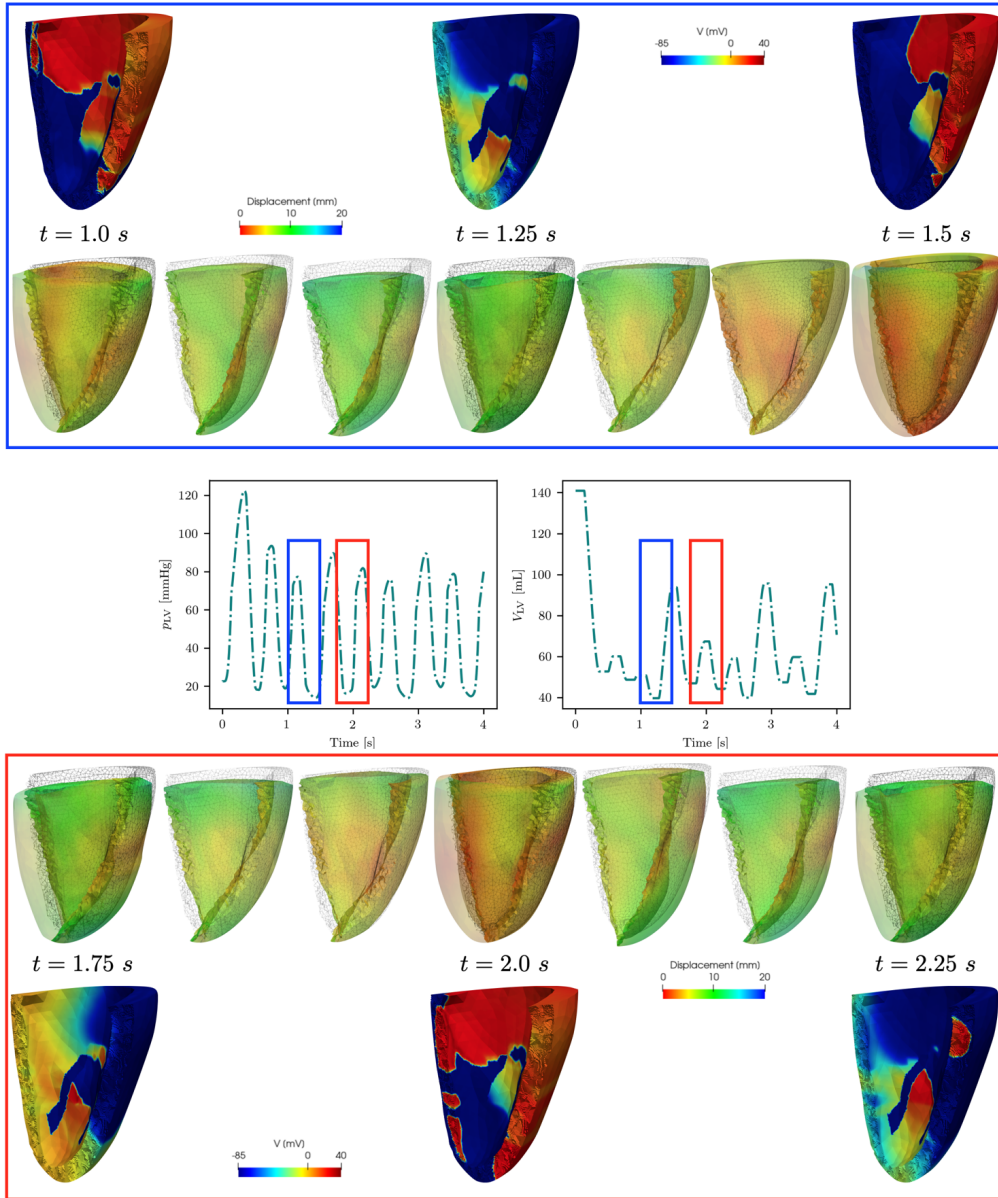
Figure 4.29: Coupled effects of electrophysiology, mechanics and hemodynamics for the numerical simulation with $(\mathscr{E}_{\text{gMEF-full, SAC}})$ model. The extra stimuli in the upper right part of the LV, which is driven by SACs, activate the LV electrophysiologically and mechanically. This has a direct impact on both pressure and volume transients, which in turn have an effect on the electromechanical behavior of the LV.

nate among the four different phases of the PV loop as in prior formulations of electromechanical models [32, 61, 111].

For SR simulations, we observe major differences in the hemodynamics of an LV with ICM with respect to a reference healthy case. Specifically, when incorporating the pathological remodeling, we notice an increase in EDV and EDP, and a significant reduction in SV/EF and contractility. Regarding the electromechanical simulations under arrhythmia, we notice that geometry-mediated MEFs alter the morphology of the VT, along with the overall CV, which decreases with respect to the electrophysiological simulations. Indeed, the wave propagation is partially influenced by the displacement of the myocardium while running electromechanical simulations. This is due to the presence of the ventricular deformation inside the formulation of the monodomain equation.

The ØD circulation model allows to compute the evolution over time of LV pressure and volume, LA pressure and volume, arterial system pressure, MV and AV flow rates. With this information, we could classify a VT as either hemodynamically stable or unstable: the former would let the LV stabilize on a PV loop that does not compromise its function, while the latter entails an unstable behavior of the arterial pressure over time, small variations of the blood pool volume of the LV over time, valves flow rates that are not synchronized [206]. We conclude that this specific VT is unstable. Having the ability to non-invasively assess a hemodynamically unstable VT is very useful from the clinical perspective. Indeed, our electromechanical model allows a thorough understanding of this VT using numerical simulations, whereas investigating this intraprocedurally could be difficult, since the patient might not support hemodynamically unstable VT.

For this specific patient, very different parametrizations of the ØD closed-loop circulation model did not change the hemodynamic nature of the VT, which remained unstable. This may suggest that the hemodynamic nature of the VT is linked to the electromechanical substrate. Furthermore, this may have strong clinical implications, in particular when the parameters of the cardiovascular system of the patient are either not known or very uncertain. This type of electromechanical simulations can be employed for precision medicine and to gain a deeper understanding of VT mechanisms thanks to detailed electric, mechanical and hemodynamic descriptions.

Finally, in Sec. 4.2 we investigate how several types of geometry-mediated MEFs and different parametrizations for nonselective SACs affect the electric and hemodynamic stability of VT [163]. In particular, we focus on the sustainment and the morphology of VT macro-reentrant circuits and blood supply, which is analyzed by means of PV loops. Differently from previous studies [36, 85, 179], we keep into account tissue heterogeneity by introducing an idealized distribution of scars, grey zones and non-remodelled regions over the myocardium. We also consider a more sophisticated mathematical model that embraces electrophysiology, activation, mechanics and cardiovascular fluid dynamics to analyze these mechano-electric couplings.

We notice that if a VT is triggered by following a certain stimulation protocol and by neglecting all MEFs, the very same pacing protocol induces a VT for all possible combinations of MEFs, while keeping the same parameters for the electromechanical model coupled with closed-loop circulation in all cases. Nevertheless, even if this behavior was also observed in the second patient-specific LV with ICM (Sec. 4.1.2), we still cannot conclude that it is completely general.

We do not observe a significant impact of geometry-mediated MEFs on the induction and sustainment of the VT. Most of the modeling choices for geometry-mediated MEFs, namely $(\mathscr{E})$, $(\mathscr{E}_{\text{gMEF-enhanced}})$ and $(\mathscr{E}_{\text{gMEF-full}})$, present very similar VT BCLs and conduction velocities, while showing a few differences in the depolarization wave [36]. On the other hand, $(\mathscr{E}_{\text{gMEF-minimal}})$ manifests major differences in the VT BCL, which increases, and its exit site with respect to $(\mathscr{E})$, $(\mathscr{E}_{\text{gMEF-enhanced}})$ and $(\mathscr{E}_{\text{gMEF-full}})$, as shown in [162] for a patient-specific unstable VT. This can be justified by the simplifications introduced in $(\mathscr{E}_{\text{gMEF-minimal}})$, while moving towards $(\mathscr{E}_{\text{gMEF-full}})$ we almost totally recover the behavior observed in $(\mathscr{E})$. Therefore, the minimal MEFs modeling choice might lead to biased results which are in favor of less severe VT.

We observe that nonselective SACs may affect the hemodynamic nature of the VT, as they may induce EADs or DADs, which lead to ectopic foci that reactivate the LV [73]. These extra stimuli are generally located in the regions of the myocardium in which there is a transition between scar and border zone or between border zone and non-remodeled areas, where high stretches are likely to be present [82]. According to the specific combination of $G_s$ and $V_{\text{rev}}$, nonselective SACs affects both APD and AP resting values [184]. Indeed, it is known that nonselective SACs may determine wavebreaks, irregular rhythms or possibly the onset of fibrillation [36, 85]. We remark that such spontaneous arrhythmias triggered by myocardial stretches cannot be assessed in electrophysiological simulations, where the mechanical behavior is neglected.

To conclude, we also investigate the combined effects of geometry-mediated MEFs and nonselective SACs. Significant differences between $(\mathscr{E}_{\text{gMEF, full, SAC}})$ and $(\mathscr{E}_{\text{SAC}})$ are observed when geometry-mediated MEFs are combined with a parametrization of SACs that entails extra stimuli. Specifically, the VT BCL with $(\mathscr{E}_{\text{gMEF, full, SAC}})$ is lower than the one of $(\mathscr{E}_{\text{SAC}})$ because the extra stimuli driven by SACs is triggered more often in the former case. This completely changes the PV dynamics of the VT, whose stability is however still not affected by the geometry-mediated MEFs.

# A MACHINE LEARNING METHOD FOR REAL-TIME ELECTROMECHANICAL SIMULATIONS

In this chapter, we propose a Machine Learning method to build a ROM of cardiac electromechanical models. We rely on the ANN-based method proposed in [141], which can learn a time-dependent differential equation from a collection of input-output pairs. After presenting the application of our technique to the electromechanical function, we show and discuss some numerical results in the context of global sensitivity analysis and Bayesian parameter estimation.

## 5.1 METHODS

Thanks to its non-intrusive nature, this Machine Learning method can be applied to virtually any cardiac electromechanical model. Therefore, at this stage, we introduce our method in an abstract formulation for cardiac electromechanics.

### 5.1.1 *The full-order model*

Let us consider a generic model of cardiac electromechanics, that is a set of differential equations describing physical processes involved in the heart function. We introduce the state vector $\mathbf{y}(t)$, collecting the state variables associated with this multiphysics system. These may include the transmembrane potential, gating variables, ionic concentrations, protein states, tissue displacement, or simply phenomenological variables. In this thesis, we focus on the single-chamber case of the human heart (e.g. the LV), as the generalization to multiple chambers is straightforward. By introducing a nonlinear differential operator $\mathcal{L}$ that collectively encodes the differential equations and boundary conditions associated with the electromechanical model, the latter reads:

$$\begin{cases} \dfrac{\partial \mathbf{y}(t)}{\partial t} = \mathcal{L}(\mathbf{y}(t), p_{LV}(t), t; \mathbf{p}_{\mathcal{M}}) & \text{for } t \in (0, T], \\ \mathbf{y}(0) = \mathbf{y}_0, \end{cases} \tag{5.1}$$

where $p_{LV}(t)$ denotes the LV endocardial pressure (here seen as an input), $\mathbf{p}_{\mathcal{M}}$ are the model parameters (possibly including, e.g., electrical conductivities, cell membrane conductances, protein binding affinities, contractility, passive tissue properties) and $\mathbf{y}_0$ is the initial state. We denote by $\mathscr{P}_{\mathcal{M}} \subseteq \mathbb{R}^{N_{\mathcal{M}}}$ the space of parameters such that $\mathbf{p}_{\mathcal{M}} \in \mathscr{P}_{\mathcal{M}}$, being $N_{\mathcal{M}}$ the number of parameters. We notice that the right-hand side of (5.1) depends on $t$, as heartbeats are paced by externally applied stimuli, that we assume to have a period of duration $T_{HB}$, which is fixed a priori.

The 3D cardiac electromechanical model (5.1), henceforth denoted by $\mathcal{M}_{3D}$, must be coupled with a closure relationship assigning the pressure $p_{LV}(t)$. One possible option is to couple the $\mathcal{M}_{3D}$ model with a $\emptyset$D model for the external circulation (see e.g. [10, 76, 147]), thus obtaining a system in the form of:

$$
\begin{cases}
\dfrac{\partial \mathbf{y}(t)}{\partial t} = \mathcal{L}(\mathbf{y}(t), p_{LV}(t), t; \mathbf{p}_{\mathcal{M}}) & \text{for } t \in (0, T], \\
\dfrac{d\mathbf{c}(t)}{dt} = \mathbf{f}(\mathbf{c}(t), p_{LV}(t), t; \mathbf{p}_{\mathcal{C}}) & \text{for } t \in (0, T], \\
V_{LV}^{\mathcal{C}}(\mathbf{c}(t)) = V_{LV}^{3D}(\mathbf{y}(t)) & \text{for } t \in (0, T], \\
\mathbf{y}(0) = \mathbf{y}_0, \\
\mathbf{c}(0) = \mathbf{c}_0.
\end{cases}
\tag{5.2}
$$

where $\mathbf{c}(t)$ are the state variables of the circulation model (pressures, volumes and fluxes in the circulatory network) and $\mathbf{p}_{\mathcal{C}} \in \mathscr{P}_{\mathcal{C}} \subseteq \mathbb{R}^{N_{\mathcal{C}}}$ is a vector of $N_{\mathcal{C}}$ parameters (e.g. vascular resistances and conductances). The two models are coupled through the geometric consistency relationship $V_{LV}^{3D}(\mathbf{y}(t)) = V_{LV}^{\mathcal{C}}(\mathbf{c}(t))$, where the left-hand and right-hand sides represent the LV volume predicted by the $\mathcal{M}_{3D}$ and by the $\mathcal{C}$ models, respectively. The LV pressure $p_{LV}$ is determined as a Lagrange multiplier that enforces the consistency relationship. An alternative approach is to adopt different closure relationships in the different phases of the heartbeat [61, 95] with suitable preload and afterload models, such as windkessel models [197]. These relationships link the changes in LV pressure $p_{LV}$ with its volume, obtained as $V_{LV} = V_{LV}^{3D}(\mathbf{y})$. In both cases, should the $\mathcal{M}_{3D}$ be coupled to a closed-loop circulation model or to an afterload-preload relationship, we denote by $\mathcal{M}_{3D}$-$\mathcal{C}$ the resulting coupled model. In Fig. 5.1 we show an $\mathcal{M}_{3D}$-$\mathcal{C}$ model in which $\mathcal{C}$ consists of a the lumped-parameter closed-loop model of [147], which is employed to produce the numerical results.

We remark that the closure relationships never directly involve the state $\mathbf{y}$ of the model $\mathcal{M}_{3D}$, but only the LV volume $V_{LV} = V_{LV}^{3D}(\mathbf{y})$. This is a key observation since it suggests that a ROM that is able to surrogate the relationship between $p_{LV}$ and $V_{LV}$, albeit agnostic of the state $\mathbf{y}$, can replace the $\mathcal{M}_{3D}$ model in its coupling to the $\mathcal{C}$ model. In what follows, we present our strategy to build an ANN-based ROM of the $\mathcal{M}_{3D}$ model, denoted by $\mathcal{M}_{ANN}$, that can be coupled with the $\mathcal{C}$ model resulting in the $\mathcal{M}_{ANN}$-$\mathcal{C}$ coupled model, that will surrogate the $\mathcal{M}_{3D}$-$\mathcal{C}$ model.

### 5.1.2 *The reduced-order model*

To setup a ROM surrogating the $\mathcal{M}_{3D}$ model of Eq. (5.1), we employ the Machine Learning method proposed in [141]. This method is designed to learn a differential equation from time-dependent input-output pairs, by training an
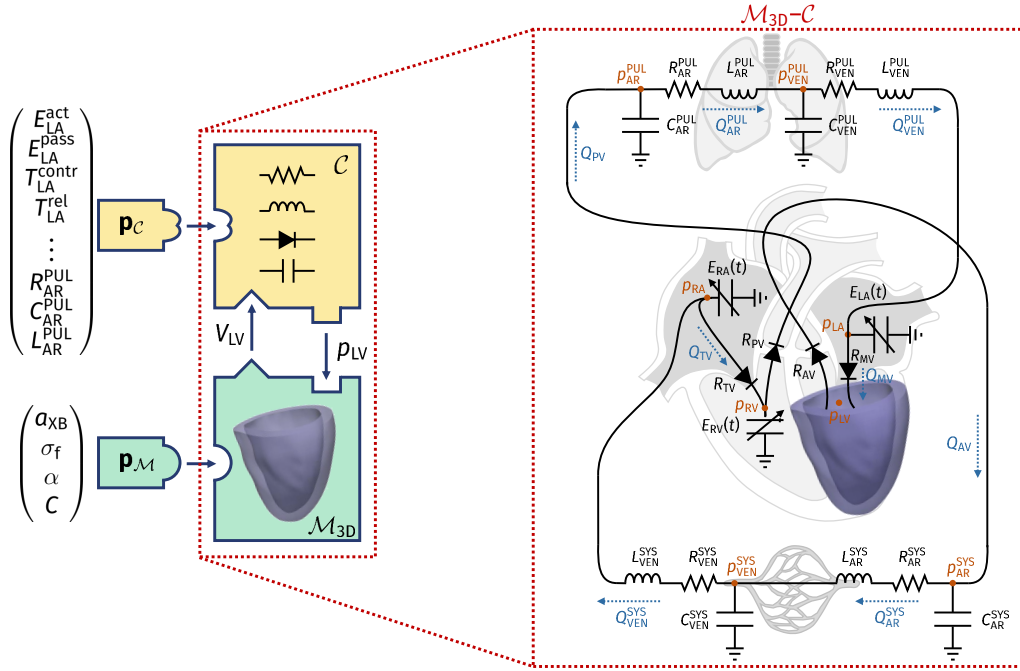
Figure 5.1: The $\mathcal{M}_{3D}$-$\mathcal{C}$ model. From left to right: The parameters $\mathbf{p}_{\mathcal{C}}$ and $\mathbf{p}_{\mathcal{M}}$ are associated with the $\mathcal{C}$ and $\mathcal{M}_{3D}$ respectively. The two models are coupled via the variables $p_{LV}$ and $V_{LV}$. Their union constitutes the model $\mathcal{M}_{3D}$-$\mathcal{C}$. The model $\mathcal{M}_{3D}$-$\mathcal{C}$ considered to produce the numerical results of this thesis is shown on the right. For more details on the $\mathcal{M}_{3D}$-$\mathcal{C}$ model and for the definition of the parameters $\mathbf{p}_{\mathcal{C}}$ and $\mathbf{p}_{\mathcal{M}}$, see Sec. 5.1.6.

ODE model, whose right-hand side is represented by an ANN. We define our ANN-based ROM $\mathcal{M}_{ANN}$ as:

$$\begin{cases} \dfrac{d\mathbf{z}(t)}{dt} = \mathcal{NN}\left(\mathbf{z}(t), p_{LV}(t), \cos(\tfrac{2\pi t}{T_{HB}}), \sin(\tfrac{2\pi t}{T_{HB}}), \mathbf{p}_{\mathcal{M}}; \widehat{\mathbf{w}}\right) & \text{for } t \in (0, T], \\ \mathbf{z}(0) = \mathbf{z}_0, \end{cases} \tag{5.3}$$

where $\mathbf{z}(t) \in \mathbb{R}^{N_z}$ is the reduced state and $\mathcal{NN} \colon \mathbb{R}^{N_z + N_{\mathcal{M}} + 3} \to \mathbb{R}^{N_z}$ is a fully connected ANN. The ANN input consists indeed of $N_z$ state variables, $N_{\mathcal{M}}$ scalar parameters, the pressure $p_{LV}$, and the two periodic inputs $\cos(2\pi t/T_{HB})$ and $\sin(2\pi t/T_{HB})$ (whose role will be clarified later), for a total of $N_z + N_{\mathcal{M}} + 3$ input neurons. The vector $\widehat{\mathbf{w}} \in \mathbb{R}^{N_w}$ encodes the weights and biases of the ANN, that need to be suitably trained. We remark that, among the arguments of the ANN, we have not introduced the time variable $t$, but rather $\cos(2\pi t/T_{HB})$ and $\sin(2\pi t/T_{HB})$, that are the coordinates of a point cyclically moving along a circumference with period $T_{HB}$. In this way, the ROM encodes by construction the periodicity associated with the heartbeat pacing. This expedient allows for the use of the ROM also for time spans longer than those shown during the training phase. Moreover, by introducing the parametric dependence (i.e. on $\mathbf{p}_{\mathcal{M}}$) within the ANN, the latter is not specific to a particular parameter setting.

In this work, according to [141], we adopt an output-inside-the-state approach, that is we train the model so that the LV volume coincides with the first state variable. More precisely, the LV volume predicted by the $\mathcal{M}_{ANN}$ model is by

definition $V_{LV}^{ANN}(\mathbf{z}(t)) := \mathbf{z}(t) \cdot \mathbf{e}_1$, where $\mathbf{e}_1$ is the first element of the canonical basis of $\mathbb{R}^{N_z}$. Therefore, the first ROM state variable has a clear physical interpretation (i.e. it coincides with the LV volume), while the other ROM states are latent variables with no immediate physical interpretation, providing however a compact representation of the full-order state $\mathbf{y}(t)$. Coherently with this choice, we define the initial state as $\mathbf{z}_0 = (V_{LV}^{3D}(\mathbf{y}_0), \mathbf{o})^\top$. The remaining initial states are set, without loss of generality, to zero (this choice does not reduce the space of candidate models, as proved in [141]).

Here we need to determine the optimal value of the weights $\widehat{\mathbf{w}}$, such that the $\mathcal{M}_{ANN}$ model reproduces the outputs of the $\mathcal{M}_{3D}$ model as accurately as possible. With this goal, we generate a training set, by sampling the parameter space $\mathscr{P}_{\mathcal{M}} \times \mathscr{P}_{\mathcal{C}}$ with $N_{train}$ sample points. For each sample, we perform a simulation with the $\mathcal{M}_{3D}$-$\mathcal{C}$ model until time $T_{train}$, and we record the LV pressure and volume transients. The training set is thus given by:

$$\mathbf{p}_{\mathcal{C}}^i, \mathbf{p}_{\mathcal{M}}^i, p_{LV}^i(t), V_{LV}^i(t) \qquad t \in [0, T_{train}], \qquad \text{for } i = 1, \dots, N_{train}.$$

We remark that, due to the non-intrusive nature of our method, there is no need to retain the FOM states $\mathbf{y}(t)$. Finally, we train the ANN weights $\widehat{\mathbf{w}}$ by minimizing the discrepancy between the training data and the model outputs, that is by considering the following constrained optimization problem:

$$\begin{cases} \widehat{\mathbf{w}} = \underset{\mathbf{w} \in \mathbb{R}^{N_w}}{\text{argmin}} \left[ \sum_{i=1}^{N_{train}} \int_0^{T_{train}} |V_{LV}^i(t) - V_{LV}^{ANN}(\mathbf{z}^i(t))|^2 \, dt + \beta |\mathbf{w}|^2 \right] \\ \text{such that, for each } i = 1, \dots, N_{train}: \\ \quad \dfrac{d\mathbf{z}^i(t)}{dt} = \mathcal{NN}\left( \mathbf{z}^i(t), p_{LV}^i(t), \cos(\tfrac{2\pi t}{T_{HB}}), \sin(\tfrac{2\pi t}{T_{HB}}); \mathbf{p}_{\mathcal{M}}^i; \mathbf{w} \right) \quad \text{for } t \in (0, T_{train}], \\ \quad \mathbf{z}^i(0) = \mathbf{z}_0, \end{cases}$$

$$(5.4)$$

where $\beta > 0$ is a regularization hyperparameter. We remark that the optimization problem (5.4) is not a standard Machine Learning problem of data fitting. Indeed, the ANN appears at the right-hand side of a differential equation that acts as a constraint under which the loss function is minimized. To train this model, we use the algorithm proposed in [141], which envisages approximating the differential equation by the Forward Euler method, the loss function by the trapezoidal method, and then computing the gradients by solving the adjoint equations. The parameters are then optimized by means of the Levenberg-Marquardt method [112]. The training process is summarized in Fig. 5.2.

Once the ANN has been trained (that is, the optimal weights $\widehat{\mathbf{w}}$ have been determined), the $\mathcal{M}_{ANN}$ model can be used as a surrogate of the $\mathcal{M}_{3D}$ model, also for different combinations of the parameters than those contained in the training set. Moreover, it can be coupled with the closure relationships $\mathcal{C}$, thus
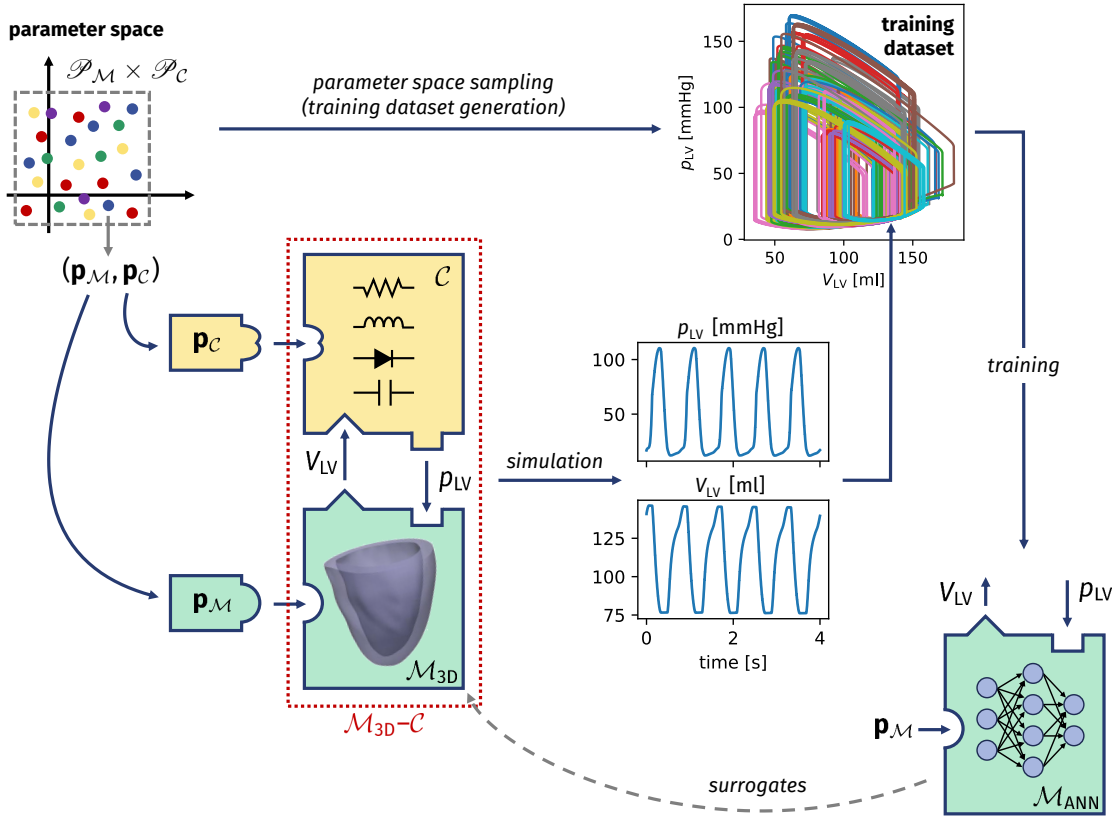
Figure 5.2: Training algorithm of the $\mathcal{M}_{\text{ANN}}$ model. We sample the parameter space $\mathscr{P}_{\mathcal{M}} \times \mathscr{P}_{\mathcal{C}}$ (top left) and, for each parameter instance $(\mathbf{p}_{\mathcal{M}}, \mathbf{p}_{\mathcal{C}})$, we simulate some heartbeats through the $\mathcal{M}_{\text{3D}}$-$\mathcal{C}$ model (center). Finally, from the training set obtained by collecting the resulting pressure and volume transients (top right), we train the ANN-based model $\mathcal{M}_{\text{ANN}}$ (bottom right), according to Eq. (5.4).

obtaining the $\mathcal{M}_{\text{ANN}}$-$\mathcal{C}$ model. For example, by considering the case of a closed-loop circulation model, as in (5.2), its reduced counterpart $\mathcal{M}_{\text{ANN}}$-$\mathcal{C}$ reads:

$$
\begin{cases}
\dfrac{d\mathbf{z}(t)}{dt} = \mathcal{NN}\left(\mathbf{z}(t), p_{\text{LV}}(t), \cos(\tfrac{2\pi t}{T_{\text{HB}}}), \sin(\tfrac{2\pi t}{T_{\text{HB}}}); \mathbf{p}_{\mathcal{M}}; \widehat{\mathbf{w}}\right) & \text{for } t \in (0, T], \\[2mm]
\dfrac{d\mathbf{c}(t)}{dt} = \mathbf{f}(\mathbf{c}(t), p_{\text{LV}}(t), t; \mathbf{p}_{\mathcal{C}}) & \text{for } t \in (0, T], \\[2mm]
V_{\text{LV}}^{\mathcal{C}}(\mathbf{c}(t)) = V_{\text{LV}}^{\text{ANN}}(\mathbf{z}(t)) & \text{for } t \in (0, T], \\[2mm]
\mathbf{z}(0) = \mathbf{z}_0, \\[1mm]
\mathbf{c}(0) = \mathbf{c}_0.
\end{cases}
\tag{5.5}
$$

As matter of fact, the $\mathcal{M}_{\text{3D}}$ model has the same input-output structure of the model being surrogated, that is $\mathcal{M}_{\text{ANN}}$. Hence, the latter can be employed in replacement of the former in approximating the outputs associated with a given set of parameters $(\mathbf{p}_{\mathcal{M}}, \mathbf{p}_{\mathcal{C}})$, as shown in Fig. 5.3.
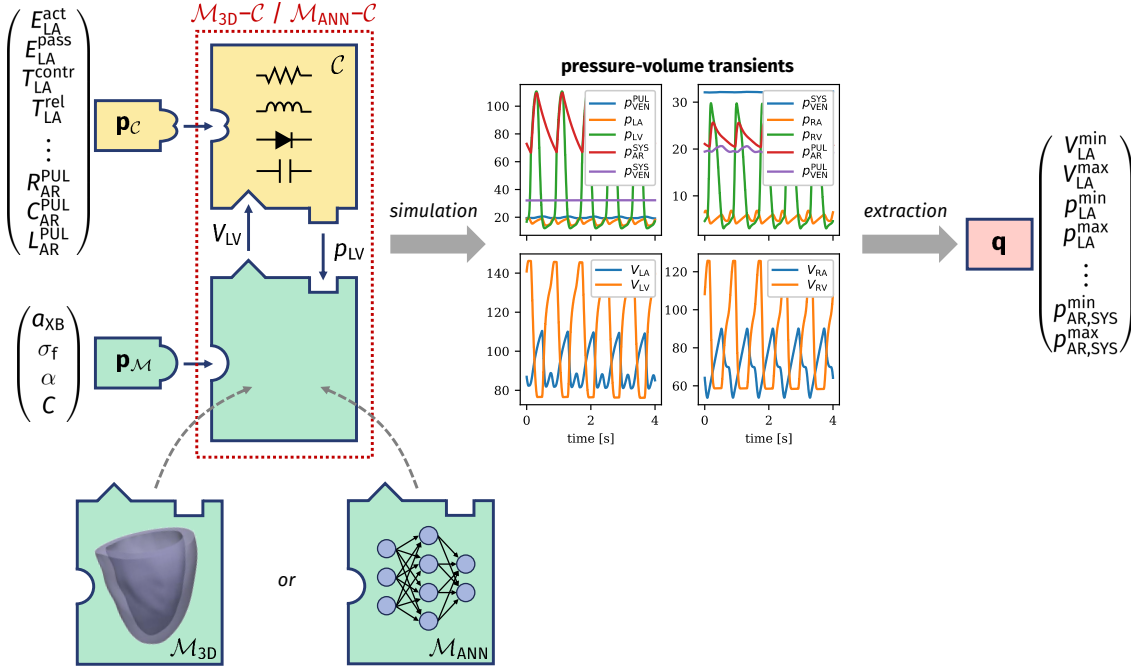
Figure 5.3: Parameters-to-QoIs computation using either the $\mathcal{M}_{3D}$ or the $\mathcal{M}_{ANN}$ model. Given a parameter instance $(\mathbf{p}_{\mathcal{M}}, \mathbf{p}_{\mathcal{C}})$, either the $\mathcal{M}_{3D}$ or the $\mathcal{M}_{ANN}$ model can be coupled with the $\mathcal{C}$ model to obtain pressure and volume transients, from which a set of QoIs are extracted. See Tabs. 5.1, 5.2 and 5.3 for the definition of $\mathbf{p}_{\mathcal{M}}$, $\mathbf{p}_{\mathcal{C}}$ and $\mathbf{q}$, respectively.

### 5.1.3 Hyperparameters tuning

Like any Machine Learning method, there is a dependence on a set of hyperparameters, that is variables that are not trained (they are not part of the vector $\widehat{\mathbf{w}}$), but are used to control the training process. These include ANN architecture hyperparameters (namely the number of layers $N_{layers}$ and the number of neurons per layer $N_{neurons}$), the regularization factor $\beta$ and the number of reduced states $N_z$. To tune the hyperparameters, we rely on a $k$-fold cross-validation procedure. Specifically, after splitting the training set into $k = 5$ non-overlapping subsets, we cyclically train the model by excluding one subset that is used as validation set. Finally, we evaluate the average validation errors and we select the hyperparameters setting that attains the lowest validation error and better generalization properties (see Appendix B.4 for more details).

### 5.1.4 Global sensitivity analysis

To assess how much each parameter contributes to the determination of a QoI, e.g. a biomarker of clinical interest, we perform a variance-based global sensitivity analysis, which relies on a probabilistic approach. The sensitivity of a QoI (say $\mathbf{q}_j$) with respect to a parameter (say $\mathbf{p}_i$) can be quantified through Sobol indices [172]. Specifically, the so-called first-order Sobol index (denoted by $S_{ij}$)

indicates the impact on the j-th QoI (i.e. $\mathbf{q}_j$) of the i-th parameter (i.e. $\mathbf{p}_i$) when the latter varies alone, according to the definition:

$$S_{ij} = \frac{\mathbb{V}\mathrm{ar}_{\mathbf{p}_i}\left[\mathbb{E}_{\mathbf{p}_{\sim i}}\left[\mathbf{q}_j|\mathbf{p}_i\right]\right]}{\mathbb{V}\mathrm{ar}\left[\mathbf{q}_j\right]},$$

where $\mathbf{p}_{\sim i}$ indicates the set of all parameters excluding the i-th one. The first-order Sobol index $S_{ij}$, however, only accounts for the variations of the parameter $\mathbf{p}_i$ alone, averaged over variations in the other parameters, and thus does not account for the interactions among parameters. Conversely, it is possible to assess the importance of a parameter in determining a QoI, also accounting for the interactions among parameters, by resorting to the so-called total-effect Sobol index $S_{ij}^{\mathsf{T}}$, defined as:

$$S_{ij}^{\mathsf{T}} = \frac{\mathbb{E}_{\mathbf{p}_{\sim i}}\left[\mathbb{V}\mathrm{ar}_{\mathbf{p}_i}\left[\mathbf{q}_j|\mathbf{p}_{\sim i}\right]\right]}{\mathbb{V}\mathrm{ar}\left[\mathbf{q}_j\right]} = 1 - \frac{\mathbb{V}\mathrm{ar}_{\mathbf{p}_{\sim i}}\left[\mathbb{E}_{\mathbf{p}_i}\left[\mathbf{q}_j|\mathbf{p}_{\sim i}\right]\right]}{\mathbb{V}\mathrm{ar}\left[\mathbf{q}_j\right]}.$$

The latter index quantifies the impact of a given parameter when it varies alone or together with other parameters.

To compute an estimate of the Sobol indices, we use the Saltelli method [78, 160], that makes use of Sobol quasi-random sequences to approximate the integrals that need to be computed. In practice, this method requires evaluating the model for a large number of parameters, and then processing the obtained QoIs to provide an estimate of the Sobol indices.

In this thesis we perform a variance-based global sensitivity analysis simultaneously with respect to the circulation model parameters $\mathbf{p}_{\mathcal{C}}$ and the electromechanical model parameters $\mathbf{p}_{\mathcal{C}}$ (that is, we set $\mathbf{p} = (\mathbf{p}_{\mathcal{M}}, \mathbf{p}_{\mathcal{C}})$). To this end, we use model $\mathcal{M}_{\mathrm{ANN}}\text{-}\mathcal{C}$ as a surrogate for model $\mathcal{M}_{\mathrm{3D}}\text{-}\mathcal{C}$ to perform the evaluations required by the Saltelli method. As we will see in Sec. 5.2, using $\mathcal{M}_{\mathrm{ANN}}\text{-}\mathcal{C}$ instead of $\mathcal{M}_{\mathrm{3D}}\text{-}\mathcal{C}$ entails a huge computational gain. In addition, for each parameter setting we simulate a certain number of heartbeats to achieve a limit cycle (i.e. a periodic solution), and we calculate QoIs with respect to the last cycle, which is the most significant one, as it removes the effects of incorrect initializations of the state variables. We remark that the need to simulate a certain number of heartbeats to overpass the transient phase (that typically lasts from 5 to 15 cycles, see Appendix B.2) makes the use of a reduced cardiac electromechanical model even more necessary.

### 5.1.5 *Parameter estimation under uncertainty*

The patient-specific personalization of a cardiac electromechanical model requires, besides the usage of a geometry derived from imaging data, the estimation of the parameters associated with the mathematical model (or at least the most important ones), starting from clinical measurements. Very often, only a few scalar quantities are available for this purpose; moreover, the resolution of this inverse problem (i.e. estimating $\mathbf{p}$ from $\mathbf{q}$) should account for the noise

that unavoidably affects the measurement of $\mathbf{q}$ and that reflects in uncertainty on $\mathbf{p}$.

Bayesian estimation is a technique that permits to address these issues within a rigorous statistical framework, by providing the likelihood, expressed as a probability distribution, of the parameters values, given the observed QoIs (denoted by $\mathbf{q}_{\text{obs}}$). The likelihood computation accounts for the uncertainty on measurements (associated with measurement noise and encoded in the noise covariance matrix $\mathbf{\Sigma}$), as well as a prior distribution on parameters (denoted by $\pi_{\text{prior}}(\mathbf{p})$), that is previous knowledge or belief about the parameters. By denoting the parameters-to-QoIs map by $\mathcal{F}\colon \mathbf{p} \mapsto \mathbf{q}$, we have $\mathbf{q}_{\text{obs}} = \mathcal{F}(\mathbf{p}) + \boldsymbol{\epsilon}$, where $\boldsymbol{\epsilon} \sim \mathcal{N}(\cdot|\mathbf{o}, \mathbf{\Sigma})$ denotes the measurement error (that we assume for simplicity to be distributed as a Gaussian random variable). Bayes' theorem states that the posterior distribution of parameters, that is the degree of belief of their value after having observed $\mathbf{q}_{\text{obs}}$, is given by:

$$\pi_{\text{post}}(\mathbf{p}) = \frac{1}{Z}\, \mathcal{N}(\mathbf{q}_{\text{obs}}|\mathcal{F}(\mathbf{p}), \mathbf{\Sigma})\, \pi_{\text{prior}}(\mathbf{p}),$$

where the normalization constant $Z$ is defined as

$$Z = \int_{\mathscr{P}} \mathcal{N}(\mathbf{q}_{\text{obs}}|\mathcal{F}(\widehat{\mathbf{p}}), \mathbf{\Sigma})\, \mathrm{d}\pi_{\text{prior}}(\widehat{\mathbf{p}}).$$

In practice, the computation of $\pi_{\text{post}}$ may be challenging from the computational viewpoint, because of the need to approximate the integral that defines $Z$. The MCMC method permits to approximate the distribution $\pi_{\text{post}}$ with a relatively small computational effort. Similarly to the Saltelli method that we use for sensitivity analysis, also the MCMC method requires a large number of model evaluations, for different parameter values. Moreover, this method is non-intrusive, that is it only requires evaluations of the map $\mathcal{F}\colon \mathbf{p} \mapsto \mathbf{q}$. Therefore, we can employ for this purpose the $\mathcal{M}_{\text{ANN}}\text{-}\mathcal{C}$ model as a surrogate for the $\mathcal{M}_{\text{3D}}\text{-}\mathcal{C}$ model, which drastically reduces the necessary computational time.

Moreover, we remark that the Bayesian framework permits to rigorously account for the approximation error introduced by replacing the high fidelity model $\mathcal{M}_{\text{3D}}\text{-}\mathcal{C}$ by its surrogate $\mathcal{M}_{\text{ANN}}\text{-}\mathcal{C}$. Indeed, if we denote by $\widetilde{\mathcal{F}}$ the approximated parameters-to-QoIs map represented by the surrogate model $\mathcal{M}_{\text{ANN}}\text{-}\mathcal{C}$, we have $\mathcal{F}(\mathbf{p}) = \widetilde{\mathcal{F}}(\mathbf{p}) + \boldsymbol{\epsilon}_{\text{ROM}}$, where $\boldsymbol{\epsilon}_{\text{ROM}}$ is the ROM approximation error. It follows $\mathbf{q}_{\text{obs}} = \widetilde{\mathcal{F}}(\mathbf{p}) + \boldsymbol{\epsilon}_{\text{ROM}} + \boldsymbol{\epsilon}_{\text{exp}}$, where $\boldsymbol{\epsilon}_{\text{exp}}$ is the experimental measurement error. Since the two sources of error can be assumed independent, the covariance of the total error $\boldsymbol{\epsilon} = \boldsymbol{\epsilon}_{\text{ROM}} + \boldsymbol{\epsilon}_{\text{exp}}$ satisfies $\mathbf{\Sigma} = \mathbf{\Sigma}_{\text{ROM}} + \mathbf{\Sigma}_{\text{exp}}$, where $\mathbf{\Sigma}_{\text{ROM}}$ is the ROM approximation error covariance (which can be estimated by evaluating the ROM on a testing set) and $\mathbf{\Sigma}_{\text{exp}}$ is the experimental error covariance (that depends on the measurement protocol at hand). This permits to take into account in the estimation process the error introduced by the surrogate model.

To assess the capability of our ROM to accelerate the estimation of parameters for multiscale electromechanical models, we perform the following test. We perform a simulation with the $\mathcal{M}_{\text{3D}}\text{-}\mathcal{C}$ model, from which we derive a set of QoIs ($\mathbf{q}_{\text{obs}}$). Then, by employing the $\mathcal{M}_{\text{ANN}}\text{-}\mathcal{C}$ model as a surrogate of the $\mathcal{M}_{\text{3D}}\text{-}\mathcal{C}$

| Parameter | Baseline | Unit | Description |
|---|---|---|---|
| $a_{XB}$ | 160.0 | MPa | Cardiomyocytes contractility |
| $\sigma_f$ | 76.43 | $mm\,s^{-1}$ | Electrical conductivity along fibers |
| $\alpha$ | 60.0 | degrees | Fibers angle rotation |
| C | 0.88 | kPa | Passive stiffness |

Table 5.1: Parameters $\mathbf{p}_{\mathcal{M}}$ of the $\mathcal{M}_{3D}$ model considered in this thesis and associated baseline values.

model, we obtain a Bayesian estimate of the parameters, that we validate against the values used to generate $\mathbf{q}_{obs}$.

### 5.1.6 *The cardiac electromechanical model*

As mentioned above, due to its non-intrusive nature, our method is not limited to a specific electromechanical model, but can be applied to virtually any electromechanical model as long as pressure and volume transients are available for the training procedure. Nevertheless, to produce the numerical results of this thesis, we apply it to the electromechanical model that is presented in Chap. 2.

Specifically, we consider an LV geometry processed from the Zygote 3D heart model [80] endowed with a fiber architecture generated by means of the Bayer-Blake-Plank-Trayanova algorithm [16, 130]. Before starting the numerical simulations, we recover the reference unstressed configuration through the algorithm is reported in Secs. 2.5 and 2.5.1. To model the AP propagation, we employ the monodomain equation [35], coupled with the TTP06 ionic model [185] (see Sec. 2.1.1). We model the microscale generation of active force through the biophysically detailed RDQ20-MF model [142] (see Sec. 2.1.2), that is coupled, within an active stress approach, with the elastodynamics equations describing tissue mechanics (see Sec. 2.1.3). On the other hand, the passive behavior of the tissue is modeled through a quasi-incompressible exponential constitutive law [187]. We model the interaction with the pericardium by means of spring-damper boundary conditions at the epicardium, while we adopt energy-consistent boundary conditions [143] to model the interaction with the part of the myocardium beyond the artificial ventricular base. To model blood circulation, that is $\mathcal{C}$, we rely on the $\emptyset$D closed-loop model presented in [147] (see Sec. 2.1.4), consisting of a compartmental description of the cardiac chambers, systemic and pulmonary, arterial and venous circulatory networks, based on an electrical analogy. The different compartments are modeled as RLC (resistance, inductance, capacitance) circuits, while cardiac valves are described as diodes.

Among the parameters associated with the $\mathcal{M}_{3D}$ model, in this thesis we focus on the four ones reported in Tab. 5.1. Similarly, we report in Tab. 5.2 the parameters associated with the $\mathcal{C}$ model.

| Parameter | Baseline | Unit | Description |
|---|---|---|---|
| $V_{heart}^{tot}$ | 400.15 | mL | Initial blood pool volume of the heart |
| $E_{LA}^{act}$, $E_{RA}^{act}$, $E_{RV}^{act}$ | 0.07, 0.06, 0.55 | $mmHg\,mL^{-1}$ | LA/RA/RV active elastance |
| $E_{LA}^{pass}$, $E_{RA}^{pass}$, $E_{RA}^{pass}$ | 0.18, 0.07, 0.05 | $mmHg\,mL^{-1}$ | LA/RA/RV passive elastance |
| $T_{LA}^{contr}$, $T_{RA}^{contr}$, $T_{RV}^{contr}$ | 0.14, 0.14, 0.20 | s | LA/RA/RV contraction time |
| $T_{LA}^{rel}$, $T_{RA}^{rel}$, $T_{RV}^{rel}$ | 0.14, 0.14, 0.32 | s | LA/RA/RV relaxation time |
| $V_{0,LA}$, $V_{0,RA}$, $V_{0,RV}$ | 4.0, 4.0, 16.0 | mL | LA/RA/RV reference volume |
| $t_L^{av}$, $t_R^{av}$ | 0.16, 0.16 | s | Left/right atrioventricular delay |
| $R_{min}$, $R_{max}$ | 0.0075, 75006.2 | $mmHg\,s\,mL^{-1}$ | Valve minimum/maximum resistance |
| $R_{AR}^{SYS}$, $R_{VEN}^{SYS}$ | 0.64, 0.32 | $mmHg\,s\,mL^{-1}$ | Systemic arterial/venous resistance |
| $R_{AR}^{PUL}$, $R_{VEN}^{PUL}$ | 0.032, 0.036 | $mmHg\,s\,mL^{-1}$ | Pulmonary arterial/venous resistance |
| $C_{AR}^{SYS}$, $C_{VEN}^{SYS}$ | 1.2, 60.0 | $mL\,mmHg^{-1}$ | Systemic arterial/venous capacitance |
| $C_{AR}^{PUL}$, $C_{VEN}^{PUL}$ | 10.0, 16.0 | $mL\,mmHg^{-1}$ | Pulmonary arterial/venous capacitance |
| $L_{AR}^{SYS}$, $L_{VEN}^{SYS}$ | 0.005, 0.0005 | $mmHg\,s^2\,mL^{-1}$ | Systemic arterial/venous inductance |
| $L_{AR}^{PUL}$, $L_{VEN}^{PUL}$ | 0.0005, 0.0005 | $mmHg\,s^2\,mL^{-1}$ | Pulmonary arterial/venous inductance |

Table 5.2: Parameters $\mathbf{p}_{\mathcal{C}}$ of the $\mathcal{C}$ model considered in this thesis and associated baseline values.

We report in Tab. 5.3 the list of all the QoIs, computed from the numerical solution of the $\mathcal{M}_{3D}$-$\mathcal{C}$ model, and outputs of interest that are used through this thesis. The last column of the table indicates which variables are used for cross-validation during the training phase (see Sec. 5.1.3), those that are used for sensitivity analysis purposes (see Sec. 5.1.4) and those that are used to run Bayesian parameter estimations (see Sec. 5.1.5).

To numerically approximate this multiphysics and multiscale model, we adopt the SIS2 scheme [148] (see Sec. 2.4). For space discretization, we rely on bilinear Finite Elements defined on hexahedral meshes, adopting a different spatial resolution for the electrophysiological and the mechanical variables. For time discretization, we employ a staggered scheme, where different time steps are used according to the specific subproblem. Moreover, to avoid the numerical oscillations arising from the mechanical feedback on force generation (that are commonly cured by recurring to a monolithic scheme [95, 124]), we use the stabilized-staggered scheme that is proposed in [146]. This numerical model requires, on a 32 cores computer platform, nearly 4 hours of computational time to simulate a heartbeat. More details on the numerical discretization and the computational platform employed to generate the training data used in this thesis are available in Appendix B.1.

### 5.1.7 *Software libraries*

The electromechanical simulations are performed by means of the life$^x$ library, a high-performance C++ platform developed within the iHEART project. To train the ANN-based models, we employ the open source MATLAB library

| Parameter | Unit | Description | Usage |
|---|---|---|---|
| **Left atrium** | | | |
| $V_{LA}^{min}, V_{LA}^{max}$ | mL | End-systolic and end-diastolic volume | GSA |
| $p_{LA}^{min}, p_{LA}^{max}$ | mmHg | Minimum and maximum pressure | GSA |
| **Left ventricle** | | | |
| $V_{LV}(t)$ | mL | Volume transient | X-validation |
| $p_{LV}(t)$ | mmHg | Pressure transient | X-validation |
| $V_{LV}^{min}, V_{LV}^{max}$ | mL | End-systolic and end-diastolic volume | X-validation, GSA |
| $p_{LV}^{min}, p_{LV}^{max}$ | mmHg | Minimum and maximum pressure | X-validation, GSA |
| $SV_{LV}$ | mL | Stroke volume ($V_{LV}^{max} - V_{LV}^{min}$) | X-validation, GSA |
| **Right atrium** | | | |
| $V_{RA}^{min}, V_{RA}^{max}$ | mL | End-systolic and end-diastolic volume | GSA |
| $p_{RA}^{min}, p_{RA}^{max}$ | mmHg | Minimum and maximum pressure | GSA |
| **Right ventricle** | | | |
| $V_{RV}^{min}, V_{RV}^{max}$ | mL | End-systolic and end-diastolic volume | GSA |
| $p_{RV}^{min}, p_{RV}^{max}$ | mmHg | Minimum and maximum pressure | GSA |
| $SV_{RV}$ | mL | Stroke volume ($V_{RV}^{max} - V_{RV}^{min}$) | GSA |
| **Systemic arterial circulation** | | | |
| $p_{AR,SYS}^{min}, p_{AR,SYS}^{max}$ | mmHg | Minimum and maximum pressure | GSA, MCMC |

Table 5.3: List of QoIs used through this thesis, either for cross-validation (X-validation), global sensitivity analysis (GSA) or MCMC based Bayesian parameter estimation (MCMC).

model-learning[1], that implements the Machine Learning method proposed in [141] and used in this thesis. Sensitivity analysis is carried out through the open source Python library SALib[2] [75]. Finally, for the MCMC based Bayesian parameter estimation we rely on the open source Python library UQpy[3] [116]. To employ the ANN-based models trained with the MATLAB library model-learning within the Python environment of SALib and UQpy, we exploit pyModelLearning, a Python wrapper for the model-learning library[4].

## 5.2 NUMERICAL RESULTS

### 5.2.1 *Trained models*

To generate the pressure and volume transients needed to train an ANN-based ROM, we sample the parameter space $\mathscr{P}_{\mathcal{M}} \times \mathscr{P}_{\mathcal{C}}$ with a Monte Carlo approach, even if more sophisticated sampling strategies – such as Latin Hypercube Design – can be considered as well. For simplicity, in this stage we only consider a subset of the parameters $\mathbf{p}_{\mathcal{C}}$, selected as the most significant ones, on the basis of a preliminary variance-based global sensitivity analysis, obtained with a

---

1 https://model-learning.readthedocs.io/
2 https://salib.readthedocs.io/
3 https://uqpyproject.readthedocs.io/
4 https://github.com/FrancescoRegazzoni/model-learning

| Trained model | Parameters $\mathbf{p}_{\mathcal{M}}$ | Training set size $N_{train}$ | Hyperparameters | | | |
|---|---|---|---|---|---|---|
| | | | $N_z$ | $N_{layers}$ | $N_{neurons}$ | $\beta$ |
| $\mathcal{M}_{ANN}^{single}$ | $[a_{XB}]$ | 30 | 2 | 1 | 8 | 0 |
| $\mathcal{M}_{ANN}^{full}$ | $[a_{XB}, \sigma_f, \alpha, C]$ | 40 | 1 | 1 | 12 | 0.01 |

Table 5.4: Optimal sets of hyperparameters for the two trained models $\mathcal{M}_{ANN}^{single}$ and $\mathcal{M}_{ANN}^{full}$.

version of the closed-loop model in which the LV is also represented by a $\emptyset$D circuit element (see Appendix B.3).

We consider two scenarios. We study the variability with respect to a single parameter, namely the active contractility. Thus, we set $\mathbf{p}_{\mathcal{M}} = [a_{XB}]$. Under this setting, we generate 30 simulations through the $\mathcal{M}_{3D}$-$\mathcal{C}$ model to train a ROM, henceforth denoted by $\mathcal{M}_{ANN}^{single}$. For this ROM, the remaining parameters (i.e. $\sigma_f$, $\alpha$ and $C$) are kept constant (more precisely, equal to the baseline values of Tab. 5.1). Then, we consider the full parametric variability (that is, we set $\mathbf{p}_{\mathcal{M}} = [a_{XB}, \sigma_f, \alpha, C]$), we generate 40 training samples and we train a second ROM, denoted by $\mathcal{M}_{ANN}^{full}$. All the simulations included in the training set are 5 heartbeats long. The optimal sets of hyperparameters, tuned through the algorithm of Sec. 5.1.3, are reported in Tab. 5.4. In both the considered cases, training an ANN-based model takes approximately 18 hours on a single core standard laptop.

Once trained, the two ROMs ($\mathcal{M}_{ANN}^{single}$ and $\mathcal{M}_{ANN}^{full}$) can be coupled with the circulation model $\mathcal{C}$, thus obtaining the models $\mathcal{M}_{ANN}^{single}$-$\mathcal{C}$ and $\mathcal{M}_{ANN}^{full}$-$\mathcal{C}$, according to Eq. (5.5). These two models represent two surrogates of the $\mathcal{M}_{3D}$-$\mathcal{C}$ model, capable of approximating its output at a dramatically reduced computational cost. As a matter of fact, numerical simulations with either the $\mathcal{M}_{ANN}^{single}$ or the $\mathcal{M}_{ANN}^{full}$ model take nearly one second of computational time per heartbeat on a single core standard laptop.

To test the accuracy of the $\mathcal{M}_{ANN}^{single}$-$\mathcal{C}$ and $\mathcal{M}_{ANN}^{full}$-$\mathcal{C}$ models with respect to the $\mathcal{M}_{3D}$-$\mathcal{C}$ model, we consider a testing dataset, by taking unobserved samples in the parameter space $\mathscr{P}_{\mathcal{M}} \times \mathscr{P}_{\mathcal{C}}$. For both models, we consider 15 testing simulations of the same duration of the ones included in the training set. In addition, to test the reliability of the ROMs over a longer time horizon than the one considered in the training set, we include in the testing set 5 simulations of double length (i.e. 10 heartbeats). Then, we compare the simulations obtained with the two ROMs ($\mathcal{M}_{ANN}^{single}$ and $\mathcal{M}_{ANN}^{full}$) with the ones obtained with the $\mathcal{M}_{3D}$-$\mathcal{C}$ model for the same parameters $\mathbf{p}_{\mathcal{M}}$ and $\mathbf{p}_{\mathcal{C}}$.

The accuracy of the two ROMs is summarized Tabs. 5.5 and 5.6. Specifically, in Tab. 5.5 we report metrics regarding the ability of the ROMs to correctly predict the function of the LV, that is the chamber surrogated by the ANN-based model. Specifically, we report the relative errors in $L^2$ norm (i.e. the mean square errors) associated with pressure and volume transients ($p_{LV}$ and $V_{LV}$) and the

| | | 5 heartbeats | | | | | |
|---|---|---|---|---|---|---|---|
| | | $p_{LV}(t)$ | $V_{LV}(t)$ | $p_{LV}^{min}$ | $p_{LV}^{max}$ | $V_{LV}^{min}$ | $V_{LV}^{max}$ |
| $\mathcal{M}_{ANN}^{single}$-$\mathcal{C}$ vs $\mathcal{M}_{3D}$-$\mathcal{C}$ | relative error | 0.0336 | 0.0090 | 0.0097 | 0.0046 | 0.0139 | 0.0035 |
| | $R^2$ | | | 99.691 | 99.864 | 99.896 | 99.948 |
| $\mathcal{M}_{ANN}^{full}$-$\mathcal{C}$ vs $\mathcal{M}_{3D}$-$\mathcal{C}$ | relative error | 0.0620 | 0.0285 | 0.0517 | 0.0272 | 0.0471 | 0.0127 |
| | $R^2$ | | | 94.370 | 95.302 | 95.942 | 97.061 |
| | | 10 heartbeats | | | | | |
| | | $p_{LV}(t)$ | $V_{LV}(t)$ | $p_{LV}^{min}$ | $p_{LV}^{max}$ | $V_{LV}^{min}$ | $V_{LV}^{max}$ |
| $\mathcal{M}_{ANN}^{single}$-$\mathcal{C}$ vs $\mathcal{M}_{3D}$-$\mathcal{C}$ | relative error | 0.0293 | 0.0071 | 0.0113 | 0.0037 | 0.0096 | 0.0031 |
| | $R^2$ | | | 99.924 | 99.980 | 99.851 | 99.944 |
| $\mathcal{M}_{ANN}^{full}$-$\mathcal{C}$ vs $\mathcal{M}_{3D}$-$\mathcal{C}$ | relative error | 0.0631 | 0.0265 | 0.0442 | 0.0147 | 0.0382 | 0.0122 |
| | $R^2$ | | | 92.227 | 99.957 | 99.229 | 99.063 |

Table 5.5: Testing errors and $R^2$ coefficients on the LV outputs obtained with the two models $\mathcal{M}_{ANN}^{single}$ and $\mathcal{M}_{ANN}^{full}$, for 5 heartbeats long (top) and 10 heartbeats long (bottom) numerical simulations.

| | | 5 heartbeats | | | | | |
|---|---|---|---|---|---|---|---|
| | | $p_{RV}(t)$ | $V_{RV}(t)$ | $p_{RV}^{min}$ | $p_{RV}^{max}$ | $V_{RV}^{min}$ | $V_{RV}^{max}$ |
| $\mathcal{M}_{ANN}^{single}$-$\mathcal{C}$ vs $\mathcal{M}_{3D}$-$\mathcal{C}$ | relative error | 0.0048 | 0.0035 | 0.0015 | 0.0027 | 0.0028 | 0.0004 |
| | $R^2[\%]$ | | | 100.000 | 99.993 | 99.998 | 100.000 |
| $\mathcal{M}_{ANN}^{full}$-$\mathcal{C}$ vs $\mathcal{M}_{3D}$-$\mathcal{C}$ | relative error | 0.0069 | 0.0040 | 0.0029 | 0.0079 | 0.0072 | 0.0069 |
| | $R^2[\%]$ | | | 99.994 | 99.807 | 99.819 | 99.997 |

Table 5.6: Testing errors and $R^2$ coefficients on the RV outputs obtained with the two models $\mathcal{M}_{ANN}^{single}$ and $\mathcal{M}_{ANN}^{full}$, for 5 heartbeats long numerical simulations.

relative errors on some biomarkers of clinical interest (maximum and minimum pressures and volumes). For the latter, we also report the coefficient of determination $R^2$. We notice that both model $\mathcal{M}_{ANN}^{single}$-$\mathcal{C}$ and model $\mathcal{M}_{ANN}^{full}$-$\mathcal{C}$ are able to surrogate model $\mathcal{M}_{3D}$-$\mathcal{C}$ with remarkably good accuracy. Model $\mathcal{M}_{ANN}^{full}$-$\mathcal{C}$ features slightly larger errors than model $\mathcal{M}_{ANN}^{single}$-$\mathcal{C}$; this is not surprising since model $\mathcal{M}_{ANN}^{full}$-$\mathcal{C}$ explores a much larger parametric space than model $\mathcal{M}_{ANN}^{single}$-$\mathcal{C}$ (four parameters instead of one). Interestingly, the errors obtained over a long time horizon are very similar to those obtained for simulations of the same duration as those used to train the ANNs. This demonstrates the reliability of the ROMs in long-term simulations. Similarly, in Tab. 5.6 we report the errors and $R^2$ coefficients associated with the RV output (for simplicity, we here consider only 5 heartbeats long simulations). The accuracy obtained in reproducing the RV function is even better than that for the LV, coherently with the fact that the RV is included in the $\mathcal{C}$ model and thus it is not surrogated by the ANN-based model.

| | | $p_{LV}(t)$ | $V_{LV}(t)$ | $p_{LV}^{min}$ | $p_{LV}^{max}$ | $V_{LV}^{min}$ | $V_{LV}^{max}$ |
|---|---|---|---|---|---|---|---|
| $\mathcal{M}_{ANN}^{single}$-$\mathcal{C}'$ vs $\mathcal{M}_{3D}$-$\mathcal{C}'$ | relative error | 0.0459 | 0.0518 | 0.0065 | 0.0004 | 0.0080 | 0.0009 |
| $\mathcal{M}_{ANN}^{full}$-$\mathcal{C}'$ vs $\mathcal{M}_{3D}$-$\mathcal{C}'$ | relative error | 0.0510 | 0.0219 | 0.0116 | 0.0027 | 0.0110 | 0.0063 |

Table 5.7: Testing errors on the LV outputs obtained with the two models $\mathcal{M}_{ANN}^{single}$ and $\mathcal{M}_{ANN}^{full}$ coupled with the $\mathcal{C}'$ model for 5 heartbeats long numerical simulations.

In Figs. 5.4 and 5.5 we compare 10 heartbeats long transients obtained with the $\mathcal{M}_{ANN}^{single}$-$\mathcal{C}$ and $\mathcal{M}_{ANN}^{full}$-$\mathcal{C}$ models, respectively, to those obtained with the $\mathcal{M}_{3D}$-$\mathcal{C}$ model. All these transients were not used to train the ANN-based models (that is, they belong to the testing set). In Fig. 5.6 we show the LV biomarkers predicted by the $\mathcal{M}_{ANN}^{single}$-$\mathcal{C}$ and $\mathcal{M}_{ANN}^{full}$-$\mathcal{C}$ models versus those predicted by the $\mathcal{M}_{3D}$-$\mathcal{C}$ model.

### 5.2.2 *Coupling the electromechanical reduced-order model with different circulation models*

To generate the data used to train the $\mathcal{M}_{ANN}$ model, we employ the $\mathcal{M}_{3D}$-$\mathcal{C}$ coupled model (that is, we couple the $\mathcal{M}_{3D}$ model with the circulation model $\mathcal{C}$). However, the ANN-based ROM $\mathcal{M}_{ANN}$ surrogates the $\mathcal{M}_{3D}$ model regardless of its coupling with a specific circulation model. In fact, thanks to Eq. (5.5), the trained $\mathcal{M}_{ANN}$ model can be coupled with circulation models that are different from the one used to generate the training data. We remind that predictions are reliable only if pressure and volume values are inside the ranges explored during the training phase.

We demonstrate the flexibility of our Machine Learning algorithm by coupling the $\mathcal{M}_{ANN}$ model with a pressure-volume closure relationship that is different from the closed-loop circulation model $\mathcal{C}$ used during the training phase (see Sect. 5.1.6). Specifically, we consider a circulation model $\mathcal{C}'$ with a windkessel type relationship during the ejection phase and a linear pressure ramp during the filling phase [144]. In spite of the different nature of the two circulation models (the one used during the training and the one used during the testing), the ANN-based ROM trained with the $\mathcal{C}$ model proves to be reliable also when it is coupled with the $\mathcal{C}'$ model. Indeed, as shown in Tab. 5.7, the results obtained by the $\mathcal{M}_{ANN}$-$\mathcal{C}'$ coupled model approximate those of the $\mathcal{M}_{3D}$-$\mathcal{C}'$ coupled model with an excellent accuracy. These errors are indeed comparable to the ones obtained by surrogating the $\mathcal{M}_{ANN}$-$\mathcal{C}$ model with the $\mathcal{M}_{3D}$-$\mathcal{C}$ model (see Tab. 5.5).

### 5.2.3 *Global sensitivity analysis*

Once we have verified that models $\mathcal{M}_{ANN}^{single}$-$\mathcal{C}$ and $\mathcal{M}_{ANN}^{full}$-$\mathcal{C}$ are able to reproduce the outputs of model $\mathcal{M}_{3D}$-$\mathcal{C}$ with high accuracy, we use them to perform a global senstivity analysis. The aim is to determine which of the parameters of the circulation model ($\mathbf{p}_\mathcal{C}$) and the electromechanical model ($\mathbf{p}_\mathcal{M}$) contribute
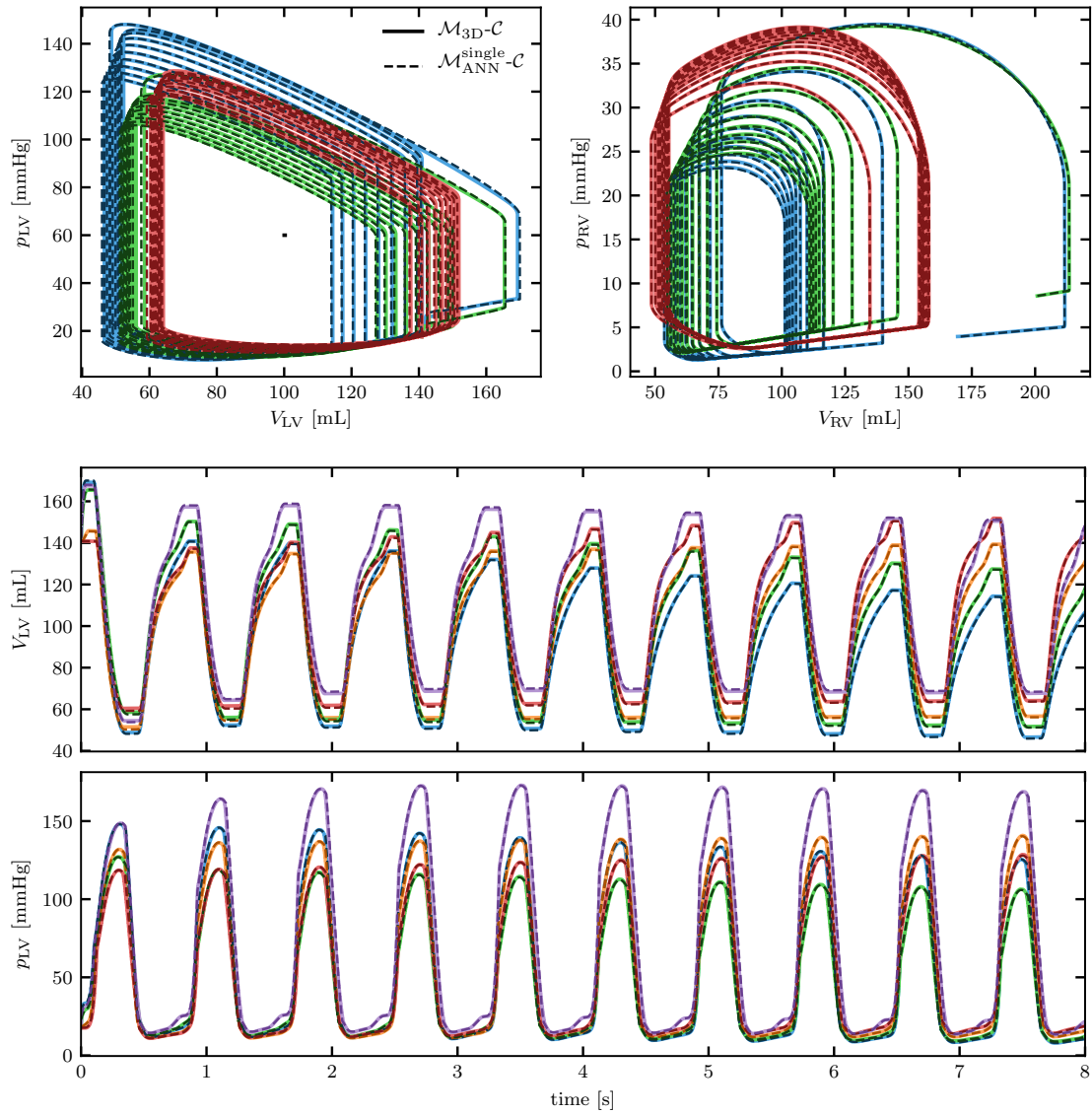
Figure 5.4: Pressure and volume transients obtained with the $\mathcal{M}_{\text{ANN}}^{\text{single}}$-$\mathcal{C}$ (dashed lines), compared to those obtained with the $\mathcal{M}_{\text{3D}}$-$\mathcal{C}$ model (solid lines). The different colors correspond to different samples of the testing set. For the sake of clarity, only three samples are shown in the first row.
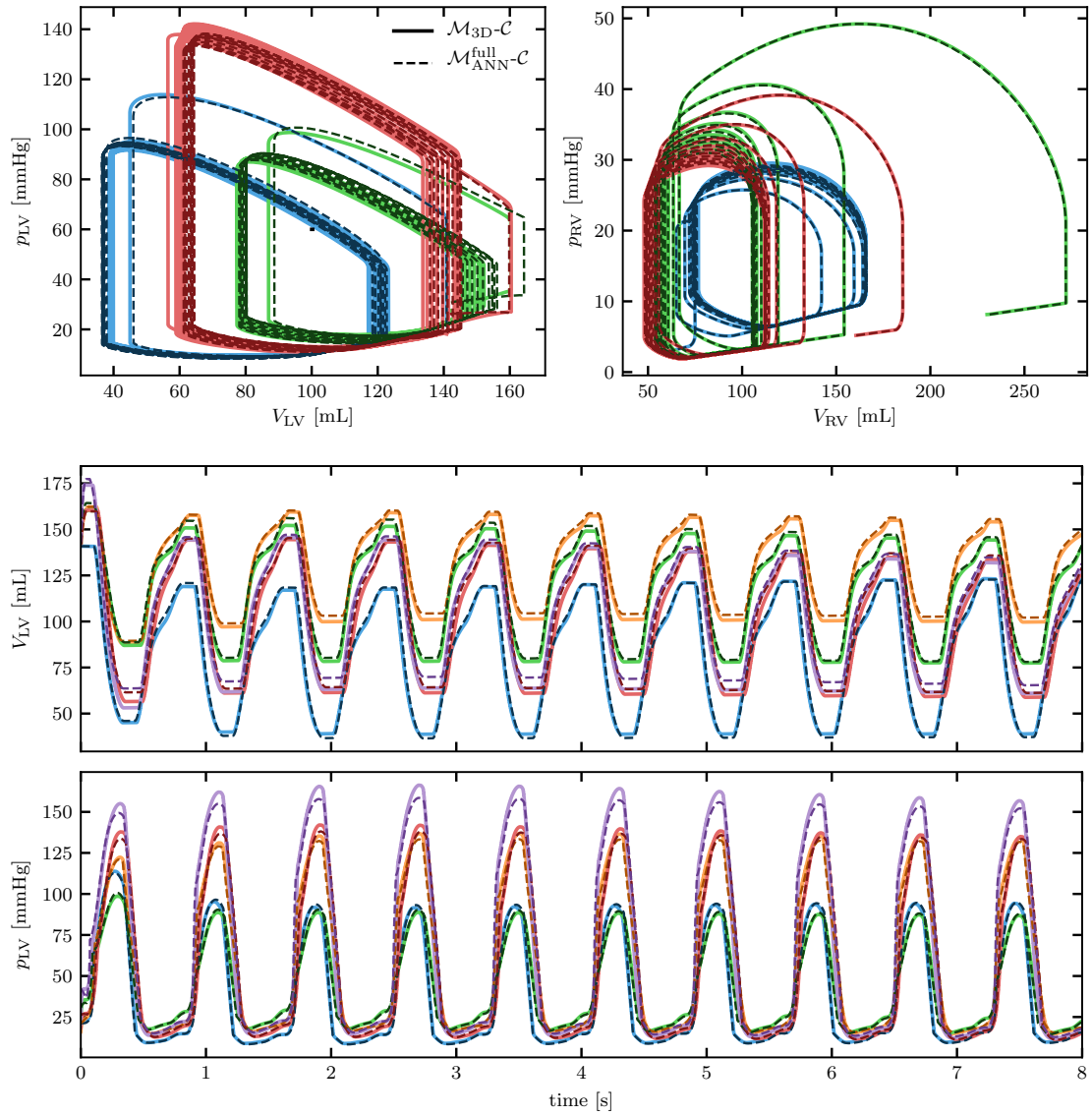
Figure 5.5: Pressure and volume transients obtained with the $\mathcal{M}_{\mathrm{ANN}}^{\mathrm{full}}$-$\mathcal{C}$ (dashed lines), compared to those obtained with the $\mathcal{M}_{\mathrm{3D}}$-$\mathcal{C}$ model (solid lines). The different colors correspond to different samples of the testing set. For the sake of clarity, only three samples are shown in the first row.

## Model $\mathcal{M}_{3D}$-$\mathcal{C}$ vs $\mathcal{M}_{ANN}^{single}$-$\mathcal{C}$



## Model $\mathcal{M}_{3D}$-$\mathcal{C}$ vs $\mathcal{M}_{ANN}^{full}$-$\mathcal{C}$
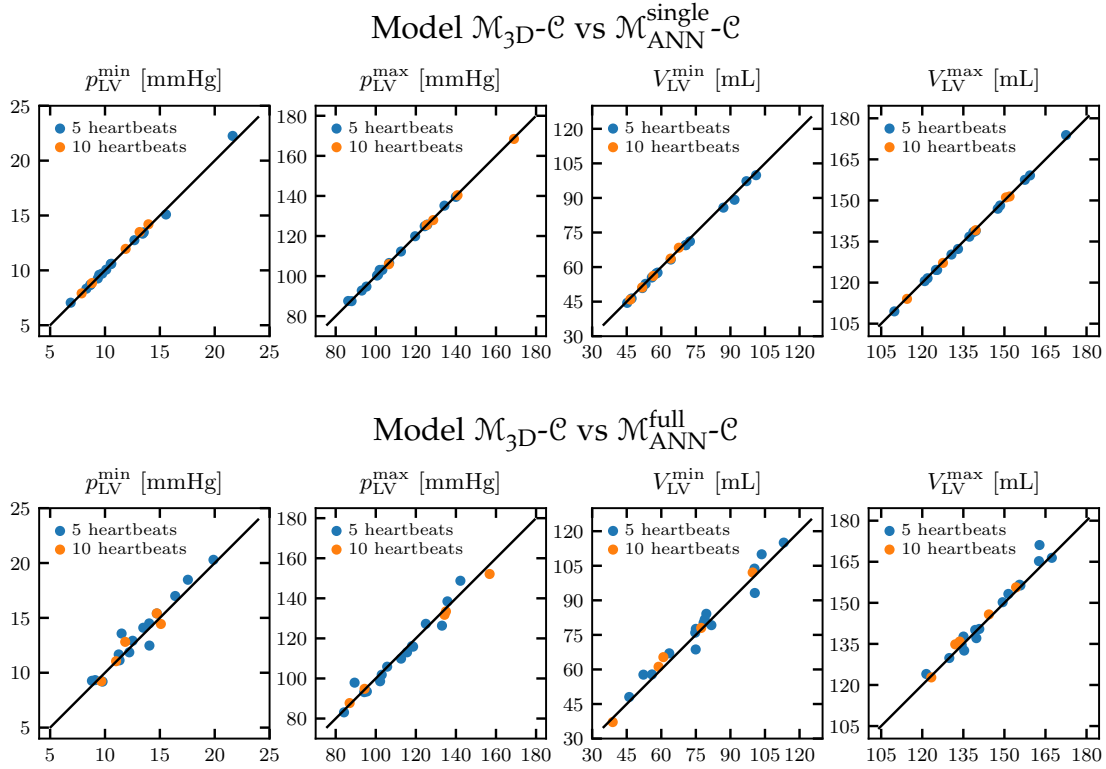


Figure 5.6: LV biomarkers obtained with the $\mathcal{M}_{ANN}^{single}$-$\mathcal{C}$ and $\mathcal{M}_{ANN}^{full}$-$\mathcal{C}$ models versus those obtained with the $\mathcal{M}_{3D}$-$\mathcal{C}$ model in the testing set. The different marker colors are associated with 5 heartbeats and 10 heartbeats long simulations, respectively.

the most to the determination of a list of outputs of interest, the so-called QoIs (see Tab. 5.3). For this purpose, we compute the Sobol indices $S_{ij}$ and $S_{ij}^{\mathsf{T}}$, as described in Sec. 5.1.4. When replacing model $\mathcal{M}_{3D}$-$\mathcal{C}$ with a ROM, we can only estimate sensitivity indices with respect to the parameters $\mathbf{p}_{\mathcal{M}}$ that were considered during the training phase. On the other hand, we can compute sensitivity indices with respect to all parameters $\mathbf{p}_{\mathcal{C}}$ of the circulation model, even those that were not varied during training. It would even be possible – at least in principle – to consider a circulation model different from the one used to generate the training data. In fact, as pointed out in Sec. 5.1.2, the model $\mathcal{M}_{ANN}^{single}$ and $\mathcal{M}_{ANN}^{full}$ surrogate the model $\mathcal{M}_{3D}$ independently of the circulation model to which it is coupled with.

We only report the results obtained by means of the most complete ROM, that is $\mathcal{M}_{ANN}^{full}$-$\mathcal{C}$. The results are shown in Figs. 5.7 and 5.8, respectively. We notice that the $S_{ij}$ and $S_{ij}^{\mathsf{T}}$ indices have only small differences from each other. This means that the interaction among the different parameters is less significant, in the determination of the QoIs, than the variation of the individual parameters. Furthermore, we note that, as expected, the QoIs associated with a given chamber or compartment are mostly determined by the parameters associated with the same region of the cardiovascular network. However, there are some important exceptions. Indeed, the venous resistance of the systemic circulation

$R_{VEN}^{SYS}$ has a strong impact on the right heart (RA and RV), i.e. the part of the network located immediately upstream. In addition, the systemic arterial resistance $R_{AR}^{SYS}$ significantly impacts the maximum LV pressure. In fact, this parameter is known to contribute in the determination of the so-called afterload [182]. We also note that total circulating blood volume $V_{heart}^{tot}$ has a major impact on almost all biomarkers. Conversely, the parameters associated with the pulmonary circulation network have a minimal impact. In addition, parameters describing the resistance of opened and closed valves also have a very little impact. This is an interesting result, since it shows that these parameters, chosen as a very low and very high value respectively (since for reasons of numerical stability they cannot be set equal to zero and infinity), have virtually no impact (at least within the ranges considered here) on the output quantities of biomechanical interest.

Regarding individual compartments, we note that variability can be explained by only a few parameters. Specifically, atria are mainly influenced by passive stiffness and atrioventricular delay, whereas for the RV the most relevant parameters are active and passive stiffness. As expected, the biomarkers associated with the LV – the only chamber included in the $\mathcal{M}_{3D}$ model – are mainly influenced by the parameters $\mathbf{p}_{\mathcal{M}}$. Among these, the most influential one is the active contractility $a_{XB}$, followed the fibers orientation $\alpha$ and, to a lesser extent, the passive stiffness C. Finally, the electrical conductivity $\sigma_f$ has a minimal impact on the biomarkers under consideration.

It is important to note that Sobol indices are affected by the amplitude of the ranges in which the parameters are varied. In particular, the wider the range associated with a parameter, the greater the associated Sobol indices will be, as the parameter in question potentially generates greater variability in the QoI. Therefore, the results shown here are valid for the specific ranges we used, which are reported in Appendix B.5.

### 5.2.4 *Bayesian parameter estimation*

In this section we present a further practical use of the cardiac electromechanics ROM presented in this thesis. In particular, we show that the ROM can be used to enable Bayesian parameter estimation for the $\mathcal{M}_{3D}$-$\mathcal{C}$ model, which, due to the prohibitive computational cost, would not be affordable without the use of a ROM.

We consider a prescribed value for the parameter vector $\mathbf{p} = (\mathbf{p}_{\mathcal{M}}, \mathbf{p}_{\mathcal{C}})$ (specifically, we employ the values reported in Tabs. 5.1 and 5.2) and we run a simulation using the $\mathcal{M}_{3D}$-$\mathcal{C}$ model. Based on the output of this simulation, we consider a couple of QoIs, consisting of minimum and maximum arterial pressure (i.e. we set $\mathbf{q} = (p_{AR,SYS}^{min}, p_{AR,SYS}^{max})$). The choice of these two QoIs is motivated by the fact that they are two variables that can be measured non invasively, and in fact they are often monitored in clinical routine. We reconstruct the value of a couple of parameters, namely the active contractility $a_{XB}$ and the systemic arterial resistance $R_{AR}^{SYS}$, assuming known and keeping fixed the values of the remain-

Figure 5.7: First-order Sobol indices $S_{ij}$ computed by exploiting the $\mathcal{M}_{ANN}^{full}$-$\mathcal{C}$ model. Each row corresponds to a parameter of either the electromechanical model (i.e. $\mathbf{p}_{\mathcal{M}}$, see Tab. 5.1) or the circulation model (i.e. $\mathbf{p}_{\mathcal{C}}$, see Tab. 5.2). Each column corresponds to a QoI (i.e. $\mathbf{q}$, see Tab. 5.3). Both parameters and QoIs are split into a number of groups, separated by a black solid line. Specifically, from left to right, we list QoIs referred to LA, LV, RA, RV and systemic circulation. Similarly, from top to bottom, we list parameters associated with LA, LV, RA, RV, systemic circulation, pulmonary circulation, valves and blood total volume.

| | $V_{LA}^{min}$ | $V_{LA}^{max}$ | $p_{LA}^{min}$ | $p_{LA}^{max}$ | $V_{LV}^{min}$ | $V_{LV}^{max}$ | $p_{LV}^{min}$ | $p_{LV}^{max}$ | $SV\ LV$ | $V_{RA}^{min}$ | $V_{RA}^{max}$ | $p_{RA}^{min}$ | $p_{RA}^{max}$ | $V_{RV}^{min}$ | $V_{RV}^{max}$ | $p_{RV}^{min}$ | $p_{RV}^{max}$ | $SV\ RV$ | $p_{AR,SYS}^{min}$ | $p_{AR,SYS}^{max}$ |
|---|---|---|---|---|---|---|---|---|---|---|---|---|---|---|---|---|---|---|---|---|
| $E_{LA}^{act}$ | 0.01 | 0.00 | 0.00 | 0.00 | 0.00 | 0.00 | 0.00 | 0.00 | 0.00 | 0.00 | 0.00 | 0.00 | 0.00 | 0.00 | 0.00 | 0.00 | 0.00 | 0.00 | 0.00 | 0.00 |
| $E_{LA}^{pass}$ | 0.23 | 0.26 | 0.00 | 0.00 | 0.00 | 0.00 | 0.00 | 0.00 | 0.00 | 0.00 | 0.00 | 0.00 | 0.00 | 0.00 | 0.00 | 0.01 | 0.00 | 0.00 | 0.00 | 0.00 |
| $T_{LA}^{contr}$ | 0.00 | 0.00 | 0.00 | 0.00 | 0.00 | 0.00 | 0.00 | 0.00 | 0.00 | 0.00 | 0.00 | 0.00 | 0.00 | 0.00 | 0.00 | 0.00 | 0.00 | 0.00 | 0.00 | 0.00 |
| $T_{LA}^{rel}$ | 0.00 | 0.00 | 0.00 | 0.00 | 0.00 | 0.00 | 0.00 | 0.00 | 0.00 | 0.00 | 0.00 | 0.00 | 0.00 | 0.00 | 0.00 | 0.00 | 0.00 | 0.00 | 0.00 | 0.00 |
| $t_{L}^{av}$ | 0.03 | 0.00 | 0.00 | 0.13 | 0.01 | 0.04 | 0.00 | 0.02 | 0.02 | 0.00 | 0.00 | 0.00 | 0.00 | 0.00 | 0.00 | 0.00 | 0.00 | 0.00 | 0.01 | 0.02 |
| $V_{0,LA}$ | 0.00 | 0.00 | 0.00 | 0.00 | 0.00 | 0.00 | 0.00 | 0.00 | 0.00 | 0.00 | 0.00 | 0.00 | 0.00 | 0.00 | 0.00 | 0.00 | 0.00 | 0.00 | 0.00 | 0.00 |
| C | 0.03 | 0.02 | 0.04 | 0.03 | 0.01 | 0.05 | 0.05 | 0.05 | 0.06 | 0.00 | 0.00 | 0.00 | 0.00 | 0.01 | 0.00 | 0.00 | 0.01 | 0.01 | 0.02 | 0.05 |
| $\alpha$ | 0.03 | 0.02 | 0.07 | 0.04 | 0.14 | 0.03 | 0.08 | 0.10 | 0.13 | 0.00 | 0.00 | 0.00 | 0.00 | 0.01 | 0.00 | 0.02 | 0.01 | 0.00 | 0.05 | 0.10 |
| $\sigma_f$ | 0.00 | 0.00 | 0.00 | 0.00 | 0.02 | 0.00 | 0.01 | 0.01 | 0.01 | 0.00 | 0.00 | 0.00 | 0.00 | 0.00 | 0.00 | 0.00 | 0.00 | 0.00 | 0.01 | 0.01 |
| $a_{XB}$ | 0.10 | 0.07 | 0.15 | 0.09 | 0.51 | 0.16 | 0.18 | 0.22 | 0.26 | 0.00 | 0.00 | 0.00 | 0.00 | 0.02 | 0.00 | 0.00 | 0.04 | 0.04 | 0.10 | 0.22 |
| $E_{RA}^{act}$ | 0.00 | 0.00 | 0.00 | 0.00 | 0.00 | 0.00 | 0.00 | 0.00 | 0.00 | 0.04 | 0.03 | 0.05 | 0.01 | 0.00 | 0.00 | 0.01 | 0.00 | 0.00 | 0.00 | 0.00 |
| $E_{RA}^{pass}$ | 0.00 | 0.00 | 0.00 | 0.00 | 0.00 | 0.00 | 0.00 | 0.00 | 0.00 | 0.17 | 0.21 | 0.05 | 0.01 | 0.00 | 0.00 | 0.04 | 0.00 | 0.00 | 0.00 | 0.00 |
| $T_{RA}^{contr}$ | 0.00 | 0.00 | 0.00 | 0.00 | 0.00 | 0.00 | 0.00 | 0.00 | 0.00 | 0.00 | 0.00 | 0.00 | 0.00 | 0.00 | 0.00 | 0.00 | 0.00 | 0.00 | 0.00 | 0.00 |
| $T_{RA}^{rel}$ | 0.00 | 0.00 | 0.00 | 0.00 | 0.00 | 0.00 | 0.00 | 0.00 | 0.00 | 0.00 | 0.00 | 0.00 | 0.00 | 0.00 | 0.00 | 0.00 | 0.00 | 0.00 | 0.00 | 0.00 |
| $t_{R}^{av}$ | 0.00 | 0.00 | 0.01 | 0.00 | 0.00 | 0.01 | 0.01 | 0.00 | 0.00 | 0.42 | 0.18 | 0.35 | 0.54 | 0.00 | 0.01 | 0.03 | 0.01 | 0.02 | 0.00 | 0.00 |
| $V_{0,RA}$ | 0.00 | 0.00 | 0.00 | 0.00 | 0.00 | 0.00 | 0.00 | 0.00 | 0.00 | 0.00 | 0.00 | 0.00 | 0.00 | 0.00 | 0.00 | 0.00 | 0.00 | 0.00 | 0.00 | 0.00 |
| $E_{RV}^{act}$ | 0.01 | 0.01 | 0.01 | 0.01 | 0.00 | 0.00 | 0.00 | 0.00 | 0.00 | 0.02 | 0.01 | 0.03 | 0.02 | 0.37 | 0.15 | 0.13 | 0.01 | 0.00 | 0.00 | 0.00 |
| $E_{RV}^{pass}$ | 0.00 | 0.00 | 0.00 | 0.00 | 0.00 | 0.01 | 0.00 | 0.00 | 0.01 | 0.15 | 0.12 | 0.22 | 0.16 | 0.02 | 0.03 | 0.42 | 0.01 | 0.02 | 0.00 | 0.00 |
| $T_{RV}^{contr}$ | 0.00 | 0.00 | 0.00 | 0.00 | 0.00 | 0.00 | 0.00 | 0.00 | 0.00 | 0.00 | 0.02 | 0.00 | 0.00 | 0.00 | 0.00 | 0.00 | 0.04 | 0.00 | 0.00 | 0.00 |
| $T_{RV}^{rel}$ | 0.00 | 0.00 | 0.00 | 0.00 | 0.00 | 0.00 | 0.00 | 0.00 | 0.00 | 0.00 | 0.03 | 0.00 | 0.00 | 0.00 | 0.00 | 0.06 | 0.00 | 0.00 | 0.00 | 0.00 |
| $V_{0,RV}$ | 0.00 | 0.00 | 0.00 | 0.00 | 0.00 | 0.00 | 0.00 | 0.00 | 0.00 | 0.00 | 0.00 | 0.00 | 0.00 | 0.06 | 0.03 | 0.00 | 0.00 | 0.00 | 0.00 | 0.00 |
| $R_{AR}^{SYS}$ | 0.02 | 0.01 | 0.03 | 0.01 | 0.10 | 0.02 | 0.04 | 0.23 | 0.08 | 0.00 | 0.00 | 0.00 | 0.00 | 0.00 | 0.00 | 0.00 | 0.00 | 0.01 | 0.53 | 0.24 |
| $C_{AR}^{SYS}$ | 0.00 | 0.00 | 0.00 | 0.00 | 0.01 | 0.00 | 0.00 | 0.05 | 0.01 | 0.00 | 0.00 | 0.00 | 0.00 | 0.00 | 0.00 | 0.00 | 0.00 | 0.00 | 0.13 | 0.05 |
| $R_{VEN}^{SYS}$ | 0.07 | 0.09 | 0.10 | 0.09 | 0.01 | 0.09 | 0.09 | 0.02 | 0.09 | 0.10 | 0.30 | 0.18 | 0.15 | 0.10 | 0.51 | 0.16 | 0.24 | 0.82 | 0.00 | 0.02 |
| $C_{VEN}^{SYS}$ | 0.00 | 0.00 | 0.00 | 0.00 | 0.00 | 0.00 | 0.00 | 0.00 | 0.00 | 0.00 | 0.00 | 0.00 | 0.00 | 0.00 | 0.00 | 0.00 | 0.00 | 0.00 | 0.00 | 0.00 |
| $L_{AR}^{SYS}$ | 0.00 | 0.00 | 0.00 | 0.00 | 0.00 | 0.00 | 0.00 | 0.00 | 0.00 | 0.00 | 0.00 | 0.00 | 0.00 | 0.00 | 0.00 | 0.00 | 0.00 | 0.00 | 0.00 | 0.00 |
| $L_{VEN}^{SYS}$ | 0.00 | 0.00 | 0.00 | 0.00 | 0.00 | 0.00 | 0.00 | 0.00 | 0.00 | 0.00 | 0.00 | 0.00 | 0.00 | 0.00 | 0.00 | 0.00 | 0.00 | 0.00 | 0.00 | 0.00 |
| $R_{AR}^{PUL}$ | 0.00 | 0.00 | 0.00 | 0.00 | 0.00 | 0.00 | 0.00 | 0.00 | 0.00 | 0.00 | 0.00 | 0.00 | 0.00 | 0.00 | 0.00 | 0.00 | 0.00 | 0.00 | 0.00 | 0.00 |
| $C_{AR}^{PUL}$ | 0.00 | 0.00 | 0.00 | 0.00 | 0.00 | 0.00 | 0.00 | 0.00 | 0.00 | 0.00 | 0.00 | 0.00 | 0.00 | 0.01 | 0.00 | 0.00 | 0.00 | 0.00 | 0.00 | 0.00 |
| $R_{VEN}^{PUL}$ | 0.00 | 0.00 | 0.01 | 0.00 | 0.00 | 0.01 | 0.00 | 0.00 | 0.01 | 0.00 | 0.00 | 0.00 | 0.00 | 0.00 | 0.00 | 0.00 | 0.00 | 0.00 | 0.00 | 0.00 |
| $C_{VEN}^{PUL}$ | 0.00 | 0.00 | 0.00 | 0.00 | 0.00 | 0.00 | 0.00 | 0.00 | 0.00 | 0.00 | 0.00 | 0.00 | 0.00 | 0.00 | 0.00 | 0.00 | 0.00 | 0.00 | 0.00 | 0.00 |
| $L_{AR}^{PUL}$ | 0.00 | 0.00 | 0.00 | 0.00 | 0.00 | 0.00 | 0.00 | 0.00 | 0.00 | 0.00 | 0.00 | 0.00 | 0.00 | 0.00 | 0.00 | 0.00 | 0.00 | 0.00 | 0.00 | 0.00 |
| $L_{VEN}^{PUL}$ | 0.00 | 0.00 | 0.00 | 0.00 | 0.00 | 0.00 | 0.00 | 0.00 | 0.00 | 0.00 | 0.00 | 0.00 | 0.00 | 0.00 | 0.00 | 0.00 | 0.00 | 0.00 | 0.00 | 0.00 |
| $R_{min}$ | 0.00 | 0.00 | 0.00 | 0.00 | 0.00 | 0.00 | 0.01 | 0.00 | 0.00 | 0.01 | 0.01 | 0.01 | 0.01 | 0.00 | 0.00 | 0.01 | 0.03 | 0.00 | 0.00 | 0.00 |
| $R_{max}$ | 0.00 | 0.00 | 0.00 | 0.00 | 0.00 | 0.00 | 0.00 | 0.00 | 0.00 | 0.00 | 0.00 | 0.00 | 0.00 | 0.00 | 0.00 | 0.00 | 0.00 | 0.00 | 0.00 | 0.00 |
| $V_{heart}^{tot}$ | 0.39 | 0.45 | 0.53 | 0.52 | 0.15 | 0.53 | 0.49 | 0.27 | 0.31 | 0.04 | 0.07 | 0.06 | 0.05 | 0.32 | 0.24 | 0.11 | 0.55 | 0.03 | 0.14 | 0.26 |

| | $V_{LA}^{min}$ | $V_{LA}^{max}$ | $p_{LA}^{min}$ | $p_{LA}^{max}$ | $V_{LV}^{min}$ | $V_{LV}^{max}$ | $p_{LV}^{min}$ | $p_{LV}^{max}$ | SV LV | $V_{RA}^{min}$ | $V_{RA}^{max}$ | $p_{RA}^{min}$ | $p_{RA}^{max}$ | $V_{RV}^{min}$ | $V_{RV}^{max}$ | $p_{RV}^{min}$ | $p_{RV}^{max}$ | SV RV | $p_{AR,SYS}^{min}$ | $p_{AR,SYS}^{max}$ |
|---|---|---|---|---|---|---|---|---|---|---|---|---|---|---|---|---|---|---|---|---|
| $E_{LA}^{act}$ | 0.01 | 0.00 | 0.00 | 0.01 | 0.00 | 0.00 | 0.00 | 0.00 | 0.00 | 0.00 | 0.00 | 0.00 | 0.00 | 0.00 | 0.00 | 0.00 | 0.00 | 0.00 | 0.00 | 0.00 |
| $E_{LA}^{pass}$ | 0.26 | 0.28 | 0.00 | 0.01 | 0.00 | 0.00 | 0.00 | 0.00 | 0.00 | 0.00 | 0.00 | 0.00 | 0.00 | 0.00 | 0.00 | 0.00 | 0.01 | 0.00 | 0.00 | 0.00 |
| $T_{LA}^{contr}$ | 0.00 | 0.00 | 0.00 | 0.00 | 0.00 | 0.00 | 0.00 | 0.00 | 0.00 | 0.00 | 0.00 | 0.00 | 0.00 | 0.00 | 0.00 | 0.00 | 0.00 | 0.00 | 0.00 | 0.00 |
| $T_{LA}^{rel}$ | 0.00 | 0.00 | 0.00 | 0.00 | 0.00 | 0.00 | 0.00 | 0.00 | 0.00 | 0.00 | 0.00 | 0.00 | 0.00 | 0.00 | 0.00 | 0.00 | 0.00 | 0.00 | 0.00 | 0.00 |
| $t_L^{av}$ | 0.04 | 0.01 | 0.01 | 0.16 | 0.01 | 0.04 | 0.00 | 0.02 | 0.03 | 0.00 | 0.00 | 0.00 | 0.00 | 0.01 | 0.00 | 0.00 | 0.00 | 0.00 | 0.01 | 0.02 |
| $V_{0,LA}$ | 0.00 | 0.00 | 0.00 | 0.00 | 0.00 | 0.00 | 0.00 | 0.00 | 0.00 | 0.00 | 0.00 | 0.00 | 0.00 | 0.00 | 0.00 | 0.00 | 0.00 | 0.00 | 0.00 | 0.00 |
| C | 0.04 | 0.03 | 0.05 | 0.04 | 0.02 | 0.07 | 0.06 | 0.05 | 0.07 | 0.00 | 0.00 | 0.00 | 0.00 | 0.01 | 0.00 | 0.00 | 0.02 | 0.01 | 0.02 | 0.05 |
| $\alpha$ | 0.05 | 0.03 | 0.08 | 0.04 | 0.15 | 0.04 | 0.09 | 0.10 | 0.13 | 0.00 | 0.00 | 0.00 | 0.00 | 0.02 | 0.00 | 0.00 | 0.02 | 0.02 | 0.05 | 0.10 |
| $\sigma_f$ | 0.01 | 0.01 | 0.01 | 0.00 | 0.02 | 0.01 | 0.01 | 0.01 | 0.02 | 0.00 | 0.00 | 0.00 | 0.00 | 0.00 | 0.00 | 0.00 | 0.00 | 0.00 | 0.01 | 0.01 |
| $a_{XB}$ | 0.11 | 0.08 | 0.17 | 0.11 | 0.52 | 0.18 | 0.19 | 0.24 | 0.29 | 0.00 | 0.00 | 0.00 | 0.00 | 0.04 | 0.00 | 0.00 | 0.05 | 0.05 | 0.11 | 0.23 |
| $E_{RA}^{act}$ | 0.00 | 0.00 | 0.00 | 0.00 | 0.00 | 0.00 | 0.00 | 0.00 | 0.00 | 0.04 | 0.03 | 0.04 | 0.01 | 0.00 | 0.00 | 0.01 | 0.00 | 0.00 | 0.00 | 0.00 |
| $E_{RA}^{pass}$ | 0.00 | 0.00 | 0.00 | 0.00 | 0.00 | 0.00 | 0.00 | 0.00 | 0.00 | 0.18 | 0.21 | 0.07 | 0.02 | 0.00 | 0.04 | 0.00 | 0.00 | 0.00 | 0.00 | 0.00 |
| $T_{RA}^{contr}$ | 0.00 | 0.00 | 0.00 | 0.00 | 0.00 | 0.00 | 0.00 | 0.00 | 0.00 | 0.01 | 0.01 | 0.01 | 0.04 | 0.00 | 0.00 | 0.00 | 0.00 | 0.00 | 0.00 | 0.00 |
| $T_{RA}^{rel}$ | 0.00 | 0.00 | 0.00 | 0.00 | 0.00 | 0.00 | 0.00 | 0.00 | 0.00 | 0.00 | 0.00 | 0.01 | 0.00 | 0.00 | 0.00 | 0.00 | 0.00 | 0.00 | 0.00 | 0.00 |
| $t_R^{av}$ | 0.01 | 0.01 | 0.01 | 0.01 | 0.00 | 0.01 | 0.01 | 0.00 | 0.01 | 0.44 | 0.19 | 0.38 | 0.57 | 0.01 | 0.02 | 0.04 | 0.02 | 0.03 | 0.00 | 0.00 |
| $V_{0,RA}$ | 0.00 | 0.00 | 0.00 | 0.00 | 0.00 | 0.00 | 0.00 | 0.00 | 0.00 | 0.00 | 0.00 | 0.00 | 0.00 | 0.00 | 0.00 | 0.00 | 0.00 | 0.00 | 0.00 | 0.00 |
| $E_{RV}^{act}$ | 0.00 | 0.00 | 0.00 | 0.00 | 0.00 | 0.00 | 0.00 | 0.00 | 0.00 | 0.02 | 0.02 | 0.04 | 0.03 | 0.39 | 0.16 | 0.15 | 0.01 | 0.00 | 0.00 | 0.00 |
| $E_{RV}^{pass}$ | 0.00 | 0.01 | 0.01 | 0.01 | 0.00 | 0.01 | 0.01 | 0.00 | 0.00 | 0.16 | 0.12 | 0.22 | 0.17 | 0.02 | 0.03 | 0.43 | 0.01 | 0.02 | 0.00 | 0.00 |
| $T_{RV}^{contr}$ | 0.00 | 0.00 | 0.00 | 0.00 | 0.00 | 0.00 | 0.00 | 0.00 | 0.00 | 0.00 | 0.01 | 0.00 | 0.00 | 0.00 | 0.00 | 0.00 | 0.04 | 0.00 | 0.00 | 0.00 |
| $T_{RV}^{rel}$ | 0.00 | 0.00 | 0.00 | 0.00 | 0.00 | 0.00 | 0.00 | 0.00 | 0.00 | 0.00 | 0.03 | 0.00 | 0.00 | 0.00 | 0.00 | 0.06 | 0.00 | 0.00 | 0.00 | 0.00 |
| $V_{0,RV}$ | 0.00 | 0.00 | 0.00 | 0.00 | 0.00 | 0.00 | 0.00 | 0.00 | 0.00 | 0.00 | 0.00 | 0.00 | 0.00 | 0.07 | 0.03 | 0.00 | 0.00 | 0.00 | 0.00 | 0.00 |
| $R_{AR}^{SYS}$ | 0.02 | 0.02 | 0.04 | 0.02 | 0.10 | 0.03 | 0.04 | 0.23 | 0.09 | 0.00 | 0.00 | 0.00 | 0.00 | 0.01 | 0.00 | 0.00 | 0.01 | 0.02 | 0.54 | 0.24 |
| $C_{AR}^{SYS}$ | 0.00 | 0.00 | 0.01 | 0.00 | 0.01 | 0.00 | 0.01 | 0.06 | 0.01 | 0.00 | 0.00 | 0.00 | 0.00 | 0.00 | 0.00 | 0.00 | 0.00 | 0.00 | 0.13 | 0.06 |
| $R_{VEN}^{SYS}$ | 0.08 | 0.11 | 0.11 | 0.11 | 0.02 | 0.11 | 0.10 | 0.03 | 0.11 | 0.10 | 0.30 | 0.19 | 0.15 | 0.11 | 0.51 | 0.16 | 0.25 | 0.83 | 0.00 | 0.03 |
| $C_{VEN}^{SYS}$ | 0.00 | 0.00 | 0.00 | 0.00 | 0.00 | 0.00 | 0.00 | 0.00 | 0.00 | 0.00 | 0.00 | 0.00 | 0.00 | 0.00 | 0.00 | 0.00 | 0.00 | 0.00 | 0.00 | 0.00 |
| $L_{AR}^{SYS}$ | 0.00 | 0.00 | 0.00 | 0.00 | 0.00 | 0.00 | 0.00 | 0.00 | 0.00 | 0.00 | 0.00 | 0.00 | 0.00 | 0.00 | 0.00 | 0.00 | 0.00 | 0.00 | 0.00 | 0.00 |
| $L_{VEN}^{SYS}$ | 0.00 | 0.00 | 0.00 | 0.00 | 0.00 | 0.00 | 0.00 | 0.00 | 0.00 | 0.00 | 0.00 | 0.00 | 0.00 | 0.00 | 0.00 | 0.00 | 0.00 | 0.00 | 0.00 | 0.00 |
| $R_{AR}^{PUL}$ | 0.00 | 0.00 | 0.00 | 0.00 | 0.00 | 0.00 | 0.00 | 0.00 | 0.00 | 0.00 | 0.00 | 0.00 | 0.00 | 0.00 | 0.00 | 0.00 | 0.00 | 0.00 | 0.00 | 0.00 |
| $C_{AR}^{PUL}$ | 0.00 | 0.00 | 0.00 | 0.00 | 0.00 | 0.00 | 0.00 | 0.00 | 0.00 | 0.00 | 0.00 | 0.00 | 0.00 | 0.01 | 0.00 | 0.00 | 0.00 | 0.00 | 0.00 | 0.00 |
| $R_{VEN}^{PUL}$ | 0.00 | 0.00 | 0.01 | 0.00 | 0.00 | 0.01 | 0.00 | 0.00 | 0.00 | 0.00 | 0.00 | 0.00 | 0.00 | 0.00 | 0.00 | 0.00 | 0.00 | 0.00 | 0.00 | 0.00 |
| $C_{VEN}^{PUL}$ | 0.00 | 0.00 | 0.00 | 0.00 | 0.00 | 0.00 | 0.00 | 0.00 | 0.00 | 0.00 | 0.00 | 0.00 | 0.00 | 0.00 | 0.00 | 0.00 | 0.00 | 0.00 | 0.00 | 0.00 |
| $L_{AR}^{PUL}$ | 0.00 | 0.00 | 0.00 | 0.00 | 0.00 | 0.00 | 0.00 | 0.00 | 0.00 | 0.00 | 0.00 | 0.00 | 0.00 | 0.00 | 0.00 | 0.00 | 0.00 | 0.00 | 0.00 | 0.00 |
| $L_{VEN}^{PUL}$ | 0.00 | 0.00 | 0.00 | 0.00 | 0.00 | 0.00 | 0.00 | 0.00 | 0.00 | 0.00 | 0.00 | 0.00 | 0.00 | 0.00 | 0.00 | 0.00 | 0.00 | 0.00 | 0.00 | 0.00 |
| $R_{min}$ | 0.00 | 0.00 | 0.00 | 0.00 | 0.00 | 0.00 | 0.01 | 0.00 | 0.00 | 0.01 | 0.01 | 0.01 | 0.02 | 0.00 | 0.00 | 0.01 | 0.03 | 0.00 | 0.00 | 0.00 |
| $R_{max}$ | 0.00 | 0.00 | 0.00 | 0.00 | 0.00 | 0.00 | 0.00 | 0.00 | 0.00 | 0.00 | 0.00 | 0.00 | 0.00 | 0.00 | 0.00 | 0.00 | 0.00 | 0.00 | 0.00 | 0.00 |
| $V_{heart}^{tot}$ | 0.42 | 0.48 | 0.56 | 0.54 | 0.16 | 0.54 | 0.52 | 0.27 | 0.32 | 0.04 | 0.08 | 0.07 | 0.06 | 0.33 | 0.24 | 0.13 | 0.56 | 0.04 | 0.13 | 0.27 |

Figure 5.8: Total-effect Sobol indices $S_{ij}^T$ computed by exploiting the $\mathcal{M}_{ANN}^{full}$-$\mathcal{C}$ model. For a description of the figure see caption of Fig. 5.7.

ing parameters. Indeed, we aim at demonstrating that the ROM we propose is suitable for estimating parameters of both the $\mathcal{M}_{3D}$ model (such as $a_{XB}$) and of the $\mathcal{C}$ model (such as $R_{AR}^{SYS}$). Specifically, in this section we rely on the $\mathcal{M}_{ANN}^{single}$-$\mathcal{C}$ model.

To mimic the presence of measurement error, we artificially add to the exact values of the QoIs $p_{AR,SYS}^{min}$ and $p_{AR,SYS}^{max}$ a synthetic noise, with increasing magnitude. Specifically, we add an artificial noise by sampling from independent Gaussian variables with zero mean and with variance $\sigma_{exp}^2$. We consider three cases: $\sigma_{exp}^2 = 0$ (i.e. no noise), $\sigma_{exp}^2 = 0.1 \, \text{mmHg}^2$ and $\sigma_{exp}^2 = 1 \, \text{mmHg}^2$.

We use the MCMC method to derive a Bayesian estimate of the parameters value from (possibly noisy) measurements of the minimum and maximum arterial pressure. For both unknown parameters we employ a non-informative prior, that is a uniform distribution on the ranges used to train the ROM ($a_{XB} \in [80, 320] \, \text{MPa}$ and $R_{AR}^{SYS} \in [0.4, 1.2] \, \text{mmHg s mL}^{-1}$). According to Sec. 5.1.5, we set $\boldsymbol{\Sigma} = \boldsymbol{\Sigma}_{ROM} + \boldsymbol{\Sigma}_{exp}$, where the experimental measurement error covariance is given by $\boldsymbol{\Sigma}_{exp} = \sigma_{exp}^2 \, \mathbb{I}_2$ ($\mathbb{I}_2$ being the 2-by-2 identity matrix) and where the ROM approximation error covariance is estimated from its statistical distribution on the validation set as $\boldsymbol{\Sigma}_{ROM} = 0.2 \, \text{mmHg}^2 \, \mathbb{I}_2$. More details on the MCMC setup are available in Appendix B.6.

In Fig. 5.9 we show the posterior distribution $\pi_{post}$ on the parameters pair ($a_{XB}$, $R_{AR}^{SYS}$) obtained for the three noise levels considered. We depict with a red line the 90% credibility region, that is the region in the parameter space with largest posterior probability such that it covers 90% of $\pi_{post}$. We notice that for each value of noise, the credibility region contains the exact value of the parameters (namely $a_{XB} = 160 \, \text{MPa}$ and $R_{AR}^{SYS} = 0.64 \, \text{mmHg s mL}^{-1}$), represented by a red star. As expected, for larger values of noise, the size of the credibility region increases (that is, the estimate is more uncertain). As a matter of fact, an advantage of Bayesian parameter estimation methods, compared to deterministic methods, is their ability of quantifying the uncertainty associated with the parameters estimate. A further feature of Bayesian methods stands in capturing correlations among the estimated parameters. Indeed, this aspect emerges clearly because of the oblique shape of the credibility regions. This is due to the fact that an increase in $a_{XB}$ or a decrease in $R_{AR}^{SYS}$ leads to similar changes in terms of the measured QoIs ($p_{AR,SYS}^{min}$ and $p_{AR,SYS}^{max}$), thus making their posterior distributions highly correlated.

## 5.3 DISCUSSION

In this thesis, we propose a Machine Learning method to build ROMs of 3D cardiac electromechanical models. Thanks to the reduced-order differential equations, learned through our algorithm, it is possible to approximate the cardiac dynamics in terms of pressure and volume transients with great fidelity and with a huge computational saving. As a matter of fact, once trained, the ANN-based ROM permits to simulate a heartbeat virtually in real time (about one
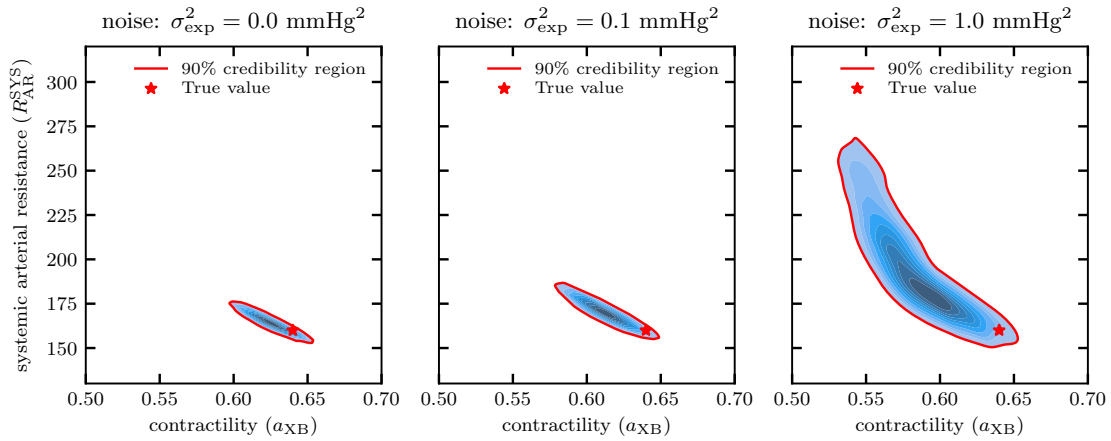
Figure 5.9: Output of the Bayesian estimation presented in Sec. 5.2.4. The figures show the posterior distribution $\pi_{\text{post}}$, estimated by means of the MCMC method, for $\sigma_{\text{exp}}^2 = 0$ (left), $\sigma_{\text{exp}}^2 = 0.1\,\text{mmHg}^2$ (middle) and $\sigma_{\text{exp}}^2 = 1\,\text{mmHg}^2$ (right). The red lines show the 90% credibility regions, while the red stars represent the exact value of the unknown parameters $a_{\text{XB}}$ and $R_{\text{AR}}^{\text{SYS}}$.

second of numerical simulation for a heartbeat on a standard laptop), when the original electromechanical model requires about four hours per heartbeat on a supercomputer with 32 cores. By taking into account the number of cores, our ANN-based ROM yields the impressive speedup of 460'000x. A fair evaluation of the computational saving should also take into account the time required to generate the training dataset and to train the model. To this aim, we consider two test cases, corresponding to the examples of global sensitivity analysis and Bayesian parameter estimation presented in Secs. 5.1.4 and 5.1.5, respectively. In both cases, we consider 5 computer nodes with 32 cores each available, and we compare the total computational times using either the $\mathcal{M}_{3D}$-$\mathcal{C}$ or the $\mathcal{M}_{\text{ANN}}$-$\mathcal{C}$ model with these computational resources (see Fig. 5.10).

The global sensitivity analysis presented in Sec. 5.1.4 requires the numerical simulation of 74'000 parameter cases. On average, the limit cycle is reached in 10 heartbeats, for a total of 740'000 heartbeats to be simulated. Running this huge amount of numerical simulations with the FOM $\mathcal{M}_{3D}$-$\mathcal{C}$ model would not be feasible, as it would require about 68 years of uninterrupted use of the 5 nodes endowed with 32 cores. On the contrary, by virtue of our Machine Learning algorithm, we are able to perform a global sensitivity analysis, albeit with a small approximation (see Tabs. 5.5 and 5.6) in the results, in 7.5 days (6.7 days to generate the training dataset, 18 hours to train the model and 1 hour and 17 minutes to perform the sensitivity analysis using the $\mathcal{M}_{\text{ANN}}$-$\mathcal{C}$ model). Therefore, taking into account the time required to build the ROM, our approach yields a 3'300x speedup. Bayesian parameter estimation, on the other hand, requires the numerical simulation of approximately 960'000 heartbeats. In this case, despite using only 20 cores to run the MCMC, we are able to obtain a result in just 6 days and 8 hours (including generation of the training dataset), when with the FOM $\mathcal{M}_{3D}$-$\mathcal{C}$ model it would take more than 87 years. We thus obtain an

| model | task | computational platform | | computational time |
|---|---|---|---|---|
| $\mathcal{M}_{3D}\text{-}\mathcal{C}$ | simulation of a heartbeat | | 32 cores supercomputer | 4 hours |
| $\mathcal{M}_{ANN}\text{-}\mathcal{C}$ | simulation of a heartbeat | | single core standard laptop | 1 second |
| $\mathcal{M}_{ANN}$ | training | | single core standard laptop | 18 hours |

**460'000x speedup**

### Global Sensitivity Analysis

| model | task | computational platform | | computational time |
|---|---|---|---|---|
| $\mathcal{M}_{3D}\text{-}\mathcal{C}$ | simulation of 740'000 heartbeats | | 160 cores | **592'000 h (68 years)** |
| $\mathcal{M}_{ANN}\text{-}\mathcal{C}$ | training dataset generation | | 160 cores | 160 h |
| | reduced model training | | 1 core | 18 h |
| | simulation of 740'000 heartbeats | | 160 cores | 1 h 17 min |
| | | | | **180 h (~7.5 days)** |

**3'300x speedup**

### Bayesian Parameter Estimation

| model | task | computational platform | | computational time |
|---|---|---|---|---|
| $\mathcal{M}_{3D}\text{-}\mathcal{C}$ | simulation of 960'000 heartbeats | | 160 cores | **768'000 h (87 years)** |
| $\mathcal{M}_{ANN}\text{-}\mathcal{C}$ | training dataset generation | | 160 cores | 120 h |
| | reduced model training | | 1 core | 18 h |
| | simulation of 960'000 heartbeats | | 20 cores | 13 h 20 min |
| | | | | **162 h (~6.25 days)** |

**5'000x speedup**

Figure 5.10: Summary of the computational times required to solve and train the models (top) or associated with global sensitivity analysis (center) and Bayesian parameter estimation (bottom).

overall speedup of 5'000x. Moreover, we notice that in case we need to execute a Bayesian calibration for different data, it is not necessary to repeat the training of the ANN-based model, but it is sufficient to re-run only the MCMC algorithm, which takes – thanks to our ROM – only 13 hours and 20 minutes. Finally, we remark that the cost required to train the ANN or to perform simulations with the $\mathcal{M}_{ANN}$-$\mathcal{C}$ model does not depend on the specific $\mathcal{M}_{3D}$ model at hand, as it is only based on the generated pressure and volume transients. In particular, it is not expected to raise if the biophysical detail or the number of degree of freedom of the computational mesh increase.

In recent times, a number of surrogate models of cardiac electromechanics have been proposed in the literature. They are built using Machine Learning techniques and they are often called emulators [27, 44, 47, 98]. These emulators are based on a collection of pre-computed numerical simulations obtained by sampling the parameter space, similarly to what has been done in this work. However, the approach behind these emulators is very different from the one we follow. These emulators are in fact functions that fit the parameters-to-QoIs map ($\mathcal{F}\colon \mathbf{p} \mapsto \mathbf{q}$) in a static manner. On the contrary, with our approach, the ROM makes it possible to perform a real numerical simulation of the cardiac function, since the circulation model $\mathcal{C}$ is kept in its full-order form, while only the computationally demanding part, i.e. the 3D electromechanical model ($\mathcal{M}_{3D}$), is surrogated. This has a number of advantages:

1. The ROM $\mathcal{M}_{ANN}$ is independent of the circulation model $\mathcal{C}$ to which is coupled and it can also be coupled to models different from those used during training, or with different values of its parameters.

2. Unlike the emulators in [27, 44, 47, 98], our ROM allows for time extrapolation, i.e. reliable predictions even over longer time spans than those used during training, as demonstrated by our numerical results. This observation is very important since, while for emulators that fit the parameters-to-QoIs map the simulations contained in the training set must have reached a limit cycle (otherwise the associated QoIs would be meaningless), with our approach it is possible to defer the reaching of the limit cycle to the ROM, during the online phase. This permits to lighten the computational cost associated with the creation of the training set, which typically represents the main component of the total cost (see use cases cited above).

3. The output of the simulations obtained with our ROM is not limited to a list of QoIs. Indeed, it contains the transient of pressures and volumes of the heart chamber that is surrogated and of the compartments of the circulation model. We notice that the latter is not hidden as a black-box in the parameters-to-QoIs map, as for emulators, but is rather represented explicitly.

4. With our approach, the ROM only needs to learn the variability with respect to $\mathbf{p}_{\mathcal{M}}$ since the circulation model (involving the parameters $\mathbf{p}_{\mathcal{C}}$) remains explicitly represented. Conversely, emulators based on a parameters-to-QoIs map must capture the dependence on both $\mathbf{p}_{\mathcal{M}}$ and $\mathbf{p}_{\mathcal{C}}$ and thus the

training set must be large enough to accurately represent their statistical variability. Indeed, we obtained accurate results with only 30–40 samples, a very low number compared to the ones typically required to construct emulators (e.g. 825 samples in [98], 9000 samples in [27]).

A limitation of our ANN-based ROM is that the online phase may be slower than the one of emulators, which do not require to approximate a differential equation but only need to evaluate a function. However, our ANN-based ROM enables real-time simulations and can be readily applied in a number of use cases, such as global sensitivity analysis, parameter estimation and uncertainty quantification. Furthermore, as highlighted above, most of the computational cost is not due to the evaluation of the ROM, but rather to the construction of the training set, which our approach allows to keep very small (30–40 samples in our test cases). Therefore, we conclude that keeping the circulation model in its full-order form and surrogating only the computationally intensive electromechanical model allows for a very favorable trade-off between what is reduced (variability that must be explored during the offline phase) and what is not reduced (variability that must be account for in the online phase).

A different type of emulator is the one proposed in [145], that permits - similarly to what done in this thesis - to couple a reduced version of the 3D electromechanical model to a circulation model, thus enabling for real-time numerical simulations. However, the emulator of [145] either is built for a fixed value of the parameters $\mathbf{p}_{\mathcal{M}}$, or accounts (through a linear interpolation) for the variability of a single parameter at most. On the other hand, its construction only requires one or two numerical simulations performed through the FOM. Therefore, the emulator of [145] is advantageous when one needs to surrogate the model for a given parametrization (e.g. to quickly converge to a limit cycle, or to perform sensitivity analysis on $\mathbf{p}_{\mathcal{C}}$ only); conversely, when one needs to explore the parametric dependence of an electromechanical model, our ANN-based approach turns out to be advantageous.

The Machine Learning technique proposed in [141] features several differences with respect to projection-based ROMs, which have been used in the cardiovascular field as well (see e.g. [22, 118, 119, 135]), or Deep Learning based approximations of the parameters-to-solution map (see e.g. [58]). The latter families of ROMs indeed provide a richer output than our ROM, as they allow for the approximation of spatially varying outputs of the 3D model, such as the transmembrane potential and tissue displacement. However, the online phase of projection-based ROMs is typically more computationally demanding [22, 119]. Moreover, projection-based ROMs are intrusive in the equations to be reduced and suitable hyper-reduction techniques should be addressed to handle the nonlinearities of cardiac models. The Deep Learning based method of [58] features a training phase that is more computationally demanding, due to the larger size of the output. Conversely, in applications in which the knowledge of pressures, volumes and blood fluxes associated with the cardiac chambers are sufficient, our ROM permits to accurately approximate the outputs of the FOM at a very

reduced computational cost and in a non-intrusive manner (only pressure and volume recordings are required from the FOM).

We remark that the proposed method is limited to electromechanical simulations that feature a periodic behavior, such as in SR. The ROM is indeed periodic by construction, due to the presence of the sine and cosine terms, as highlighted in Eq. (5.3). Therefore, the ROM is not suitable, e.g., to simulate an irregular electrophysiological behavior, such as arrhythmias and other electric dysfunctions.

In this thesis, we developed a novel and comprehensive mathematical and numerical model for the simulation of cardiac electromechanics in human ventricles with ICM, where the different physical phenomena therein involved are described by means of biophysically detailed core models [6, 162]. We modeled scars and grey zones of the myocardium by properly changing the electromechanical properties of these regions. In particular, regions of dense scars do not contract at all and are very stiff. With respect to healthy areas, grey zones show a reduced CV, a lower AP peak after the upstroke and a longer APD. Moreover, they have intermediate contractility and stiffness properties among scars and healthy regions.

Our 3D electromechanical model for the LV is coupled with either a windkessel afterload model or a ∅D closed-loop model that accounts for the rest of the cardiocirculatory system. We proved that the 3D-∅D closed-loop model fulfills the principle of conservation of mechanical energy [147]. Indeed, the power exerted by the cavity pressure in the 3D electromechanical model balances the power exchanged with the ∅D circulation model at the coupling interface. We analyzed the mechanical work associated with the different compartments of our circulation model and we proved that a balance of mechanical energy is satisfied by the model. This balance holds both when we consider the ∅D circulation model alone and when we consider the 3D-∅D coupled problem too. We showed that the circulation model considered in this thesis can be exploited to provide better quantitative insights into the heart energy distribution than the relationships used in daily clinical practice. In particular, if common formulas from daily clinical practice are employed, the mechanical work is understimated by 16%, the LV work is underestimated by 11% and the total work of the myocardium is underestimated by 24%.

We proposed two numerical schemes that are aimed at coupling, in a computationally efficient and accurate manner, mathematical models with different space and time characteristic scales [148, 161]. Our computational framework is based on three main pillars, namely: (1) a fully partitioned coupling of the different core models; (2) parallel and flexible intergrid transfer operators to interpolate relevant Finite Element functions among different meshes that reflect the space resolution needed to approximate a specific core model; (3) IMEX schemes to approximate the single core physics in a staggered fashion by using a suitable time step. The two SIS strategies we developed are numerically stable, and prove to be faster and less memory-demanding than the monolithic approach [146, 162]. Moreover, the SIS2 scheme enforces the coupling between the ∅D circulation model and the 3D electromechanical model by reinterpreting the LV cavity pressure as a Lagrange multiplier associated with a volumetric constraint [148]. This allows for the effective simulation of VT. Indeed, the nu-

merical scheme does not distinguish among the four different phases of the PV loop as in previous formulations of electromechanical models [162].

As a further new contribution, we introduced an algorithm to reconstruct the reference (i.e. stress-free) configuration of the LV starting from a stressed configuration obtained from medical images, by solving a suitable inverse problem [148]. Determining such configuration is essential to correctly initialize electromechanical simulations. This is especially useful in patient-specific scenarios where the EDP and/or the EDV are possibly known. Furthermore, this reference configuration recovery algorithm keeps into account the distribution of infarct zones, peri-infarct areas and non-remodeled regions in its numerical resolution.

We carried out several numerical simulations in the context of cardiac electromechanics, based on idealized or realistic LV geometries, with and without ICM [148, 161–163]. We varied different parameters of the 3D-ØD coupled model for an LV without ICM to affect preload, afterload and contractility, thus investigating the response of our mathematical model to different situations of clinical interest. The increase of SV as a consequence of increased preload is correctly reproduced, coherently with the Frank-Starling law, thus guaranteeing the matching between the venous return and the cardiac output. We also performed numerical simulations of patient-specific LVs with ICM in SR to fit clinical data, by manually calibrating the parameters of our electromechanical model coupled with a 2-element windkessel afterload model. We commented on the main differences observed in the PV loop of an LV with ICM with respect to a reference healthy case. Specifically, there is an increase in EDV and EDP, and a significant reduction in SV/EF and contractility. We studied the effects of geometry-mediated MEFs and nonselective SACs on sustained VT for LVs with ICM by exploiting the coupling between our 3D electromechanical model and a ØD closed-loop circulation model of the whole cardiovascular system. By combining electrophysiology, activation, mechanics and hemodynamics, we observed several differences on VT propagation with respect to electrophysiological simulations. In particular, geometry-mediated MEFs do not affect VT stability but may alter the VT BCL, along with its exit site. On the other hand, the recruitment of SACs may generate EADs or DADs, which may change the hemodynamic nature of VT. These extra stimuli are driven by myocardial contraction and are induced by changes in the APD or in the resting value of the transmembrane potential. We concluded that both geometry-mediated MEFs and nonselective SACs define important contributions in electromechanical models with hemodynamic coupling, especially when numerical simulations under arrhythmia are carried out. Thanks to the ØD circulation model, we get the evolution in time of LV pressure and volume, LA pressure and volume, arterial system pressure, MV and AV flow rates, which allow to classify the hemodynamic nature of VT. This has important clinical implications for VT treatment planning [162].

Finally, we presented a Machine Learning method to build ANN-based ROMs of cardiac electromechanical models [149]. Our algorithm is capable of learning, on the basis of pressure and volume transients generated with the FOM, a system of differential equations that approximate the dynamics of the cardiac

chamber to be surrogated. This differential equation, linking pressure and volume of a cardiac chamber, is coupled with lumped-parameter models of cardiac hemodynamics, thus allowing for the numerical simulation of the cardiac function at a dramatically reduced computational cost with respect to the original FOM. As a matter of fact, our ANN-based ROM permits to perform numerical simulations virtually in real-time while keeping the relative errors with respect to the pressure and volume transients of the FOM small, i.e. of the order of $10^{-3}$-$10^{-2}$. Moreover, thanks to its non-intrusive nature, the proposed method can be easily applied to other electromechanical models besides the one considered in this thesis. We presented two test cases in which we employ the ANN-based ROM. We carried out a global sensitivity analysis to assess the influence of the parameters of the electromechanical and hemodynamic models on a list of outputs of clinical interest. Then, we performed a Bayesian estimation of a couple of parameters, starting from the noisy measurement of a couple of scalar quantities (namely maximum and minimum arterial pressure). In both the cases, performing through the FOM the large number of numerical simulations needed would not have been possible, due to their high computational cost (it would in fact have taken tens of years on a supercomputer computational platform). Replacing the FOM with its ANN-based surrogate allowed us to obtain an approximate solution in a few hours of computation. Taking into account that generating the numerical simulations of the training set required less than 7 days on the same computational platform, our ANN-based ROM allowed us to reduce the total computational time by more than 3'000 times.

FUTURE DEVELOPMENTS

Several future developments can be foreseen, on the ground of the achievements of this thesis.

- Our computational model for ICM can be further improved by avoiding using only three discrete levels for scars, grey zones and healthy regions. This can be obtained for example by integrating different types of non-invasive imaging data with invasive high-density catheter mapping data [6, 59, 120, 167, 176].

- There are other types of MEFs that could be investigated in future works. Among them, an important role is certainly played by the mechanical effects mediated by fibroblasts in the extracellular matrix, $[Ca^{2+}]_i$ buffers handling, alterations in transmembrane capacitance $C_m$ due to local stretch and ions selective SACs [89]. Indeed, modeling different cellular processes in cardiac electromechanics might be of interest to shed further light on the underlying mechanisms of arrhythmias [163].

- Our SIS2 scheme leaves room for the study of high-order methods in the context of cardiac electromechanics. Indeed, wave propagation problems, such as the one arising in cardiac electrophysiology, can be suitably represented using high-order basis functions, which can be obtained for ex-

ample by Isogeometric Analysis or Spectral Element Methods [24, 28, 63]. These techniques potentially guarantee higher accuracy and lead to lower numerical dispersion and dissipation than FEM while using a smaller number of DOFs [63, 127].

- The numerical simulations of the FOM of cardiac electromechanics can be accelerated by means of matrix-free solvers [93], which are more efficient and less memory demanding than matrix-based approaches. In particular, the fairly reduced memory requirements of matrix-free solvers leave room to parallel frameworks based on graphics processing units (GPUs) or tensor processing units (TPUs), where RAM usage must be generally limited with respect to standard CPU-based HPC architectures [194].

- Albeit in this thesis we focused on LV numerical simulations, the 3D-ØD coupling that we described can be also extended to a biventricular [131] or a four chambers representation of the human heart. Similarly, the procedure to reconstruct the reference geometry can be generalized and employed for both atria and ventricles.

- Our Machine Learning method can be also employed to build ANN-based ROMs of whole-heart electromechanics and to account for various cardiovascular diseases.

- Finally, we may also design ANN-based ROMs for space- and time-dependent fields associated to PDEs, such as action potential, ionic variables, protein states and mechanical displacement. This would allow for global sensitivity analysis and uncertainty quantification on all the parameters of the 3D electromechanical model, ranging from the cell to the tissue level.

# Appendices

# A

## PARAMETERS OF THE ELECTROMECHANICAL MODEL

In this appendix, we report the electromechanical parameters that we use to run the numerical simulations of this thesis in both physiological and pathological conditions.

### A.1 PHYSIOLOGICAL CONDITIONS

#### A.1.1 *Idealized left ventricle*

In Tab. A.1 we provide the full list of the electromechanical parameters for the SR simulation with an idealized LV (Sec. 3.1), which has been performed by means of the $(\mathscr{E})$–$(\mathscr{I})$–$(\mathscr{A}_{\text{strain}})$–$(\mathscr{W})$–$(\mathscr{M})$ mathematical model.

| $\sigma_l$ | $\sigma_t, \sigma_n$ | $\lambda_{\text{epi}}$ | $\lambda_{\text{endo}}$ | $\bar{k}_{\text{epi}}$ | $\bar{k}_{\text{endo}}$ | $\bar{k}'$ | $\alpha$ |
|---|---|---|---|---|---|---|---|
| 120.4 | 17.61 | 0.8 | 0.5 | 0.75 | 1.0 | -7.0 | -6.0 |
| $[Ca^{2+}]_{i,o}$ | $\hat{\mu}_A^1$ | $\hat{\mu}_A^2$ | $\hat{\mu}_A^3$ | $\hat{\mu}_A^4$ | $SL_{\min}$ | $SL_{\max}$ | $SL_o$ |
| 0.05 | 2.1 | 7.0 | 12 | 500 | 1.7 | 2.6 | 1.95 |
| $d_o$ | $d_1$ | $d_2$ | $d_3$ | $e_1$ | $e_2$ | $e_3$ | $\rho$ |
| -4.33e3 | 2.57e3 | 1.33e3 | 0.10e3 | -2.05e3 | 0.30e3 | 0.22e3 | 1e-3 |
| B | $C_{\text{guccione}}$ | $K_\perp^{epi}$ | $K_\parallel^{epi}$ | $C_\perp^{epi}$ | $C_\parallel^{epi}$ | C | R |
| 50000 | 880 | 0.2 | 0.0 | 0.005 | 0.0 | 4500 | 3.5e-5 |

Table A.1: Parameters used in the electromechanical simulation with an idealized LV: longitudinal and transversal conductivities $\sigma_l$, $\sigma_t$ and $\sigma_n$ $\left(\frac{mm^2}{s}\right)$; transmurally heterogeneous wall thickening coefficients $\lambda_{\text{epi}}$, $\lambda_{\text{endo}}$, $\bar{k}_{\text{epi}}$, $\bar{k}_{\text{endo}}$ and $\bar{k}'$; active strain coefficients $\alpha$ $\left(\mu M^{-2}\right)$, $[Ca^{2+}]_{i,o}$, and $\hat{\mu}_A$ $\left(\mu M^2 \cdot s\right)$ of the four cardiac phases; minimum, maximum, reference sarcomere lengths $SL_{\min}$, $SL_{\max}$ and $SL_o$ ($\mu m$) respectively; coefficients of the truncated Fourier series approximation of the force-length relationship $d_o$, $d_1$, $d_2$, $d_3$, $e_1$, $e_2$, $e_3$; density $\rho$ $\left(\frac{g}{mm^3}\right)$; bulk modulus B (Pa); Guccione parameter $C_{\text{guccione}}$ (Pa); Robin boundary condition coefficients $K_\perp^{epi}$ and $K_\parallel^{epi}$ $\left(\frac{kPa}{mm}\right)$, $C_\perp^{epi}$ and $C_\parallel^{epi}$ $\left(\frac{kPa \cdot s}{mm}\right)$; windkessel model parameters C and R $\left(\frac{mm^3}{kPa}, \frac{kPa \cdot s}{mm^3}\right)$.

We provide the full list of parameters adopted for the baseline electromechanical simulation in SR on the Zygote LV (Sec. 3.2), which has been performed with the $(\mathscr{E})$–$(\mathscr{I})$–$(\mathscr{A}_{\text{stress}})$–$(\mathscr{C})$–$(\mathscr{V})$–$(\mathscr{M})$ mathematical model. Specifically, Tab. A.2 contains the parameters related to the electrophysiological model, Tab. A.3 those related to the mechanical model and Tab. A.4 the ones of the circulation model. For the TTP06 model, we adopt the parameters reported in the original paper (for mid-myocardial cells) [186]. For the RDQ18 model, we employ the parameters of the original paper [140].

| Variable | Value | Unit | Variable | Value | Unit |
|---|---|---|---|---|---|
| **Conductivity tensor** | | | **Applied current** | | |
| $\sigma_l$ | $0.7643 \cdot 10^{-4}$ | $\mathrm{m^2\,s^{-1}}$ | $\widetilde{\jmath}_{\text{app}}^{\max}$ | $35$ | $\mathrm{V\,s^{-1}}$ |
| $\sigma_t$ | $0.3494 \cdot 10^{-4}$ | $\mathrm{m^2\,s^{-1}}$ | $t_{\text{app}}$ | $3 \cdot 10^{-3}$ | $\mathrm{s}$ |
| $\sigma_n$ | $0.1125 \cdot 10^{-4}$ | $\mathrm{m^2\,s^{-1}}$ | | | |

Table A.2: Parameters of the electrophysiological model for the Zygote LV in physiological conditions.

| Variable | Value | Unit | Variable | Value | Unit |
|---|---|---|---|---|---|
| **Constitutive law** | | | **Boundary conditions** | | |
| B | $50 \cdot 10^3$ | Pa | $K_\perp^{\text{epi}}$ | $2 \cdot 10^5$ | $\mathrm{Pa\,m^{-1}}$ |
| C | $0.88 \cdot 10^3$ | Pa | $K_\parallel^{\text{epi}}$ | $2 \cdot 10^4$ | $\mathrm{Pa\,m^{-1}}$ |
| $b_{ff}$ | $8$ | – | $C_\perp^{\text{epi}}$ | $2 \cdot 10^4$ | $\mathrm{Pa\,s\,m^{-1}}$ |
| $b_{ss}$ | $6$ | – | $C_\parallel^{\text{epi}}$ | $2 \cdot 10^3$ | $\mathrm{Pa\,s\,m^{-1}}$ |
| $b_{nn}$ | $3$ | – | | | |
| $b_{fs}$ | $12$ | – | **Activation** | | |
| $b_{fn}$ | $3$ | – | $T_a^{\max}$ | $180 \cdot 10^3$ | Pa |
| $b_{sn}$ | $3$ | – | $SL_0$ | $2$ | $\mu\mathrm{m}$ |
| $\rho_s$ | $10^3$ | $\mathrm{kg\,m^{-3}}$ | | | |

Table A.3: Parameters of the mechanical model for the Zygote LV in physiological conditions.

## A.2 PATHOLOGICAL CONDITIONS

### A.2.1 *First patient-specific left ventricle*

We reuse the same parametrization reported in Sec. A.1.1 for the electromechanical simulation in SR on the first LV with ICM that we analyzed by means of the $(\mathscr{E})$–$(\mathscr{I})$–$(\mathscr{A}_{\text{strain}})$–$(\mathscr{W})$–$(\mathscr{M})$ mathematical model. This is motivated by the lack of additional clinical data, especially regarding the pressure-volume relationship, for this patient.

| Variable | Value | Unit | Variable | Value | Unit |
|---|---|---|---|---|---|
| **External circulation** | | | **Cardiac chambers** | | |
| $R_{AR}^{SYS}$ | 0.8 | $\mathrm{mmHg\,s\,mL^{-1}}$ | $E_{LA}^{pass}$ | 0.09 | $\mathrm{mmHg\,mL^{-1}}$ |
| $R_{AR}^{PUL}$ | 0.1625 | $\mathrm{mmHg\,s\,mL^{-1}}$ | $E_{RA}^{pass}$ | 0.07 | $\mathrm{mmHg\,mL^{-1}}$ |
| $R_{VEN}^{SYS}$ | 0.26 | $\mathrm{mmHg\,s\,mL^{-1}}$ | $E_{RV}^{pass}$ | 0.05 | $\mathrm{mmHg\,mL^{-1}}$ |
| $R_{VEN}^{PUL}$ | 0.1625 | $\mathrm{mmHg\,s\,mL^{-1}}$ | $E_{LA}^{act,max}$ | 0.07 | $\mathrm{mmHg\,mL^{-1}}$ |
| $C_{AR}^{SYS}$ | 1.2 | $\mathrm{mL\,mmHg^{-1}}$ | $E_{RA}^{act,max}$ | 0.06 | $\mathrm{mmHg\,mL^{-1}}$ |
| $C_{AR}^{PUL}$ | 10.0 | $\mathrm{mL\,mmHg^{-1}}$ | $E_{RV}^{act,max}$ | 0.55 | $\mathrm{mmHg\,mL^{-1}}$ |
| $C_{VEN}^{SYS}$ | 60.0 | $\mathrm{mL\,mmHg^{-1}}$ | $V_{0,LA}$ | 4.0 | mL |
| $C_{VEN}^{PUL}$ | 16.0 | $\mathrm{mL\,mmHg^{-1}}$ | $V_{0,RA}$ | 4.0 | mL |
| $L_{AR}^{SYS}$ | $5 \cdot 10^{-3}$ | $\mathrm{mmHg\,s^2\,mL^{-1}}$ | $V_{0,RV}$ | 10.0 | mL |
| $L_{AR}^{PUL}$ | $5 \cdot 10^{-4}$ | $\mathrm{mmHg\,s^2\,mL^{-1}}$ | **Cardiac valves** | | |
| $L_{VEN}^{SYS}$ | $5 \cdot 10^{-4}$ | $\mathrm{mmHg\,s^2\,mL^{-1}}$ | $R_{min}$ | 0.0075 | $\mathrm{mmHg\,s\,mL^{-1}}$ |
| $L_{VEN}^{PUL}$ | $5 \cdot 10^{-4}$ | $\mathrm{mmHg\,s^2\,mL^{-1}}$ | $R_{max}$ | 75006.2 | $\mathrm{mmHg\,s\,mL^{-1}}$ |

Table A.4: Parameters of the circulation model for the Zygote LV in physiological conditions. We consider a heartbeat period $T = 0.8\,\mathrm{s}$.

### A.2.2 *Second patient-specific left ventricle*

We provide the list of parameters adopted for both SR and VT simulations on the second LV with ICM (Sec. 4.1.2). SR simulations exploit the $(\mathscr{E})$–$(\mathscr{I})$–$(\mathscr{A}_{\text{strain}})$–$(\mathscr{W})$–$(\mathscr{M})$ mathematical model, while VT simulations employ the $(\mathscr{E})$–$(\mathscr{I})$–$(\mathscr{A}_{\text{strain}})$–$(\mathscr{C})$–$(\mathscr{V})$–$(\mathscr{M})$ mathematical model. Tab. A.5 contains the parameters related to the electrophysiological model and Tab. A.6 those related to the mechanical model. For the TTP06 model, we adopt the parameters of the original paper (for mid-myocardial cells) [186]. Tab. A.8 and Tab. A.9 contain the parameters of the circulation model in healthy and pathological conditions, respectively. In particular, for the pathological case we increase the resistance of the arterial system while decreasing its capacitance, to maintain their product almost constant. Morever, we raise the passive elastance of the RV while reducing the active one. Indeed, both from LGE-MRI and Cine MRI, we noticed that the RV of this patient might be affected by ICM as well. We observed that the RV presents a small dimension and a low SV ($\approx 25\,\mathrm{mL}$). Finally, we consider a fibrosis-free dilated LA, with higher active elastance and higher resting volume.

| Variable | Value | Unit | Variable | Value | Unit |
|---|---|---|---|---|---|
| **Conductivity tensor** | | | **Applied current** | | |
| $\sigma_l$ | $0.6714 \cdot 10^{-4}$ | $\mathrm{m^2\,s^{-1}}$ | $\widetilde{\jmath}_{\text{app}}^{\text{max}}$ | 35 | $\mathrm{V\,s^{-1}}$ |
| $\sigma_t$ | $0.0746 \cdot 10^{-4}$ | $\mathrm{m^2\,s^{-1}}$ | $t_{\text{app}}$ | $5 \cdot 10^{-3}$ | s |
| $\sigma_n$ | $0.0746 \cdot 10^{-4}$ | $\mathrm{m^2\,s^{-1}}$ | | | |

Table A.5: Parameters of the electrophysiological model for the second LV with ICM (taken from [6, 148]).

| Variable | Value | Unit | Variable | Value | Unit |
|---|---|---|---|---|---|
| **Constitutive law** | | | **Boundary conditions** | | |
| $B$ | $5 \cdot 10^4$ | $\mathrm{Pa}$ | $K_\perp^{\mathrm{epi}}$ | $2 \cdot 10^5$ | $\mathrm{Pa\,m^{-1}}$ |
| $C$ | $0.88 \cdot 10^3$ | $\mathrm{Pa}$ | $K_\parallel^{\mathrm{epi}}$ | $2 \cdot 10^5$ | $\mathrm{Pa\,m^{-1}}$ |
| $b_{ff}$ | $8$ | $-$ | $C_\perp^{\mathrm{epi}}$ | $2 \cdot 10^4$ | $\mathrm{Pa\,s\,m^{-1}}$ |
| $b_{ss}$ | $6$ | $-$ | $C_\parallel^{\mathrm{epi}}$ | $2 \cdot 10^3$ | $\mathrm{Pa\,s\,m^{-1}}$ |
| $b_{nn}$ | $3$ | $-$ | | | |
| $b_{fs}$ | $12$ | $-$ | **Activation** | | |
| $b_{fn}$ | $3$ | $-$ | $\hat{\mu}_A^1$ | $1.5$ | $\mathrm{s\,\mu M^2}$ |
| $b_{sn}$ | $3$ | $-$ | $\hat{\mu}_A^2$ | $3$ | $\mathrm{s\,\mu M^2}$ |
| $\rho_s$ | $10^3$ | $\mathrm{kg\,m^{-3}}$ | $\hat{\mu}_A^3$ | $1.2$ | $\mathrm{s\,\mu M^2}$ |
| | | | $\hat{\mu}_A^4$ | $5$ | $\mathrm{s\,\mu M^2}$ |

Table A.6: Parameters for passive mechanics (taken from [148]), boundary conditions and mechanical activation (manually calibrated) for the second LV with ICM. The other parameters of the active strain model are reported in Sec. A.1.1.

| Variable | Value | Unit |
|---|---|---|
| $C$ | 4.0e-10 | $\mathrm{m^3\,Pa^{-1}}$ |
| $R$ | 5.0e7 | $\mathrm{Pa\,s\,m^{-3}}$ |

Table A.7: Parameters of the windkessel model, which are manually calibrated to fit the clinical data reported in Tab. 4.2, for the second LV with ICM.

| Variable | Value | Unit | Variable | Value | Unit |
|---|---|---|---|---|---|
| **External circulation** | | | **Cardiac chambers** | | |
| $R_{AR}^{SYS}$ | $0.64$ | $\mathrm{mmHg\,s\,mL^{-1}}$ | $E_{RV}^{pass}$ | $0.05$ | $\mathrm{mmHg\,mL^{-1}}$ |
| $R_{VEN}^{SYS}$ | $0.035684$ | $\mathrm{mmHg\,s\,mL^{-1}}$ | $E_{LA}^{act,max}$ | $0.07$ | $\mathrm{mmHg\,mL^{-1}}$ |
| $R_{VEN}^{PUL}$ | $0.1625$ | $\mathrm{mmHg\,s\,mL^{-1}}$ | $E_{RV}^{act,max}$ | $0.55$ | $\mathrm{mmHg\,mL^{-1}}$ |
| $C_{AR}^{SYS}$ | $1.2$ | $\mathrm{mL\,mmHg^{-1}}$ | $V_{0,LA}$ | $4.0$ | $\mathrm{mL}$ |

Table A.8: Parameters of the circulation model in healthy conditions for the second LV with ICM. We consider a heartbeat period $T = 0.92\,\mathrm{s}$. The remaining parameters are reported in Sec. A.1.2.

## A.2.3  *Zygote left ventricle*

We provide the full list of parameters adopted for the VT simulations on the Zygote LV endowed with an idealized distribution of the ischemia (Sec. 4.2), where we use the $(\mathscr{E})$–$(\mathscr{I})$–$(\mathscr{A}_{\mathrm{stress}})$–$(\mathscr{C})$–$(\mathscr{V})$–$(\mathscr{M})$ mathematical model. Specifically, Tab. A.10 contains the parameters related to the electrophysiological model, Tab. A.11 those related to the sarcomere model RDQ20-MF, Tab. A.12 the parameters of the mechanical model and Tab. A.13 the ones associated with the circulation model. For the TTP06 model, we adopt the parameters reported in the original paper (for endocardial cells) [185], with the only difference that we

| Variable | Value | Unit | Variable | Value | Unit |
|---|---|---|---|---|---|
| **External circulation** | | | **Cardiac chambers** | | |
| $R_{AR}^{SYS}$ | 1.0 | $mmHg\, s\, mL^{-1}$ | $E_{RV}^{pass}$ | 0.3 | $mmHg\, mL^{-1}$ |
| $R_{VEN}^{SYS}$ | 0.26 | $mmHg\, s\, mL^{-1}$ | $E_{LA}^{act,max}$ | 0.14 | $mmHg\, mL^{-1}$ |
| $R_{VEN}^{PUL}$ | 0.035684 | $mmHg\, s\, mL^{-1}$ | $E_{RV}^{act,max}$ | 0.4 | $mmHg\, mL^{-1}$ |
| $C_{AR}^{SYS}$ | 0.8 | $mL\, mmHg^{-1}$ | $V_{0,LA}$ | 5.0 | $mL$ |

Table A.9: Parameters of the circulation model in pathological conditions for the second LV with ICM. We consider a heartbeat period $T = 0.92\,s$. The remaining parameters are reported in Sec. A.1.2.

rescale the intracellular calcium concentration $[Ca^{2+}]_i$ by a factor of $\omega_{Ca}$ to get more physiological values [39].

| Variable | Value | Unit | Variable | Value | Unit |
|---|---|---|---|---|---|
| **Conductivity tensor** | | | **Applied current** | | |
| $\sigma_l$ | $0.7643 \cdot 10^{-4}$ | $m^2\, s^{-1}$ | $\widetilde{J}_{app}^{max}$ | 17 | $V\, s^{-1}$ |
| $\sigma_t$ | $0.3494 \cdot 10^{-4}$ | $m^2\, s^{-1}$ | $t_{app}$ | $3 \cdot 10^{-3}$ | $s$ |
| $\sigma_n$ | $0.1125 \cdot 10^{-4}$ | $m^2\, s^{-1}$ | **Calcium rescaling** | | |
| | | | $\omega_{Ca}$ | 0.48 | - |

Table A.10: Parameters of the electrophysiological model for the Zygote LV with an idealized ischemia.

| Variable | Value | Unit | Variable | Value | Unit |
|---|---|---|---|---|---|
| **Regulatory units steady-state** | | | **Crossbridge cycling** | | |
| $\mu$ | 10 | - | $\mu_{f,p}^0$ | 32.255 | $s^{-1}$ |
| $\gamma$ | 30 | - | $\mu_{f,p}^1$ | 0.768 | $s^{-1}$ |
| $Q$ | 2 | - | $r_0$ | 134.31 | $s^{-1}$ |
| $\bar{k}_d$ | 0.4 | $\mu M$ | $\alpha$ | 25.184 | - |
| $\alpha_{k_d}$ | $-0.2083$ | $\mu M\, \mu m^{-1}$ | **Upscaling** | | |
| **Regulatory units kinetics** | | | $a_{XB}$ | 160 | $MPa$ |
| $k_-$ | 40 | $s^{-1}$ | $SL_0$ | 1.9 | $\mu m$ |
| $k_T$ | 8 | $s^{-1}$ | | | |

Table A.11: Parameters of the sarcomere model RDQ20-MF for the Zygote LV with an idealized ischemia (for the definition of the parameters, see [142]).

| Variable | Value | Unit | Variable | Value | Unit |
|---|---|---|---|---|---|
| **Constitutive law** | | | **Boundary conditions** | | |
| B | $50 \cdot 10^3$ | Pa | $K_\perp^{epi}$ | $2 \cdot 10^5$ | $Pa\,m^{-1}$ |
| C | $0.88 \cdot 10^3$ | Pa | $K_\parallel^{epi}$ | $2 \cdot 10^4$ | $Pa\,m^{-1}$ |
| $b_{ff}$ | 8 | – | $C_\perp^{epi}$ | $2 \cdot 10^4$ | $Pa\,s\,m^{-1}$ |
| $b_{ss}$ | 6 | – | $C_\parallel^{epi}$ | $2 \cdot 10^3$ | $Pa\,s\,m^{-1}$ |
| $b_{nn}$ | 3 | – | **Tissue density** | | |
| $b_{fs}$ | 12 | – | $\rho_s$ | $10^3$ | $kg\,m^{-3}$ |
| $b_{fn}$ | 3 | – | | | |
| $b_{sn}$ | 3 | – | | | |

Table A.12: Parameters of the mechanical model for the Zygote LV with an idealized ischemia.

| Variable | Value | Unit | Variable | Value | Unit |
|---|---|---|---|---|---|
| **External circulation** | | | **Cardiac chambers** | | |
| $R_{AR}^{SYS}$ | 0.64 | $mmHg\,s\,mL^{-1}$ | $E_{LA}^{pass}$ | 0.18 | $mmHg\,mL^{-1}$ |
| $R_{AR}^{PUL}$ | 0.032116 | $mmHg\,s\,mL^{-1}$ | $E_{RA}^{pass}$ | 0.07 | $mmHg\,mL^{-1}$ |
| $R_{VEN}^{SYS}$ | 0.32 | $mmHg\,s\,mL^{-1}$ | $E_{RV}^{pass}$ | 0.05 | $mmHg\,mL^{-1}$ |
| $R_{VEN}^{PUL}$ | 0.035684 | $mmHg\,s\,mL^{-1}$ | $E_{LA}^{act,max}$ | 0.07 | $mmHg\,mL^{-1}$ |
| $C_{AR}^{SYS}$ | 1.2 | $mL\,mmHg^{-1}$ | $E_{RA}^{act,max}$ | 0.06 | $mmHg\,mL^{-1}$ |
| $C_{AR}^{PUL}$ | 10.0 | $mL\,mmHg^{-1}$ | $E_{RV}^{act,max}$ | 0.55 | $mmHg\,mL^{-1}$ |
| $C_{VEN}^{SYS}$ | 60.0 | $mL\,mmHg^{-1}$ | $V_{0,LA}$ | 4.0 | mL |
| $C_{VEN}^{PUL}$ | 16.0 | $mL\,mmHg^{-1}$ | $V_{0,RA}$ | 4.0 | mL |
| $L_{AR}^{SYS}$ | $5 \cdot 10^{-3}$ | $mmHg\,s^2\,mL^{-1}$ | $V_{0,RV}$ | 16.0 | mL |
| $L_{AR}^{PUL}$ | $5 \cdot 10^{-4}$ | $mmHg\,s^2\,mL^{-1}$ | **Cardiac valves** | | |
| $L_{VEN}^{SYS}$ | $5 \cdot 10^{-4}$ | $mmHg\,s^2\,mL^{-1}$ | $R_{min}$ | 0.0075 | $mmHg\,s\,mL^{-1}$ |
| $L_{VEN}^{PUL}$ | $5 \cdot 10^{-4}$ | $mmHg\,s^2\,mL^{-1}$ | $R_{max}$ | 75006.2 | $mmHg\,s\,mL^{-1}$ |

Table A.13: Parameters of the circulation model for the Zygote LV with an idealized ischemia. We consider a heartbeat period $T = 0.8\,s$.

# REDUCED-ORDER MODELING OF CARDIAC ELECTROMECHANICS

In this appendix we report the main numerical approaches that we employ to develop and test our ROM of cardiac electromechanics.

## B.1 NUMERICAL SIMULATIONS

We use the same choices in terms of space and time discretization for all the numerical simulations involving the FOM. Specifically, we employ a finer mesh for cardiac electrophysiology, which consists of 258'415 DOFs and 240'864 elements (with an average mesh size of $h_{mean} = 1.7\,mm$), and a coarser one for cardiac mechanics, which is made by 35'725 DOFs and 30'108 elements ($h_{mean} = 3.4\,mm$). To advance the electrophysiological variables we use a time step $\Delta t = 100\,\mu s$, while a five times larger time step is employed to advance the mechanical variables. The numerical simulations have run by using one cluster node endowed with 32 cores (four Intel Xeon E5-4610 v2, 2.3 GHz) which is available at MOX, Dipartimento di Matematica.

## B.2 CONVERGENCE TO THE LIMIT CYCLE

To determine when a numerical simulation reached a limit cycle (i.e. a periodic solution), we employ a criterion based on the increment between successive cycles. In particular, we consider the limit cycle to be reached when the maximum difference between two consecutive cycles in the pressures and volumes of all four chambers is less than $0.8\,mmHg$ and $0.8\,mL$, respectively. This criterion is typically satisfied in 5 to 15 cycles. In any case, we always perform a minimum of 5 cycles.

## B.3 TRAINING ALGORITHM

To generate the training datasets, we employ a Monte Carlo based sampling of the parameter space $\mathscr{P}_M \times \mathscr{P}_C$. We consider a subset of the parameters $\mathbf{p}_C$ which is made by:

$$V_{heart}^{tot}, E_{LA}^{pass}, t_L^{av}, E_{RA}^{pass}, t_R^{av}, E_{RV}^{act}, E_{RV}^{pass}, R_{AR}^{SYS}, R_{VEN}^{SYS}.$$

To define the sampling spaces $\mathscr{P}_M$ and $\mathscr{P}_C$, we consider 50% to 200% ranges of the baseline values reported in Tabs. 5.1 and 5.2 for $V_{heart}^{tot}$, $E_{LA}^{pass}$, $\alpha_{XB}$, $E_{RA}^{pass}$, $E_{RV}^{act}$, $E_{RV}^{pass}$, $R_{AR}^{SYS}$ and $R_{VEN}^{SYS}$, 50% to 150% for $\sigma_f$ and C. We vary $\alpha \in (40°, 80°)$ and $t_L^{av}, t_R^{av} \in (0.08, 0.24)$ s.

To train the ANN-based model according to Eq. (5.4), we employ the algorithm that we proposed in [141]. More precisely, we approximate the trained ODE with a time step size of $\Delta t = 5\,\mathrm{ms}$ and the objective functional with a twice as wide time step. To train the ANN, we employ 2000 iterations of the Levenberg-Marquardt algorithm.

## B.4 HYPERPARAMETERS TUNING

To tune the hyperparameters, we adopt a k-fold cross-validation procedure as described in Sec. 5.1.3. Specifically, we consider a given hyperparameter setting and we partition the training dataset in $k = 5$ non-overlapping subsets. Then, by retaining a single subset as validation data, we train, on the remaining $k - 1$ subsets, three different models (with three different random initializations of the ANN weights) and we keep the model attaining the lowest validation error. This procedure is repeated k times, once for each subset. Finally, we average the errors over the k trained models, and we compare the resulting average errors for different hyperparameter settings. More precisely, to compare the performances of the models obtained with different hyperparameter settings, we consider the validation errors associated with the QoIs reported in Tab. 5.3, in terms of relative errors. Moreover, we assess the generalization skills of the trained models by computing the ratio between validation errors and training errors. Indeed, a ratio that is much larger than one indicates overfitting. By following these criteria, we get to the final configurations of Tab. 5.4.

## B.5 GLOBAL SENSITIVITY ANALYSIS

To perform global sensitivity analysis, we consider all parameters $\mathbf{p}_{\mathcal{M}}$ and $\mathbf{p}_{\mathcal{C}}$, which are reported in Tabs. 5.1 and 5.2, respectively. To define the sampling spaces $\mathscr{P}_{\mathcal{M}}$ and $\mathscr{P}_{\mathcal{C}}$, we consider 80% to 120% ranges of the baseline values in Tabs. 5.1 and 5.2, except for $V_{\mathrm{heart}}^{\mathrm{tot}} \in (193, 593)$ mL and for $t_{\mathrm{L}}^{\mathrm{av}}, t_{\mathrm{R}}^{\mathrm{av}} \in (0.04, 0.28)$ s.

We employ the Saltelli's method to sample the parametric space $\mathscr{P}_{\mathcal{M}} \times \mathscr{P}_{\mathcal{C}}$. A naive sampling of the space would require an exponential increase with respect to the number of parameters to guarantee a prescribed accuracy; conversely, Saltelli's method leads to a linear increase. More precisely, the number of samples required is $N(2D + 2)$, where D is the number of parameters and N is a user defined setting. In this thesis we set $N = 1000$, for a total of 74'000 samples, that guarantees small confidence intervals around the first-order Sobol indices and the total-effect Sobol indices reported in Figs. 5.7 and 5.8, respectively. We use one cluster node endowed with 20 cores (four Intel Xeon E5-2640 v4, 2.4 GHz), which is available at MOX, Dipartimento di Matematica, to run global sensitivity analysis.

We perform Bayesian parameter estimation by means of the MCMC method. We consider 500 samples per chain, a jump period of 10 samples and a burn-in equal to 1000, for a total number of 20 chains. Indeed, we use one cluster node endowed with 20 cores (four Intel Xeon E5-2640 v4, 2.4 GHz), which is available at MOX, Dipartimento di Matematica, where each core manages a single chain and then all final results are collected together at the end of the numerical simulation.

[1] P. C. Africa. "Scalable adaptive simulation of organic thin-film transistors." PhD thesis. Politecnico di Milano, 2019.

[2] D. Ambrosi and S. Pezzuto. "Active stress vs. active strain in mechanobiology: constitutive issues." In: *Journal of Elasticity* 107 (2012), pp. 199–212.

[3] D. Ambrosi, G. Arioli, F. Nobile, and et al. "Electromechanical coupling in cardiac dynamics: the active strain approach." In: *SIAM Journal on Applied Mathematics* 71 (2011), pp. 605–621.

[4] W. Anderson. *Coronary Artery Disease (Ischemic Heart Disease): Overview & Pathophysiology*. 2019. URL: https://schoolworkhelper.net/coronary-artery-disease-ischemic-heart-disease-overview-coronary-artery-disease-ischemic-heart-disease-overview-pathophysiology/.

[5] L. Antiga, M. Piccinelli, L. Botti, and et al. "An image-based modeling framework for patient-specific computational hemodynamics." In: *Medical and Biological Engineering and Computing* 46 (2008), pp. 1097–1112.

[6] H. Arevalo, F. Vadakkumpadan, E. Guallar, and et al. "Arrhythmia risk stratification of patients after myocardial infarction using personalized heart models." In: *Nature Communications* 7 (2016), pp. 113–128.

[7] D. Arndt, W. Bangerth, B. Blais, and et al. "The `deal.II` Library, Version 9.2." In: *Journal of Numerical Mathematics* 28.3 (2020), pp. 131–146.

[8] C. M. Augustin, A. Neic, M. Liebmann, and et al. "Anatomically accurate high resolution modeling of human whole heart electromechanics: A strongly scalable algebraic multigrid solver method for nonlinear deformation." In: *Journal of Computational Physics* 305 (2016), pp. 622–646.

[9] C. M. Augustin, Fastl T. E., A. Neic, and et al. "The impact of wall thickness and curvature on wall stress in patient-specific electromechanical models of the left atrium." In: *Biomechanics and Modeling in Mechanobiology* 19 (2019), pp. 1015–1034.

[10] C. M. Augustin, M. A. F. Gsell, E. Karabelas, and et al. "A computationally efficient physiologically comprehensive 3D-0D closed-loop model of the heart and circulation." In: *Computer Methods in Applied Mechanics and Engineering* 386 (2021), p. 114092.

[11] L. Azzolin, L. Dede', A. Gerbi, and A. Quarteroni. "Effect of fibre orientation and bulk modulus on the electromechanical modelling of human ventricles." In: *Mathematics in Engineering* 2.mine-02-04-028 (2020), p. 614.

[12] Y. Bao, A. Donev, and B. E. Griffith. "An immersed boundary method with divergence-free velocity interpolation." In: *Journal of Computational Physics* 347 (2017), pp. 183–206.

[13] L. Barbarotta, S. Rossi, L. Dede', and A. Quarteroni. "A transmurally heterogeneous orthotropic activation model for ventricular contraction and its numerical validation." In: *Numerical Methods in Biomedical Engineering* 34 (2018).

[14] C. Bartolucci, E. Passini, J. Hyttinen, and et al. "Simulation of the Effects of Extracellular Calcium Changes Leads to a Novel Computational Model of Human Ventricular Action Potential With a Revised Calcium Handling." In: *Frontiers in Physiology* 11 (2020), p. 314.

[15] M. B. Bastos, D. Burkhoff, J. Maly, and et al. "Invasive left ventricle pressure-volume analysis: overview and practical clinical implications." In: *European Heart Journal* 41.12 (2019), pp. 1286–1297.

[16] J. D. Bayer, R. C. Blake, G. Plank, and N. Trayanova. "A novel rule-based algorithm for assigning myocardial fiber orientation to computational heart models." In: *Annals of Biomedical Engineering* 40 (2012), pp. 2243–2254.

[17] M. Bendahmane, R. Bürger, and R. Ruiz-Baier. "A finite volume scheme for cardiac propagation in media with isotropic conductivities." In: *Mathematics and Computers in Simulation* 80 (2010), pp. 1821–1840.

[18] M. Benzi, G. H. Golub, and J. Liesen. "Numerical solution of saddle point problems." In: *Acta numerica* 14 (2005), pp. 1–137.

[19] D. Bers. *Excitation-contraction coupling and cardiac contractile force*. Vol. 237. Springer Science & Business Media, 2001.

[20] P. J. Blanco, R. A. Feijóo, and et al. "A 3D-1D-0D computational model for the entire cardiovascular system." In: *Computational Mechanics, eds. E. Dvorking, M. Goldschmit, M. Storti* 29 (2010), pp. 5887–5911.

[21] D. Boffi, L. F. Pavarino, G. Rozza, and et al. *Mathematical and Numerical Modeling of the Cardiovascular System and Applications*. Vol. 16. Springer, 2018.

[22] D. Bonomi, A. Manzoni, and A. Quarteroni. "A matrix DEIM technique for model reduction of nonlinear parametrized problems in cardiac mechanics." In: *Computer Methods in Applied Mechanics and Engineering* 324 (2017), pp. 300–326.

[23] W. F. Boron and E. L. Boulpaep. *Medical Physiology*. Elsevier, 2016.

[24] M. Bucelli, M. Salvador, L. Dede', and A. Quarteroni. "Multipatch Isogeometric Analysis for Electrophysiology: Simulation in a Human Heart." In: *Computer Methods in Applied Mechanics and Engineering* 376 (2021), p. 113666.

[25] A. Bueno-Orovio, E. M. Cherry, and F. H. Fenton. "Minimal model for human ventricular action potentials in tissue." In: *Journal of Theoretical Biology* 253 (2008), pp. 544–560.

[26] M. D. Buhmann. *Radial Basis Functions: Theory and Implementations*. Cambridge University Press, 2003.

[27] L. Cai, L. Ren, Y. Wang, and et al. "Surrogate models based on machine learning methods for parameter estimation of left ventricular myocardium." In: *Royal Society Open Science* 8.1 (2021), p. 201121.

[28] C. Canuto, M. Y. Hussaini, A. Quarteroni, and T. Zang. *Spectral Methods. Fundamentals in Single Domains*. Springer, 2006.

[29] B. Carsten, C. W. Lucas, and G. Omar. "`p4est`: Scalable Algorithms for Parallel Adaptive Mesh Refinement on Forests of Octrees." In: *SIAM Journal on Scientific Computing* 33 (2011), pp. 1103–1133.

[30] M. Caruel and L. Truskinovsky. "Physics of muscle contraction." In: *Reports on Progress in Physics* 81.3 (2018), p. 036602.

[31] R. Chabiniok, V. Y. Wang, M. Hadjicharalambous, and et al. "Multiphysics and multiscale modelling, data-model fusion and integration of organ physiology in the clinic: ventricular cardiac mechanics." In: *Interface Focus* 6 (2016), pp. 15–83.

[32] D. Chapelle, M. A. Fernández, J. F. Gerbeau, and et al. "Numerical simulation of the electromechanical activity of the heart." In: *International Conference on Functional Imaging and Modeling of Heart* 5528 (2009), pp. 357–365.

[33] A. Cheng, F. Langer, F. Rodriguez, and et al. "Transmural cardiac strains in the lateral wall of the ovine left ventricle." In: *American Journal of Physiology. Heart and Circulatory Physiology* 288 (2005), pp. 1546–1556.

[34] P. Colli Franzone, L. F. Pavarino, and G. Savaré. "Computational electrocardiology: mathematical and numerical modeling." In: *Complex systems in Biomedicine*. Springer, 2006, pp. 187–241.

[35] P. Colli Franzone, L. F. Pavarino, and S. Scacchi. *Mathematical Cardiac Electrophysiology*. Springer, 2014.

[36] P. Colli Franzone, L. F. Pavarino, and S. Scacchi. "Effects of mechanical feedback on the stability of cardiac scroll waves: A bidomain electro-mechanical simulation study." In: *Chaos: An Interdisciplinary Journal of Nonlinear Science* 27.9 (2017), p. 093905.

[37] P. Colli Franzone, L. F. Pavarino, and S. Scacchi. "A Numerical Study of Scalable Cardiac Electro-Mechanical Solvers on HPC Architectures." In: *Frontiers in Physiology* 9 (2018), p. 268.

[38] A. Collin, S. Imperiale, P. Moireau, and et al. "Apprehending the effects of mechanical deformations in cardiac electrophysiology: A homogenization approach." In: *Mathematical Models and Methods in Applied Sciences* 29.13 (2019), pp. 2377–2417.

[39] R. Coppini, C. Ferrantini, L. Yao, and et al. "Late sodium current inhibition reverses electromechanical dysfunction in human hypertrophic cardiomyopathy." In: *Circulation* 127.5 (2013), pp. 575–584.

[40] C. M. Costa, E. Hoetzl, B. M. Rocha, and et al. "Automatic parameterization strategy for cardiac electrophysiology simulations." In: *Computing in Cardiology 2013*. IEEE. 2013, pp. 373–376.

[41] F. S. Costabal, F. A. Concha, D. E. Hurtado, and et al. "The importance of mechano-electrical feedback and inertia in cardiac electromechanics." In: *Computer Methods in Applied Mechanics and Engineering* 320 (2017), pp. 352–368.

[42] S. Coveney, C. Corrado, J. E. Oakley, and et al. "Bayesian Calibration of Electrophysiology Models using Restitution Curve Emulators." In: *Frontiers in Physiology* (2021), p. 1120.

[43] E. J. Crampin, M. Halstead, P. Hunter, and et al. "Computational physiology and the physiome project." In: *Experimental Physiology* 89.1 (2004), pp. 1–26.

[44] Y. Dabiri, A. Van der Velden, K. L. Sack, and et al. "Prediction of left ventricular mechanics using machine learning." In: *Frontiers in physics* 7 (2019), p. 117.

[45] L. Dede', A. Gerbi, and A. Quarteroni. "Segregated Algorithms for the Numerical Simulation of Cardiac Electromechanics in the Left Human Ventricle." In: *The Mathematics of Mechanobiology: Cetraro, Italy 2018*. Cham: Springer International Publishing, 2020, pp. 81–116.

[46] S. Deparis, D. Forti, and A. Quarteroni. "A Rescaled Localized Radial Basis Function Interpolation on Non-Cartesian and Nonconforming Grids." In: *SIAM Journal on Scientific Computing* 36 (2014).

[47] P. Di Achille, A. Harouni, S. Khamzin, and et al. "Gaussian process regressions for inverse problems and parameter searches in models of ventricular mechanics." In: *Frontiers in physiology* 9 (2018), p. 1002.

[48] G. Diamond and J. Forrester. "Effect of Coronary Artery Disease and Acute Myocardial Infarction on Left Ventricular Compliance in Man." In: *Circulation* 45 (1972), pp. 11–19.

[49] S. Doll and K. Schweizerhof. "On the development of volumetric strain energy functions." In: *Journal of Applied Mathematics* 67 (2000), pp. 17–21.

[50] R. Doste, D. Soto-Iglesias, and G. Bernardino. "A rule-based method to model myocardial fiber orientation in cardiac biventricular geometries with outflow tracts." In: *Numerical Methods in Biomedical Engineering* 35 (2019).

[51] P. Duchon. "Splines minimizing rotation invariant semi-norms in sobolev spaces." In: *Constructive Theory of Functions of Several Variables*. Springer, 1977, pp. 85–100.

[52] A. E. Epstein and et al. "ACC/AHA/HRS 2008 Guidelines for Device-Based Therapy of Cardiac Rhythm Abnormalities: a report of the American College of Cardiology/American Heart Association Task Force on Practice Guidelines (Writing Committee to Revise the ACC/AHA/NASPE 2002 Guideline Update for Implantation of Cardiac Pacemakers and Antiarrhythmia Devices): developed in collaboration with the American Association for Thoracic Surgery and Society of Thoracic Surgeons." In: *Circulation* 117 (2008), e350–e408.

[53] M. Fedele and A. Quarteroni. "Polygonal surface processing and mesh generation tools for the numerical simulation of the cardiac function." In: *International Journal for Numerical Methods in Biomedical Engineering* 37 (2021), e3435.

[54] C. A. Felippa, K. C. Park, and C. Farhat. "Partitioned analysis of coupled mechanical systems." In: *Computer Methods in Applied Mechanics and Engineering* 190.24 (2001), pp. 3247–3270.

[55] M. Fink, S. A. Niederer, E. M. Cherry, and et al. "Cardiac cell modelling: observations from the heart of the cardiac physiome project." In: *Progress in Biophysics and Molecular Biology* 104.1 (2011), pp. 2–21.

[56] D. Forti and L. Dede'. "Semi-implicit BDF time discretization of the Navier-Stokes equations with VMS-LES modeling in a High Performance Computing framework." In: *Computers & Fluids* 117 (2015), pp. 168–182.

[57] J. A. S. Freeman and D. Saad. "Learning and generalisation in radial basis function networks." In: *Neural computation* 7 (1995), pp. 1000–1020.

[58] S. Fresca, A. Manzoni, L. Dede', and A. Quarteroni. "Deep learning-based reduced order models in cardiac electrophysiology." In: *PLOS ONE* 15.10 (2020), pp. 1–32.

[59] A. Frontera, S. Pagani, L. R. Limite, and et al. "Outer loop and isthmus in ventricular tachycardia circuits: Characteristics and implications." In: *Heart Rhythm* 17.10 (2020), pp. 1719–1728.

[60] T. Gerach, S. Schuler, J. Fröhlich, and et al. "Electro-Mechanical Whole-Heart Digital Twins: A Fully Coupled Multi-Physics Approach." In: *Mathematics* 9.11 (2021).

[61] A. Gerbi, L. Dede', and A. Quarteroni. "A monolithic algorithm for the simulation of cardiac electromechanics in the human left ventricle." In: *Mathematics in Engineering* 1 (2018), pp. 1–37.

[62] P. Gervasio and A. Quarteroni. "The INTERNODES Method for Non-conforming Discretizations of PDEs." In: *Communications on Applied Mathematics and Computation* 1 (2019), pp. 361–401.

[63] P. Gervasio, L. Dede', O. Chanon, and A. Quarteroni. "Comparing Isogeometric Analysis and Spectral Element Methods: accuracy and spectral properties." In: *Journal of Scientific Computing* 83 (2020).

[64] S. Godunov. "A difference method for numerical calculation of discontinuous solutions of the equations of hydrodynamics." In: *Matematicheskii Sbornik* 89 (1959), pp. 271–306.

[65] S. Göktepe and E. Kuhl. "Electromechanics of the heart: a unified approach to the strongly coupled excitation-contraction problem." In: *Computational Mechanics* 45 (2010), pp. 227–243.

[66] A. M. Gordon, A. F. Huxley, and F. J. Julian. "The variation in isometric tension with sarcomere length in vertebrate muscle fibres." In: *The Journal of Physiology* 184 (1966), pp. 170–192.

[67] E. D. Grech. *ABC of Interventional Cardiology, 2nd edition*. John Wiley & Sons, 2011.

[68] B. E. Griffith and N. A. Patankar. "Immersed methods for fluid-structure interaction." In: *Annual Review of Fluid Mechanics* 52 (2020), pp. 421–448.

[69] J. M. Guccione and A. D. McCulloch. "Finite element modeling of ventricular mechanics." In: *Theory of Heart*. Springer, 1991, pp. 121–144.

[70] J. M. Guccione, A. D. McCulloch, and L. K. Waldman. "Passive material properties of intact ventricular myocardium determined from a cylindrical model." In: *Journal of Biomechanical Engineering* 113 (1991), pp. 42–55.

[71] V. Gurev, T. Lee, J. Constantino, H. Arevalo, and N. Trayanova. "Models of cardiac electromechanics based on individual hearts imaging data." In: *Biomechanics and Modeling in Mechanobiology* 10 (2011), pp. 295–306.

[72] R. A. Harrington, J. Narula, and Z. J. Eapen. *Hurst's the Heart*. MacGraw-Hill, 2011.

[73] A. Hazim, Y. Belhamadia, and S. Dubljevic. "A Simulation Study of the Role of Mechanical Stretch in Arrhythmogenesis during Cardiac Alternans." In: *Biophysical Journal* 120.1 (2021), pp. 109–121.

[74] E. Heiberg, J. Sjögren, and M. Ugander. "Design and validation of Segment-freely available software for cardiovascular image analysis." In: *BMC Medical Imaging* 10 (2010), pp. 1–13.

[75] J. Herman and W. Usher. "SALib: An open-source Python library for Sensitivity Analysis." In: *The Journal of Open Source Software* 2.9 (2017).

[76] M. Hirschvogel, M. Bassilious, L. Jagschies, and et al. "A monolithic 3D-0D coupled closed-loop model of the heart and the vascular system: Experiment-based parameter estimation for patient-specific cardiac mechanics." In: *International Journal for Numerical Methods in Biomedical Engineering* 33.8 (2017), e2842.

[77] G. A. Holzapfel and R. W. Ogden. "Constitutive modelling of passive myocardium: a structurally based framework for material characterization." In: *Mathematical, Physical and Engineering Sciences* 367 (2009), pp. 3445–3475.

[78] T. Homma and A. Saltelli. "Importance measures in global sensitivity analysis of nonlinear models." In: *Reliability Engineering & System Safety* 52.1 (1996), pp. 1–17.

[79] D. E. Hurtado, S. Castro, and P. Madrid. "Uncertainty quantification of 2 models of cardiac electromechanics." In: *International Journal for Numerical Methods in Biomedical Engineering* 33.12 (2017), e2894.

[80] Zygote Media Group Inc. *Zygote Solid 3D heart Generation II Development Report*. Technical Report. 2014.

[81] G. W. Jenkins, C. P. Kemnitz, and G. J. Tortora. *Anatomy and physiology: from science to life*. Wiley Hoboken, 2007.

[82] X. Jie, V. Gurev, and N. Trayanova. "Mechanisms of Mechanically Induced Spontaneous Arrhythmias in Acute Regional Ischemia." In: *Circulation Research* 106.1 (2010), pp. 185–192.

[83] A. M. Katz. *Physiology of the Heart*. Lippincott Williams & Wilkins, 2010.

[84] J. P. Keener and J. Sneyd. *Mathematical Physiology*. Vol. 1. Springer, 2009.

[85] R. H. Keldermann, M. P. Nash, H. Gelderblom, and et al. "Electromechanical wavebreak in a model of the human left ventricle." In: *American Journal of Physiology-Heart and Circulatory Physiology* 299.1 (2010), H134–H143.

[86] R. C. P. Kerckhoffs, M. L. Neal, Q. Gu, and et al. "Coupling of a 3D finite element model of cardiac ventricular mechanics to lumped systems models of the systemic and pulmonic circulation." In: *Annals of biomedical engineering* 35.1 (2007), pp. 1–18.

[87] R. Klabunde. *Cardiovascular Physiology Concepts*. Lippincott Williams & Wilkins, 2011.

[88] S. Klotz, I. Hay, M. L. Dickstein, and et al. "Single-beat estimation of end-diastolic pressure-volume relationship: a novel method with potential for noninvasive application." In: *American journal of physiology. Heart and circulatory physiology* 291 (2006), H403–H412.

[89]    P. Kohl, F. Sachs, and M. R. Franz. *Cardiac Mechano-Electric Coupling and Arrhythmias*. Oxford University Press, 2013.

[90]    B. Koplan and W. Stevenson. "Ventricular Tachycardia and Sudden Cardiac Death." In: *Mayo Clinic Proceedings* 84 (2009), pp. 289–297.

[91]    S. Krishnamoorthi, M. Sarkar, and W. S. Klug. "Numerical quadrature and operator splitting in finite element methods for cardiac electrophysiology." In: *International Journal for Numerical Methods in Biomedical Engineering* 29 (2003), pp. 1243–1266.

[92]    S. Land and S. A. Niederer. "Influence of atrial contraction dynamics on cardiac function." In: *International Journal for Numerical Methods in Biomedical Engineering* 34 (2018).

[93]    S. Land, S. A. Niederer, and N. Smith. "Efficient Computational Methods for Strongly Coupled Cardiac Electromechanics." In: *IEEE transactions on bio-medical engineering* 59 (2011), pp. 1219–28.

[94]    S. Land, S. J. Park-Holohan, N. P. Smith, and et al. "A model of cardiac contraction based on novel measurements of tension development in human cardiomyocytes." In: *Journal of Molecular and Cellular Cardiology* 106 (2017), pp. 68–83.

[95]    F. Levrero-Florencio, F. Margara, E. Zacur, and et al. "Sensitivity analysis of a strongly-coupled human-based electromechanical cardiac model: Effect of mechanical parameters on physiologically relevant biomarkers." In: *Computer methods in applied mechanics and engineering* 361 (2020), p. 112762.

[96]    *LifeV finite element library*. https://bitbucket.org/lifev-dev/lifev-release/wiki/Home.

[97]    M. Lloyd, J. Wight, F. Schneider, and et al. "Clinical experience of stereotactic body radiation for refractory ventricular tachycardia in advanced heart failure patients." In: *Heart Rhythm* 17 (2020), pp. 415–422.

[98]    S. Longobardi, A. Lewalle, S. Coveney, and et al. "Predicting left ventricular contractile function via Gaussian process emulation in aortic-banded rats." In: *Philosophical Transactions of the Royal Society A: Mathematical, Physical and Engineering Sciences* 378.2173 (2020), p. 20190334.

[99]    C. Luo and Y. Rudy. "A dynamic model of the cardiac ventricular action potential. I. Simulations of ionic currents and concentration changes." In: *Circulation Research* 74 (1994), pp. 1071–1096.

[100]   S. Marchesseau, H. Delingette, M. Sermesant, and et al. "Personalization of a cardiac electromechanical model using reduced order unscented Kalman filtering from regional volumes." In: *Medical Image Analysis* 17.7 (2013), pp. 816–829.

[101]   F. Margara, Z. J. Wang, F. Levrero-Florencio, and et al. "In-silico human electromechanical ventricular modelling and simulation for drug-induced pro-arrhythmia and inotropic risk assessment." In: *Progress in Biophysics and Molecular Biology* 159 (2021), pp. 58–74.

[102]   B. Martinez, W. Baker, A. Konopka, and et al. "Systematic review and meta-analysis of catheter ablation of ventricular tachycardia in ischemic heart disease." In: *Heart Rhythm* 17 (2020), e206–e219.

[103] L. Marx, M. A. F. Gsell, A. Rund, and et al. "Personalization of electro-mechanical models of the pressure-overloaded left ventricle: fitting of windkessel-type afterload models." In: *Philosophical Transactions of the Royal Society A: Mathematical, Physical and Engineering Sciences* 378.2173 (2020), p. 20190342.

[104] J. W. Mason, D. J. Ramseth, D. O. Chanter, and et al. "Electrocardiographic reference ranges derived from 79,743 ambulatory subjects." In: *Journal of Electrocardiology* 40 (2007), 228–234.e8.

[105] *Materialise Mimics website.* https://www.materialise.com/en/medical/mimics-innovation-suite/mimics.

[106] M. Minicucci, P. Azevedo, B. Polegato, and et al. "Heart Failure After Myocardial Infarction: Clinical Implications and Treatment." In: *Clinical Cardiology* 34 (2011), pp. 410–414.

[107] J. R. Mitchell and J. Wang. "Expanding application of the Wiggers diagram to teach cardiovascular physiology." In: *Advances in Physiology Education* 38.2 (2014), pp. 170–175.

[108] C. J. L. Murray, K. F. Ortblad, C. Guinovart, and et al. "Global, regional, and national incidence and mortality for hiv, tuberculosis, and malaria during 1990-2013: a systematic analysis for the global burden of disease study 2013." In: *The Lancet* 384 (2014), pp. 1005–1070.

[109] J. M. Nerbonne and W. Guo. "Heterogeneous expression of voltage-gated potassium channels in the heart: roles in normal excitation and arrhythmias." In: *Journal of cardiovascular electrophysiology* 13 (2002), pp. 406–409.

[110] S. A. Niederer, P. J. Hunter, and N. P. Smith. "A quantitative analysis of cardiac myocyte relaxation: a simulation study." In: *Biophysical Journal* 90.5 (2006), pp. 1697–1722.

[111] F. Nobile, A. Quarteroni, and R. Ruiz-Baier. "An active strain electromechanical model for cardiac tissue." In: *International Journal for Numerical Methods in Biomedical Engineering* 28 (2012), pp. 52–71.

[112] J. Nocedal and S. Wright. *Numerical optimization.* second. Springer Science & Business Media, 2006.

[113] D. A. Nordsletten, S. A. Niederer, M. P. Nash, and et al. "Coupling multi-physics models to cardiac mechanics." In: *Progress in Biophysics and Molecular Biology* 104 (2011), pp. 77–88.

[114] T. M. Nosek. *Essentials of Human Physiology.* Gold Standard Multimedia, 1998.

[115] R. W. Ogden. *Non-linear elastic deformations.* Dover Publications, 1997.

[116] A. Olivier, D.G. Giovanis, B.S. Aakash, and et al. "UQpy: A general purpose Python package and development environment for uncertainty quantification." In: *Journal of Computational Science* 47 (2020), p. 101204.

[117] J. H. Omens, K. D. May, and A. D. McCulloch. "Transmural distribution of three-dimensional strain in the isolated arrested canine left ventricle." In: *The American Journal of Physiology* 261 (1991), pp. 918–928.

[118] S. Pagani. "Reduced-order models for inverse problems and uncertainty quantification in cardiac electrophysiology." PhD thesis. Politecnico di Milano, 2017.

[119] S. Pagani and A. Manzoni. "Enabling forward uncertainty quantification and sensitivity analysis in cardiac electrophysiology by reduced order modeling and machine learning." In: *International Journal for Numerical Methods in Biomedical Engineering* (2021), e3450.

[120] S. Pagani, L. Dede', A. Frontera, and et al. "A Computational Study of the Electrophysiological Substrate in Patients Suffering From Atrial Fibrillation." In: *Frontiers in Physiology* 12 (2021), p. 927.

[121] S. Park, S. Hong, C. Ahn, and et al. "Different impacts of acute myocardial infarction on left ventricular apical and basal rotation." In: *European Heart Journal-Cardiovascular Imaging* 13 (2011), pp. 483–489.

[122] A. S. Patelli, L. Dede', T. Lassila, and et al. "Isogeometric approximation of cardiac electrophysiology models on surfaces: an accuracy study with application to the human left atrium." In: *Computer Methods in Applied Mechanics and Engineering* 317 (2017), pp. 248–273.

[123] P. Pathmanathan, J. M. Cordeiro, and R. A. Gray. "Comprehensive uncertainty quantification and sensitivity analysis for cardiac action potential models." In: *Frontiers in physiology* 10 (2019), p. 721.

[124] P. Pathmanathan, S. J. Chapman, D. J. Gavaghan, and J. P. Whiteley. "Cardiac electromechanics: the effect of contraction model on the mathematical problem and accuracy of the numerical scheme." In: *The Quarterly Journal of Mechanics & Applied Mathematics* 63.3 (2010), pp. 375–399.

[125] P. Pathmanathan, G. R. Mirams, J. Southern, and et al. "The significant effect of the choice of ionic current integration method in cardiac electro-physiological simulations." In: *International Journal for Numerical Methods in Biomedical Engineering* 27 (2011), pp. 1751–1770.

[126] P. Pathmanathan, M. O. Bernabeu, S. A. Niederer, and et al. "Computational modelling of cardiac electrophysiology: explanation of the variability of results from different numerical solvers." In: *International Journal for Numerical Methods in Biomedical Engineering* 28 (2012), pp. 890–903.

[127] L. Pegolotti, L. Dede', and A. Quarteroni. "Isogeometric Analysis of the electrophysiology in the human heart: Numerical simulation of the bidomain equations on the atria." In: *Computer Methods in Applied Mechanics and Engineering* 343 (2019), pp. 52–73.

[128] M. Peirlinck, F. S. Costabal, and et al. "Precision medicine in human heart modeling." In: *Biomechanics and Modeling in Mechanobiology* 20 (2021), pp. 803–831.

[129] M. Pfaller, J. Hörmann, M. Weigl, and et al. "The importance of the pericardium for cardiac biomechanics: from physiology to computational modeling." In: *Biomechanics and modeling in mechanobiology* 18 (2019), pp. 503–529.

[130] R. Piersanti, P. C. Africa, M. Fedele, and et al. "Modeling cardiac muscle fibers in ventricular and atrial electrophysiology simulations." In: *Computer Methods in Applied Mechanics and Engineering* 373 (2021), p. 113468.

[131] R. Piersanti, F. Regazzoni, M. Salvador, and et al. "3D-0D closed-loop model for the simulation of cardiac biventricular electromechanics." In: *MOX Report 57* (Politecnico di Milano, 2021).

[132] M. Potse, B. Dubé, J. Richer, and et al. "A comparison of monodomain and bidomain reaction-diffusion models for action potential propagation in the human heart." In: *IEEE Transactions on Biomedical Engineering* 53 (2006), pp. 2425–2435.

[133] A. Prakosa, H. Arevalo, D. Dongdong, and et al. "Personalized virtual-heart technology for guiding the ablation of infarct-related ventricular tachycardia." In: *Nature Biomedical Engineering* 2 (2018), pp. 732–740.

[134] A. Quarteroni. *Numerical Models for Differential Problems*. Springer, 2017.

[135] A. Quarteroni, A. Manzoni, and F. Negri. *Reduced Basis Methods for Partial Differential Equations. An Introduction*. Vol. 92. Springer, 2016.

[136] A. Quarteroni, R. Sacco, and F. Saleri. *Numerical Mathematics*. Springer, 2010.

[137] A. Quarteroni, T. Lassila, S. Rossi, and et al. "Integrated heart - coupling multiscale and multiphysics models for the simulation of the cardiac function." In: *Computer Methods in Applied Mechanics and Engineering* 314 (2017), pp. 345–407.

[138] A. Quarteroni, L. Dede', A. Manzoni, and C. Vergara. *Mathematical Modelling of the Human Cardiovascular System: Data, Numerical Approximation, Clinical Applications*. Cambridge University Press, 2019.

[139] T. A. Quinn and P. Kohl. "Combining wet and dry research: experience with model development for cardiac mechano-electric structure-function studies." In: *Cardiovascular Research* 97 (2013), pp. 601–611.

[140] F. Regazzoni, L. Dede', and A. Quarteroni. "Active contraction of cardiac cells: a model for sarcomere dynamics with cooperative interactions." In: *Biomechanics and modeling in mechanobiology* 17 (2018), pp. 1663–1686.

[141] F. Regazzoni, L. Dede', and A. Quarteroni. "Machine learning for fast and reliable solution of time-dependent differential equations." In: *Journal of Computational Physics* 397 (2019), p. 108852.

[142] F. Regazzoni, L. Dede', and A. Quarteroni. "Biophysically detailed mathematical models of multiscale cardiac active mechanics." In: *PLoS computational biology* 16 (2020), e1008294.

[143] F. Regazzoni, L. Dedè, and A. Quarteroni. "Machine learning of multiscale active force generation models for the efficient simulation of cardiac electromechanics." In: *Computer Methods in Applied Mechanics and Engineering* 370 (2020), p. 113268.

[144] F. Regazzoni, L. Dedè, and A. Quarteroni. "Machine learning of multiscale active force generation models for the efficient simulation of cardiac electromechanics." In: *Computer Methods in Applied Mechanics and Engineering* 370 (2020), p. 113268.

[145] F. Regazzoni and A. Quarteroni. "Accelerating the convergence to a limit cycle in 3D cardiac electromechanical simulations through a data-driven 0D emulator." In: *Computers in Biology and Medicine* 135 (2021), p. 104641.

[146] F. Regazzoni and A. Quarteroni. "An oscillation-free fully partitioned scheme for the numerical modeling of cardiac active mechanics." In: *Computer Methods in Applied Mechanics and Engineering* 373 (2021), p. 113506.

[147] F. Regazzoni, M. Salvador, P. C. Africa, and et al. "A cardiac electromechanics model coupled with a lumped parameters model for closed-loop blood circulation. Part I: model derivation." In: *arXiv preprint arXiv:2011.15040* (2020).

[148] F. Regazzoni, M. Salvador, P. C. Africa, and et al. "A cardiac electromechanics model coupled with a lumped parameters model for closed-loop blood circulation. Part II: numerical approximation." In: *arXiv preprint arXiv:2011.15051* (2020).

[149] F. Regazzoni, M. Salvador, L. Dede', and A. Quarteroni. "A machine learning method for real-time numerical simulations of cardiac electromechanics." In: *arXiv preprint arXiv:2110.13212* (2021).

[150] J. J. Rice, F. Wang, D. M. Bers, and P. P. de Tombe. "Approximate model of cooperative activation and crossbridge cycling in cardiac muscle using ordinary differential equations." In: *Biophysical Journal* 95.5 (2008), pp. 2368–2390.

[151] D. Romero, R. Sebastian, B. H. Bijnens, and et al. "Effects of the Purkinje system and cardiac geometry on biventricular pacing: a model study." In: *Annals of Biomedical Engineering* 38 (2010), pp. 1388–1398.

[152] S. Rossi, R. Ruiz-Baier, L. F. Pavarino, and A. Quarteroni. "Orthotropic active strain models for the numerical simulation of cardiac biomechanics." In: *International journal for numerical methods in biomedical engineering* 28 (2012), pp. 761–788.

[153] S. Rossi, T. Lassila, R. Ruiz-Baier, and et al. "Thermodynamically consistent orthotropic activation model capturing ventricular systolic wall thickening in cardiac electromechanics." In: *European Journal of Mechanics - A/Solids* 48 (2014), pp. 129–142.

[154] C. F. Royse and A. G. Royse. "The myocardial and vascular effects of bupivacaine, levobupivacaine, and ropivacaine using pressure volume loops." In: *Anesthesia & Analgesia* 101 (2005), pp. 679–687.

[155] R. Ruiz-Baier, A. Gizzi, S. Rossi, and et al. "Mathematical modelling of active contraction in isolated cardiomyocytes." In: *Mathematical Medicine and Biology: a Journal of the IMA* 31 (2014), pp. 259–283.

[156] K. L. Sack, E. Aliotta, D. B. Ennis, and et al. "Construction and Validation of Subject-Specific Biventricular Finite-Element Models of Healthy and Failing Swine Hearts From High-Resolution DT-MRI." In: *Frontiers in Physiology* 9 (2018), p. 539.

[157] J. E. Saffitz, H. L. Kanter, K. G. Green, and et al. "Tissue-specific determinants of anisotropic conduction velocity in canine atrial and ventricular myocardium." In: *Circulation Research* 74 (1994), pp. 1065–1070.

[158] J. Sainte-Marie, D. Chapelle, R. Cimrman, and et al. "Modeling and estimation of the cardiac electromechanical activity." In: *Computers & Structures* 84 (2006), pp. 1743–1759.

[159] S. Sakamoto, T. Nitta, Y. Ishii, and et al. "Interatrial electrical connections: the precise location and preferential conduction." In: *Journal of Cardiovascular Electrophysiology* 16 (10 2005), pp. 1077–1086.

[160] A. Saltelli. "Making best use of model evaluations to compute sensitivity indices." In: *Computer physics communications* 145.2 (2002), pp. 280–297.

[161]  M. Salvador, L. Dede', and A. Quarteroni. "An intergrid transfer operator using radial basis functions with application to cardiac electromechanics." In: *Computational Mechanics* 66 (2020), pp. 491–511.

[162]  M. Salvador, M. Fedele, P. C. Africa, and et al. "Electromechanical modeling of human ventricles with ischemic cardiomyopathy: numerical simulations in sinus rhythm and under arrhythmia." In: *Computers in Biology and Medicine* 136 (2021), p. 104674.

[163]  M. Salvador, F. Regazzoni, S. Pagani, and et al. "The role of mechano-electric feedbacks and hemodynamic coupling in scar-related ventricular tachycardia." In: *Computers in Biology and Medicine* (2022), p. 105203.

[164]  F. H. Samie and J. Jalife. "Mechanisms underlying ventricular tachycardia and its transition to ventricular fibrillation in the structurally normal heart." In: *Cardiovascular research* 50 (2001), pp. 242–250.

[165]  A. M. Scher. "The sequence of ventricular excitation." In: *The American Journal of Cardiology* 14 (1964), pp. 287–293.

[166]  W. J. Schroeder, B. Lorensen, and K. Martin. *The visualization toolkit: an object-oriented approach to 3D graphics*. Kitware, 2004.

[167]  J. K. Shade, A. Prakosa, D. M. Popescu, and et al. "Predicting risk of sudden cardiac death in patients with cardiac sarcoidosis using multimodality imaging and personalized heart modeling in a multivariable classifier." In: *Science Advances* 7.31 (2021).

[168]  A. A. Sher, K. Wang, A. Wathen, and et al. "A local sensitivity analysis method for developing biological models with identifiable parameters: Application to cardiac ionic channel modelling." In: *Future Generation Computer Systems* 29.2 (2013), pp. 591–598.

[169]  Y. Shirai, J. Liang, P. Santangeli, and et al. "Comparison of the Ventricular Tachycardia Circuit Between Patients With Ischemic and Nonischemic Cardiomyopathies." In: *Circulation: Arrhythmia and Electrophysiology* 12 (2019), e007249.

[170]  D. Sidebotham and I. Le Grice. "Chapter 1-Physiology and Pathophysiology." In: *Cardiothoracic Critical Care*. Butterworth-Heinemann, 2007, pp. 3–27.

[171]  N. P. Smith, D. P. Nickerson, E. J. Crampin, and et al. "Multiscale computational modelling of the heart." In: *Acta Numerica* 13 (2004), pp. 371–431.

[172]  I. M. Sobol'. "On sensitivity estimation for nonlinear mathematical models." In: *Matematicheskoe modelirovanie* 2.1 (1990), pp. 112–118.

[173]  M. Strocchi, C. M. Augustin, M. A. F. Gsell, and et al. "A publicly available virtual cohort of four-chamber heart meshes for cardiac electro-mechanics simulations." In: *PLOS ONE* 15 (2020), pp. 1–26.

[174]  M. Strocchi, M. A. F. Gsell, C. M. Augustin, and et al. "Simulating ventricular systolic motion in a four-chamber heart model with spatially varying robin boundary conditions to model the effect of the pericardium." In: *Journal of Biomechanics* 101 (2020), p. 109645.

[175]  J. Sundnes, G. T. Lines, X. Cai, and et al. *Computing the Electrical Activity in the Heart*. Vol. 1. Springer, 2007.

[176] E. Sung, A. Prakosa, K. N. Aronis, and et al. "Personalized Digital-Heart Technology for Ventricular Tachycardia Ablation Targeting in Hearts With Infiltrating Adiposity." In: *Circulation: Arrhythmia and Electrophysiology* 13.12 (2020), e008912.

[177] P. Taggart and P. M. Sutton. "Cardiac mechano-electric feedback in man: clinical relevance." In: *Progress in Biophysics and Molecular Biology* 71.1 (1999), pp. 139–154.

[178] *The Vascular Modeling Toolkit website*. www.vmtk.org.

[179] V. Timmermann, L. A. Dejgaard, K. Haugaa, and et al. "An integrative appraisal of mechano-electric feedback mechanisms in the heart." In: *Progress in biophysics and molecular biology* 130 Pt B (2017), pp. 404–417.

[180] J. Tomek, A. Bueno-Orovio, E. Passini, and et al. "Development, calibration, and validation of a novel human ventricular myocyte model in health, disease, and drug block." In: *eLife* 8 (2019), e48890.

[181] K. Tøndel, S. Land, S. A. Niederer, and N. P. Smith. "Quantifying inter-species differences in contractile function through biophysical modelling." In: *The Journal of Physiology* 593.5 (2015), pp. 1083–1111.

[182] G. J. Tortora and B. H. Derrickson. *Principles of anatomy and physiology*. John Wiley & Sons, 2008.

[183] N. Trayanova. "Whole-heart modeling: applications to cardiac electrophysiology and electromechanics." In: *Circulation Research* 108 (2011), pp. 113–128.

[184] N. Trayanova, W. Li, J. Eason, and P. Kohl. "Effect of stretch-activated channels on defibrillation efficacy." In: *Heart Rhythm* 1 (June 2004), pp. 67–77.

[185] K. H. W. J. ten Tusscher and A. V. Panfilov. "Alternans and spiral breakup in a human ventricular tissue model." In: *American Journal of Physiology-Heart and Circulatory Physiology* 291 (2006), H1088–H1100.

[186] K. H. ten Tusscher and A. V. Panfilov. "Alternans and spiral breakup in a human ventricular tissue model." In: *American Journal of Physiology. Heart and Circulatory Physiology* 291 (2006), pp. 1088–1100.

[187] T. P. Usyk, I. J. LeGrice, and A. D. McCulloch. "Computational model of three-dimensional cardiac electromechanics." In: *Computing and Visualization in Science* 4 (2002), pp. 249–257.

[188] M. Varela, A. Roy, and J. Lee. "A survey of pathways for mechano-electric coupling in the atria." In: *Progress in Biophysics and Molecular Biology* 159 (2021), pp. 136–145.

[189] M. Vázquez, R. Arís, J. Aguado-Sierra, and et al. "Alya Red CCM: HPC-based cardiac computational modelling." In: *Selected topics of computational and experimental fluid mechanics*. Springer, 2015, pp. 189–207.

[190] C. Vergara, M. Lange, S. Palamara, and et al. "A coupled 3D-1D numerical monodomain solver for cardiac electrical activation in the myocardium with detailed Purkinje network." In: *Journal of Computational Physics* 308 (2016), pp. 218–238.

[191] E. J. Vigmond, M. Hughes, G. Plank, and L. Joshua Leon. "Computational tools for modeling electrical activity in cardiac tissue." In: *Journal of Electrocardiology* 36 (2003), pp. 69–74.

[192]  E. J. Vigmond, C. Clements, D. M. McQueen, and C. S. Peskin. "Effect of bundle branch block on cardiac output: a whole heart simulation study." In: *Progress in Biophysics and Molecular Biology* 97.2-3 (2008), pp. 520–542.

[193]  E. J. Vigmond, R. Weber dos Santos, A. J. Prassl, and et al. "Solvers for the cardiac bidomain equations." In: *Progress in Biophysics and Molecular Biology* 96.1 (2008), pp. 3–18.

[194]  G. Vigueras, I. Roy, A. Cookson, and et al. "Toward GPGPU accelerated human electromechanical cardiac simulations." In: *International journal for numerical methods in biomedical engineering* 30.1 (2014), pp. 117–134.

[195]  Z. J. Wang, A. Santiago, X. Zhou, and et al. "Human biventricular electromechanical simulations on the progression of electrocardiographic and mechanical abnormalities in post-myocardial infarction." In: *EP Europace* 23.Supplement1 (2021), pp. i143–i152.

[196]  T. Washio, K. Yoneda, J. Okada, and et al. "Ventricular fiber optimization utilizing the branching structure." In: *International Journal for Numerical Methods in Biomedical Engineering* (2015).

[197]  N. Westerhof, J. W. Lankhaar, and B. E. Westerhof. "The arterial windkessel." In: *Medical & Biological Engineering & Computing* 47 (2009), pp. 131–141.

[198]  C. Carton de Wiart, L. T. Diosady, A. Garai, and et al. "Design of a modular monolithic implicit solver for multi-physics applications." In: *2018 AIAA Aerospace Sciences Meeting*. 2018, p. 1400.

[199]  Wikipedia. *Heart conduction system - Wikipedia, The Free Encyclopedia*. `https://en.wikipedia.org/wiki/File:RLS_12blauLeg.png`.

[200]  Wikipedia. *Heart walls - Wikipedia, The Free Encyclopedia*. `https://en.wikipedia.org/wiki/File:2004_Heart_Wall.jpg`.

[201]  Wikipedia. *Wiggers diagram - Wikipedia, The Free Encyclopedia*. `https://it.wikipedia.org/wiki/File:Wiggers_Diagram_IT.svg`.

[202]  S. Willems, R. Tilz, D. Steven, and et al. "Preventive or Deferred Ablation of Ventricular Tachycardia in Patients with Ischemic Cardiomyopathy and Implantable Defibrillator (BERLIN VT): A Multicenter Randomized Trial." In: *Circulation* (2020).

[203]  A. L. Wit and M. R. Rosen. "Pathophysiologic mechanisms of cardiac arrhythmias." In: *Heart Rhythm* 17 (1983), pp. 798–811.

[204]  L. A. Woodworth, B. Cansiz, and M. Kaliske. "A numerical study on the effects of spatial and temporal discretization in cardiac electrophysiology." In: *International Journal for Numerical Methods in Biomedical Engineering* 37.5 (2021), e3443.

[205]  J. Xi, P. Lamata, J. Lee, and et al. "Myocardial transversely isotropic material parameter estimation from in-silico measurements based on a reduced-order unscented Kalman filter." In: *Journal of the mechanical behavior of biomedical materials* 4.7 (2011), pp. 1090–1102.

[206]  T. Yamada and G. N. Kay. "Optimal ablation strategies for different types of ventricular tachycardias." In: *Nature Reviews Cardiology* 9 (2012), pp. 512–525.

[207]  F. C. Yin, C. C. Chan, and R. M. Judd. "Compressibility of perfused passive myocardium." In: *American Journal of Physiology. Heart and Circulatory Physiology* 271 (1996), pp. 1864–1870.

[208]  O. C. Zienkiewicz and J. Z. Zhu. "The superconvergent patch recovery and a posteriori error estimates. Part 1: The recovery technique." In: *International Journal for Numerical Methods in Engineering* 33 (1992), pp. 1331–1364.

[209]  O. C. Zienkiewicz and J. Z. Zhu. "The superconvergent patch recovery and a posteriori error estimates. Part 2: Error estimates and adaptivity." In: *International Journal for Numerical Methods in Engineering* 33 (1992), pp. 1365–1382.